Experiments and modeling on an air-water interface populated by biological molecules

Yu-Lin Huang

Experiments and Modeling on an Air-water Interface Populated by Biological Molecules

by

Yu-Lin Huang

A dissertation submitted in partial satisfaction
of the requirements for the degree of

Doctor of Philosophy

in

Mechanics and Energy

in the

GRADUATE DIVISION

of the

Université Joseph Fourier - Grenoble I
National Taiwan University

Committee in charge:

Advisors:	Prof. Laurent Davoust (Examiner)
	Prof. Shuo-Hung Chang (Examiner)
Chair:	Prof. Shyan-Fu Chou (Chairman)
	Prof. Nicolas Riviere (Reviewer)
	Prof. Tong-Miin Liou (Reviewer)
	Prof. Horn-Jiunn Sheen (Examiner)

October 20, 2009

Université Joseph Fourier – Grenoble I & National Taiwan University

T H E S E

pour obtenir le grade de

Docteur de l'UJF & NTU

Spécialité : **Mécanique des Fluides et Transfers**

préparée au **Laboratoire des Ecoulements Géophysiques et Industriels**

dans le cadre de l'**Ecole Doctorale Mécanique et Énergétique**

présentée et soutenue publiquement

par :

Yu-Lin HUANG

le _____

Ecoulement d'un Film de Biomolécules Tensioactives : Expériences et Modélisation

Directeur de thèse : Laurent DAVOUST

Co-Directeur de thèse : Shuo-Hung CHANG

JURY

M. Nicolas RIVIERE, Rapporteur

M. Tong-Miin LIOU, Rapporteur

M. Laurent DAVOUST, Directeur de thèse

M. Shuo-Hung CHANG, Co-directeur de thèse

M. Shyan-Fu CHOU, Examinateur

M. Horn-Jiunn SHEEN, Examinateur

國立臺灣大學工學院機械工程學系

博士論文

Department of Mechanical Engineering
College of Engineering
National Taiwan University

Doctoral Dissertation

生物分子聚集於空氣–水界面之實驗及模擬

Experiments and Modeling on an Air-water Interface Populated by Biological Molecules

黃裕霖

Yu-Lin Huang

指導教授：達悟士 博士 和 張所鋐 教授

Advisor: Dr. Laurent Davoust & Prof. Shuo-Hung Chang

中華民國98年10月

October, 2009

Experiments and Modeling on an Air-water Interface Populated by Biological Molecules

by

Yu-Lin Huang

Abstract

Experiments and Modeling on an Air-water Interface Populated by Biological Molecules

by

Yu-Lin Huang

This dissertation is the first stage of a research program devoted to the development of a new hydrodynamic process in which the object is to facilitate the recognition of certain important proteins structures (such as membrane protein) in the field of molecular biology. The major objective is to find hydrodynamic conditions which favor the growth of a two-dimensional (2-D) crystal of proteins at a chemically-functionnalized air-water interface. It includes researching the best hydrodynamic conditions for growing 2-D crystal protein sufficiently large and regular, e.g. a single (mono) crystal. Obtaining such a single (mono) crystal would helpful for X-ray diffraction technique to identify the primary structure of a protein rapidly.

The state of the art today is based upon a water surface at rest, functionalized (covered) by a monolayer of lipids thus obtained for Langmuir film (nanometer thick) at equilibrium. Under the effect of chemical diffusion within water subphase, solubilize dproteins in the subphase adsorb to the lipids specifically designed to trap them (consider for instance the molecular complex [biotinylated lipid–avidin protein]). A protein crystal obtained at 2-D interface limited to its 2-D diffusion in the lipid monolayer is more like a crystalline powder. The irregularity of the molecular self-assembly in the crystalline powder is particularly ill-suited to the X-ray diffraction technique to identify its structure.

The aim of this dissertation is to control a recirculating flow in the subphase to:

◇ accelerate the capture of proteins to lipids presented in the liquid surface,

◇ densification of 2-D complexes [lipid–protein] after adsorption,

◇ ultimately, should logically lead to a 2-D single crystal assembly.

This dissertation contributes to the experimental and modeling tools needed to develop a enhanced 2-D single crystal protein assembly.

Initially, we used a fatty acid (pentadecanoic acid) to anticipate the behavior of a lipid monolayer subjected to flow structuring. To test this concept, an experiment based on an annular tank has been developed and

A first part of this dissertation is devoted to the experimental set-up which is based upon an annular channel whose floor is put in rotation whilst its two vertical (cylindrical) side walls are maintained stationary. The channel is filled with a supporting subphase of acidified ultra-pure water. In order to confirm the feasibility of a flow-induced molecular densification, the user-friendly pentadecanoic acid (PDA) is chosen to mimic the response of a lipidic Langmuir monolayer when it is put out of equilibrium. A monolayer of PDA is therefore submitted to an annular shear flow. we have studied the behavior of a monolayer of pentadecanoic acid (PDA) simultaneously subject to two types of shear, one is in-plane shear, the other one is subphase shear valued at the surface. It is worthy to note that transition between liquid-expanded and liquid-condensed phases is conserved even in conditions far from thermodynamical equilibrium. Brewster angle microscopy (BAM) is used to image selectively the mesoscopic morphology of the subsequent two-phase PDA film. The area fraction of the condensed phase is carefully investigated after a permanent regime is established. The distribution of the area fraction demonstrates radially-inwards packing along the liquid surface which is induced by a centripetal surface flow originating from centrifugation of subphase along the rotating floor. For a growing level of centrifugation, a circular segregation front arises along the liquid surface. For a high enough level of centrifugation, the Langmuir film even experiences a strong morphological transition driven by a balance between surface shearing and reduced line tension. As a result, a

shear-induced melting of the condensed phase generates a new patterning which can be described as a 2-D monodispersed matrix of tiny condensed droplets.

The last part of this dissertation is devoted to modelling the previous annular shear flow. The liquid surface at the top of the channel is again supposed to be covered by a layer of chemically-functionnalised hydrophobic molecules. The flow is considered as permanent, axisymmetric and creeping. The ratio of the liquid depth to the outer radius of the channel is small enough (shallow flow) so that it is possible to develop a matched asymptotic technique. In the rotating subphase, a core flow is therefore distinguished from the boundary layers along side walls. The modeling includes the possibility to take into account the impact of the radially-inwards molecular packing induced by centrifugation of the underlying bulk. More particularly, radial stratification of surface viscosity is taken into account *via* the jump momentum balance at the liquid surface (Boussinesq-Scriven balance).

Résumé

Ecoulement d'un Film de Biomolécules Tensioactives : Expériences et Modélisation

par

Yu-Lin Huang

Cette thèse constitue la première étape d'un programme de recherche consacré à l'élaboration d'un nouveau procédé hydrodynamique dont l'enjeu est de faciliter la reconnaissance structurale de certaines protéines importantes dans le domaine de la biologie moléculaire (les protéines membranaires par exemple). L'objectif à moyen terme est de mettre au point un procédé de croissance bidimensionnelle (2-D) de cristaux de protéines à une interface eau-air fonctionnalisée chimiquement. Il s'agit notamment de rechercher les meilleures conditions hydrodynamiques pour obtenir un cristal 2-D de protéine suffisamment large et régulier, par exemple un monocristal. L'obtention d'un tel monocristal permettrait d'identifier rapidement la structure primaire d'une protéine élémentaire en s'adaptant parfaitement à une technique de diffraction par rayons X sous incidence rasante.

L'état de l'art actuel consiste à utiliser une surface d'eau au repos, fonctionnalisée (recouverte) par une monocouche de lipides : on obtient ainsi un film de Langmuir (épaisseur nanométrique) à l'équilibre. Sous l'effet de la diffusion chimique en sous-phase, des protéines solubilisées dans la sous-phase aqueuse s'adsorbent à la monocouche lipidique dès lors que les lipides sont choisis pour s'apparier aux protéines (lipides ligands, exemple typique d'appariement lipide biotynilé – avidine). Un cristal de protéine, plus ou moins régulier, s'apparentant davantage à une poudre cristalline est classiquement obtenu en 2-D sous l'effet de la seule diffusion 2-D dans la monocouche lipidique. L'irrégularité de l'auto-assemblage moléculaire dans cette poudre cristalline se prête particulièrement mal à la diffraction aux rayons X.

L'objectif de la thèse est de contrôler un écoulement recirculant dans la sous-phase afin :

- ◇ d'accélérer la capture des protéines aux lipides présents à la surface liquide,
- ◇ de densifier en 2-D après adsorption les complexes [lipide – protéine],
- ◇ ce qui, à terme, devrait logiquement mener à un assemblage moléculaire 2-D plus régulier.

Cette thèse contribue ainsi à mettre en place les outils expérimentaux et théoriques nécessaires au développement d'un futur procédé de cristallisation en 2-D.

Dans un premier temps, nous avons utilisé un acide gras (acide pentadecanoïque) afin d'anticiper sur le comportement d'une monocouche lipidique assujettie à un écoulement structurant. Pour cela, une expérience basée sur une cuve annulaire a été développée et nous avons étudié le comportement d'une monocouche d'acide pentadecanoïque (PDA) soumise simultanément à deux types de cisaillement, l'un de nature volumique, l'autre de nature intrinsèquement surfacique. Ces deux cisaillements sont produits par la rotation d'une couronne annulaire aimantée disposée au fond de la cuve annulaire. D'un point de vue conditions aux limites hydrodynamiques, un écoulement annulaire cisaillé de nature toroïdale (ou *swirl*), est ainsi engendré par un fond tournant tandis que les deux parois verticales du canal demeurent fixes. Une nouvelle organisation mésoscopique dans le film de PDA, sous la forme de deux phases 2-D (dites liquide expansée et liquide condensée), a été mise en évidence et étudiée en régime permanent. En mesurant par microscopie Brewster la distribution de la fraction aréolaire de phase condensée le long de l'interface, nous avons montré que l'écoulement centrifuge le long du fond tournant engendre un écoulement radial centripète le long de l'interface (par conservation de la masse) et que celui-ci privilégie la condensation de domaines liquides condensés vers les rayons les plus petits. Pour un niveau suffisamment important de centrifugation, le film de Langmuir expérimente une transition morphologique marquée, pilotée par un équilibre entre le cisaillement

de surface et la tension de ligne (analogue 1-D de la tension de surface). Nous avons montré en particulier qu'un cisaillement surfacique non négligeable peut induire la fusion des domaines condensés et engendrer une nouvelle organisation morphologique sous la forme d'une matrice monodispersée de gouttelettes 2-D condensés.

La dernière partie de la thèse est consacrée à une modélisation analytique de l'écoulement annulaire cisaillé lorsque la surface liquide est recouverte par une distribution radiale de tensioactifs. L'écoulement est considéré comme permanent, axisymétrique et rampant (petit nombre de Reynolds, approximation de Stokes). A l'instar des expériences réalisées durant la thèse, le rapport de la profondeur liquide au rayon extérieur du canal est également considéré comme petit, ce qui permet l'usage de développements asymptotiques raccordés. Cette modélisation intégre la stratification radiale de la viscosité surfacique due à la densification moléculaire engendrée par la composante centripète de l'écoulement le long de l'interface (prise en compte éventuelle de la présence d'un cristal de protéines à une monocouche lipidique restructurée par un écoulement).

摘要

生物分子聚集於空氣-水界面之實驗及模擬

黃裕霖 撰

本文屬最初階段的研究計劃，致力於開發一個新的流體力學的方法，以實現辨識分子生物學中某些重要的蛋白質結構（例如:薄膜蛋白質）。其主要目標是建立在空氣-水的化學官能界面中，增長二維蛋白質晶體的流體力學條件。這包括尋找最佳的流體力學條件，以大量且穩定的增長二維蛋白質晶體，即單分子層蛋白質晶體。獲得這種單分子層晶體將能利用X-射線繞射的技術進一步分析蛋白質結構。

目前發展中的技術主要是利用靜置的水面上先覆蓋單分子層的脂質（在平衡狀態下產生的Langmuir膜，僅奈米大小的厚度）。溶解於亞相(subphase)水溶液中的蛋白質分子，在化學擴散的作用下，會選擇性的吸附（結合）於單分子層的脂質膜，形成脂質複合體（典型的脂質複合體，例如:生物血脂-抗生物素蛋白）。這種方式在界面中所形成蛋白晶體，受限於單分子層脂質膜在界面中的二維擴散，或多或少會形成類似於粉末狀結晶體。不規則的分子自我組裝所形成的粉末狀結晶體，不適合利用X射線繞射的技術來分析其蛋白質的結構。

本論文的概念是藉由控制亞相水溶液的循環流動，讓：

◇ 蛋白質分子加快吸附於亞相水溶液介面上的脂質，自我組裝為脂質複合體（脂質-蛋白質），

◇ 讓吸附於界面中的脂質複合體排列緊密，

◇ 最終使二維分子的自我組裝更加容易，以形成排列整齊的二維蛋白質晶體。

利用這樣的概念，我們建立實驗和理論的工具，以利於實現一個促進二維蛋白

質晶體生長的過程。

首先，我們使用脂肪酸（十五碳酸，pentadecanoic acid）模擬單分子層的脂質膜結構受到流動影響下的行為。要實現這樣的構想，實驗裝置設計為一環形渠道，由環形渠道底部的環形磁環旋轉而渠道兩側的垂直壁面固定不動，產生剪切性質的流動（或漩渦）。從流體力學的觀點來看，這樣的流動會使渠道的界面上所形成的單分子層的十五碳酸（或十五碳酸薄膜）同時受到兩種類型的剪應力（一個是渠道整體流動所造成的剪應力，另一個是界面上的流動所造成的剪應力）。我們研究十五碳酸單分子層同時承受這兩個剪應力時的行為。在十五碳酸薄膜中新的界觀的組織結構所形成的二維的共存相（即所謂的擴散液體相和壓縮液體相）仍被維持，即使其完全不在熱力學穩態平衡狀態下。利用Brewster角顯微鏡，測量界面中十五碳酸薄膜的壓縮液體相的分量分佈，我們已經證實，渠道底部的旋轉讓亞相水溶液流動而造成的離心力，會在亞相水溶液的界面（以大部分數據的觀察）產生一個沿徑向方向上向心力量的流動，它有利於壓縮液體相聚集在靠近渠道表面半徑較小處。在一個夠大的離心力作用下，Langmuir薄膜（十五碳酸薄膜）經由明顯的形態(或稱為圖案結構，這裡指的是擴散液體相和壓縮液體相兩相共存的分佈狀態)上的轉變，維持剪應力和線張力(類似一維表面張力)兩者之間的平衡。因此，剪切所導致的壓縮液體相的熔化，會生成新的圖案結構，類似一個二維驅散的小凝結液滴。

論文最後我們建立一個分析前述環形渠道剪切流動的數學模型。渠道上方的液體表面覆蓋一層表面活性劑。假設流體流動為永久的，軸對稱且為潛變流（低Reynolds數，Stokes近似）。由於亞相水溶液深度和渠道外徑的比值夠小（淺流），所以能發展漸近匹配技術來求解。在旋轉的亞相液體中，核心流動可以從沿著側壁的邊界層區分出來。該模型能考慮到由離心力所造成的渠道表面徑向方向上分子向內(半徑較小處)聚集的影響。更具體地說，此數學模型藉由考慮在液體表面的突然轉變之動量平衡（Boussinesq-Scriven平衡），來分析徑向方向表面粘度的分層現象。

Contents

List of Tables

List of Figures

List of Symbols

a	area of the interface, Eq. (3.1); mean molecular area occupied by one PDA molecule
a, b, c	constants, Eq. (6.24)
A	molecular area
A_{image}	(total) area of BAM image, Eq. (4.1)
A_{LC}	area of liquid condensed (LC) phase, Eq. (4.1)
$A_{LC,t}$	total area of LC phase
A_{LE}	area of liquid expanded (LE) phase, Eq. (4.1)
$A_{LE,t}$	total area of LE phase
$A(r^*)$	coefficient of Green function $G(r^*\|\xi)$, Eq. (6.34)
$\overrightarrow{B}$	magnetic field vector
$B(r^*)$	coefficient of Green function $G(r^*\|\xi)$, Eq. (6.34)
c	length, Eq. (3.1)
C	compressibility of Langmuir monolayer, Eq. (2.2)
$C(r^*)$	coefficient of Green function $G(r^*\|\xi)$, Eq. (6.34)
d	immersed depth of the rectangular plate, Eq. (3.4); typical diameter, Fig. 5.5
d_{eq}	equilibrium diameter of one condensed drop
div_s	surface divergence operator
ds, ds'	line elements attached to its outer boundary, Eq. (5.1)
$D(r^*)$	coefficient of Green function $G(r^*\|\xi)$, Eq. (6.34)
D_s	surface diffusion coefficient of PDA molecules
$\overline{\overline{D_s}}$	surface (excess) rate of deformation tensor, Eq. (3.10)
e	exp(1), Eq. (5.2)
e_{gap}	channel gap, Fig. 4.1, Fig. 6.1
$\overrightarrow{E}$	electric field vector
E_0	amplitude of electric field
E^i	amplitude of incident wave

E_p^i	p-component of incident electric field, Eq. (3.25)
E_s^i	s-component of incident electric field, Eq. (3.25)
E_p	p-polarized (or transverse magnetic) wave in which the electric field vector is in the plane of the incidence of the EM wave
E^r	amplitude of reflected wave
E_p^r	p-component of reflected field for optically isotropic domains, Eq. (3.26)
E_s^r	s-component of reflected field for optically isotropic domains, Eq. (3.26)
E^t	amplitude of transmission wave
E_s	s-polarized (or transverse electric) wave where the electric vector is perpendicular to the plane of incidence
E_{p0}^i	amplitude of incident electric field components, parallel (p-) to the plane of incidence
E_{s0}^i	amplitude of incident electric field components, perpendicular (s-) to the plane of incidence
E_{p0}^r	amplitude of the electric field components after the reflection, which is parallel (p-) to the plane of incidence
E_{s0}^r	amplitude of the electric field components after the reflection, which is perpendicular (s-) to the plane of incidence
f	forcing function, Eq. (6.32)
F	force, Eq. (3.1)
$\vec{F}$	net downwards force, Eq. (3.4)
F_s	total energy of a condensed domain, Eq. (5.1)
g	gravity, Eq. (3.4)
$g(r^*)$	a regular non-uniformity function, Eq. (6.6)
G	Gibbs surface free energy, Eq. (3.1)
G^{BO}	bond orientational correlation function, Eq. (A.2)
G^{PO}	positional order correlation function, Eq. (A.1)

$G(r^*\|\xi)$	Green function (ξ denotes the influence variable) associated to the differential operator $\Im$
$G(\xi\|r^*)$	Green function
$G_1(r\|\xi)$	separable (degenerate) kernel of Green function $G(r^*\|\xi)$
$G_2(r\|\xi)$	separable (degenerate) kernel of Green function $G(r^*\|\xi)$
h	depth of a annular channel, Fig. 4.1, Fig. 6.1
H	surface enthalpy, Eq. (3.9)
$\mathcal{H}$	Heaviside step function
I	the first kind modified Bessel function
I_0	intensity amplitude of the light crossing the analyzer, Eq. (3.27)
I_r	intensity of the light crossing the analyzer, Eq. (3.27)
$\overline{\overline{I_s}}$	tensor which transforms any 3-D vector located at the vicinity of the interface into its corresponding 2-D vector, tangential to the interface (in-plane vector), Eq. (3.10)
j	the square root of -1, Eq. (3.14)
J	the first kind Bessel function
k	Boltzmann's constant (1.381×10^{-23} J·K^{-1}), Eq. (2.1)
k_e	the extinction coefficient (spatial damping of light intensity), Eq. (3.14)
$k(r^*\|\xi)$	continuous piecewise kernel, Eq. (6.50)
$k_{ij}(r^*\|\xi)$	kernel, Eq. (6.44)
$k_L(r^*,\xi)$	iterated kernel
$k_R(r^*,\xi)$	iterated kernel
K	the second kind modified Bessel function
l	length of the rectangular plate, Eq. (3.4)
l_t	interfacial thickness, Eq. (3.24)
M_{PDA}	molecular mass of PDA
n	refractive index, Eq. (3.14); mean density of sample
n_1	refractive index of dielectric medium #1

n_2	refractive index of dielectric medium #2
$n_{1\to 2}$	the normal vector at the dividing surface, directed from the phase 1 to the phase 2, Eq. (3.13)
n_i	molar amount of the i^{th} chemical species which make the interface, Eq. (3.1)
n_{LC}	number of LC domains
$n(\overrightarrow{r})$, $n(\overrightarrow{r}')$	molecular densities at positions $\overrightarrow{r}$, $\overrightarrow{r}'$, Eq. (A.2), Eq. (A.1)
N	typical number of PDA molecules packed inside one circular LC domain; number; number of direction neighbors, Eq. (A.2)
$\mathcal{N}_{\mathcal{A}}$	Avogadro's constant (6.022×10^{23})
N_d	number density of LC domain, Fig. 5.5
N_i	the sequence number of the BAM image, Eq. (4.2)
$\widetilde{N}$	complex index of refraction, Eq. (3.14)
$\widetilde{N_1}$	complex index of refraction of medium #1
$\widetilde{N_2}$	complex index of refraction of medium #2
p	perimeter of the 2-D condensed domain boundary, Eq. (3.9)
P	length of LC domain, Eq. (5.1); pressure, Eq. (B.2)
pH	minus the decimal logarithm of the hydrogen ion activity in an aqueous solution
r	local variable, Eq. (5.1); radial coordinate, Fig. 6.1
$\overrightarrow{r}$, $\overrightarrow{r}'$	positions , Eq. (A.2), Eq. (A.1)
r_F	location of a segregation front, Eq. (6.51)
r_i	inner radius of a annular channel, Fig. 4.1, Fig. 6.1
r_k	series
r_o	outer radius of a annular channel, Fig. 4.1, Fig. 6.1
r_p	Fresnel reflection coefficient for p-polarized wave, Eq. (3.17)
r_s	Fresnel reflection coefficient for s-polarized wave, Eq. (3.17)
r^*	dimensionless radius, $r^* = \frac{r}{r_o}$
r, θ, z	cylindrical polar coordinate system

R	radius of a circular LC domain, Eq. (5.2)
R_{eq}	equilibrium radius of a LC domain, Eq. (5.3)
R_p	reflectance coefficient for p-polarization component, Eq. (3.19)
R_s	reflectance coefficient for s-polarization component, Eq. (3.19)
$R\delta\theta$	typical length of a condensed domain along the direction of shearing (azimuthal cross section), Fig. 5.1
s_i, t_i	separated modes, Eq. (6.24)
S	surface entropy, Eq. (3.9)
S_{LC}	typical area of one condensed domain, Eq. (5.8)
$\overline{\overline{S_s}}$	viscous part of the surface stress tensor, Eq. (3.10)
t	thickness of the rectangular plate, Eq. (3.4); time
t_p	Fresnel transmission coefficient for p-polarized wave, Eq. (3.18)
t_s	Fresnel transmission coefficient for s-polarized wave, Eq. (3.18)
T	temperature
^{T}	transpose
T_{diff}	timescale for surface diffusion of PDA molecules
T_{flow}	timescale for the flow-induced molecular packing
$\overline{\overline{T_{s,i}}}$	the familiar 3-D stress tensor within the i^{th} phase staying below ($i = 1$) or above ($i = 2$) the dividing interface, Eq. (3.13)
$\overline{\overline{T_s}}$	surface (excess) stress tensor, Eq. (3.10)
T_t	temperature of the G–LE–LC triple point
$\left[\left[\overline{\overline{T}} \cdot n\right]\right]$	jump notation, Eq. (3.12)
$\overrightarrow{u_r}$, $\overrightarrow{u_\theta}$, $\overrightarrow{u_z}$	unite vector in cylindrical coordinates for r-axis, θ component (the angle measured counterclockwise from the positive x-axis), z-axis, respectively, Fig. 3.3
$\overrightarrow{u_x}$, $\overrightarrow{u_y}$, $\overrightarrow{u_z}$	unite vector in Cartesian coordinates for x-axis, y-axis, z-axis, respectively, Fig. 6.1
u_r, v_θ, w_z	r-axis, θ, z component of velocity vector
$u_{r,s}, v_{\theta,s}$	r-axis, θ component of surface velocity vector

$\overrightarrow{v}$	velocity vector, Eq. (B.2)
v_r	r component of velocity vector, Eq. (5.14)
$v_{r,s}$	r component of surface velocity vector
v_s	surface velocity
$v_{s,k}$	series
$\overrightarrow{v_s}$	surface velocity vector, Eq. (3.10)
v_θ	main shear flow along the channel whose circular streamlines are closing within any horizontal cross-section of the channel; azimuthal velocity
v_θ^*	dimensionless velocity in (azimuthal) θ component, $v_\theta^* = \frac{v_\theta}{r_o\Omega}$
v_θ^{*c}	solution for azimuthal velocity in the core (for the core solution)
$v_\theta^{*c,0}$	solution for dimensionless azimuthal velocity in the core flow(for the core solution) at leading order
v_θ^{*i}	solution for dimensionless azimuthal velocity in the boundary layers flow along left side wall (for the inner solution)
$v_\theta^{*i,0}$	solution for dimensionless azimuthal velocity in the boundary layers flow along left side wall (for the inner solution) at leading order
$v_\theta^{*i/c,0}$	matching condition of inner (left side wall) and core solutions
v_θ^{*o}	solution for dimensionless azimuthal velocity in the boundary layers flow along right side wall (for the inner solution)
$v_\theta^{*o,0}$	solution for dimensionless azimuthal velocity in the boundary layers flow along right side wall (for the inner solution) at leading order
$v_\theta^{*o/c,0}$	matching condition of inner (right side wall) and core solutions
$v_{\theta,s}$	θ component of surface velocity vector
$v_{\theta,s}^*$	dimensionless velocity along the surface, $v_{\theta,s}^* = \frac{v_{\theta,s}}{r_o\Omega}$
$v_{\theta,s}^{*0}$	dimensionless velocity along the surface at leading order
$v_{\theta,s,measured}^*$	measured dimensionless (azimuthal) velocity along the surface
$v_{\theta,s,prediction}^*$	prediction dimensionless (azimuthal) velocity along the surface

$v_\perp$	centrifugal recirculating (secondary) flow whose circular streamlines are closing within a meridian cross-section
w	width of the rectangular plate, Eq. (3.4)
x	length in x-axis
x_i, x_o	transformation parameters, Eq. (6.5)
y	length in y-axis
Y	the second kind Bessel function
z	direction normal to the interface; vertical coordinate, Fig. 6.1
z^*	dimensionless vertical coordinate, $z^* = \frac{z}{h}$

Greek symbols

α^{AF}	area fraction of LC phase (condensed fraction)
$\overline{\alpha^{AF}}$	mean area fraction, Eq. (4.3)
α_i^{AF}	the i^{th} area fraction calculated from the N_i^{th} BAM image
$\overline{\alpha_i^{AF}}$	mean area fraction of the i^{th} area fraction calculated from the N_i^{th} BAM image, Eq. (4.2)
α_p	phase lag of the incident electric field component attached to the p-polarisation state, Eq. (3.17)
α_s	phase lag of the incident electric field component attached to the s-polarisation state, Eq. (3.17)
α_w	wavelength of light, Eq. (3.24)
β_p	phase lag of the p-polarized component of the reflected electric field, Eq. (3.17)
β_s	phase lag of the s-polarized component of the reflected electric field, Eq. (3.17)
γ	stretching parameter, Eq. (6.5)
$\overset{o}{\gamma}$	a transient shear rate imposed from the subphase
Γ	surface concentration
δ	aspect ratio, $\frac{h}{r_o}$

δR	typical width of a condensed domain (radial cross section), Fig. 5.1
Δ	phase difference of light wave that occurs upon reflection, Eq. (3.21)
Δr	constant width
Δ_t	a cutoff thickness below which the dipole-dipole repulsive forces are more and more negligible and increasingly replaced by short-range forces, Eq. (5.1)
ε	modified electrostatic energy per unit area within the LC domain in Eq. (5.1)
ε_o	electrostatic energy per unit area within the LC domain
ζ	a stiffness parameter, Eq. (6.51)
θ_B	Brewster angle
θ_C	contact angle, Eq. (3.3)
θ_i	angle of incidence
$\theta_i(\overrightarrow{r})$	angle between a near neighbor bond at position $\overrightarrow{r}$ and external reference line
θ_r	angle of reflection
θ_t	angle of refraction
κ_s	surface dilatational viscosity
$\kappa(\xi)$	perturbation, Eq. (6.41)
λ	line tension, Eq. (3.9); modified line tension in Eq. (5.1)
λ_{eff}	effective line tension
λ_o	line (excess) tension
λ_w	wavelength of the light
μ_b	(Newtonian) shear viscosity of subphase
$\mu_{LC/LE}$	difference in dipole densities between the dipolar PDA molecules within the LC domain and those diluted in the surrounding LE continuous phase, Eq. (5.1)
μ_s, $\mu_s(r)$	surface shear viscosity
μ_s^*	dimensionless surface shear viscosity, $\mu_s^* = \frac{\mu_s(r)}{\overline{\mu_s}}$

$\overline{\mu_s}$	uniform term of surface viscosity
$\mu_{s,crystal}$	viscosity of the flow-induced molecular packing made from the complexes [protein-lipid], Eq. (6.51)
$\mu_{s,LC}$	surface shear viscosity in LC domain
$\mu_{s,LE}$	surface shear viscosity in LE domain
$\mu_{s,monolayer}$	viscosity of the water surface topped with the lipidic matrix, Eq. (6.51)
ν_b	molecular viscosity of subphase
ξ	influence variable of Green function asociated to the differential operator $\Im$
Π	surface pressure
Π_c	collapse surface pressure
Π_d	dynamical surface pressure, Eq. (5.14)
Π_{ESP}	equilibrium spreading pressure
Π_{LC}	surface pressure in LC phase
Π_{LE}	surface pressure in LE phase
ρ_a	complex relative amplitude attenuation, Eq. (3.20)
$\rho_{a,B}$	ellipticity at Brewster angle incidence, Eq. (3.23)
$\rho_{a,B}{}'$	ellipticity at Brewster angle incidence without reflected light, Eq. (3.28)
ρ_b	density of subphase, Eq. (C.4)
ρ_p	density of the rectangular plate, Eq. (3.4)
ρ_s	surface mass density, Eq. (5.14)
ρ_w	density of the liquid, Eq. (3.4)
σ	surface tension, Eq. (3.1)
σ_0	initial surface tension of the liquid surface (72.8 mN·m^{-1} for water at 298 K, 1 atm), Eq. (3.2)
σ_{LG}	surface tension due to the interaction between liquid and gaseous (air) phases, Eq. (3.3)

σ_{LS}	surface tension due to the interaction between liquid and solid phases, Eq. (3.3)
σ_{GS}	surface tension due to the interaction between gaseous (air) and solid phases, Eq. (3.3)
$\tau^*_{b,comp}$	dimensionless shear stress at the liquid surface based on the composite solution for the flow of the subphase
$\tau^*_{b,Couette}$	dimensionless shear stress at the liquid surface based on the assumption of a Couette flow along the vertical direction within the subphase, $\tau^*_{b,Couette} = v^*_{\theta,s}(r^*) - r^*$
$\tau_b\big\vert_s$	shear stress valued at the surface, Fig. 5.1
τ_s	in-plane shear stress, Fig. 5.1
τ^*_s	dimensionless shear stress along the liquid surface, $\tau^*_s = \frac{dv^*_{\theta,s}}{dr^*} - \frac{v^*_{\theta,s}}{r^*}$
$\tau^*_{s,comp}$	dimensionless shear stress along the liquid surface with $\tau^*_{s,comp} = \tau^*_s$ if $v^*_{\theta,s}(r^*)$ is calculated from Eq. (6.27)
$\tau^*_{s,Couette}$	dimensionless shear stress along the liquid surface with $\tau^*_{s,Couette} = \tau^*_s$ if the surface velocity $v^*_{\theta,s}(r^*)$ is calculated from Eq. (6.18)
ϕ	angle between the direction of polarization and the plane of incidence
$\phi(\xi)$	forcing term, Eq. (6.41)
φ	angle between the polarization of the light before the quarter wave plate and the plane of incidence, Eq. (3.25)
Ψ	angle whose tangent is the ratio of the amplitude of the Fresnel reflection coefficients, Eq. (3.21)
$\Psi_n\left(\overrightarrow{r}\right)$	bond orientational order parameter for n-fold symmetry, Eq. (A.2)
ω_n	eigenvalue
Ω	angular velocity

Other symbols

∂A_{LC}	dividing edge around LC domain

∇	gradient operator
∇_r	radial gradient operator, Eq. (C.4)
∇_s	surface gradient operator, Eq. (3.11)
$\Im$	differential operator
$(\ominus, \oplus)$	either the values $(\frac{r_i}{r_o}, r^*)$ or the values $(r^*, 1)$
$\langle\rangle$	statistical average, Eq. (A.2), Eq. (A.1)
%	percent

Dimensionless groups

Bo	Boussinesq number, $\frac{\overline{\mu_s} v_{\theta,s} / {r_o}^2}{\mu_b v_{\theta,s} / h}$, Eq. (6.8)
$\widetilde{Bo}$	(macroscopic) Boussinesq number, $\frac{\mu_s h}{\mu_b {e_{gap}}^2}$, Eq. (4.5); macroscopic Boussinesq number, $\frac{Ca_s}{Bo_s}$
Bo_{comp}	local Boussinesq number based on the composite solution for the flow of the subphase, $\frac{\tau^*_{s,comp}}{\tau^*_{b,comp}} Bo$
$Bo_{Couette}$	local Boussinesq number based on the assumption of a Couette flow along the vertical direction within the subphase, $\frac{\tau^*_{s,Couette}}{\tau^*_{b,Couette}} Bo$
$\widetilde{Bo_{LC}}$	mesoscopic Boussinesq number at the scale of one LC domain, $\frac{Ca_{LC,s}}{Bo_{LC,s}}$, Eq. (5.10)
Bo_s	surface Bond number at macroscopic scale, $\frac{\mu_b {r_o}^3 \Omega / h}{\lambda_{eff}}$, Eq. (5.6)
$Bo_{LC,s}$	surface Bond number at the scale of an individual LC domain, $\frac{\tau_b\vert_s S_{LC}}{\lambda_{eff}}$, Eq. (5.8)
Ca_s	surface capillary number at macroscopic scale, $\frac{\mu_s r_o \Omega}{\lambda_{eff}}$, Eq. (5.7)
$Ca_{LC,s}$	mesoscopic surface capillary number at the scale of one LC domain, $\frac{\tau_s R \delta\theta}{\lambda_{eff}}$, Eq. (5.9)
Re	Reynolds number, $\frac{r_o \Omega e_{gap}}{\nu_b}$, Eq. (4.4)

Abbreviations

2-D	two-dimensional

3-D	three-dimensional
A	analyzer
BAM	Brewster angle microscope
BC	boundary condition
C	carbon; Compensator
CCD	charge-coupled device
DNA	deoxyribonucleic acid
DNS	direct numerical simulation
EM	electromagnetic
EPS	equilibrium spreading pressure
FM	fluorescence microscope
G	gaseous
H	hydrogen
IR	infra red
JMB	jump of momentum balance
L	liquid
LE	liquid-expanded
LC	liquid-condensed
LHS	left hand side
LM	Langmuir monolayer(s)
N	nitrogen; north
NN	nearest neighbor
NNN	next-nearest neighbor
O	oxygen
ODE	ordinary differential equation
P	phosphorus; polarizer
PDA	pentadecanoic acid
PDMS	poly(dimethyl)siloxane
RHS	right hand side

RMSE	root mean square errors
S	sample/surface; solid; south
Sm	smectic
TE	transverse electric
TM	transverse magnetic
U	untilted

Symbols for units

atm	atmosphere
Å	ångström, 10^{-10}
°C	degree Celsius
°	degree
c	centi, 10^{-2}
g	gram
h	hour
J	joule
k	kilo, 10^{3}
K	degree Kelvin
l	liter
μ	micro, 10^{-6}
m	meter
m	milli, 10^{-3}
M	molar
min	minute
mol	mole
molecule	molecule
N	newton
p	pico, 10^{-12}
Pa	pascal

rpm	revolution per minute
s	second
sP	surface poise

Acknowledgements

This dissertation could be finished due to the help and support of many people who are gratefully acknowledged here.

At the very first, I am honored to express my deepest gratitude to my dedicated supervisors, Dr. Laurent DAVOUST (Université Joseph Fourier) and Prof. Shuo-Hung Chang (張所鋐 教授, National Taiwan University), with whose able guidance, I could have worked out this dissertation. Especially thanks to Dr. Laurent DAVOUST, he has offered me valuable ideas, suggestions and criticisms with his profound knowledge in forensic linguistics and rich research experience. His patience and kindness are greatly appreciated. Besides, he always puts high priority on this dissertation writing and is willing to discuss with me anytime he is available. I have learnt from him a lot not only about dissertation writing, but also the professional ethics. I am much obliged to his efforts of helping me complete this dissertation.

I am extremely grateful to the encouraging advices of Prof. Shyan-Fu Chou (周賢福 教授, National Taiwan University) and Associate Prof. Tien-Tung Chung (鐘添東 教授, National Taiwan University). Also I am grateful to my master's supervisor, Prof. Sih-Li Chen (陳希立 教授, National Taiwan University). Their patient and meticulous guidance and invaluable suggestions are indispensable to the completion of this dissertation. I cannot make it without their support and encouragement.

Thanks are also due to my postgraduate friends, who never failed to give me great encouragement and suggestions. Special thanks should go to Dr. Huan-Ruei Shiu (許桓瑞 博士), Asistance Prof. Yuan-Ching Chiang (江沅晉 助理教授, Chinese Culture University), Dr. Kuo-Chih Chuang (莊國志 博士), Mr. Sheng-Kai Chang (張勝凱 先生), Mr. Bau-Liang Chen (陳保良 先生), Dr. Chia-Fang Liu (劉嘉芳 博士), Dr. Chao-Yaug Liao (廖昭仰 博士), and Dr. Chao-Yu Lee (李炤佑 博士) in Taiwan. During my research in France, I am grateful to Prof. Sedat TARDU (Université Joseph Fourier), Prof. Diana Broboana (University Politehnica of

Bucharest), Dr. Cyril PICARD, Dr. Ervin Amet, Mr. Aurélien BIDEAUD, and Mr. Florian ROHR not only for their brainstorming with me when I failed coming up with ideas but also for their assistance allowing me to integrate into life in France easily. I deeply appreciate Miss Hui-Chuan Tseng (曾慧娟 小姐) for her encouraging me all the time to finish this dissertation.

I am grateful to Mr. Joseph VIRONE (Laboratoire des Ecoulements Géophysiques et Industriels) for his valuable skills to manufacture the mechanical pieces involved in the experimental set-up. Furthermore, I appreciate Prof. Jean-François LEGRAND (Université Joseph Fourier), Prof. Franck FIESCHI (Université Joseph Fourier) and Prof. Eva PEBAY-PEYROULA (Université Joseph Fourier) for helpful comments on 2-D crystallization at a lipidic monolayer. Also I am grateful to the encouraging advices of Prof. Dominique Aymer de la Chevalerie (French Institute at Taiwan). Special thanks are due to the French Institute at Taipei and the Taiwanese Ministry of Education providing me scholarship to finish my research in France. Special thanks are also due to all committees for their detailed and discerning review during revision process.

At last but not least, I would like to thank my family for their support all the way from the very beginning of my postgraduate study. I am thankful to all my family members for their thoughtfulness and encouragement.

Curriculum Vitæ

Yu-Lin Huang

Personal

Born	Taipei, Taiwan
E-mail	d91522016@ntu.edu.tw

Education

2005–2009	Université Joesph Fourier (UJF) - Grenoble I, Grenoble, France
Ph.D.	Mechanical Engineering, Laboratoire des Ecoulements Géophysiques et Industriels
2002–2009	National Taiwan Univeristy (NTU), Taipei, Taiwan
Ph.D.	Mechanical Engineering, Precision Micro Mechanism Laboratory
2000–2002	National Taiwan University (NTU), Taipei, Taiwan
M.S.	Mechanical Engineering, Fluid Mechanics Division
1996–2000	Tatung University (TTU), Taipei, Taiwan
B.S.	Mechanical Engineering

Publications

Journal papers

1. Laurent Davoust, Yu-Lin Huang, and Shuo-Hung Chang. Shearing of a stratified layer of amphiphilic (bio)molecules. *Surf. Sci.*, 603:2777–2788, 2009 (SCI, Impact Factor = 1.731).
2. Laurent Davoust, Yu-Lin Huang, and Shuo-Hung Chang. Flow-induced melting of condensed domains within a dispersed Langmuir film. *Phys. Fluids*, 20(8):082105-1–082105-8, 2008 (SCI, Impact Factor = 1.738).

3. Yu-Lin Huang, Huan-Ruei Shiu, Shuo-Hung Chang, Wen-Fang Wu, and Sih-Li Chen. Comparison of combustion models in cleanroom fire. *J. Mech.*, 24(3):267–275, 2008 (SCI).
4. Yaw-Shen Chen, Yu-Lin Huang, Chia-Hsin Kuo, and Shuo-Hung Chang. Investigation of design parameters for droplet generators driven by piezoelectric actuators. *Int. J. Mech. Sci.*, 49(6):733–740, 2007 (SCI, Impact Factor = 1.077).

Conference papers

1. Laurent Davoust, Yu-Lin Huang, Shuo-Hung Chang, and Laurent Drazek. Impact of a molecular packing upon a surface stokes flow. In Proceedings of the 1st European Conference on Microfluidics - Microfluidics 2008, Bologna, Italy, 2008.
2. Yaw-Shen Chen, Yu-Lin Huang, Chia-Hsin Kuo, and Shuo-Hung Chang. Investigation on design parameters of droplet generators. In the 2nd International Symposium on Micro & Nano Technology, IEEE, Hsinchu, Taiwan, 2006.
3. Yu-Lin Huang, Shuo-Hung Chang, Chin-Horng Wang, and Chiung-I Lee. Piezoelectric actuating sprayed phase-change cooling technique for VLSI chips. In ASME Summer Heat Transfer Conference, 4:503–509, San Francisco, USA, 2005.
4. C. H. Cheng, Jung-Tang Huang, Yu-Lin Huang, Fu-Chiang Hsu, Thung-Han Wu, Ching-Cheng Li, L. S. Huang, and Shuo-Hung Chang. Micromachined droplet on demand formation with shear mode piezoelectricity and micron size nozzles. In the 5th IEEE Conference on Nanotechnology, 1:301–304, Nagoya, Japan, 2005.
5. Yu-Lin Huang, Bin-Chen Wei, and Shuo-Hung Chang. Array microdroplet ejection using an ultrasonic PZT ring actuator. In the 29th National Conference on Theoretical and Applied Mechanics, H011-1–H011-8, Hsinchu, Taiwan, 2005.
6. Yu-Lin Huang, Chia-Hsin Kuo, Shuo-Hung Chang, Chin-Horng Wang, and Chiung-I Lee. An innovative cooling technique enhanced by piezoelectric actuating spray in vacuum. In Proceedings of the 21st National Conference on Mechanical Engineering, CSME, 6057–6062, Kaohsiung, Taiwan, 2004.

Chapter 1

General introduction

1.1 Context

This dissertation is the first stage of a research program on a new hydrodynamical process supposed to help the identification of the primary structure of certain proteins which reveal to be important in molecular biology (membrane proteins for instance) though impossible to crystallise in three dimensions. The practical goal is to develop a new process which would permit the flow-assisted growth of a large two-dimensional (2-D) crystal of protein along a air-water interface. This includes to find the best hydrodynamical conditions for the 2-D crystal protein to be sufficiently large and regular, such as a single crystal. Obtaining such a single crystal would allow the biochemist to identify with the best resolution the primary structure of one given protein as the size and the spatial regularity of a 2-D single crystal could fit well to a technique like grazing incidence X-rays diffraction (GIXD).

At the time being, the available state of the art on 2-D crystal growth is based on a water surface chemically functionnalised by a lipidic matrix [30, 68, 50, 176, 25, 52, 143]. The protein of interest, introduced within water subphase, is free to move under molecular diffusion up to the lipids forming a Langmuir monolayer (LM) at the liquid surface. A dedicated chemical affinity between lipids and proteins allows them to be

trapped at the LM and to move along it in a 2-D way. Under quiescent condition, 2-D molecular diffusion along the liquid surface is responsible for the percolation and growth of a 2-D self-assembly of proteins whose structure resembles to a crystalline powder. This 2-D crystalline powder does not really lend itself to accurate determination of the protein structure from X-ray diffraction [99]. Consequently, it is necessary to improve the spatial periodicity of the 2-D self-assembly.

1.2 Motivations and aims

The goal beyond the dissertation is to control a flow recirculation in the subphase:

- ◇ in order to accelerate the binding probability of proteins to lipids at the liquid surface,
- ◇ in order to pack molecular complexes, [lipid+protein], along the liquid surface after binding process,
- ◇ what should lead ultimately to a 2-D molecular assembly of proteins, characterised by a high level of spatial regularity.

Historically, the complexity of the hydrodynamical, chemical and physico-chemical phenomena involved in such a flow process led us to reduce our original ambitions. This is the reason why, in this dissertation, we primarily decided to focus our research effort on the following scientific question: how the mesoscopic features of a fluid interface populated by biological amphiphilic molecules can be changed when the supporting interface is subjected to a flow reorganisation. As shown in this dissertation, this issue involves to cope with a delicate coupling between at least four hydrodynamical and physico-chemical mechanisms (chemical transport disregarded). A fundamental understanding of this multiphysics requires a significant research effort which, in this dissertation, was based on an experimental investigation as well as some theoretical developments.

As a result, this dissertation delivers experimental and theoretical tools necessary for the future development of a 2-D crystal growth process based on hydrodynamics.

1.3 Outline of this dissertation

A first chapter (Chapter 2) is devoted to the state of the art on the functionalization of a air-water interface by a Langmuir monolayer. This allows us to better justify the choice of one particular model system, namely the pentadecanoic acid (or PDA). This fatty acid is hope to provide a first insight into the dynamic behavior of condensed domains such as lipidic domains or single-crystalline grains.

Chapter 3 is devoted to the introduction of the instrumental techniques used to characterize a Langmuir monolayer when thermodynamical equilibrium applies or when it is submitted to a flow. In particular, the choice of a Brewster angle microscope is justified as a relevant tool to investigate the impact of a flow at meso scale upon the morphology of a PDA Langmuir monolayer undergoing a phase transition. The latter is characterized by the arising of liquid condensed (LC) domains surrounded by a continuum of liquid expanded (LE) phase. The size and the geometry of these domains varies greatly depending on the surface concentration in PDA.

To create an end-driven rotating flow inside a channel, which is capable of reorganising the Langmuir monolayer at the same time, a new hydrodynamical process based on an annular channel has been developed and is presented in detail in Chapter 4. With the coupling between the underlying rotating flow and the surface flow along the monolayer, we are led to investigate the monolayer when subjected to two types of shearing, a first one from the subphase, an other one of two-dimensional nature, which is in-plane, inherent to the liquid surface. Both shears are produced by the rotation of an annular magnetic ring disposed at the bottom of the annular channel. From the viewpoint of the boundary conditions, a swirling (toroidal) flow is caused by the rotating ring while the two vertical sides of the channel remains fixed.

Chapter 5 is devoted to experimental results. A new two-phase patterning at mesoscopic scale in the PDA monolayer is confirmed and studied in steady state. In the experiments on the morphological characterization induced by the imposed flow, the distribution of a surface fraction in condensed phase is measured along the interface by making use of Brewster angle microscopy. Evidence is given that, due to mass conservation, centrifugation along the rotating ring causes a radially-inwards flow along the liquid surface, which finally favors the packing of LC domains towards the smallest radii. For both a channel depth and a level of centrifugation large enough, the Langmuir film experiments an interesting morphological change essentially driven by a balance between surface shear and line tension (1-D quantity analogous to surface tension). Among consequences, the surface shear stress is demonstrated for the first time (to our knowledge) as capable of melting the condensed domains. As a result, a new morphological organisation is found which can be described as a 2-D matrix of tiny condensed droplets.

Susceptibility to various control parameters such as PDA surface concentration, depth of the annular channel, or the magnitude of subphase centrifugation, leads us to distinguish a second physico-chemical regime within the Langmuir monolayer, referred to as highly-densified (or stratified) regime. This corresponds to a vanishing role of flow-induced surface compression at the expense of end-driven shear which plays a growing role. If the depth of the annular tank is small enough and if the angular velocity of the ring becomes large enough to yield a significant centrifugation, the subphase shear at the surface is amplified so that it leads to a widespread fragmentation of the condensed domains all along the liquid surface. The latter regime, already listed in the literature, is certainly the one that we must avoid in future experiments devoted to 2-D flow-focused crystal growth.

The last chapter of this dissertation (Chapter 6) is a contribution to the modelling of a shear flow within an annular channel whose floor is put in rotation while its two vertical cylindrical side walls are maintained stationary. The liquid surface at the top of the annular channel is supposed to be covered by a layer of hydrophobic

molecules. The flow is considered as permanent, axisymmetric and creeping. The ratio of the liquid depth to the outer radius is small enough (shallow flow) so that it is possible to develop a matched asymptotic model. All these geometrical and boundary conditions are in agreement with our experiments. In the rotating subphase, a core flow is therefore distinguished from the boundary layers along side walls. In order to take into account some of the findings made evident from our experiments (Chapter 5), the modelling includes the possibility to take into account the impact of the radially-inwards molecular packing induced by centrifugation of the underlying bulk. To this purpose, a radial distribution of surface viscosity is taken into account *via* the transport equation for surface momentum. In this chapter, the well-known model by Mannheimer & Schechter [112] can be considered as revisited: a new integral formulation is made evident which enables a fair estimation of the Boussinesq number as well as a simple measurement of a stratified surface viscosity.

To end this general introduction, it is important to mention that much effort has been paid to write this dissertation so as to allow, as far as possible, a relatively independent reading of each of the chapters, while not neglecting the logical connection between them.

Chapter 2

On monolayers

Monolayers, and more particularly Langmuir monolayers (LM), are one of the most interesting state of soft matter. Within a monolayer, the molecules are perfectly arranged according to a 2-D film one molecule thick, so that from the study of a LM, much can be learned as to the size, shape, and other properties of the individual molecules. Growing interest in monolayer is driven in part by their numerous applications, including coating technologies, chemical and bio-sensors, and optoelectronic devices. The advantage of studying monolayers at the air-water interface is that they are easy to handle and that their properties can be easily manipulated by relatively simple experimental methods. In this chapter, a background knowledge of monolayers is recalled.

2.1 Basic features of monolayers

A *monomolecular film* or, briefly, a *monolayer*[1], is defined from two typical characteristics:

[1]Strictly speaking, a film is a layer of substance, spread over a surface, whose thickness is small enough for gravitational effect to be negligible. A monolayer is a film considered to be only one molecule thick.

- ◇ A monolayer is made from surfactants (surface active agents) whose self-assembly generates a perfect 2-D film one molecule thick.

- ◇ Surfactants are typically organic molecules which are straddling at a fluid interface minimising thus its free energy.

Depending on the properties of the surfactants, monolayers can be distinguished as follows:

- ◇ When surfactants are not soluble in the liquid subphase, the monolayer is called a *Langmuir monolayer (or Langmuir film).*

- ◇ In contrast, when surfactants are partially soluble in the liquid subphase while a significant amount of them is adsorbed at the interface, the monolayer is called a Gibbs monolayer [94].

Because a Langmuir monolayer (LM) can be considered as a perfectly two-dimensional (2-D) self-assembly; they have given a lot of consideration. For a physicist, monolayers provide an excellent model system to investigate thermodynamical equilibrium of soft matter because the 2-D variables can be controlled properly. In biophysics, LM is also a good mimetic of biological membranes and a more convenient tool to investigate some of their biological features. For instance, life scientists usually investigate phospholipids LM in order to have an insight into the structure and properties of bilayers involved in cell membranes. Also the applications of Langmuir-Blodgett (LB) films are based on the control of LM before any transfer upon a solid support. By definition, LB films are multi- or single-layers transferred layer-by-layer from a liquid surface covered by a LM to a solid substrate. In this way, LB technique is a tool of nanolithography which permits to manipulate molecules and to construct artificially structured materials at nanoscale for optical, electronics or sensor applications. LB films can also be used as well-defined coatings in some applications of tribology, wetting or physicochemical sorption.

To prepare a LM, surfactant molecules are solubilised in a volatile solvent (such as chloroform or ethanol) at a concentration of the order of mM. This solution is usually deposited droplet after droplet over a liquid surface (air-water interface, for instance) from a micro-syringe. As soon as a droplet of spreading solution touches the air-water interface, it spreads out all over the entire water surface. Finally, the solvent evaporates and leaves a monolayer afterwards.

To form a monolayer, a surfactant molecule must own a special chemical structure. In the following section, we will focus on usual surfactants involved to build Langmuir monolayers.

2.2 Molecular structure of amphiphiles

Most of the surfactant molecules used in a LM are amphiphilic[2]), which means their structure is composed of both a hydrophilic group and a hydrophobic chain. The hydrophilic group is commonly referred to as *polar head* and the hydrophobic chain is often made from a sequence of alkyl groups. Because of its dual affinity, an amphiphilic molecule exhibits a strong tendency to migrate towards a liquid surface and to orientate so that its polar head lies in water whilst its chain is placed out of it.

There are lots of amphiphiles, some of them are molecules such as fatty acids, alcohols, esters; others are a little bit more complicated such as di- or tri-glycerides, phosphoglycerides, sterols or chlorophyll, usually found in biological systems. The common amphiphiles, which are used to prepare Langmuir monolayers on a water surface are fatty acids, fatty methyl ester and phospholipids, as shown in Fig. 2.1. The head group may be ionized if pH and ionic conditions allow dissociation into underlying subphase (*e.g.*, fatty acid, Fig. 2.1 (a)). The head group may be neutral as well (*e.g.*, fatty ester, Fig. 2.1 (b)) [85]. The amphiphiles encountered most frequently

[2]The term *amphiphilic* means *loves both*. In other words, the polar head of an amphiphilic molecule is soluble while its chain behaves as a non-polar solvent [13].

in nature are the phospholipids[3] (Figs. 2.1 (c) and (d)) which consist of coupled fatty acids.

2.3 The case of amphiphilic fatty acids

In chemistry, especially in biochemistry, carboxylic acids containing at least 4 carbon atoms can be considered to be a fatty acid. Fatty acids derived from natural fats and oils. They are known to behave as amphiphilic species in presence of water if their hydrophobic chain is made from at least 8 carbon atoms.

A saturated (no double bonds) long-chain fatty acid is a typical monolayer-former; it consists of a linear chain (C_nH_{2n+1}), an *alkyl chain*, and of a carboxylic acid group (COOH) which behaves as a polar head. The magnitude of the hydrophobicity is obtained from the length of the alkyl chain. Any change in the nature of either the alkyl chain or the polar end group will affect the monolayer properties, especially its percentage of solubility [133]. Chains longer than about 12 carbons are necessary to get a solubility low enough, however, not all water-insoluble amphiphilic molecules spread with the aid of a volatile solvent to a monolayer on the water surface. When the hydrophobic character of the chain is dominant, i.e. the cohesive forces between the amphiphilic molecules overcome the attraction with the water subphase and between the polar heads of the amphiphilic molecules, the amphiphilic molecules will form a lens rather than a uniform monolayer on the liquid surface. To summarise, the conditions for which a chemical specie can form a LM are that the chain length must be sufficiently long to make the molecules insoluble, and that there must be a balance with the hydrophilic interaction with the surface. Due to the opposing natures of these two requirements, only some amphiphilic molecules will fulfill these requirements simultaneously. Table 2.1 lists some common fatty acids used in monolayer studies. At room temperature, molecules with 22 carbon atoms or more tend to form lenses rather than monolayers on a water surface.

[3] A main ingredient of cell membranes.

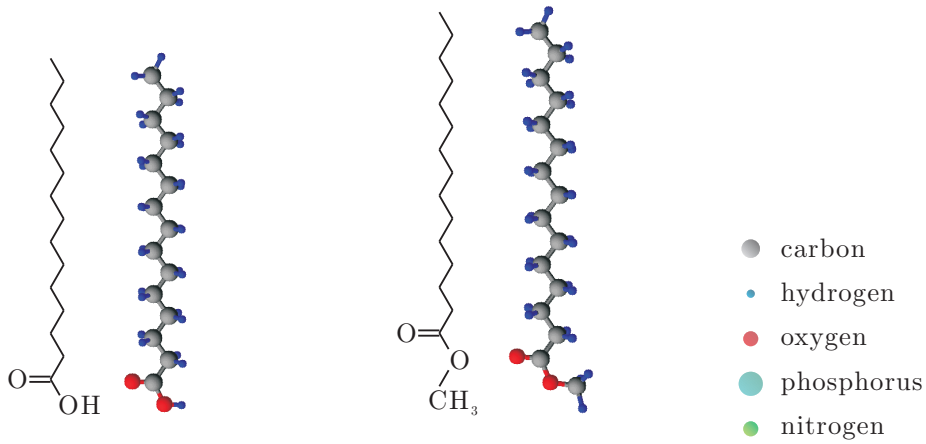

(a) pendecanoic acid

(b) pentadecanoic acid methyl ester

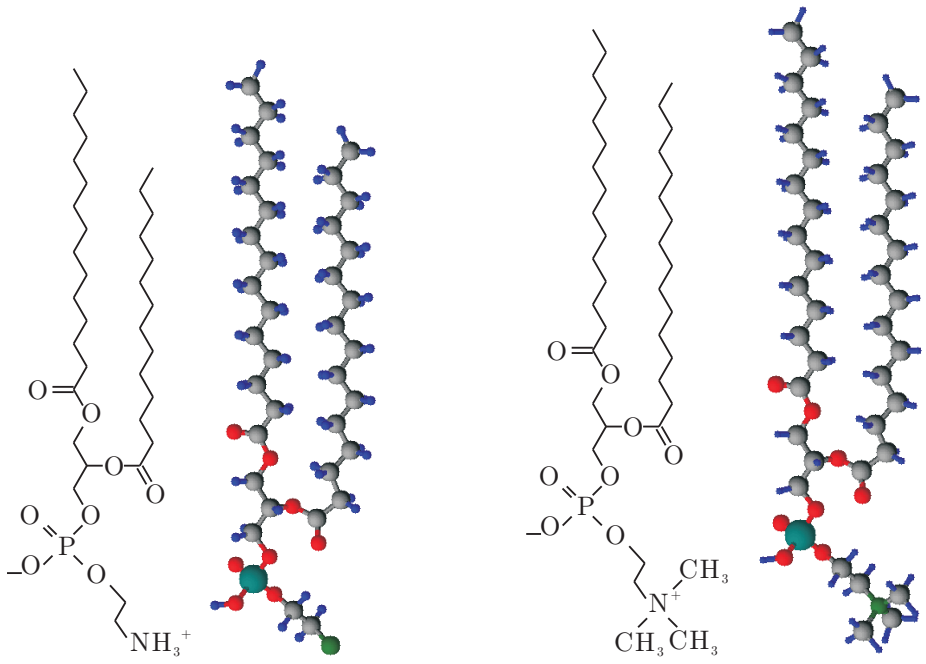

(c) diacylphosphatidylethanolamine

(d) diacylglycerophosphocholine

Figure 2.1. Some common amphiphiles forming Langmuir monolayers on surface of water: (a) fatty acid, (b) fatty methyl ester, (c) and (d) phospholipids.

Table 2.1. Properties of long-chain fatty acids used for monolayer studies (adopted from Ref. [102]). The first column indicates the carbon chain number of the fatty acids.

	Structure	Systematic name	Common name	M_r [1]	T_m [2]	S_w [3]
C_{13}	$C_{12}H_{25}COOH$	tridecanoic	tridecylic	214.35	42	0.0033
C_{14}	$C_{13}H_{27}COOH$	tetradecanoic	myristic	228.38	54	0.0020
C_{15}	$C_{14}H_{29}COOH$	pentadecanoic	pentadecanoic	242.40	52	0.0012
C_{16}	$C_{15}H_{31}COOH$	hexadecanoic	palmitic	256.43	62	0.00072
C_{18}	$C_{17}H_{35}COOH$	octadecanoic	stearic	284.48	69	0.00029
C_{20}	$C_{19}H_{39}COOH$	eicosanoic	arachidic	312.54	75	
C_{22}	$C_{21}H_{43}COOH$	docosanoic	behenic	340.59	81	
C_{24}	$C_{23}H_{47}COOH$	tricosanoic	lignoceric	368.64	84	

[1] molecular weight ($g \cdot mol^{-1}$)

[2] melting point (°C)

[3] water solubility at 20 °C in units of grams of solute per 100 g of water

To obtain an insoluble monolayer of a nonionized fatty acid (a common situation at sufficiently low pH values), the molecules must contain at least 12 carbon atoms [133]. For instance, if the monolayer of myristic acid ($C_{13}H_{27}COOH$) is held at a surface pressure of 10 $mN \cdot m^{-1}$ and a temperature of 20 °C, the loss in monolayer area due to a small but nevertheless existing solubility of myristic acid in a water subphase is estimated to be 0.1 $\% \cdot min^{-1}$ [163]. This contrasts with stearic acid ($C_{17}H_{35}COOH$) which shows a decrease in monolayer area of less than 0.001 $\% \cdot min^{-1}$ under similar conditions [51]. The different solubilities of the long-chain fatty acids in a water subphase at 20 °C are displayed in Table 2.1.

2.4 Phases behavior of Langmuir monolayers

A Langmuir monolayer can be considered to exist in different phases with thermodynamic properties analogous to those of three-dimensional (3-D) gases, liquids, or solids. Various monolayer phases (or states) represent different degrees of molecular freedom or order, resulting from the intermolecular forces within LM or between LM and subphase.

The traditional method to study monolayer is to measure the surface pressure, Π ($\mathrm{N{\cdot}m^{-1}}$), as a function of the molecular area, A ($\mathrm{\AA^2{\cdot}molecule^{-1}}$), which is defined as the averaged surface made available all around one molecule in the LM. The surface pressure, Π, originates from the reduction of surface tension due to the intermolecular forces between amphiphiles along the liquid surface (described in details in section 3.1). The plot of surface pressure versus the molecular area is known as Π–A isotherm. It is therefore possible to determine phase diagrams of Langmuir monolayers by measuring their Π–A relation at different experimental conditions (such as temperature, subphase pH, etc.).

2.4.1 Isotherms of Langmuir monolayers

The first measurement of one Π–A isotherm was performed by Pockels [137]. Afterwards, Lord Rayleigh was inspired to perform his own experiments, from which he concluded that these layers were a single-molecule thick [141]. Later, Langmuir [96] was the first to provide essentially the modern understanding of their structure at the molecular scale, in particular the fact that the molecules demonstrate a preferential orientation with respect to the liquid surface.

A simple experimental setup, named as *Langmuir trough*, is devoted to the measurement of a Π–A isotherm (Fig. 2.2). The area of the monolayer is varied by moving a barrier across the water surface. The surface tension (or equivalently, the surface pressure) is determined by suspending a plate made from a material completely wet

by water (Whilhelmy technique). The liquid surface pulls down the plate under the effect of a downwards force defined as the surface tension times the perimeter of the plate (all details about surface pressure are given in section 3.1.2).

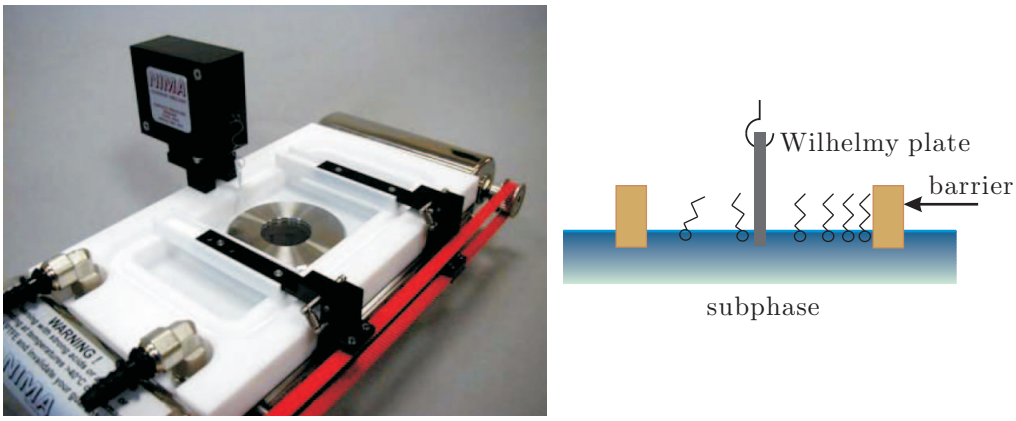

Figure 2.2. The Langmuir trough used in this dissertation (Nima Ltd.) and surface pressure as measured by the Wilhelmy plate method. The right scheme illustrates a LM submitted to a surface compression induced by inwards motion of a floating barrier.

Figure 2.3 shows a generalized isotherm of Langmuir monolayers of fatty acids. From its shape, it is possible to recognize four principal monolayer phases: a low-pressure gaseous (G) phase, a liquid like phase termed liquid-expanded (LE or L_1) phase, a liquid-condensed (LC) phase existing at a higher surface pressure or a lower temperature, and a solid phase according to the terminology introduced by Adam [89] and Harkins [61]. Later experiments by Stenhagen [160, 163] and Lundquist [107, 108] revealed isotherms with many bumps and kinks, which they viewed as evidence for additional phase transitions. However, isotherm measurements are often difficult to interpret, a point which is mainly due to uncontrolled insertion of impurities in the sample or along the walls of the trough. As a result, many small features on the isotherms have been ignored. Despite the difficulties associated with their interpretation, isotherms remain still a very convenient method to access the thermodynamic state of Langmuir monolayers. We should note that due to the narrow ranges of temperature and surface pressure available in practice, a particular monolayer may not exhibit all of the features shown in Fig. 2.3. Recent study with the aid of mod-

ern physical instruments (Small Angle X-ray Scattering for instance) confirmed that other phases also exist although their presence is somewhat hidden inside the isotherm diagram of Langmuir monolayers.

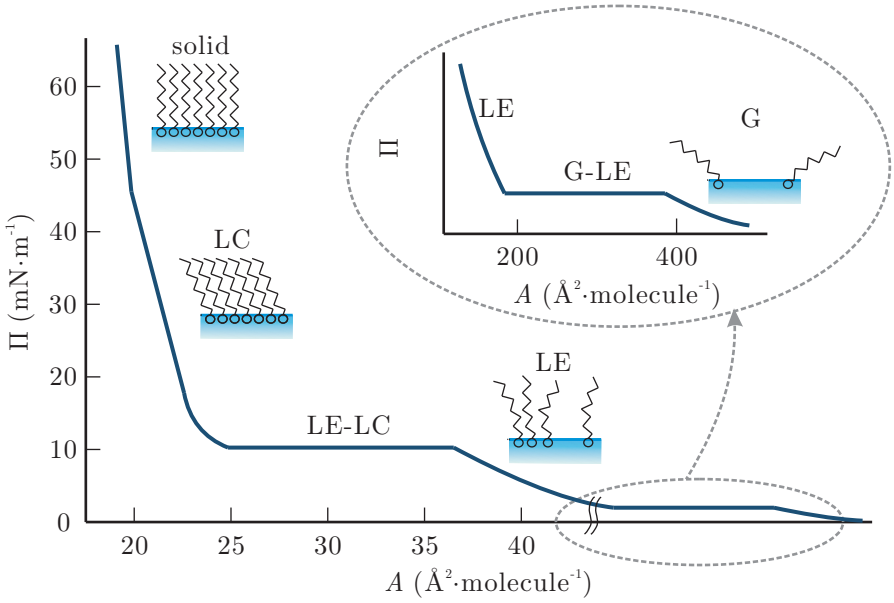

Figure 2.3. A Π–A isotherm as a plot of surface pressure Π against molecular area A at constant temperature. The molecular area A at which a change in the slope can be seen, corresponds roughly to the one found for the pentadecanoic acid (PDA) used in this dissertation (see e.g. Fig. 4.5 in Chapter 4). The insert shows the G–LE transition region at large molecular areas. Four schemes illustrate the molecular packing for each of the phases G, LE, LC and Solid.

2.4.2 Generalized phase diagrams of Langmuir monolayers

For a particular LM system under well-controlled environmental parameters such as pH, ionic strength and humidity, the Π–A relation at various temperatures can be measured, and from the features of the isotherms one can also build surface pressure–temperature (Π–T) diagrams for the phases. This is analogous to the pressure–volume–temperature diagrams for the ordinary (3-D) phases. Nevertheless, knowledge about the underlying structures of Langmuir monolayers is complicated. Since the early 1980's, many experiments at nano-scale on Langmuir monolayers have been made possible with the aid of modern developments in electronic and optical techniques. For instance, the phase diagrams of Langmuir monolayers have been classified thanks

to the development of X-ray diffraction and reflectivity measurements [84, 85]. Although the technique of X-ray crystallography has a long history, it was difficult to obtain sufficient scattered signal for a sample with only one molecule thick until the advance of synchrotron radiation as a powerful X-ray source. The high intensity of synchrotron radiation compensates for the small scattering cross sections of monolayers. As for optical measurements, with the aid of laser technologies and optical electronics development, Langmuir monolayers can be investigated on micro or larger length scales while X-ray scattering experiments provide information at the scale of several ångströms. Optical microscopy, such as fluorescence microscope (FM) [140] or Brewster angle microscope (BAM) [73, 70, 69], also offers the possibility of actually viewing Langmuir monolayers at micro scale from the optical contrast due to different properties of various co-existing phases (these techniques will be discussed later in Section 3.4). Compared to a (macroscopic) rheological measurement such as a Π–A isotherm, optical microscopy provides a complement of information about the mesoscopic morphology of transitional Langmuir monolayers.

There are elaborate structures and phase transitions in Langmuir monolayers [95, 85, 150]. Figure 2.4 shows a generalized Π–T phase diagram of Langmuir monolayers incorporated the results of Refs. [130, 92, 103, 21, 171, 88, 18, 3, 139, 74] by Overbeck & Möbius [129]. It reveals most of the condensed phases known at present and is valid for fatty acids [160, 163, 19], for ethyl [107] and other esters of long-chain acids [142], and for acetate esters of long-chain alcohols [108]. The temperature and pressure scales vary with chain length and the nature of the head group of amphiphiles (see Fig. A.2 for fatty acid monolayers). However, up to now, researchers used discrepancy of nomenclatures for different phases of Langmuir monolayers. The following Table 2.2 lists phases observed in monolayers, and the nomenclatures used by different authors [85].

Table 2.2. LM phases observed in different studies and nomenclatures used by different authors (adapted from Ref. [85]).

Literature Refs.	Nomenclatures							
Adam [1]	LE	close-packed heads				close-packed chains		
Dervichian [35]	liquid	mesomorphous				solid		
Harkins *et al.* [66]	LE	LC				superliquid	solid	
Harkins & Copeland [64]	L_1	L_2				LS	S	
Stenhagen [163]	L_1	L_2		L_2'		LS	S	CS
Lundquist [107, 108]	L_1	L_2		L_2'	L_2''	LS/LS'	S/S'	CS/CS'
Lin *et al.* [103], Shih *et al.* [155]		D		C	B	RI-RII	A′	A
Bibo *et al.* [18]: monolayer phases		L_2/L_2'		S'/L_2^*	L_2''	LS	S	CS
Bibo *et al.* [18]: related smectic (Sm) categories	Sm A	Sm I/Sm L		Sm H/Sm F	Sm K	Sm BH	Sm E	
Schwartz *et al.* [152]		I		F	I'		U	U'
Overbeck & Möbius [129], Durbin *et al.* [44], and Riviére *et al.* [147]		L_2	Ov	L_2'	L_2''	LS	S	CS
Durbin *et al.* [43]		L_2		I-L_2'		LS	S	
Theory: Kaganer & Loginov [84]		L_{2d} L_{2h}	Ov	L_2'	L_2''	LS	S	CS
Azimuth of tilt[1]		NN NN	NNN	NNN	NN	U	U	U
Azimuth of unit-cell distortion[1]		U NNN	U	NN	NN	U	NN	NN

[1] (normal to chains), NN = tilt or distortion to the nearest-neighbor molecule, NNN = tilt to the next-nearest neighbor molecule, U = untilted or undistorted hexagonal. Azimuth of distortion is that of stretching of the unit cell.

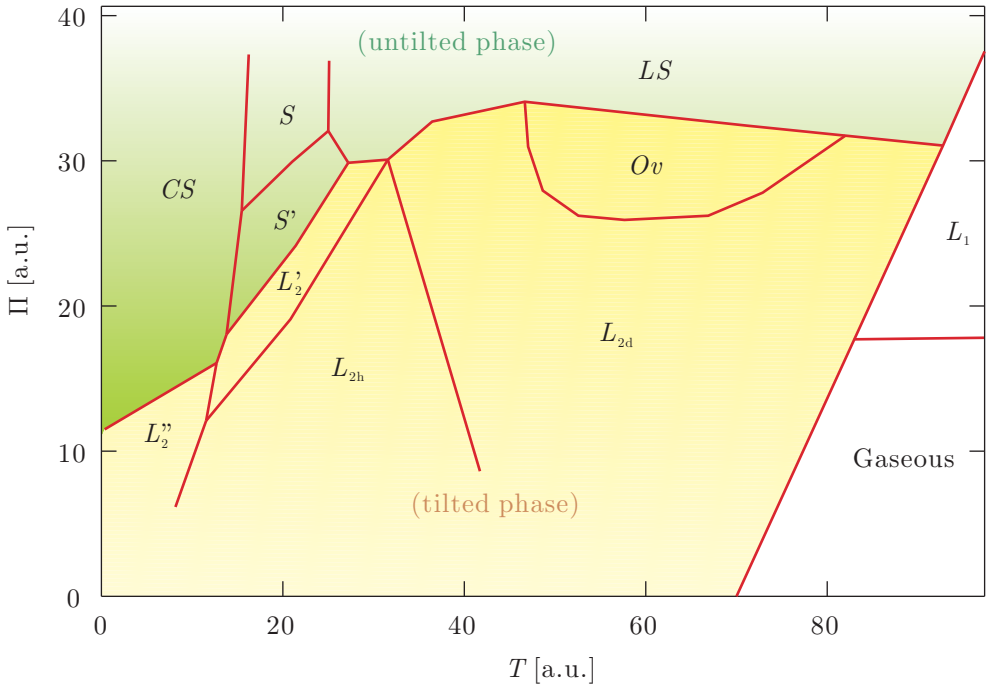

Figure 2.4. Generalized phase diagram of Langmuir monolayers that was incorporated the results of Refs. [130, 92, 103, 21, 171, 88, 18, 3, 139, 74] by Overbeck & Möbius [129]. The phases are designated according to the Harkins-Stenhagen notation. *Ov* denotes the phase discovered by Overbeck & Möbius [128]. The separation of the L_2 phase into herringbone ordered L_{2h} and disordered L_{2d} is proposed by Kaganer *et al.* [85].

2.4.3 Properties and structures of LM phases

All phases presented in the phase diagram (Fig. 2.4), characterized by using X-ray diffraction or optical microscopy techniques, have been found to exhibit a variety of molecular arrangements [95, 129].

Gaseous (G) phase

Generally, a very dilute monolayer, with a molecular area A in the range of hundreds of square angstroms (or more), can be well described as a 2-D gaseous (G) phase. In the G-phase, a main part of the hydrocarbon chain is hydrated by water, the amphiphilic molecules are seen to behave as a 2-D ideal gas[4] if the surface concentration,

[4] *e.g.* at molecular areas of the order 50000 Å^2·molecule^{-1}, the monolayer of PDA exhibits a behavior consistent with a 2-D ideal gas law [61]

Γ ($\Gamma \equiv \frac{1}{A}$), is small enough. Hence, the 2-D ideal gas law (Henry's model [104]) can be described as:

$$\Pi A = kT, \tag{2.1}$$

where Π is the surface pressure, A is the molecular area, k is the Boltzmann's constant (1.381×10^{-23} J·K^{-1}) and T is the thermodynamic temperature. In principle, any monolayer-forming substance will exist as a gaseous film if the molecules are sufficiently widely separated (large enough molecular area). Other equations of state, based on various assumptions that to consider the monolayer to be a non-ideal 2-D gas have been reported (*e.g.* Volmer model, ven der Waals model, Langmuir model and Frumkin model etc. [104]).

Liquid-expanded (LE) phase

With further decrease of molecular area (by increasing surface pressure for instance), the monolayer can exhibit LE phase as shown in Fig. 2.3. As for the G phase, the polar heads of the molecules are disordered and the chains are conformationally disordered [85]. The surface potential does not show fluctuations, indicating that the monolayers are homogeneous and the LE phase resembles to a 2-D isotropic arrangement of amphiphiles. The quantitative interpretation of Π–A curves for LE monolayers is in a less satisfactory state (similar to the theoretical treatment of classical liquids). Langmuir [97] derived the first equation of state for LE monolayers by assuming that the upper surface of the monolayer behaves as a bulk hydrocarbon liquid, and therefore exhibits a normal liquid surface tension. Various attempts have been made to complement Langmuir's ideas with the aim to derive a relevant equation of state for LE monolayers ([51]). Up to now, there is still a strong debate in the literature on the criteria which could permit to select the more relevant equation of state for LE phase [47].

Condensed phases

The term *condensed* is used to denote all phases of the monolayer with the hydrocarbon chains aligned, in contrast to the G and LE phases for which the chains are conformationally disordered. On the Π–A isotherm (Fig. 2.3) at a low molecular area, we can typically note a kink[5] which divides the isotherm into two regions. Each region possesses different level of surface compressibility, generally referred to as "liquid-condensed" (LC) phase and "solid" phase (see Fig. 2.3). The compressibility of Langmuir monolayer can be defined as,

$$C = -\frac{1}{A}\left(\frac{\partial A}{\partial \Pi}\right)_T, \tag{2.2}$$

where C is of the order of 10^{-3} m·(mN)$^{-1}$ for LC phase. From this definition, the slope of the isotherm is directly related to surface compressibility.

In fact, terminology of LC phase and solid phase for a monolayer was proposed long before structural data on monolayers became available, and it can be confusing today since it is inconsistent with the present knowledge. Theoretically, a monolayer possesses the same degree of translational order in both regions in the isotherm. Depending on the temperature, the two regions can be either long range in crystalline phases or short range in mesophases [84]. According to X-ray diffraction studies [84], the hydrocarbon chains of the amphiphile are aligned parallel to each other. The orientation of the chains is respectively tilted to the water surface in LC phase but perpendicular to the water surface in solid phase, as illustrated in Fig. 2.3. The two condensed regions in the isotherms can also be named tilted condensed phase and untilted condensed phase. The monolayer is relatively easier to compress in the tilted phase (LC phase): by decreasing the tilt angle, the surface area will be decreased. However, in the untilted phase (solid phase), the gap between close-packed vertical molecules determines a large area density (or surface concentration Γ), therefore, the solid phase is much less compressible than the LC phase.

For monolayers, the phases contain only a subtle slope change in the Π–A isotherm,

[5]The kink was firstly observed and treated as a phase transition by Adam [1].

however, a rich family of condensed phases (see Fig. 2.4 and Table 2.2) have been revealed thanks to optical microscopy and X-ray-diffraction data. A detailed discussion on the molecular orientations in condensed Langmuir monolayers is available in appendix A. It can be nevertheless helpful to introduce briefly here basic ingredients on that subject. When a substance is close to but lower than the positional order of a crystal (solid) while being more ordered than an isotropic liquid, it is called a liquid crystal. There are many different types of liquid crystal phases with different degrees of orders ([81], Chapter 1), such as nematic, smectic, helical, cholesteric phases, etc.. In the appendix A, one focuses the presentation on smectic phases[6] because they are the more relevant to the molecular orientations in Langmuir monolayers [95].

2.4.4 Phase transitions of Langmuir monolayers

G–LE and LE–LC phase transitions

According to the modified Gibbs phase rule, if the molecular area, A, changes in a one-component monolayer while the surface pressure, Π, remains constant, there is coexistence of two phases of different condensation state at a given unchanged temperature. Generally, a fatty acid LM exhibits two major co-existing phase transitions (see Fig. 2.3), the first one is a transition from gaseous (G) phase to liquid expanded (LE) phase and the second one is a transition from liquid expanded (LE) phase to liquid condensed (LC) phase.

The G–LE phase transition is generally interpreted as a first-order phase transition. Actually, this transition is difficult to study experimentally [90, 131] due to the small surface pressure involved.

With further compression and for a significant number of amphiphilic fatty acids,

[6]The term "smectic" derives from the Greek word, meaning soap, since the smectic phases tend to have mechanical properties similar to those of the layered phases of soaps. Smectic phases are related to the mesomorphic phase of a liquid crystal in which molecules are closely aligned in a distinct series of layers, with the axis of the molecules lying perpendicular to the plane of the layers. The smectic phases do not have the highly ordered structure of a crystalline solid, but they do have a greater degree of order than liquids. More particularly, they exhibit a long-range orientational order.

the LE–LC phase transition – of interest here in this dissertation – can be observed without special effort at room temperature and pressure. Theoretically, the presence of LE–LC phase transition should be correlated with the arising of a plateau in Π–A isotherm which indicates the first-order transition (see *e.g.*, Fig. 2.5 which shows the LE–LC phase transition at different temperature for a pentadecanoic acid monolayer). However, in many monolayer systems, the phase transition is possibly contrary to the Gibbs phase rule due to a feature with continuous change of slope. In fact, this apparent noncompliance provokes a long-standing controversy about the real existence of a transition and about the order and number of phase transitions [148]. For the phenomenon of non-horizontal isotherms, some researchers presented theoretical treatments based on formation of small molecular aggregates [78, 48, 148]. Pallas & Pethica [130] were able to obtain flat features on PDA isotherms by taking extreme care to avoid contamination. Although their results shows that the introduction of impurities will cause a permanent slope on Π–A isotherm even during the course of LE–LC transition, it is still not clear that this is the exclusive interpretation (*e.g.* electrostatic interaction between domains may also been consider).

G–LE–LC triple point

According to the literature [122, 94], G–LE and LE–LC transitions merge at low temperatures. Below the G–LE–LC triple point (tamperature: $T = T_t$), a direct transition from G to LC phase takes place. The triple point for pentadecanoic acid is found close to 17 °C (as confirmed in Fig. 2.5, see also Ref. [122]). Note that for myristic acid, one gets $T_t \approx 31$ °C [168], and for stearic acid, $T_t \approx 40$ °C [87, 129]. Therefore myristic and pentadecanoic acids are the only fatty acids which can be conveniently used to study stable LE–LC co-existing phases of a LM under flow at room temperature and in the neutral form. Due to the length of its alkyl chain, PDA is expected to be slightly more amphiphilic than myristic acid. The last two points are among the reasons for which PDA was finally selected as a model system during this dissertation.

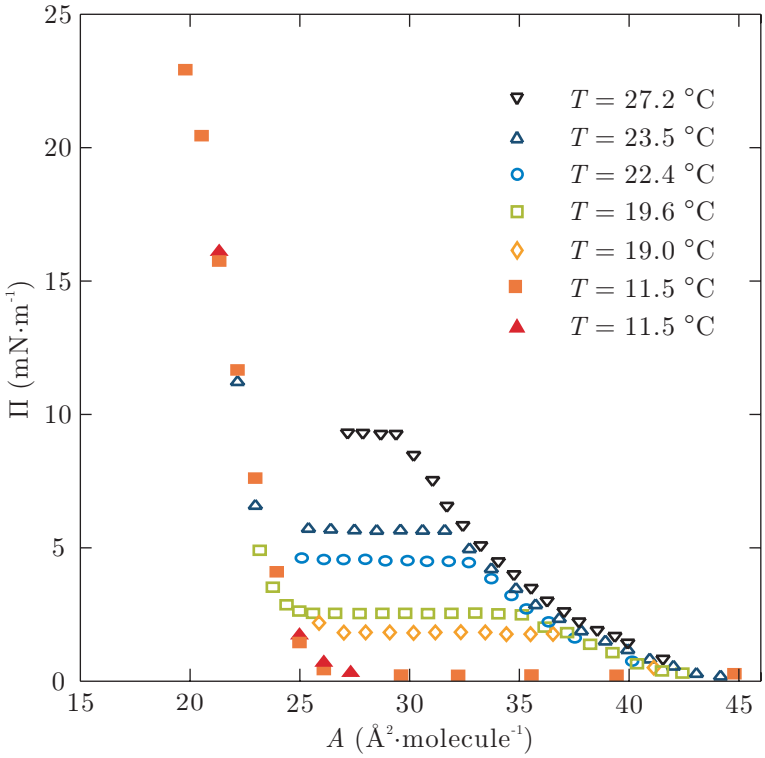

Figure 2.5. A selection of isotherms of PDA monolayers (after Ref. [45]). Those isotherms exhibiting a liquid phase (open symbols) were produced by expansion; note the flat first-order coexistence regions. Increase of surface pressure by successive addings of PDA was used at $T < T_t$ where $T_t \approx 17$ °C is the triple point for a PDA monolayer [45].

2.4.5 Dissociation of fatty acids

When the pH value of the subphaseHH is increased, fatty acid molecules in the monolayer dissociate [20, 83]. The portion of charged carboxylate in the fatty acid monolayer varies as a function of pH. The substitution of carboxylates for neutral fatty acid molecules in monolayer leads to a change in the intermolecular interactions. Hence the phase behavior of a fatty acid monolayer is expected to depend on the subphase pH. Aveyard *et al.* [8] provided the evidence that fatty acid (stearic acid) start to dissociate and change their behavior measurably at a pH value around 6. Figure 2.6 shows Π–A isotherms of arachidic acid at 25 °C within a certain range of pH. Johann [83] demonstrated that the plateau onset pressure (it can be regarded as the surface pressure of LE–LC phase transition) is a linear function of the subphase pH at constant temperature (see the inset in Fig. 2.6). It should be noted that the

cleanest subphase made from ultrapure water only is not well defined as regards charge density. A pH $\approx$ 5.5 is established after a time delay which is due to dissolution of the CO_2 from air inside water subphase, and the head groups are partially dissociated [85]. As a consequence, most studies on fatty acid monolayers are performed at pH = 2 or 3, since ionization is negligibly small. All the experiments of this dissertation were carried out with a subphase of ultrapure water acidified with hydrochloric acid of high degree of purity ([HCl] = 10^{-2} M).

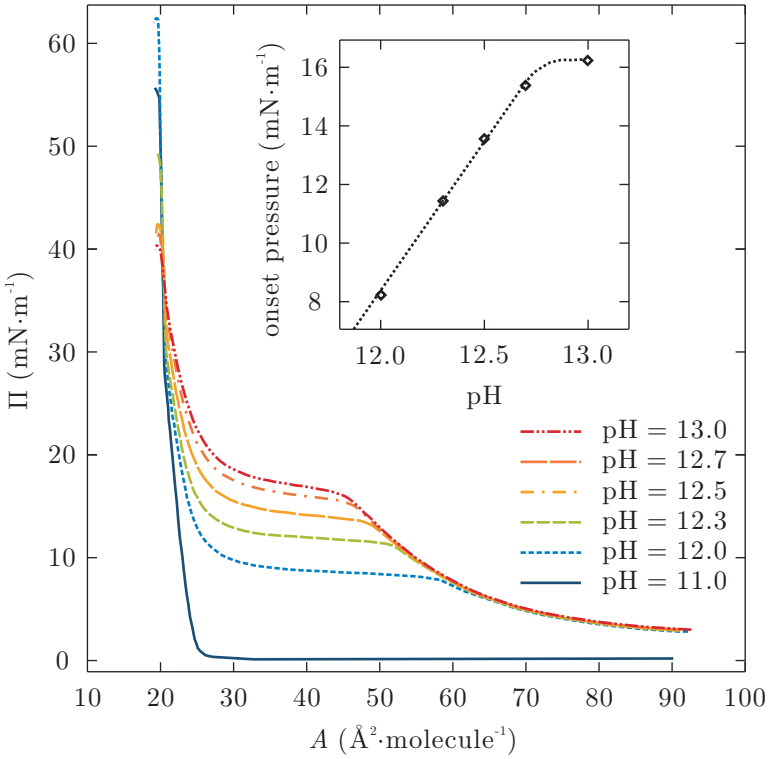

Figure 2.6. Π–A isotherms of arachidic acid at 25 °C for different pH values (adopted from Ref. [83]). The smallest surface pressure at the onset of the plateau (transition from LE to LC phases) is found to be a linear function of subphase pH at constant temperature (see insert).

2.4.6 Stability of fatty acids monolayers

The stability of Langmuir monolayers often refers to *collapse*, a process which designates the break-up of the 2-D self-assembly and the arising of a 3-D structure within the LM. This process can be regarded as a solid phase nucleation. From Π–A isotherms

recorded during a constant rate of monolayer compression, the collapse surface pressure, Π_c (the highest surface pressure to which a monolayer can be compressed without noticeable expulsion of amphiphiles out of the LM), can be usually determined from the arising of a spike or a plateau at surface pressures $\Pi > \Pi_c$ [20]. The critical surface pressure, Π_c, is highly dependent on the rate of compression and it is often difficult to find a reproducible value of Π_c [85].

The spreading pressure of a two-phase monolayer in thermodynamical equilibrium with its solid phase along an air-water interface is called *equilibrium spreading pressure* (ESP). Π_{ESP}, can be properly determined by placing tiny amounts of surfactant on a water surface and monitoring the progress in surface pressure until a steady value is achieved. However, according to Iwahashi [80], the published values for the ESP of fatty acids monolayers are seen inconsistent. He claimed that a discrepancy can be mainly attributed to the insertion of impurities within the LM, or to geometrical differences in subsequent solid domains at mesoscopic scale. With a further increase of pressure, the barrier to nucleation will decrease, and the arrangement of critical nuclei of 3-D solid phase becomes more possible; once critical nuclei have formed, they grow into the solid phase [187]. These phenomena could explain why the constant pressure exceeds ESP can result in the decrease of molecular area with time [157]. If the surface pressure of a monolayer exceeds Π_{ESP} but lower than Π_c, the monolayer is metastable with respect to the formation of a 3-D crystalline phase subsequent to a collapse.

In fact, for fatty acids, a surface pressure above ESP can also lead to a kinetic instability of the monolayer [20]. If the monolayer is not kinetically stable, molecules will move away from the interface during the course of time. In this case, the surfactant molecules can evaporate in air, can be solubilized in the subphase or can form 3-D crystals at the liquid surface. The loss of amphiphilic specie depends on surface pressure, temperature, subphase pH and the molar balance between the hydrophilic head and the hydrophobic chain of the amphiphile involved [20]. Below Π_{ESP}, amphiphilic specie can only be lost via evaporation or solubilization [83]. Causes for the

previous kinetic instability include evaporation [26], surface chemical reactions [158], monolayer dissolution into the subphase [120] and collapse [26, 187].

A monolayer below Π_{ESP} constitutes a main condition for thermodynamic stability of monolayers. In principle, the thermodynamic stability against the dissolution is determined by the hydrophilic / hydrophobic balance of the amphiphile (the larger the hydrophobic chain, the more stable the LM).

2.5 Pentadecanoic acid, as a result of selection

As briefly mentioned above, the surfactant selected for all the experiments in this dissertation is the pentadecanoic acid (PDA). Fig. 2.7 shows the molecular structure of PDA. Our reasons for this decisive choice are summed up as follows:

- ◇ The triple point and the hydrophilic / hydrophobic balance of PDA are both in favor of a LE – LC transition which is very quite stable and reproducible at room temperature.
- ◇ The hydrophilic / hydrophobic balance is also small enough to avoid any significant solubilisation in the subphase at a time-scale of one hour. Despite this care, we will see that solubility of PDA can not be considered as entirely negligible in our experiments.
- ◇ The PDA stands also as user-friendly; the protocols of use and its characterisation around thermodynamical equilibrium were particularly well-established in the two previous decades (80's-90's), as demonstrated by the literature devoted ([91, 118, 80, 29, 131, 184, 45, 166, 122, 74]).
- ◇ The PDA is also quite appropriate to imaging under Brewster angle microscope (or BAM, see also Chapters 3 and 4): the LC domains it forms exhibit a length scale particularly suitable to the use of a BAM: nor too small compared to the

spatial resolution of a BAM device, neither too large compared to the typical size of the laser spot involved (Chapter 3).

As shown in the dissertation, the adsorption isotherms measured with PDA are reproducible in spite of all the complex molecular arrangements that could arise at nanometer scale (smectic or hexatic phases, see e.g. appendix A).

As a matter of fact, the details at nanoscale of a condensed phase and more particularly, all the collective changes induced at molecular scale by a flow ([49, 114, 115, 75, 76, 77, 150]) are definitely not the focus of this dissertation. Here, our interest is entirely devoted to flow-driven phenomena induced at the mesoscopic scale of a full LC domain (surface coverage: 100 μm^2 to 1 mm^2, typically the scale of a future single-crystalline grain).

To complete this comment, just say that our approach is the one of continuum mechanics with a special emphasis on the flow of a two-phase LM made from a continuous LE phase populated by a dispersion of LC domains.

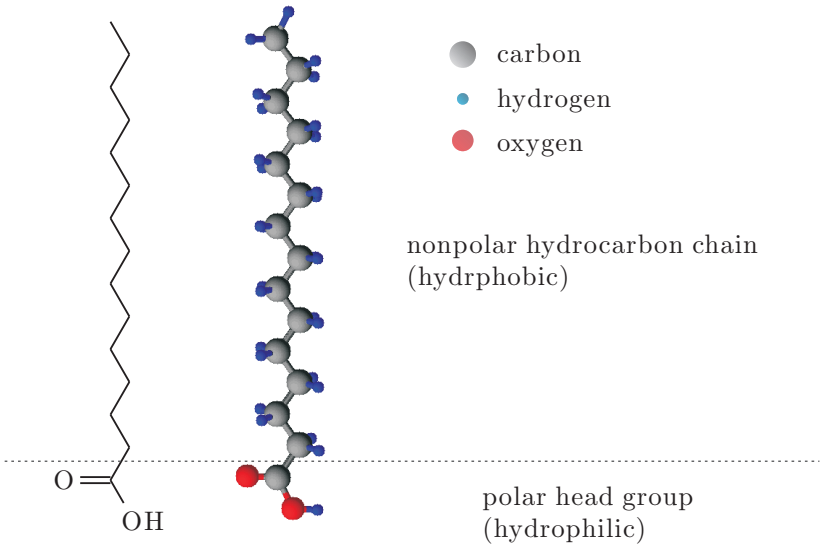

Figure 2.7. Molecular structure of pentadecanoic acid (PDA).

Chapter 3

Experimental characterisation of a Langmuir monolayer

Monolayers exhibit a variety of measurable quantities due to their specific mechanical, physico-chemical and optical properties. A lot of studies about insoluble monolayers have been carried out by using different experimental techniques. In this chapter, we consider briefly the relevant background on liquid surfaces. We present the state of the art about the experimental techniques we selected to measure the surface pressure as well as the surface viscosity, and to visualise specifically the Langmuir monolayer (LM).

3.1 Static properties of liquid surfaces

The force, due to unbalanced molecular attraction, which tends to pull molecules of the liquid surface into the inside of a supporting liquid subphase, and hence to minimize the surface area of a bulk of liquid, is commonly refereed to as surface tension. Since the work done in extending a surface against this force produces an increase in the energy of the system, it is appropriate to analyze the thermodynamics of a system involving an interface between liquid and gas bulks in an attempt to

understand surface tension effects. According to the treatment that was given by Gibbs, at thermodynamic equilibrium, surface tension σ is referred to as a *free energy per unit area* and may equally be thought of as a *force per unit length* that can be described by the following relation:

$$\sigma = \left(\frac{\partial G}{\partial a}\right)_{\Pi,T,n_i} = \left(\frac{dF}{dc}\right)_T, \tag{3.1}$$

where G is Gibbs surface free energy; a, the area of the interface; n_i, the molar amount of the i^{th} chemical species which make the interface; Π, the surface pressure; T, the temperature of the interface, and F is the force exerted by the surface upon an edge of length c. The equilibrium property of surface tension is inherent in many accepted norms of the interfacial behavior: such as the tendency for bubbles and droplets to assume a spherical shape, the beading-up of droplets on a solid surface and the rise of liquids through narrow capillaries.

When amphiphilic species adsorb at an initially clean air-water interface from the subphase (Gibbs monolayer) or when they are not soluble but directly spread over the interface (Langmuir monolayer), the initial surface tension of the liquid surface σ_0 (72.8 mN·m^{-1} for water at 298 K, 1 atm) can be reduced down to a value σ. The difference in surface tension is commonly referred to as surface pressure,

$$\Pi = \sigma_0 - \sigma, \tag{3.2}$$

and it corresponds to surface (2-D) pressure that results from the molecular interaction between amphiphilic species along the liquid surface. The quantities σ and Π have therefore the same units (mN·m^{-1})[1], although their physical meanings are different. The measurement method of surface pressure will be described in section 3.1.2.

[1] 1 mN·m^{-1} = 1 dyne·(cm)$^{-1}$

3.1.1 Contact angle

When a drop of liquid is placed on a smooth solid surface, the extent to which it will wet the solid surface is governed by a balance between the three surface tensions involved. The net force issued from the balance between:

- ◇ the surface tension, σ_{GS}, due to the interaction between gaseous and solid phases,
- ◇ the surface tension, σ_{LS}, due to the interaction between liquid and solid phases,
- ◇ and the surface tension, σ_{LG}, due to the interaction between liquid and gas phases,

gives rise to spreading (or non-wetting) of the liquid phase until an equilibrium position is found [13]. Typically, the position of the contact line will change in response to the horizontal components of the surface tensions acting on it. The zeroing of the net force (static equilibrium) can be illustrated in Fig. 3.1 (a) which shows a sessile drop of liquid (L) deposited on a flat solid (S) surface, both phases being surrounded by air (G) as a third phase. The static angle, θ_C, defined at the contact line as the angle between the L/S surface and the L/G surface, is referred to as a *contact angle*. In this particular equilibrium, the contact line being at rest, the well-known Young's equation is recovered as the horizontal projection of the previous balance between all surface tensions:

$$\sigma_{GS} = \sigma_{LS} + \sigma_{GL}\cos(\theta_C). \tag{3.3}$$

Although Eq. (3.3) describes the equilibrium contact angle in terms of the interfacial tensions, it gives no real insight into the reason that a certain value of contact angle is reached. An understanding of the origin of contact angle requires knowledge of the balance of forces between molecules in the liquid drop (cohesive forces) and those between the liquid molecules and the surface (adhesive forces).

A surface that has primarily polar groups on the surface, such as hydroxyl groups, will have a good affinity for water and therefore strong adhesive forces and a low

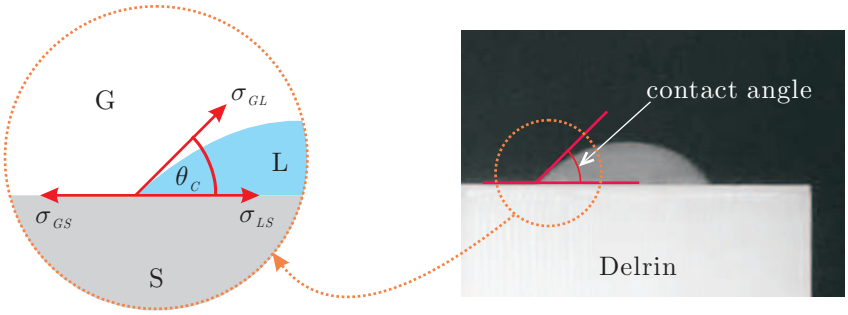

(a) (b)

Figure 3.1. (a) Surface tensions acting at the contact line for a sessile drop (adopted form Ref. [13]). (b) 25 μl water droplet on Delrin™ demonstrating the contact angle caused by the balance between all surface tensions (adopted from Ref. [60]).

contact angle. Such a surface is called *hydrophilic* (the liquid phase wets the solid surface: $\theta_C < 90°$).

If the surface is made up of non-polar groups, which is common for polymer surfaces or surfaces covered by an organic layer, we say that the surface is *hydrophobic* (the liquid phase does not wet the solid surface: $\theta_C > 90°$).

If $\theta_C = 0°$, wetting is said to be complete or perfect: this is a basic condition of the Wilhelmy method used in this dissertation.

3.1.2 Surface pressure

The most commonly measurable property of an insoluble monolayer is its surface pressure, Π. Most of the methods devoted to surface pressure measurement rely on the difference between two surface tension measurements. The first one is performed on the pure liquid surface (surface tension σ_o) whilst the second one is performed on the same liquid surface but covered by the Langmuir monolayer (surface tension σ_o). As a consequence, surface pressure is deduced from the difference: $\Pi = \sigma_o - \sigma$.

Most of these measurement methods[2], based on capillarity, are ill-suited for the

[2]such as: capillary rise method [63, 145], maximum bubble pressure method, drop weight method [170], du Nouy (ring) method [41], Wilhelmy (plate) method [183], pedant drop method [5], sessile drop or bubble method, flow method [169], capillary waves method, maximum bubble pressure method [119]...etc.

study of monolayers except the pendant drop method and the Wilhelmy method [2]. Both approaches are capable of surface pressure measurement with a similar precision: about 0.01 $mN{\cdot}m^{-1}$ [2].

For the pendant drop method, a motor-driven syringe allows changes in drop volume to study surface tension as a function of surface area (an time-dependent image processing is required). The advantage of this approach is that it is useful for materials available in limited quantities and that it can be extended to study monolayers at liquid-liquid interfaces [101]. However, it is much more time-consuming than the Wilhelmy plate method and the previous advantages are not really relevant to our study.

It is obvious that there are many possible variations around the Wilhelmy plate method[3], ranging from extremely simple and inexpensive devices to elaborate instruments with extremely thin plates and sensitive recording balances. This is one of the important advantages of the Wilhelmy plate method. Another advantage is the fact that only the plate needs to be in contact with the liquid surface; since the plate may be made from any inert materials (platinum, quartz...), the possibility of contamination is minimized. Therefore, we choose the Wilhelmy plate method to measure surface pressure of LM in our study.

Wilhelmy plate method

In the Wilhelmy plate method, an immersing plate is suspended at the air-water interface as shown in Fig. 3.2 (b). The forces acting on the plate are due to surface tension and gravity, partially compensated by buoyancy effect due to the weight of liquid displaced. For a rectangular plate of dimensions l, w and t (length, width and thickness), and the plate density ρ_p immersed to a depth d in a liquid with density of

[3] As a technique close to the Wilhelmy method, the du Nouy method makes use of a circular wire in replacement of a plate (see Fig. 3.2 (a)). In the du Nouy method, however, the ring has to be kept as horizontal as possible (a departure of 1° is found to introduce an error of 0.5 %, whereas one of 2.1° introduces an error of 1.6 % [2]). Besides, special care must be devoted to avoid any disturbance of the surface as the critical point of detachment is approached.

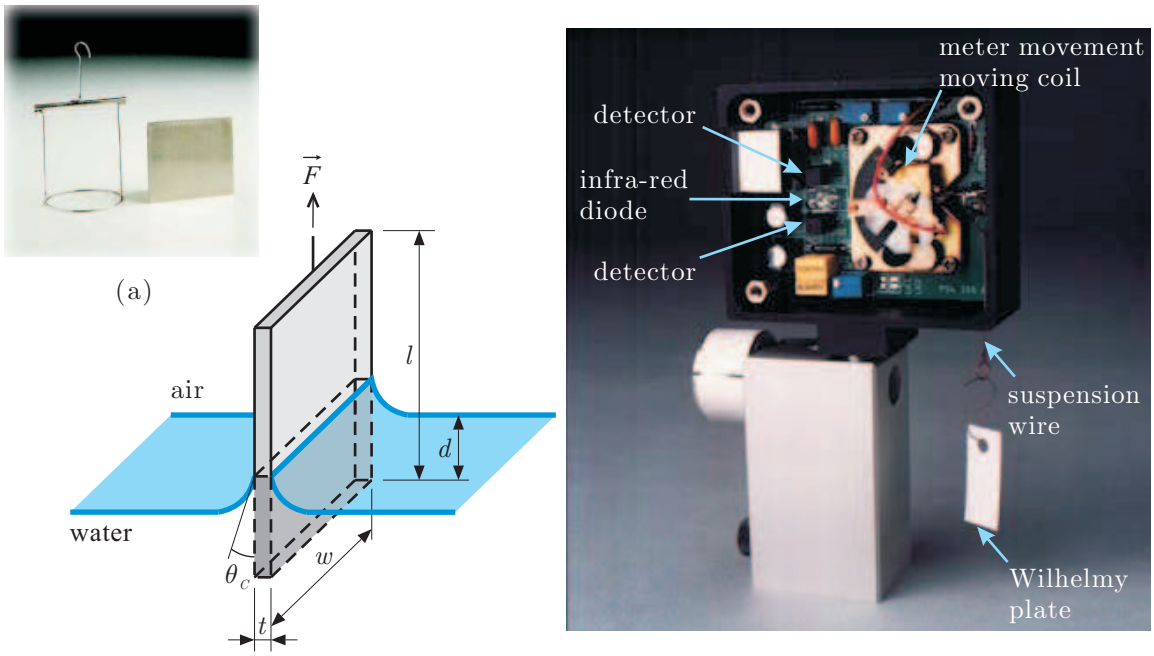

Figure 3.2. (a) Photo of a du Nouy ring (left) and a Wilhelmy plate (right). (b) Schematic of the Wilhelmy method, with d is the depth of the meniscus, t, the thickness of the Wilhelmy plate, w, its width, and θ_C the contact angle between the plate and the liquid surface. (c) Picture of the surface pressure sensor (PS4, Nima) used in this dissertation with electronics enclosure open. Infra red (IR) diode illuminates the edge of a moving coil. The position of the coil is detected from IR reflection and two position sensitive detectors.

ρ_w, the net downwards force $\vec{F}$ is given by:

$$\vec{F} = \underbrace{(\rho_p\, l\, w\, t)\, g}_{\text{weight}} + \underbrace{2\,(w+t)\,\sigma\,\cos\theta_C}_{\text{surface tension}} - \underbrace{(\rho_w\, d\, w\, t)\, g}_{\text{buoyancy}}, \tag{3.4}$$

where σ is the net surface tension; θ_C, the contact angle and g, the gravity. In Eq. (3.4), the buoyancy effect of the plate in the air is evidently neglected.

As θ_C is often unknown, use is made of a completely wetted plate, for instance a filter paper, which allows us to get $\theta_C = 0°$. In addition, when the underlying liquid is removed from any surfactants, the force reading is set to be zero before making any measurement. In this way, the surface pressure is directly measured as a difference of the surface tensions (see Eq. (3.2)). Hence, one eliminates the weight term in Eq. (3.4) as:

$$\vec{F} = -(\rho_p\, d\, w\, t)\, g + 2\,(w+t)\,\sigma. \tag{3.5}$$

We can also eliminate the buoyancy term in Eq. (3.4) because much attention is paid to keep the plate at a constant level despite downwards surface tension. As a consequence, the net force writes:

$$\vec{F} = 2\,(w + t)\,\sigma, \tag{3.6}$$

and consequently, the surface tension is deduced as follows:

$$\sigma = \frac{F}{2\,(w + t)}. \tag{3.7}$$

Measuring the relative change in F yields the surface pressure,

$$\Pi = -\Delta\sigma = -\left[\frac{\Delta F}{2\,(w + t)}\right]. \tag{3.8}$$

The pressure sensor contains a Nima 16 bit analog-digital converter. With that device, the surface tension of 70 mN·m^{-1} can be theoretically resolved with an accuracy of 10 μN·m^{-1}. However, the absolute accuracy is limited because it depends on the width of Wilhelmy plate, that is, if we increase the width of the plate, we increase the absolute accuracy. In our study, we used a piece of chromatography paper (Wattmann) as a plate (perimeter: 21 mm), which allows for an accuracy of 0.1 mN·m^{-1}. According to Eq. (3.7), a weight of 100 mg will give a surface tension reading of 46.7 mN·m^{-1}. This method was systematically used to calibrate our Nima surface pressure sensor.

3.2 Line tension

According to Gibbs [57], the line tension can be regarded as a concept of surface thermodynamics. However, the wide investigation of this quantity was undertaken only a century later because line phenomena are much more complex than surface ones to handle both from the experimental and theoretical points of view [149]. Experimentally, line tension, λ, is typically a very small force to measure ($\lambda \sim 10^{-12}$ N) and the availability of an accurate device to do this still remains challenging. Theoretically, compared to a surface which can be the merging of only two bulk phases, three bulks phases or also two surface phases merge simultaneously into one line. As

a consequence, line tension is a mechanical quantity more complicated than surface tension to model when the aim is to derive line momentum balances. Moreover, anticipating on Chapter 5 where all useful theoretical ingredients are given, line tension can not be considered as a mechanical concept only because short-range as well as long-range forces contribute simultaneously to it. Rusanov [149] presented several classifications of line tension. In our study, we will focus on the (in-place) line tension which separates two-dimensional phases (two stratifying LM for instance). According to Rusanov [149], in two-dimensional systems, because 2-D phases are separated not by surfaces but by lines, an excess surface pressure arises which yields line tension. In this situation, line tension can be seen as analogous to surface tension by reducing nevertheless one dimension.

The thermodynamic definition of line tension λ is

$$\lambda = \left(\frac{\partial G}{\partial p}\right)_{\Pi,T} = \left(\frac{\partial H}{\partial p}\right)_{\Pi,T} - T\left(\frac{\partial S}{\partial p}\right)_{\Pi,T}, \tag{3.9}$$

where H is surface enthalpy and S is surface entropy of a 2-D condensed phase. The line tension λ is therefore the free energy G required to extend the edge of a condensed domain by a unit length, or, in other words, to transfer molecules from the bulk of a 2-D condensed domain to its perimeter of boundary, p. The main contribution to λ originates from the enthalpy term, since the translational and conformational freedom of the molecules is not expected to be very different in the subphase and at the interface. The enthalpy term is the energy required to break the intermolecular bonds and construct new ones to ensure molecular transfert to (or from) the edge [83].

From the past two decades, the experimental estimates of the line tension in monolayer systems were developed [123, 16, 109, 110, 185]. From the measurement of the excess free energy of molecules between two coexisting phases of monolayer (free energy from the transition region and from the interior of the phases), one obtains virtually the line tension. Besides, from the knowledge of the average dipole moment density of the phases involved, the line tension could be estimated. By making use of the impact of a surface shearing upon a condensed domain, Benvengnu & McConnell [16] have

produced bola-shaped domains and measured their relaxation to their original circular shape after switching off imposed shearing; the line tension was determined from the estimation of the hydrodynamic drag acting against shape recovery. In this way, the line tension of a lipidic domain (LM made from a binary mixture of average composition 30 mol % cholesterol, 70 mol % dimyristoylphosphatidylcholine) was measured and found to decrease with a growing surface pressure. Mann *et al.* [110] performed a similar technique to deduce line tension of a poly(dimethyl)siloxane (PDMS) domain: $\lambda = 1.1 \pm 0.3$ pN. In a recent paper, Wurlitzer *et al.* [185], a line tension between gas and LE phases of methyl octadecanoate, $\lambda = 7.5$ pN, was measured by using fluorescence microscopy combined with optical tweezers. With an estimated temperature (35 °C), they also found that the line tension was 0.3 pN smaller than the one for the LE–LC co-existing phases.

Many phenomena, such as

- ◇ transitions between circular, ellipsoidal, and triangular shapes [167],
- ◇ the changes for the curvature radius of domains on compression [146],
- ◇ the nucleation of domains [123], and
- ◇ the buckling instability [165], etc.,

could be explained based on the competition between (excess) line tension and electrostatic interactions. On a macroscopic scale, where the width of the phase boundaries is negligible, the line tension and electrostatic interactions determine characteristic patterns of monolayers in the coexistence region of two or more phases [185].

3.3 Dynamic properties of liquid surfaces

Fluid interfaces containing surfactants may exhibit dynamic behavior that differs considerably from surfactant-free interfaces. For instance, for a surfactant-free fluid

interface, the resistance to flow under an applied stress is very small, but in the presence of surfactant, it can become significantly. This difference in flow properties associated with the presence of a monolayer can produce a number of complicated effects. The dynamic behavior of fluid interfaces involves both surface rheology and hydrodynamics.

In addition to the arising of a surface pressure gradient which can impact upon fluid motion (Marangoni effect, see next section), other interfacial rheological stresses of viscous nature may arise (Fig. 3.3). The interfacial viscosity is involved in the stress tensor in an isotropic way as well as in a non-isotropic way, and two coefficients of viscosity are usually proposed for each kind of surface deformation: the *surface shear* viscosity and *surface dilatation* viscosity, respectively. These surface viscosities cause a damping of the interfacial motion.

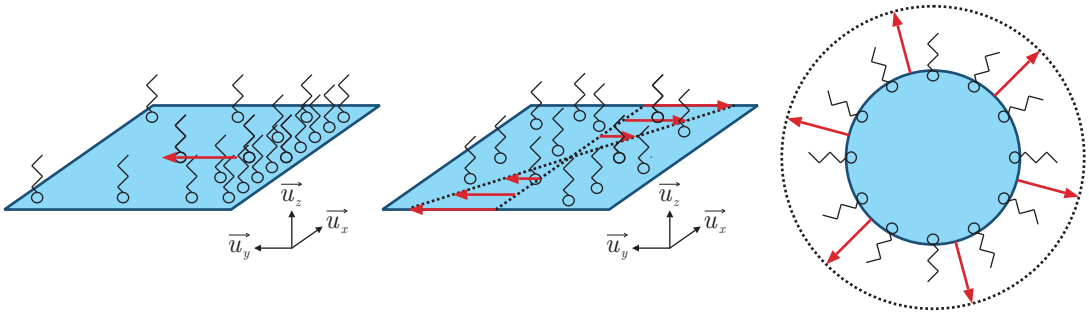

(a) Marangoni stress $\frac{\partial \sigma}{\partial y}$

(b) surface shear stress $\mu^s \frac{\partial^2 v_s}{\partial x^2}$

(c) surface dilatational stress $\kappa_s \nabla_s^2 \vec{v_s}$

Figure 3.3. Three interfacial dynamical properties (surface tension gradient (a), surface shear viscosity (b), and surface dilatational viscosity (c)) modified in presence of surfactants (adopted from Ref. [177])

3.3.1 Marangoni effect

In conventional circumstances, a fluid interface in equilibrium exhibits uniform surface tension. The magnitude of this surface tension varies with temperature, subphase pressure, and surfactant concentration within the fluid interface. Thus, should a nonuniformity (in surfactant concentration, say) develop within the fluid interface, and

interfacial pressure gradient will result, subsequently inducing both areal and volumetric fluid motions. For instance, since surfactant adsorption at a fluid interface lowers generally the surface tension, an inhomogeneous distribution of surfactant within the interface can induce local surface tension gradients and therefore, promote (or damp) a fluid flow. Such a surface gradient-driven flow (see Fig. 3.3 (a)), which attempts to restore a uniform surface tension, is basically the well-known "Marangoni effect" [113] (also referred to as Gibbs-Marangoni effect).

3.3.2 Surface shear viscosity

The shear viscosity is an important property of a Newtonian fluid. By definition, it is the force required to shear or equivalently, to produce a relative motion between fluid materials [182]. Analogously, 2-D *surface shear viscosity* is defined as follows: imagine a simple shear field imposed upon a planar fluid interface as depicted in Fig. 3.3 (b). Acting upon the linear boundaries of the 2-D fluid element are surface (2-D) shear stress τ_s. If two line elements of a surface are moving relative to each other, with a surface (2-D) shear rate, $\frac{\partial v_s}{\partial x}$, the associated surface shear stress is $\mu_s \frac{\partial v_s}{\partial x}$, where μ_s denotes the surface shear viscosity or, by analogy with bulk-fluid (3-D) hydrodynamics, the Newtonian[4] surface viscosity. The surface shear viscosity μ_s is normally reported in units of surface Poise (sP)[5]. Generally, surface shear viscosity is negligibly small for a surfactant-free interface and its magnitude increases monotonically with surfactant concentration [138].

The study of surface viscosity was initiated by Plateau [136] who observed that compared to the viscosity in the bulk of two neighbouring fluids, the viscosity at the interface between them is enhanced. At that time, surface viscosity was designated by *superficial viscosity*. In 1913, Boussinesq [23] found that a surface viscosity can also be demonstrated from the measurement of a drag force on a drop moving in another liquid. In 1959, Sternling & Scriven [164] indicated the effect of surface viscosity

[4] A fluid for which a stress is directly proportional to a deformation.
[5] 1 sP = 10^{-3} kg·s^{-1}

on Marangoni instability. Since the work of Sternling & Scriven, the role of surface viscosity in interfacial processes has received widespread attention.

Measurement of surface shear viscosity

Numerous experimental techniques have been developed with the purpose of measuring the surface shear viscosity μ_s of Newtonian interfaces. In principle, it should use viscous-traction driven flows to avoid the existence of surface-tension gradients which could appreciably complicate the absolute detection of the surface viscous stress [46]. However, many of the earliest techniques for measuring surface shear viscosity were found to be plagued by the presence of surface-tension gradients [136]. Marangoni [113] recognised that the oscillation of a needle within a surfactant-adsorbed fluid interface, as initially proposed by Plateau for the purpose of deducing the surface viscosity, should cause surface-tension gradients owing to compression of the surface. Even now, oscillating needle experiments continue to be attractive with constant improvements of modelling [37] along the lines of Marangoni.

Surface viscometer, first proposed by Dervichian & Joly [35] and Harkins & Meyers [65], utilized surface pressure-driven interfacial flows. This early technique proved impractical for measuring interfacial shear viscosity owing to the difficulty involved in unambiguously distinguishing between Marangoni and interfacial viscous effects. To avoid this complication, Davies [31] later proposed a variation of the surface viscometer (now known as the *double knife-edge viscometer*), employing viscous traction forces. However, the induced surface flow of the Davies canal viscometer suffers the disadvantage of being relatively insensitive to the interfacial viscous stress. The modern surface viscometer discussed in later section is known as the *deep-channel surface viscometer*. It was first proposed by Mannheimer & Schechter [112] as an improvement of the earlier device of Davies [31].

Modern experimental techniques succeed in avoiding the presence of interfacial-tension gradients. Therefore, the surface viscosity is often measured by generating

surface flows while avoiding dilatational motion at the same time. In reality, the surface viscosity can be measured directly or indirectly. The direct method means the measurement of the force required by a floating movable object (disc, needle, ring...etc.) in order to shear the surface. With the indirect method, the surface viscosity is calculated by fitting the velocity profile along a surface submitted to an externally-applied shearing. The direct method, is comparatively simpler but it is also less accurate than the indirect one: the range of sensitivity may be expected to be on the order of $\mu_s \geq 10^{-2}$ sP (10^{-5} kg·s^{-1}), as estimated from the single knife-edge method and its derivatives for instance [46]. In contrast, the indirect method, such as deep-channel surface viscometer, is regarded as very sensitive since it enables the detection of a surface shear viscosity as low as 10^{-4} sP (10^{-7} kg·s^{-1}) [46].

The deep-channel surface viscometer

The original design of the deep-channel surface viscometer [112] consists of two concentric cylinders lowered into a pool of liquid contained within a dish, to a depth for which the cylinders nearly touch the bottom of the dish as shown in Fig. 3.4. During operation of the instrument, the dish is rotated with a monitored angular velocity Ω. The surface motion of the interface within the channel formed by the concentric cylinders is measured from glass or Teflon hollow beads (diameter: 100 to 200 μm) distributed all along the fluid interface. The main lines of the modeling by Mannheimer & Schechter [112], devoted to the deep-channel surface viscometer, are recalled in Appendix B.

3.3.3 Surface dilatational viscosity

Material compression and expansion is a more commonplace occurrence with interfaces than with bulk fluids, owing in part to the ability of an one interface to exchange molecules with one (or two) underlying(adjacent) 3-D phase(s). Therefore, while the dilatational viscosity involved in the classical Newtonian approach for 3-D viscous flu-

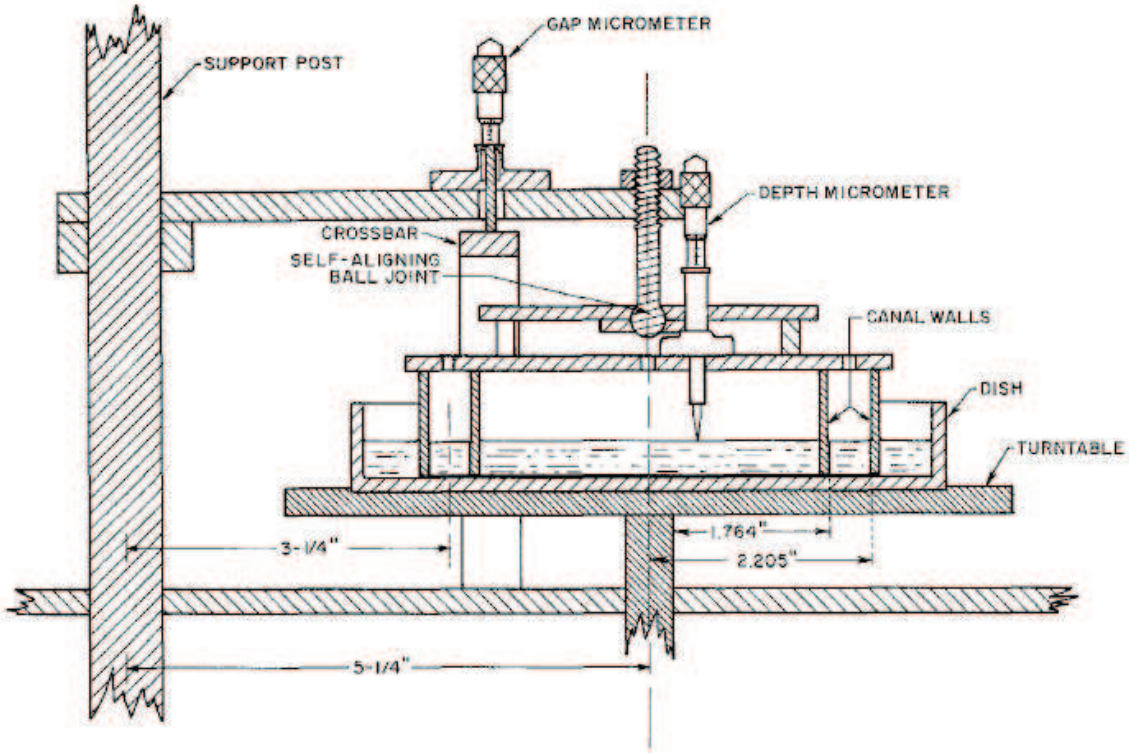

Figure 3.4. Schematic cross section of the deep-channel surface viscometer (adopted from Ref. [112])

ids is seldom encountered in practical applications, its 2-D counterpart – the surface dilatational viscosity κ_s – stands as a significant rheological property of Newtonian interfaces ([46], p. 33).

Nevertheless, the surface dilatational viscosity, κ_s, remains considerably more problematic to measure than surface shear viscosity, μ_s. This is because the surface elasticity (Marangoni stress), which acts in the same direction as the dilatational stress is often dominant in the surface stress balance. Measured values of κ_s for Newtonian interfaces are consequently distinguished in the literature (details in [46], Chapter 8).

3.3.4 Stress balance at a gas-liquid interface

Scriven [154] and Aris [6] made decisive contribution to the writing of the momentum balance at the gas-liquid interface:

acceleration or inertial force = body force
+ surface tension gradient (Marangoni stress)
+ viscous resistance to dilation (interfacial stress)
+ viscous resistance to shear (interfacial stress)
+ force due to intrinsic curvature

Here, we are principally interested in determining how the presence of monolayers plays a role in this balance, and as such, we are not interested in the effects of externally imposed body forces. A main assumption is made in the development of the stress balance: the interface is supposed to be Newtonian, which permits to write a linear constitutive law[6] between the surface (excess) rate of deformation tensor, $\overline{\overline{D_s}}$, and the surface (excess) stress tensor $\overline{\overline{T}}_s$. As a consequence, the jump momentum balance at a Boussinesq-Scriven gas-liquid interface [156] can be derived as:

$$\begin{aligned} \overline{\overline{T}}_s &= \sigma \overline{\overline{I}}_s + \overline{\overline{S_s}} \\ &= \left[\sigma + (\kappa_s - \mu_s)\, \mathrm{div}_s \overrightarrow{v_s}\right] \overline{\overline{I}}_s + 2\mu_s \overline{\overline{D_s}}, \end{aligned} \tag{3.10}$$

with $\overline{\overline{S_s}}$, the viscous part of the surface stress tensor, described as a linear function of the rate of surface deformation tensor:

$$\overline{\overline{D_s}} = \frac{1}{2}\left[\nabla_s \overrightarrow{v_s} \cdot \overline{\overline{I}}_s + \overline{\overline{I}}_s \cdot (\nabla_s \overrightarrow{v_s})^T\right]. \tag{3.11}$$

In this constitutive equation, which plays also the role of boundary condition for the flow within the adjacent bulks, the tensor $\overline{\overline{I}}_s$ transforms any 3-D vector located at the vicinity of the interface into its corresponding 2-D vector, tangential to the interface (in-plane vector), $\overrightarrow{v_s}$ is the surface velocity, ∇_s and div_s are respectively the surface gradient operator and the surface divergence operator, all defined within the interface,

[6] also referred to as Boussinesq-Scriven closure law

σ is the thermodynamical surface tension, κ_s is the surface dilatational viscosity and μ_s is the surface shear viscosity.

In the Gibb's approach, the barycentric surface (excess) density is set to zero. Among consequences, the averaged inertia of the interface does make sense and there is common agreement with the fact that the jump momentum balance at the dividing interface writes according to the intrinsic notation,

$$\nabla_s \cdot \left(\overline{\overline{T_s}} - \sigma \overline{\overline{I_s}}\right) + \left[\!\left[\overline{\overline{T}} \cdot n\right]\!\right] = 0, \tag{3.12}$$

with the assumption of no mass transfer to or from the surface and the jump notation $[\![\cdot]\!]$ which writes explicitly:

$$\left[\!\left[\overline{\overline{T}} \cdot n\right]\!\right] = \overline{\overline{T_{s,1}}}.n_{1\to 2} - \overline{\overline{T_{s,2}}}.n_{1\to 2}. \tag{3.13}$$

The quantity $\overline{\overline{T_{s,i}}}$ denotes the familiar 3-D stress tensor within the i^{th} phase staying below ($i = 1$) or above ($i = 2$) the dividing interface and where $n_{1\to 2}$ denotes the normal vector at the dividing surface, directed from the phase 1 to the phase 2, respectively.

3.4 Optical properties of monolayers

The modeling of the light passing through or reflected by a layer separating two different mediums can, in principle, allow us to characterise the layer thickness, the jump of refraction index, the absorption coefficient as a function of wavelength, and even the pattern or structure within the layer. Nevertheless, it is difficult to observe a monolayer at an air-water interface due to its extremely thin thickness. This is why few techniques were developed to investigate ultra-thin layers during the last decades. Techniques such as ellipsometry, spectroscopy, X-ray reflection, fluorescence microscopy [181, 53], and Brewster angle microscope (BAM) [15, 73, 70, 69] have been demonstrated relevant to qualitative or quantitative investigations of monolayers.

The ability to image lateral heterogeneity in Langmuir monolayers dates back to Zocher & Stiebel's study in 1930 with the use of a divergent light illumination [190].

More recently, the method shifted toward the use of fluorescence microscopy which allows the observation of coexisting domains of different phases in monolayers. For this purpose, a fluorescent amphiphilic molecule is added to the monolayer. This fluorescent probe behaves like an impurity in the monolayer, i.e., its solubility in the coexisting phases can be very different. The contrast in the fluorescence images is sufficient to visualize the domains of different phases in a monolayer. In particular, the LE–LC and the G–LE phase transitions can be visualized by this method. In the first case, the fluorescent molecules are not soluble in the LC phase which appears black; in the second case, the contrast is mainly obtained by the surface density difference between the two phases. From the images of the fluorescent microscope, one can observe the shapes of the domains and the kinetics of transitions. Polarized fluorescence microscopy, with its ability to resolve regions of different molecular tilts, can be used to infer microscopic properties of the phases directly from imaging [140].

As usual, there are also drawbacks with fluorescence microscopy to investigate Langmuir monolayers [70]:

1. Fluorescent molecules, used as probes, may affect the phase transition and the development of phase domains in a LM. Losche *et al.* [106] reduced the fluorescent molecule concentration to a very low level (0.25 %). With such a drastic restriction, their observations were found independent of the impurity concentration.

2. It is difficult to study phase transitions that appear at a very high surface density [19] since fluorescent molecules are precisely manufactured to have a very low solubility in neighbouring bulks.

3. The lighting of the monolayer can induce photochemical transformations of the fluorescent probes [144]. Photochemical products that result are expected to behave as additional impurities. They would appear locally where the monolayer is illuminated and modifies the domain shapes [70].

For all those reasons, Brewster angle microscopy (BAM) which requires none fluorescent labeling appears to be a relevant method, though less user-friendly, for the purpose of visualising Langmuir monolayers. Consequently, all along this dissertation, use was made of a BAM to investigate the monolayer behaviors at an air-water interface.

3.4.1 Physical principle of a BAM

The interaction of light with a liquid surface can usually be treated to a very good level of accuracy by the solutions of Maxwell's equations with boundary conditions defined by an infinitely sharp change in refractive index at the gas-liquid interface, assuming that both media are isotropic and perfectly transparent. Such solutions are detailed in papers or textbooks on optics [14, 15, 173]. Here, we focus on the theoretical ingredients which could reveal useful for monolayer studies (especially from a BAM).

Electromagnetic wave

Besides what is commonly called light, electromagnetic (EM) wave includes wave of longer (infrared, microwave) and shorter (ultraviolet, X-ray) wavelength. The EM wave is a transverse wave consisting of both an electric field vector $\overrightarrow{E}$ and a magnetic field vector $\overrightarrow{B}$, which are mutually perpendicular and are perpendicular to the propagation direction of the wave. It can be specified with either the electric field vector or the magnetic field vector. Here, we use the specification of the electric field $\overrightarrow{E}$ because, generally, the interaction between matter and electric field is stronger than that between matter and magnetic field.

Polarized light

Generally, light emitted from a standard source is non-polarized and therefore characterised by components of the electric field directed along all possible directions perpendicular to the optical path. In contrast, if the electric field is always oriented

along one direction only, the light is referred to as polarised light. Non-polarised light can always be resolved into two orthogonally polarized waves. If the two electric field components possess a constant phase difference and equal amplitudes, the resultant EM wave is found to be circularly polarized. If the amplitudes differ, then the wave is elliptically polarized. Two important polarisation configurations may be distinguished: p-polarized (or transverse magnetic (TM)) wave, E_p, in which the electric field vector is in the plane of the incidence of the EM wave; and s-polarized (or transverse electric (TE)) wave, E_s, where the electric vector is perpendicular to the plane of incidence.

Index of refraction and Snell's law

When light passes from one medium to another that is not totally transparent, as suggested by Fig. 3.5, several phenomena can be observed. The parameter used to describe the interaction of light with material is the complex index of refraction $\widetilde{N}$ which is a combination of a real index of refraction and an imaginary one [172]:

$$\widetilde{N} = n - j\,k, \tag{3.14}$$

where n is the refractive index, k_e is the extinction coefficient (spatial damping of light intensity), and j, the square root of -1. For a dielectric material such as glass or water, no light is absorbed and hence $k_e = 0$. When the light beam reaches the surface (see Fig. 3.5), some light is reflected and the remaining light is transmitted through the medium. The law of reflection indicates that the angle of incidence is equal to the angle of reflection (i.e. $\theta_i = \theta_r$ as shown in Fig. 3.5). The fraction of the incident light reflected depends on both the angle of incidence and the polarization state of the incident light. The angles of reflection θ_r and refraction θ_t are related to the complex index of refraction $\widetilde{N_1}$ and $\widetilde{N_2}$ of the two mediums by the Snell-Descartes' law:

$$\widetilde{N_1}\,\sin(\theta_r) = \widetilde{N_2}\,\sin(\theta_t). \tag{3.15}$$

For dielectric mediums, $k_e = 0$ and Eq. (3.15) becomes

$$n_1\,\sin(\theta_r) = n_2\,\sin(\theta_t). \tag{3.16}$$

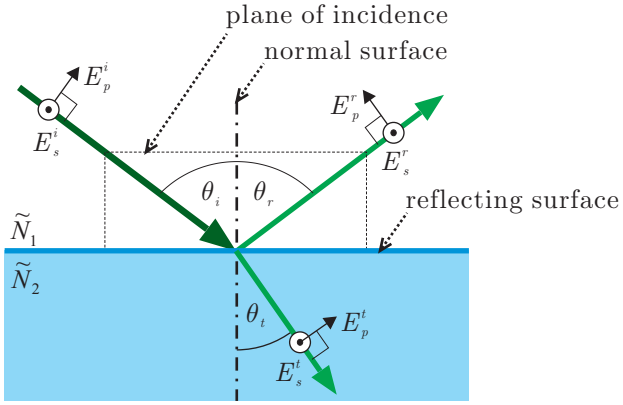

Figure 3.5. Light beams reflecting from and passing through an interface between two mediums (for instance, air and water). Their respective intensity and polarisation state are characterized respectively by the complex indexes of refraction $\widetilde{N_1}$ and $\widetilde{N_2}$. The symbols θ_i, θ_r and θ_t denote the angles of incidence, reflection and refraction, respectively.

Fresnel equation

An incident plane wave moving along the plane of incidence will reflect at a liquid surface as shown in Fig. 3.5. The plane of incidence is defined from the light beam prior to and after the reflection; it also contains the unit vector normal to the surface. A Fresnel interface is characterised by a refractive index which changes steeply from n_1 to n_2 between two separated dielectric mediums. The Fresnel reflection coefficient is the ratio of the amplitude of the reflected wave E^r to the amplitude of the incident wave E^i for a Fresnel interface. The Fresnel reflection coefficients are given by

$$\begin{aligned} r_p &= \frac{E_p^r}{E_p^i} = \frac{E_{p0}^r \exp(j\beta_p)}{E_{p0}^i \exp(j\alpha_p)} = \frac{n_2\ \cos(\theta_i) - n_1\ \cos(\theta_t)}{n_2\ \cos(\theta_i) + n_1\ \cos(\theta_t)}; \\ r_s &= \frac{E_s^r}{E_s^i} = \frac{E_{s0}^r \exp(j\beta_s)}{E_{s0}^i \exp(j\alpha_s)} = \frac{n_1\ \cos(\theta_i) - n_2\ \cos(\theta_t)}{n_1\ \cos(\theta_i) + n_2\ \cos(\theta_t)}, \end{aligned} \tag{3.17}$$

where the subscript p and s refers to p-polarized and s-polarized wave, respectively. The quantities E_{p0}^i and E_{s0}^i are the amplitudes of the incident electric field components, parallel (p-) and perpendicular (s-) to the plane of incidence, respectively. The parameters α_p and α_s are the phase lags of the incident electric field components attached to the p- and s-polarisation states, respectively. The quantities E_{p0}^r and E_{s0}^r are the amplitudes of the electric field components after the reflection, which are parallel (p-) and perpendicular (s-) to the plane of incidence, respectively. The parameters β_p and

β_s are the phase lags of the p-polarized and s-polarized components of the reflected electric field. Similarly, the ratio $\frac{E^t}{E^i}$ defines the Fresnel transmission coefficients with:

$$\begin{aligned} t_p &= \frac{E_p^t}{E_p^i} = \frac{2\, n_1\, \cos(\theta_i)}{n_1\, \cos(\theta_i) + n_2\, \cos(\theta_t)}, \\ t_s &= \frac{E_s^t}{E_s^i} = \frac{2\, n_1\, \cos(\theta_i)}{n_2\, \cos(\theta_i) + n_1\, \cos(\theta_t)}, \end{aligned} \tag{3.18}$$

where the superscript t indicates the transmission wave. Eqs. (3.17) and (3.18) are known as Fresnel equations. The reflectance is defined as the ratio of the reflected intensity (or power) to the incident intensity. For a single interface, the reflectance coefficients for both polarization directions can be written as:

$$\begin{aligned} R_p &= |\, r_p|^2, \\ R_s &= |\, r_s|^2\ . \end{aligned} \tag{3.19}$$

Ellipsometry and ellipsometer

Ellipsometry refers to the analysis of the polarization of light upon reflection. It is very sensitive optical technique which makes use of the fact that the polarization state of light may change when the light is reflected from an interface. For a ellipsometric microscope (or ellipsometer), monochromatic light (a laser beam for instance) is passed through a polarizer, rotated by passing through a compensator before it impinges on the interface to be studied [11]. The reflected light will be elliptically polarized and is measured by a polarization analyzer. In null ellipsometry, the polarizer, compensator and analyzer are rotated to produce maximum extinction.

In general, for optically absorbing materials the incident field will be attenuated and undergo a phase shift. In order to describe this behavior we define complex relative amplitude attenuation as the ratio of the Fresnel reflection coefficients of p-polarized and s-polarized wave:

$$\rho_a = \frac{r_p}{r_s} = \frac{E_{p0}^r E_{s0}^r}{E_{p0}^i E_{s0}^i} \exp\left(j[(\beta_p - \beta_s) - (\alpha_p - \alpha_s)]\right). \tag{3.20}$$

The fundamental equation of ellipsometry [11] is

$$\rho_a = \tan(\Psi) \exp(j\Delta), \tag{3.21}$$

where $\Delta = [(\beta_p - \beta_s) - (\alpha_p - \alpha_s)]$ is the phase difference of light wave that occurs upon reflection and Ψ is the angle whose tangent is the ratio of the amplitude of the Fresnel reflection coefficients. The parameters Δ and Ψ are measured by finding the polarizer and analyzer angles of ellipsometer. When a film is present, the changes in Δ and Ψ can be related in an implicit form to the complex index of refraction and to the thickness of the film.

Brewster angle

We suppose that medium #1 is air, with $n_1 = 1.0$, and medium #2 is water ($n_2 = 1.33$). Figure 3.6 (a) shows a plot of the Fresnel coefficients as a function of the angle of incidence (from Eq. (3.17)). Figure 3.6 (b) shows the resulting reflectance R_p and R_s from Eq. (3.19). At normal incidence, $\theta_i = 0$, the reflectance for both the parallel and perpendicular component is about 14 %. For other than normal incidence, we see from Fig. 3.6 (a) that r_s is always negative and nonzero. Figure 3.6 (a) also shows that r_p changes from positive to negative as the angle of incidence increases. From Eq. (3.18) one obtains that r_p and hence the reflected intensity of p-polarized wave R_p become zero for $\theta_r + \theta_t = \frac{\pi}{2}$, i.e. when the directions of reflected and refracted wave are perpendicular to each other. The corresponding angle of incidence is called Brewster angle θ_B (or polarizing angle, or principal angle). From Snell-Descartes' law (Eq. (3.16)) the Brewster angle θ_B can be determined by

$$\tan(\theta_B) = \frac{n_2}{n_1}, \tag{3.22}$$

as demonstrated by Sir David Brewster in 1815 [24]. The significance of this is that when polarized light makes a reflection with Brewster angle of incidence, none of the light polarized initially parallel to the plane of incidence is reflected, i.e., p-polarized wave is entirely transmitted through the underlying medium #2. The resulting reflected light is the s-polarized wave initially perpendicular to the plane of incidence. Taking $n_1 = 1$ for air and $n_2 = 1.33$ for water, θ_B is found to be 53.1° for an air-water interface.

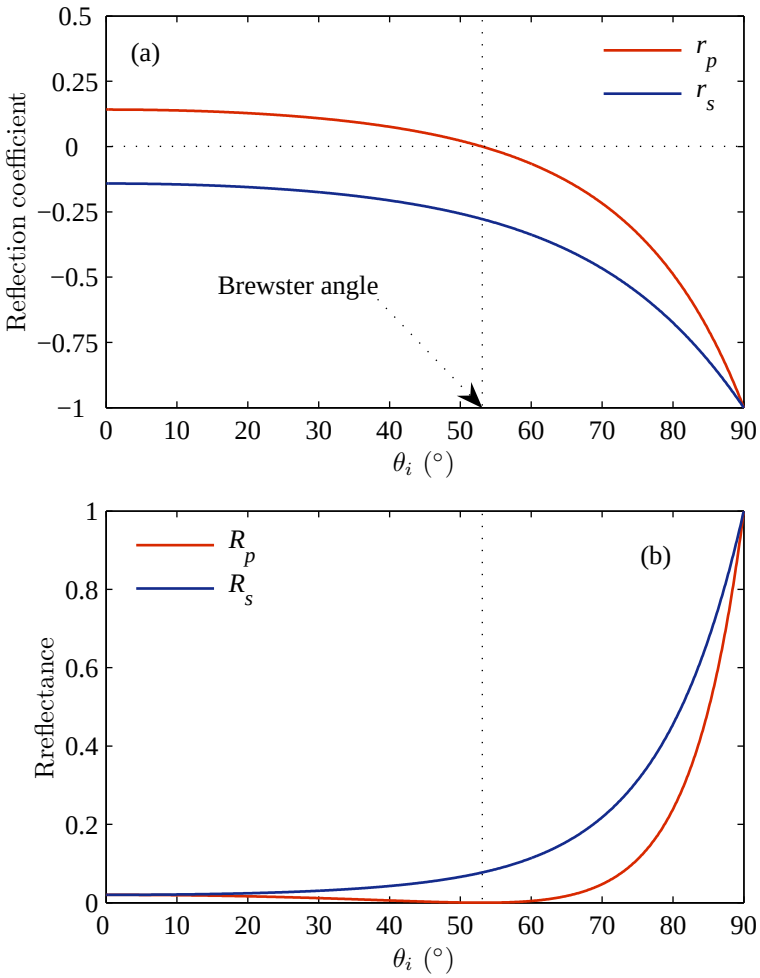

Figure 3.6. (a) The ratios of the amplitudes of the reflected wave to the amplitudes of the incident wave (the Fresnel coefficients) as a function of angle of incidence θ_1 for water with index $\widetilde{N}_2 = 1.33 - 0.0j$. (b) The ratios of the intensities of the reflected wave to the intensities of the incident wave (the reflectance) as a function of angle of incidence θ_1 for water. The Brewster angle is shown by the dashed line.

For a real interface, the reflected light is characterised by a minimum intensity at the Brewster angle, but it does not completely vanish [70]. The low reflected intensity at the Brewster angle is strongly dependent on the interfacial properties. The reflectivity change of a real interface at the Brewster angle for the p-polarized wave has three origins:

1. The thickness of the interface. The refractive index of a real interface does not behave exactly as an Heaviside dependence at the air-water interface, i.e. $z = 0$ (where z is the direction normal to the interface.). The z-dependence of the

refractive index is different from n_1 or n_2, and it can be described by the general function, $n(z)$, trough the interfacial thickness l_t. At first order in $\frac{l_t}{\lambda_w}$ (where λ_w is the wavelength of the light) , Drude [40] has calculated the reflectivity for the amplitude of a p-polarized wave at Brewster-angle incidence:

$$r_p(\theta_B) = i\, r_s(\theta_B)\, \rho_{a,B}, \tag{3.23}$$

where $r_s(\theta_B)$ is the reflectivity of a Fresnel interface for the amplitude of a s-polarized wave at Brewster angle incidence, i.e. $\theta_i = \theta_B$ in Eq. (3.17), i indicates an increase of $\frac{\pi}{2}$ between the phase difference of the s- and p-polarized wave after reflection, and $\rho_{a,B}$ is the ellipticity at Brewster angle incidence:

$$\rho_{a,B} = \pi \frac{l_t}{\lambda_w} \frac{\sqrt{{n_1}^2 + {n_2}^2}}{{n_1}^2 - {n_2}^2} \int_{-\infty}^{+\infty} \frac{[n(z)^2 - {n_1}^2]\ [n(z)^2 - {n_2}^2]}{n(z)^2}\, dz. \tag{3.24}$$

A dense monolayer of amphiphilic molecules introduces a variation of refractive index $n(z)$ over a thickness $l_t \approx 20$ Å. $n(z)$ and l_t depend on the phase domain of the monolayer: two different phase domains demonstrate a different reflectivity.

2. The roughness of real interfaces [14, 189]. At liquid interfaces, the origin of the roughness is thermal fluctuations. For monolayers at the free surface of water, the surface tension is large; the surface thermal fluctuations are small and can be neglected in a first approximation. It introduces a small error on the thickness of the monolayer (≈ 3 Å).

3. The anisotropy of monolayers. Some concentrated phases in monolayers are optically anisotropic [17]. If the optically anisotropic monolayer does not have a vertical axis z of symmetry, the reflected light is a function of the orientation of the monolayer in its plane.

Technique of BAM

In brief, when a p-polarized wave is incident from air to water on an air-water interface with Brewster angle θ_B of incidence, no reflection occurs at the interface for

p-polarized wave and most of the light is refracted into the water. A detector observing the reflected intensity of the p-polarized wave will generate a minimum output signal (ideally zero) at θ_B. Besides, when a monolayer (even one molecule thick) is present, its refractive index being different from the one of the substrate value, the Brewster angle condition is no longer fulfilled, as shown in Fig. 3.7. When a monolayer-covered air-water interface is illuminated with p-polarized wave at the interface, regions of different molecular orientations and/or different thickness will reflect differently. Use is made of an optical image system to pick up this reflected light and form a focused image upon a dedicated photodetector such as a charge-coupled device (CCD) camera. This image of the surface will be contrasted as dictated by the mesoscopic structure of the supporting monolayer.

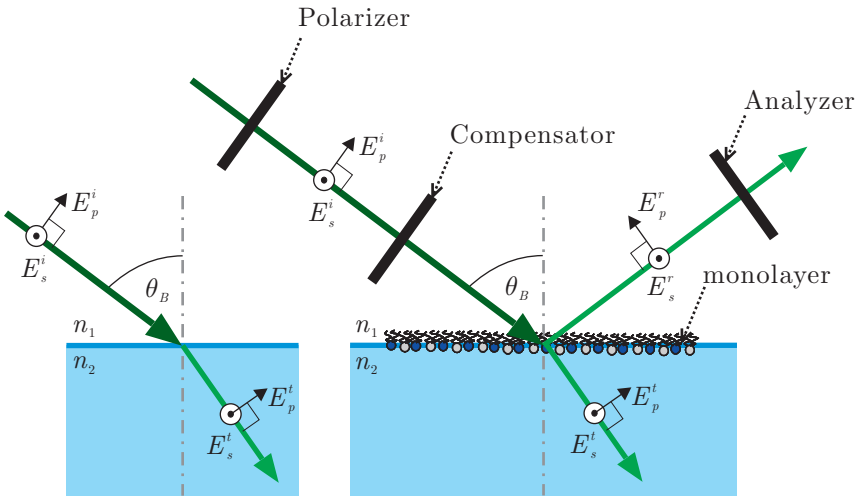

Figure 3.7. Principle of Brewster angle microscopy (BAM). The left side figure demonstrates that when a beam of p-polarized light is incident on a dielectric substrate medium such as pure water at the Brewster angle, no reflection occurs. All the light is refracted into the substrate. However, if a thin film such as monolayer is present having a refractive index different from the substrate value; some light reflection occurs as shown in the right side figure.

In Fig. 3.7, a compensator, i.e. quarter-wave plate, is added on the path of the incident beam and an analyzer is added on the path of the reflected beam. The quarter wave plate is adjusted to have one of its neutral axes in the plane of incidence. The

two components of the incident field are:

$$\begin{aligned} E_p^i &= E_0 \cos(\varphi) \cos(\omega t), \\ E_s^i &= E_0 \sin(\varphi) \sin(\omega t), \end{aligned} \tag{3.25}$$

where φ is the angle between the polarization of the light before the quarter wave plate and the plane of incidence. The s-polarized and p-polarized wave have a phase difference of $\frac{\pi}{2}$ introduced by the quarter wave plate. The reflected field for optically isotropic domains can be expressed as follows:

$$\begin{aligned} E_p^r &= E_0 \, r_s(\theta_B) \, \rho_{a,B} \cos(\varphi) \sin(\omega t) \, , \\ E_s^r &= E_0 \, r_s(\theta_B) \sin(\varphi) \sin(\omega t). \end{aligned} \tag{3.26}$$

After reflection, the two components have a phase difference of 0 or π. The direction of polarization of the analyzer makes the angle ϕ with the plane of incidence. The intensity of the light crossing the analyzer is

$$I_r = I_o \, |r_s(\theta_B)|^2 \, \left[\rho_{a,B} \cos(\varphi) \cos(\phi) + \sin(\varphi) \sin(\phi)\right]^2 . \tag{3.27}$$

If $\varphi = 0$, this corresponds to an incident light of p-polarized wave. The intensity is then proportional to the square of the ellipticity $\rho_{a,B}$. Fixing φ, it is possible to adjust ϕ to increase the contrast between domains of two different phases in the monolayer. For instance, it is possible to choose ϕ, so as to cancel the reflected light for one type of the phase domains of the monolayer where the ellipticity is

$$\rho_{a,B}{}' \cos(\varphi) \cos(\phi) + \sin(\varphi) \sin(\phi) = 0. \tag{3.28}$$

In summary, the BAM takes advantage of the minimum in the intensity of reflected p-polarized wave at the Brewster angle for an interface. Generally, a BAM operates at the Brewster angle ($\theta_B = 53.1^\circ$ for an air-water interface). The presence of a Langmuir monolayer changes the refractive index of the medium, and this modifies the reflected intensity. The refractive index of the interface with the monolayer present is dependent on both the density of the molecules and the orientation of the molecular

chains relative to the incident light [69, 174, 114, 77]. A variation of either the density or the tilt azimuth gives a corresponding variation in the reflected light intensity. If the film consists of domains characterized by unique refractive indexes, the reflected light will reveal the film morphology. A second polarizer is generally used in the reflected beam as an analyzer. If the variations in intensity are due solely to density variations, rotation of the analyzer does not change the relative brightness between distinct regions. However, if the intensity variations are due to a tilt of the molecular chains, the tensor nature of the refractive index will cause a rotation of the polarization of the reflected beam. This can be detected by rotating the analyzer. A suitably designed optical system can be utilized to focus variations in light intensity as an image on a charge coupled device (CCD) camera.

3.4.2 Brewster angle miscroscope

Brewster angle miscroscopy (BAM) was gradually developed in the early 1990s. This measurement technique follows a well-known technique known as a ellipsometery [15]. An ellipsometer is able to achieve a spatial resolution ranging from 1 μm to 10 μm. However, due to the fact that the rotation of the polarisers must be adjusted, ellipsometric measurement is too slow to allow the detection of a flow phenomenon along a liquid interface. By comparison, the non-quantitative BAM approach appears as much more simple to use. The number of optical components involved in a BAM configuration is not too large (light source, polariser, sample, analyser, and detector) [40] and the BAM resolution is high enough (few μm) to investigate dynamic phenomena at a flowing liquid surface.

BAM, as a simplified ellipsometer, is characterised by the optical chain shown in Fig. 3.8. The BAM technique was developed for the first time in the 90's, separately by Hönig & Möbius [73] and by Hénon & Meunier [70]. BAM is usually designed for the investigation of thin films supported by surfaces of water or aqueous solutions[7].

[7]Instead of a liquid surface, a transparent glass plate some millimeters thick may be also used as

The liquid surface is impacted by a laser beam, which is initially polarised in the plane of incidence and reflected at a certain angle from the surface. Then, the reflected beam is analysed by a second polariser before being detected by a CCD camera. BAM imaging is therefore performed at the scale of the cross-section of the input laser beam. The BAM image is contrasted by any mesoscopic pattern able to change locally the refraction index at the scale of the laser spot (few mm) on the liquid surface.

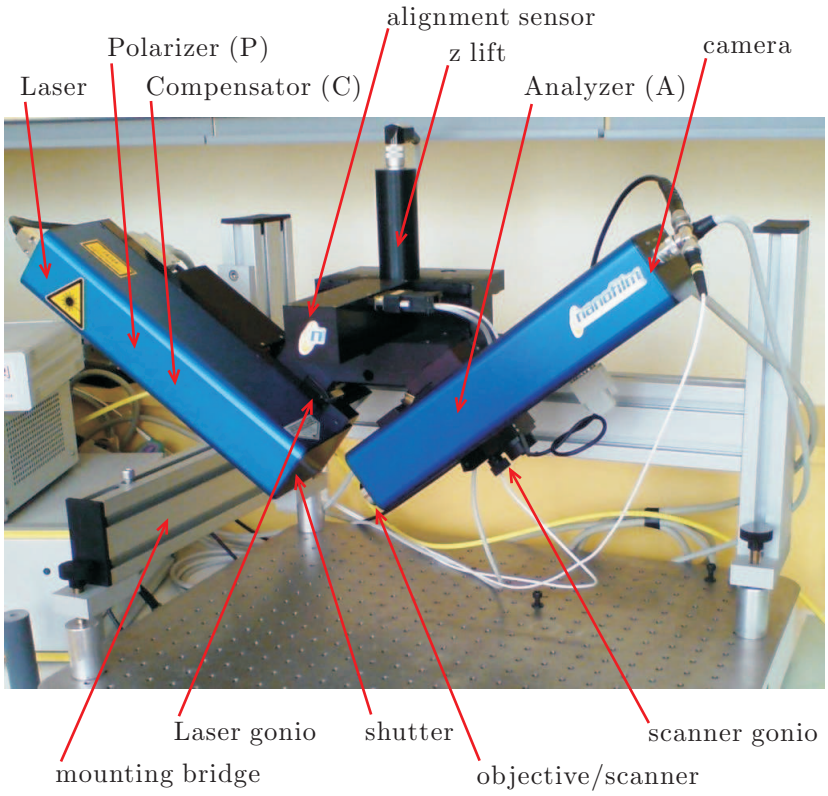

Figure 3.8. Components of a BAM.

The BAM utilized in our investigation was produced by Nanofilm Surface Analysis Company (I-Elli2000, Germany). It consists of an opto-mechanical apparatus, an electronic control unit and a personal computer. As shown in Fig. 3.8, the series of optical elements involved in the BAM chain is the following:

◇ light source (laser),

◇ polariser (P),

a support of a film coating to image, the refractive index of the glass plate should not deviate too much from that of water, in order to work at a convenient angle of incidence.

◇ compensator (C),

◇ sample/surface (S),

◇ microscope objective,

◇ analyser (A), and

◇ detector (camera), respectively.

The compensator (C) is a *quarter-wave plate* designed for the laser wavelength. Wave plates are anisotropic optical elements. The velocity of the wave depends on its orientation. In general, the wave plate has a fast axis and a slow axis, both of which are perpendicular to each other and to the direction of propagation of the wave. The component of the wave which is aligned with the fast axis passes through the optical element faster than the component aligned with the slow axis. If the two components of the wave were in phase before passing through the element (i.e., linear polarized) then, in general, they will be out of phase when they emerge (elliptically polarized). The thickness of the wave plate can be chosen such that the phase difference is exactly 90°, 180°, or 360° and they are called respectively quarter-wave plates, half-wave plates or full-wave plates [172]. The compensator (C) allows changing the state of polarization from elliptical to linear to circular and vice versa by using the effect of optical birefringence.

The polarizer (P) and analyzer (A) are linear polarizers, i.e. the emerging wave is linearly polarized. The polarizer is an optical element which has a polarizing axis. If the axis of the polarizer lines up with the angle of polarized wave, the entire wave is transmitted. When the axis does not line up with the angle of polarized wave, we separate the wave into components which are parallel to and perpendicular to the polarizer axis. The component that aligns with the axis is transmitted and the component that is perpendicular is blocked. Polarizers are used in two different ways. If the polarizer is used to convert unpolarized light to polarized light, it is called the polarizer. If it is used to determine the state of polarized light by locating the null, it

is called an analyzer [172]. The light source of the BAM is a diode pumped Nd:YAG-Laser with a wavelength of 532 nm (green light) and a primary output power of 52 mW. The field-of-view of the BAM images is 430 μm x 430 μm and its resolution is roughly, 2 μm, for a 10X objective of numerical aperture: 0.21 [125].

3.4.3 Optical characteristics of the BAM

Due to the requirement of working at a tilted geometry, BAM does not have a normal plane of view and therefore the depth of field becomes an intrinsic problem. From Fig. 3.9, we can see that a target lying along air-water interface is being imaged by an optical system (an objective and a CCD camera) with the light axis tilted away from the surface normal by the Brewster angle, θ_B. The outcomes of this tilted image plane are that the aspect ratio of the image is altered and only a part of the image is in focus (see Fig. 3.9 (a)). Since the surface is imaged at Brewster angle, the original image is shortened in one direction, so that circular objects flowing along the interface appear elliptic. As a consequence, the aspect ratio of the image must be corrected by the factor $\cos(\theta_B)$. It means that scaling the width by the quantity, $\cos(\theta_B) \approx 60$ %, while keeping the height unchanged will return the real aspect ratio (1 : 1 for circular domains, see Fig. 3.9 (b)).

To deal with the depth of field problem, we can use a scanning objective to capture a series of focused stripes and then to reconstruct a fully focused image from the concatenation of all these stripes [70, 100] (see Fig. 3.9 (c)). However, the long cycle required to sweep the entire image (about 5 seconds for our BAM) makes this technique impossible to use in presence of a surface flow. Therefore only the (central) focused region of the image was used for the characterisation of LM flow in our experiments (details in Chapter 4). Lheveder *et al.* [100] proposed another technique to solve this disadvantage; this is obtained by using a special custom-made objective. This objective has a vertical symmetry axis (it is not tilted) and consequently gives an image of the

water surface in a plane parallel to this surface. But this approach requires a high power (expensive) laser source.

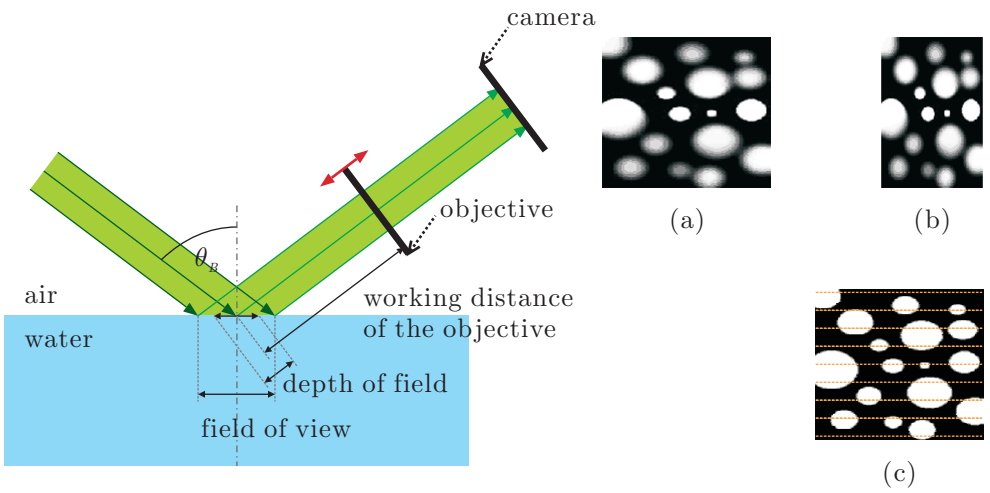

Figure 3.9. Tilt of the laser beam in Brewster angle microscopy. The right image (a) illustrates that the aspect ratio of the image is altered and that only a central region of the image is in focus on the camera. The image (b) results from the scaling of the width by a factor, $\cos(\theta_B) \approx 60$ %, keeping the height unchanged. The image (c) demonstrates the classical method of image scanning as an ideal way to provide a fully focused image.

Another problem is the inhomogeneous illumination of a BAM image. Figures 3.10 (a)-(b) show a typical BAM image with inhomogeneous illumination. Two reasons can be identified to explain it:

1. the Gaussian profile of the laser beam leads to an exponential decrease of light intensity (brightness) of the image near the edge.

2. the presence of interference fringes due to a possible imperfection of the optical components, possible "wedge" effects at the cover glass of the CCD camera or a non-coherent illumination.

There are two possible ways to remove the inhomogeneous illumination.

◇ A first one is to find a featureless image with only the inhomogeneous background illumination and interference fringes as a reference image (see e.g. Fig. 3.10 (b)). Then, the rough BAM image is submitted to a background compensation

from the reference image and it allows us to produce a homogeneous image (Fig. 3.10 (c)). Unfortunately, the background quality can slightly change in the course of time because of changes in experimental conditions: typically, the output power of the laser source may change [125]. If the sample moves (monolayer flows), it is difficult to get a constant background condition.

Therefore, the compensation technique is only suitable in stationary conditions.

◇ Another way to do is to perform a 2-D Fourier transform of the image and take out the features in the frequency domain that corresponds to the interference fringes. However, this approach works well as long as the physical pattern of interest exhibit very characteristic lengths different from the interference fringes to remove. If the patterns to image have a length scale close to the one of the interference fringes, the filtering in frequency domain will eliminate also the relevant information [174]. Moreover, a Fourier transform scheme could never succeed in removing the inhomogeneous illumination due to the Gaussian profile of the laser beam.

Finally, the first approach based on imaging calibration from a background image was finally developed in our experiments despite the slight change in lighting conditions at the time scale of our experiments (several hours).

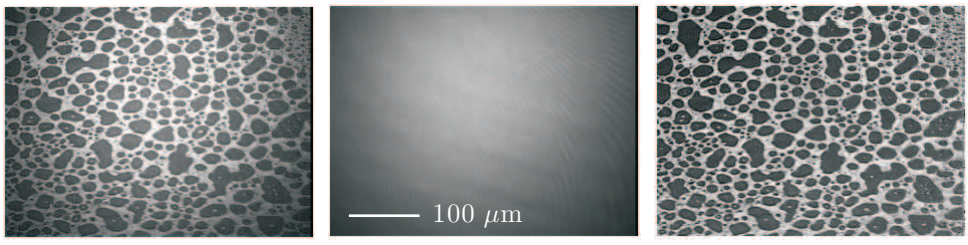

(a) (b) (c)

Figure 3.10. Original BAM image of a sample (a) that demonstrates the inhomogeneous illumination of a BAM image; reference image (b); the reconstructed image after background compensation (c) (adopted from Ref. [125]).

Finally, note that if the trough is only a few millimeters deep, the laser beams reflected at the water surface and at the floor of the trough were supposed to interfere

on the CCD sensor. These laser beams have to be separated by placing an absorbed material or a reflected material at an angle on the floor. To solve this classical problem, use is made in our experiments of an absorbing material: the floor and the side walls of the trough are all made with (black) Delrin resin.

Chapter 4

Experimental measurement of a flowing PDA Langmuir monolayer

4.1 State of the art

Studies involving flow of LM, made from fatty acids for instance, provide evidence of exotic behavior especially within the liquid or solid phases. Examples include reports of unusual (sharp) velocity profiles in channel flow [79], nonlinear response to applied shear stress [56, 54], unexpected peak of the monolayer viscosity as a function of surface pressure [55], and even shear-induced alignment of the monolayer [115, 77]. Schwartz *et al.* [151] examined the surface-pressure driven flow of a LM through a channel. A semielliptical velocity profile was found to be insensitive to the structure and composition of the monolayer within the LE–LC coexistence region. In particular, the hydrodynamic coupling between the multi-domain monolayers and the underlying liquid subphase can be neglected because the LM flow is basically surface pressure-driven.

In fact, two categories of LM hydrodynamics can be introduced:

1. the surface pressure- (or $\nabla\Pi$-) driven flows of LM, more or less inspired from the well-known technique of the Langmuir trough (barriers motion),

2. and the shear-driven flows (or surface Couette flows, say). Regarding this last category, two sub-categories can be again distinguished according to whether shear originates from the surface itself or from the motion of the underlying subphase:

   ◇ an in-plane surface shear is supplied from a moving wall (supposed to be perfectly embedded within the monolayer). This sub-category includes all viscosimetry techniques based on the measurement of a torque or a drag that a contaminated liquid surface is supposed to apply on a rotating or a translating planar mobile (disc, needles...) [127, 12, 28].

   ◇ shearing may also originate from underlying subphase. A typical configuration is the deep channel viscometer originally introduced by Mannheimer & Schechter [111, 112]. The paramount advantage of the channel technique lies in the fact that the origin of the LM deformation is unambiguously identified: this is a bulk shear in the underlying subphase which is diffused by the molecular viscosity from the rotating floor up to the surface.

As clearly shown in Fig. 4.1, the geometry of the annular channel involved in the present study is inspired from the channel viscometer. It consists of:

◇ two vertical side walls of inner and outer radii, r_i and r_o, respectively,

◇ an annular floor rotating about a vertical axis at a constant angular velocity Ω.

The rotation of the annular floor is slow enough to ensure the flow is laminar. Apart the main shear azimuthal flow, centrifugation gives rise to a weak secondary recirculating flow. The subphase flow is radially outwards along the rotating floor and radially inwards along the interface due to continuity equation. Consequently, the rotating floor causes a 3-D helicoidal flow within the underlying subphase which can be described, at a small enough Reynolds number ($Re < 100$), as the super-imposition [105, 39] of:

- ◇ a main shear flow along the channel, referred to as v_θ, whose circular streamlines are closing within any horizontal cross-section of the channel,
- ◇ a centrifugal recirculating (secondary) flow, $v_\perp$, whose circular streamlines are closing within a meridian cross-section.

Centrifugation causes a radial component of the pressure gradient within a meridian plane of the channel and is thus able to pack the LM along the interface from the outer side wall to the inner side wall.

This chapter and next one address the reorganization of a PDA LM, made from LE–LC co-existing phases of pentadecanoic acid (PDA), to a subphase-induced shear. PDA, as an amphiphilic long-chain carboxylic acid, is known to behave as a very convenient support to investigate Langmuir monolayers [151, 130, 22, 45, 122, 166, 74]. We investigate the respective impacts of the leading shear flow and the centrifugal flow on the PDA LE–LC transition at the air-water interface.

Because the BAM is a well-known tool to image selectively contaminated liquid surfaces, especially LM, it is used to measure velocity profiles along the surface and also to follow the morphology of the PDA monolayer at mesoscale by investigating the spatial distribution of the liquid condensed (LC) domains during LE–LC transition. The centrifugal shear flow considered in our study is permanent and laminar ($Re <$ 100). Experimental results thus complement existing literature devoted to:

1. shape relaxation of initially stretched domains [93, 162, 67, 4],
2. line tension measurement [16, 185, 186],
3. or dynamics of a two-phase LM strongly reorganized by a large Reynolds number flow ($Re \approx 1000$) [121, 178, 72].

The objective of this chapter is to investigate the impact of this permanent flow of moderate Re number ($Re \approx 10$ to 100) upon phase transition experienced by a LM. It brings an addition to existing literature devoted to shape relaxation of stretched

condensed domains [67], line tension [16, 186] and phase transition modified by inertial flows ($Re \approx 1000$) [72].

4.2 Materials and methods

4.2.1 PDA monolayer method

An as-received sample of PDA ($C_{15}H_{30}O_2$, stated purity > 99 %, Sigma-Aldrich) is dissolved in reagent grade chloroform (Sigma-Aldrich) at a concentration of 1 mM. To prevent PDA from dissociation, the ultrapure water subphase delivered by a Milli-Q system (Ohmic resistance: 18.2 MΩ) is further acidified to pH = 2 by making use of pure chlorhydric acid (HCl). This acidified subphase is topped with the PDA monolayer made from small addings of PDA solution deposited randomly (using a Hamilton syringe (Hamilton 801N, Switzerland)). After the chloroform is completely evaporated, a time delay is respected to get thermodynamic equilibrium. All the experiments are carried out at a regulated temperature of 23 ± 1 °C.

4.2.2 Conception of flow apparatus

The fluid channel geometry that we utilize to study the hydrodynamics of the PDA monolayer was chosen so as to minimize the mechanisms involved and yet still be sensitive to the nonlinearities of the PDA monolayer. The geometry is similar to the deep-channel viscometer [112] but it was modified as a closed annular channel consisting of bound inner and outer stationary walls, and the flow was primarily driven by a constant rotating floor. As shown in Fig. 4.1, the use of such a closed channel geometry, associated with a remote-control magnetic ring, is original if compared to previous similar setups [111, 105], with the main advantage that it avoids any loss of soluble chemical species. At the free surface, a monolayer of insoluble surfactant (PDA) was initially spread uniformly.

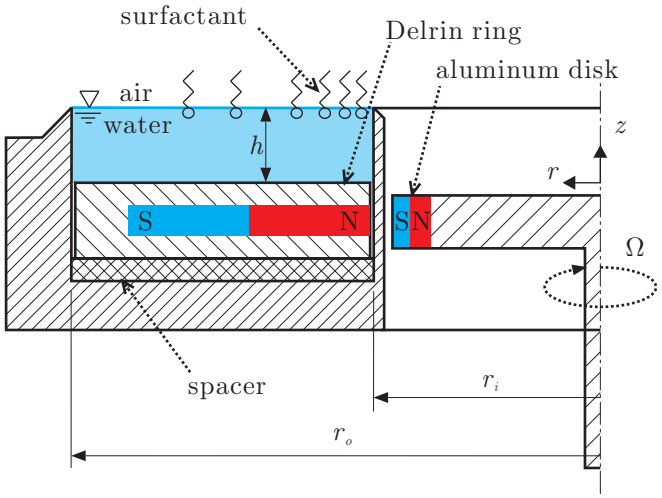

Figure 4.1. A schematic of the annular trough.

4.2.3 Flow apparatus

A schematic of the experimental setup is shown in Fig. 4.2. The entire BAM system is mounted on a large 2 in. travel translation stage (Thorlabs Inc., PT3, USA) which permits a micrometric linear motion all along the annular channel gap. Both the BAM and the annular channel are placed on an optical table (Newport inc., M-BTC-2024-OPT, USA) to eliminate, as much as possible, external vibrations. A brushless DC motor (Faulhaber) is used to rotate magnetically the annular ring at the bottom of the channel; it is isolated from both the optical table and the flow device in order to prevent the experiments from rotor vibrations. The channel is covered by a thin plastic lid to

1. minimize subphase evaporation,

2. to ensure a high and constant degree of humidity,

3. and to prevent the LM from any external contamination.

Nevertheless, a narrow window is opened through the plastic lid to allow the laser beam to scan the interface all along one radius. Finally, a magnetic sensor captured by Hall Effect was set up to measure the floor angular velocity.

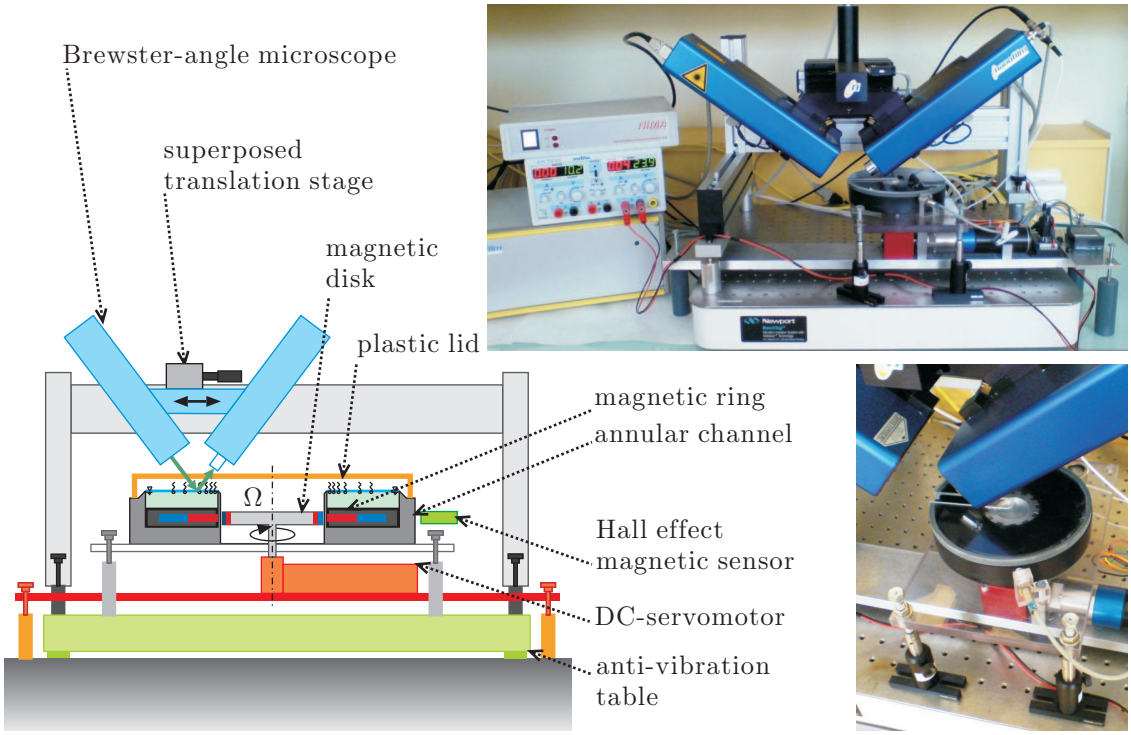

Figure 4.2. Schematic of the experimental setup with photos.

Our homemade channel is manufactured from polyoxymethylene (Delrin™, DuPont Engineering Polymers, USA). This material is a black resin whose hydrophilic character allows us to make the liquid surface as planar as possible[1]. The curvature of the meniscus is removed by pinning it on the sharp wedges located all around the channel at the top of both vertical side walls. An apparent contact angle of 90° is accurately monitored by adjusting carefully filling of the channel with a Hamilton syringe. By imaging the liquid surface under BAM while scanning all the channel gap, it is also possible to check that any surface curvature is completely removed. In fact, the level of the subphase is finely adjusted by filling more or less the annular trough so as to avoid unfocused BAM images.

[1]One makes use of a BAM to investigate the LM all over the channel gap.

Table 4.1. Physical properties of Delrin™ (adapted from Ref. [42, 60]).

Physical property	Delrin™
water absorption[1], 24 h	0.25 %
water droplet contact angle	$\approx 45°$
thermal expansion coefficient[2] (over a temperature range of −40 to 94 °C)	10.4 to 13.5 ($\times 10^{-5}$ K^{-1})
specific gravity[3]	1.42

[1]ASTM method D570.

[2]ASTM method D696.

[3]ASTM method D792.

Properties of Delrin™

Delrin™ is an acetal resin made by the polymerisation of formaldehyde (its structure is shown in Fig. 4.3). It is hydrophilic that can be seen from the contact angle of a water droplet[2] on Delrin™ surface as shown in Fig. 3.1 (b) [60]. Estimated contact angles of water on Delrin™ is given in Table 4.1 [42, 60].

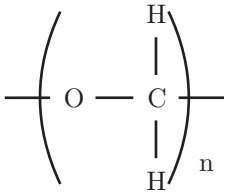

Figure 4.3. Structure diagrams for Delrin™ [60].

Delrin™ was selected due to the following reasons:

◇ Delrin™ is black; consequently, it can avert the observation of the BAM from undesired reflection light.

[2]The droplets (25 μl) were positioned at equal distances from the Delrin™ ends so any perspective/parallax effects can be ruled out.

- ◇ It is chemically neutral so that it can be cleaned without special difficulty and monolayer molecules do not adsorb to it (no leakage of chemical materials, [60]).
- ◇ Its hydrophilic character allows us to make the liquid surface as planar as possible.

The annular channel

The radii of the inner and outer vertical side walls of the channel are located at $r_i = 30$ mm and $r_o = 70$ mm, respectively. The depth of the subphase was monitored to $h = 4$, 7 and 10 mm. To do this, two ring shaped spacers of different thickness were used to adjust h, as shown in Fig. 4.1. Because the depth of subphase and the surface meniscus significantly affects the surface velocity, it is worthy to keep the same surface conditions. Therefore, sharp wedges are located at the top of the inner and outer side walls of the annular channel as shown in Fig. 4.4 (a). Accordingly, a contact angle of 90° is tuned producing thus a perfectly flat air-water interface.

Mechanical rotation system

In order to put in rotation the channel floor, a solution is adopted which consists in distributing magnets all around the peripheries of a driving disk and a ring. The magnets are inserting in such a way that their north (N) and south (S) poles are sequentially alternated (see Figs. 4.1 and 4.4). This way to do permits to produce a stable and maximum torque to rotate from a magnetic coupling the ring placed along the channel floor.

As shown in Fig 4.4 (c), a brushless DC-servomotor (Faulhaber inc., 024BS) is connected to the aluminum driving disk with twelve magnets inserted (NdFeB magnets, dimensions: 7 mm length × 7 mm width × 5 mm height). Respectively, twelve cylindrical magnets are sealed into the Delrin™ ring which is also lying on the channel floor (see Fig 4.4). Keeping in mind the important problem of a possible chemical contamination, only magnets covered with Teflon® (Fisher inc. Slim-Line® Teflon®,

dimensions: 25 mm length × 8 mm diameter) are inserted into the Delrin™ ring. Thanks to a magnetic coupling, the ring is able to rotate by way of the driving disk mounted on a motor reducer axis. The angular velocity of the ring is measured from a Hall-effect sensor whose sensitive head is inserted at the outer side wall of the annular channel. The use of a closed geometry associated to a remote-control of the shear flow is original if compared to previous rheological devices [134, 112, 105].

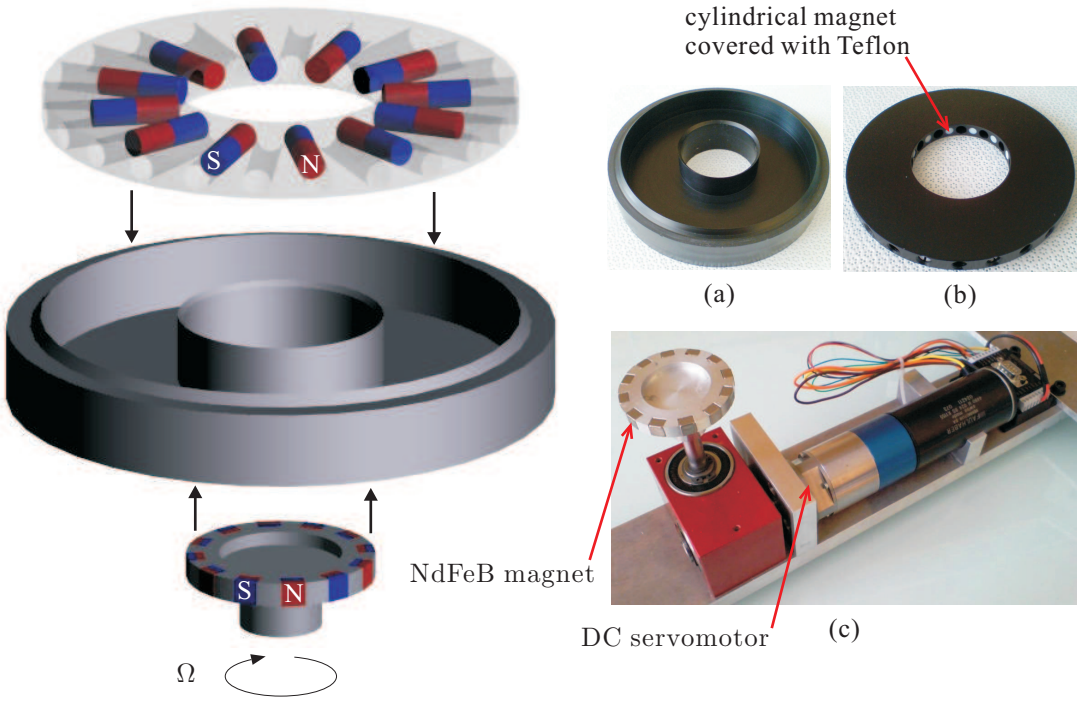

Figure 4.4. The annular channel under consideration with the magnetic ring (rotor) and the magnetic driving disk (stator). (a) Delrin™ annular channel with wedges located at the top of the cylindrical side walls. (b) Photo of the magnetic ring. (c) Photo of the magnetic disk connected to a DC-servomotor.

4.2.4 Experimental techniques

Experimental protocols

In order to reduce any possibility of external contamination in our experiment, a stringent cleaning procedure is strictly observed during sample preparation, before and after all experiments. The annular channel, the Delrin™ ring, and the spacers are cleaned independently using a multistage protocol including:

1. chloroform and ethanol wiping,

2. wash with Milli-Q water,

3. rinse in boiling Milli-Q water,

4. and continuous washes under Milli-Q water at room temperature (about 1 min).

As soon as the annular channel is filled with acidified water subphase (pH = 2), a homemade pipette is used to remove surface contamination several times until the air-water interface is perfectly clean or flat. Next, PDA monolayer is deposited droplet after droplet. Each droplet is produced from the tip of a Hamilton micro-liter syringe and is touching slowly the interface. By controlling the amount of solution deposited, we were able to regulate the surface concentration of the PDA monolayer at different molecular areas. After 30 min, the chloroform completely evaporates and thermodynamic equilibrium seems to be achieved. Afterwards, the annular channel is covered by a thin plastic lid.

The large extent of the subphase area (125.66 cm^2) ensures that the meniscus is essentially flat, eliminating optical aberrations due to surface curvature in the central part of the gap. To get a perfectly flat interface all along the liquid surface, one recalls that it is pinned to the wedges at the top of the side walls.

The surface tension was measured (± 0.1 $mN{\cdot}m^{-1}$) using a surface pressure sensor (Nima) and homemade Wilhelmy plates cut inside a sheet of Whatman's chromotography paper. An initial calibration of the surface pressure sensor was performed.

Spreading solutions typically contained 1 mM PDA in chloroform. The absence of surface-active contamination was checked by spreading a quantity of pure chloroform on water; after evaporation the surface pressure remains zero. The monolayer density is progressively increased from successive addings of spreading solutions on an acidified subphase. The subphase was prepared before each experiment from pure chlorhydric acid ([HCl] = 10^{-2} M, Chimie-Plus) dissolved in ultra-pure water supplied from a

Milli-Q water system (Millipore). Long equilibration times ($\geq$ 10 min) were observed before spreading PDA solution at the surface of the subphase.

Imaging/recording setup

The BAM is set for optimizing image contrast between the different phases of the PDA monolayer and the servomotor is started to rotate the annular ring at the bottom of the channel. The CCD signal from the BAM is redirected to an A/D video converter unit (Canopus ADVC300, Japan) and recorded on a PC hard disk with a maximum frame rate of 25 frames·s^{-1} and a spatial resolution of 720 $\times$ 576 pixels. Finally, the BAM images are analyzed frame by frame in order to extract the velocity profile and the area fraction defined in the following.

4.3 Characterization of PDA monolayer in thermodynamic equilibrium

The Π–A isotherm is measured *in situ* within the annular channel. After each adding of PDA solution, a time delay is strictly observed in order to get a constant surface pressure. BAM images are also useful to follow PDA spreading driven by Marangoni effect and to check 2-D diffusion within the LM. To prevent any initially compressed state, droplets of the spreading solution are just put in contact with the liquid surface, avoiding thus a pool of solvent which might affect the Wilhelmy plate.

Experimental uncertainty on the molecular area A

The molecular area A was calculated from the amount of PDA spreading solution added over the liquid surface which area is also known. It is difficult to prevent the evaporation of the chloroform of the PDA solution. Accordingly, it can slightly increase the concentration of the PDA solution with a possible over estimation of A.

Besides, a second experimental error on A can be also due to a weak solubility of PDA in the water subphase which tends to modify slightly A and lead ultimately to an under-estimation of A. As one can see, both effects are really difficult to quantify and moreover, they are somewhat expected to compensate each others.

4.3.1 Π–A isotherm of PDA monolayers

The identification of the monolayer phases and their distinction has been based primarily on measurements of the surface pressure Π as a function of the molecular area A. According to the phase rule, the slope of a Π–A isotherm for a one-component system must be horizontal when two phases are in thermodynamic equilibrium; the limits of a two-phase region should therefore be detectable from a slope change of the Π–A isotherm. In practice, however, many experimental factors (questionable purity of the amphiphiles, impurities released by the walls, the subphase or the air, non negligible solubility of the amphiphile into the subphase, etc.) can distort the shape of the isotherm and complicate the physical interpretation. The presence of a first order phase transition can even been called into question [130].

Most of published isotherms are obtained from the continuous or discontinuous compression of a spread film. In the compression method, a film is spread between barriers and usually, at least one barrier is moved to reduce the available area. While the barrier is moved continuously, the surface pressure is simultaneously recorded. In the discontinuous method, a barrier is moved to prearranged positions and the surface pressure is recorded until it becomes constant and supposed equal to the homogeneous pressure in the LM. In fact, due to the motion of the barrier, isotherms represent dynamic Π–A data even if they are claimed to be obtained in quasi-static conditions.

In contrast, isotherms measured from the technique of successive addings can be recommended to study the surface properties of monolayers approaching "thermodynamic equilibrium" state. Earnshaw & Winch [45] demonstrated that, for temperatures above the monolayer triple point, which is about 17 °C for PDA, the transition

Table 4.2. Molecular areas (Å^2·molecule^{-1}) at LE–LC coexistence in PDA monolayers, as measured by different authors. Phase transition is detected between molecular areas A_{LE} and A_{LC}

Literature Ref.	T (°C)	A_{LE}	A_{LC}
Moore *et al.* [122]	20	37 (36)	23
Moore *et al.* [122]	25	31 (32)	22
Moore *et al.* [122]	30	28 (29)	21
Harkins & Boyd [62]	20	38	23
Harkins & Boyd [62]	25	33	22
Harkins & Boyd [62]	30	31	21
Pallas & Pethica [130]	25	31	22
Pallas & Pethica [130]	30	28	21
Davoust *et al.* [32]	23	31	18

regions between LE and LC states are flat at thermodynamic equilibrium, indicating a first-order phase transition for the use of highly pure PDA and subphase.

However, such a first-order phase transition appears to be clearly observable only in very careful experimental conditions and for ultra-pure pentadecanoic acid [130, 29, 184]. Table 4.2 displays the limit molecular areas which characterize the LE–LC coexistence in PDA monolayers, as measured by different authors.

4.3.2 Initial thermodynamic equilibrium of PDA monolayer

Static PDA Π–A isotherm and BAM images

Figure 4.5 shows the static Π-A isotherm for a PDA monolayer at 23 °C as measured from Wilhelmy technique and simultaneously observed from our BAM (Fig. 4.6). For a higher surface concentration ($A \leq 20$ Å^2·molecule^{-1}), the PDA monolayer requires more time (≥ 1 h) to reach its thermodynamic equilibrium (steady value of

Π). When the surface concentration grows up, the surface pressure becomes close to the equilibrium spreading pressure of 18.7 ± 0.1 mN·m^{-1} (measured by Iwahashi *et al.* [80]). At a working temperature of 23 °C, the PDA monolayer exhibits LE–LC co-existing phases for a molecular area ranging from 31 Å^2·molecule^{-1} to 18.9 Å^2·molecule^{-1} (Figs. 4.6 (c) to (j)) in reasonable agreement with the literature (see Table 4.2). The LE–LC transition starts with the formation of circular LC domains (Figs. 4.6 (c) to (f)), as also reported by Knobler [94]. Note that the apparent elliptic shape of the LC domain is only due to the Brewster angular deviation of the BAM laser.

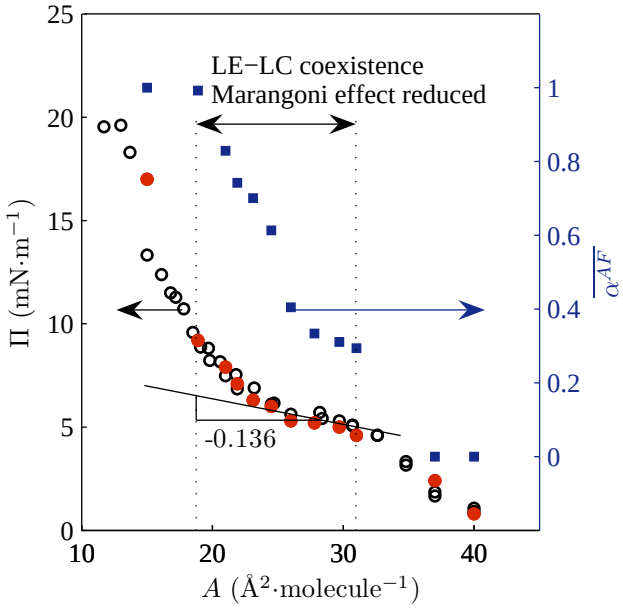

Figure 4.5. Π–A isotherm for a PDA monolayer over acidified pure water (pH = 2, HCl) at 23 °C. (●) (○) Surface pressure measurements were performed twice in order to insure repeatability (left axis). (■) Mean area fraction of the condensed phase is measured from processing of BAM images (right axis) in Fig. 4.6.

In contrast with theoretical expectations, here, the LE–LC region exhibits a non zero slope along Π–A isotherm which is probably due to the insufficient (though high) level of purity for the PDA used in our experiments without further purification stage [130]. The subsequent Π–A slope can cause a Marangoni effect in the low A region even

during phase transition. Anticipating on the following, it will be physically consistent to notice a non uniform radial distribution of the condensed domains.

For the smallest molecular areas of the LE–LC co-existing phases region, the Π–A slope is observed to increase significantly though the surface concentration is close to its maximum packing concentration. For such a high molecular densification, the arising of Marangoni effect is nevertheless inhibited by the difficulty to create surface concentration gradients.

In the following, the Langmuir dispersed film will be referred to as weakly densified or highly densified depending on the area fraction of the LC phase is small or large, respectively.

Time-dependence of PDA monolayer morphology

Time-dependence of the static organization of the PDA emulsion is investigated under BAM. When the PDA monolayer is formed at $A = 21$ Å^2·molecule^{-1} and a temperature of 23 °C, the LC phase nucleates all over the water surface. These (2-D) LC domains are thus found to grow quickly within several minutes. Afterwards, the LM continues to evolve according to a slow growth of the LC domains mainly governed by surface diffusion. In our experiments, the growth of the LC domains is followed for 15 h in order to fully investigate the establishment of the thermodynamic equilibrium. Two images of the PDA monolayer morphology are displayed in Fig. 4.7 after delays of 20 min and 15 h, respectively. As indicated by Fig. 4.7 (a), the majority of the LC domains are circular, although the biggest ones are slightly deformed. Due to mass conservation, the growth of the LC domains involves vanishing of the smallest ones. The relative amount of LC phase is found to be 0.83 and 0.79 after a delay of 20 min and a delay of 15 h, respectively, considering that the initial time corresponds to spreading of the last PDA solution droplet. Evidence is thus given here that the amount of condensed phase is weakly modified by the time delay in static conditions. Nevertheless, the LM tends to minimize its free energy by decreasing potential energy

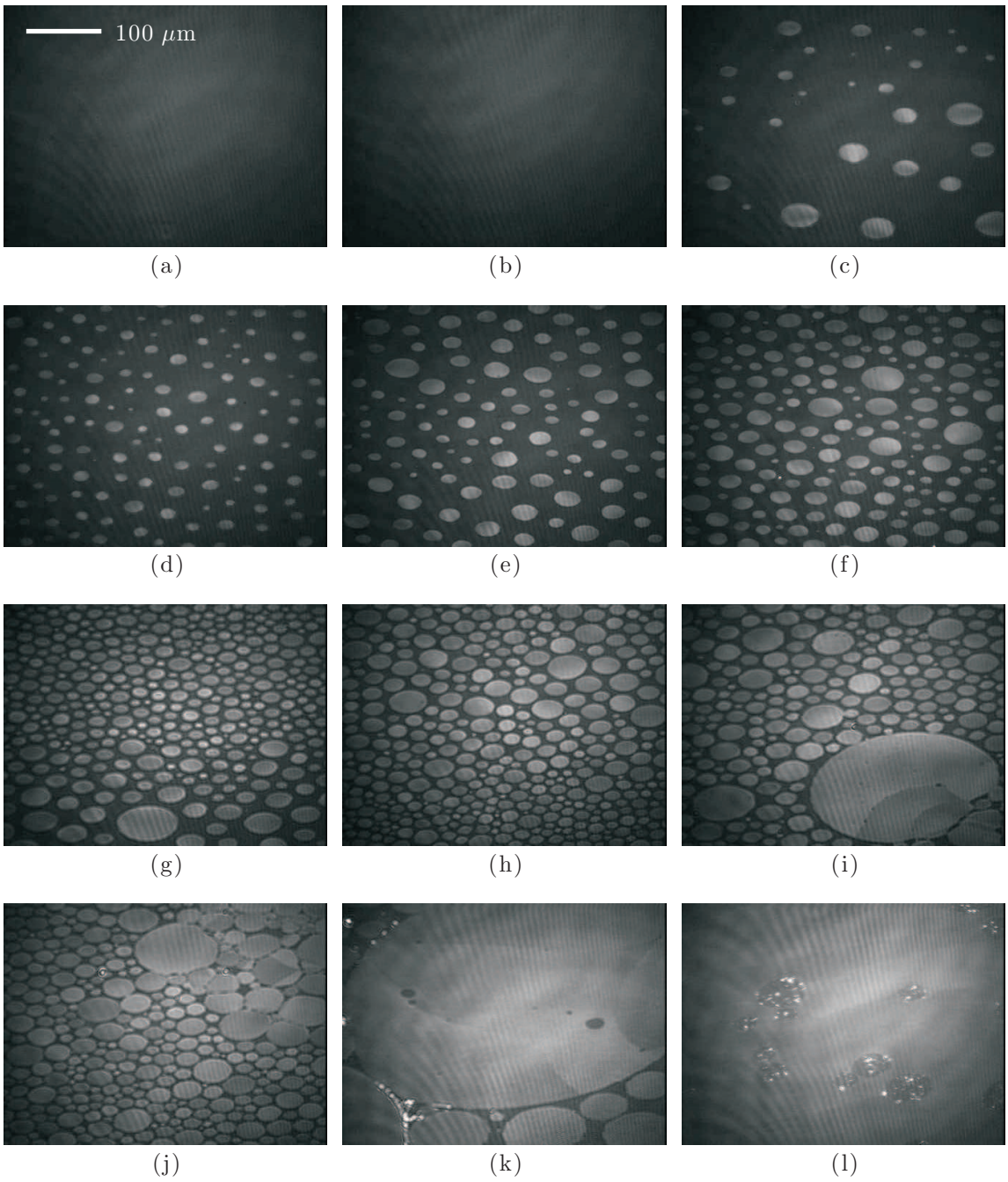

Figure 4.6. BAM images of PDA at 23 °C and pH = 2 (image dimension of 430 × 322 μm). Molecular areas: (a) 40 Å^2·molecule^{-1}; (b) 37 Å^2·molecule^{-1}; (c) 31 Å^2·molecule^{-1}; (d) 29.7 Å^2·molecule^{-1}; (e) 27.8 Å^2·molecule^{-1}; (f) 26 Å^2·molecule^{-1}; (g) 24.5 Å^2·molecule^{-1}; (h) 23.1 Å^2·molecule^{-1}; (i) 21.9 Å^2·molecule^{-1}; (j) 21 Å^2·molecule^{-1}; (k) 18.9 Å^2·molecule^{-1}; (l) 15 Å^2·molecule^{-1}. Images (a) to (b): LE phase only, (c) to (k): LE–LC co-existing phases, and (l): LC phase only.

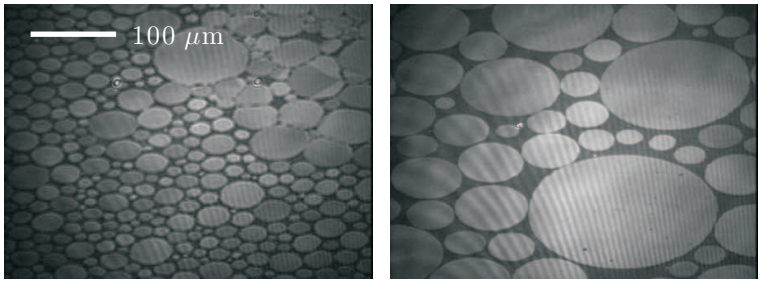

(a) (b)

Figure 4.7. Slow time-dependence of a PDA monolayer during thermodynamic equilibrium. The experiment was carried out at 23 °C and at $A = 21$ Å^2·molecule^{-1}. Time after initial formation of the PDA monolayer: (a) 20 min ($\overline{\alpha^{AF}} = 0.83$); (b) 15 h ($\overline{\alpha^{AF}} = 0.79$).

due to line tension. This is confirmed by the fact that, contrary to the area fraction of the LC phase, the lineic edge density[3] is obviously reduced (see Fig. 4.7).

4.4 Shear-induced perturbation of the thermodynamic equilibrium

4.4.1 Experimental techniques and error sources

As mentioned above, all our measurements are carried out from BAM imaging (I-elli2000, Nanofilm) which basically relies on the pioneering paper by Hénon & Meunier [70]. Not equipped with the improved objective recently developed by [100], our BAM delivers images which are only focused within a narrow horizontal strip. In order to get a complete image with the best spatial resolution (about 2 μm), it is necessary to scan a series of horizontal stripes successively and to reconstruct the final image by stacking vertically all of them side by side. Scanning and reconstructing thus one full BAM image requires several seconds; a time scale which is only possible in static conditions (see e.g. Fig. 4.6).

[3] To our knowledge, this original terminology is directly inspired from the literature on 3-D two-phase flows.

The effect of Ω on Π–A isotherm

In order to confirm that the Marangoni effect is reduced in our experiment, we tested the effect of the angular velocity Ω on Π–A isotherm. We did not found that a change in Ω induces a noticeable impact on Π whatever the value of A can be and even though Ω was as high as 4.376 rpm ($Re > 1000$). In consequence, we can expect that surface pressure gradient is negligible along the radius direction of the channel.

Velocity profile along the surface

Perfect two-dimensionality of a LM lends itself very well to particle tracking velocimetry. To characterize the flow of the PDA dispersed monolayer, only a small horizontal and well-focused stripe is selected from the central area of our BAM images. Doing so, it is possible to get contrasted BAM images compatible with the highest frame rate of the CCD camera attached to the BAM.

With none PDA molecule, the azimuthal component of the velocity along the surface is measured from hollow glass beads (3M$^{\text{TM}}$ scotchlite glass bubbles S60) selected as tracers. These beads are characterized by a density of 0.6 g·ml^{-1} and a mean diameter of 35 μm, and allow us to control with a great sensitivity whether the surface is flat or not. If the surface is a convex meniscus, the beads will gather in the center of the channel; on the contrary, if the surface is a concave meniscus, they will concentrate near the walls. These beads are chemically neutral and can be washed without difficulties. Their low density is thought of as a criterion to consider them as confident tracers of the surface motion.

The azimuthal velocity profile along the surface $v_{\theta,s}$, is determined by measuring the number of frames required for a glass bead to cross the field of view of a BAM image strip. In presence of PDA, this velocity measurement is also found to be the same as the one deduced from tracking LC domains of PDA (see enlarged Fig. 4.8). Hence, for the laminar shear flow considered here, it was not possible to detect any significant slippage between continuous LE phase and LC domains whatever their typical size (no

slip or relative velocity). This is why in our study, all LC domains are considered as intrinsic and non invasive tracers of the Langmuir emulsion under flow. In this way, the azimuthal velocity profile was estimated at each radial location by averaging 20 measurements performed from one recorded BAM video sequence.

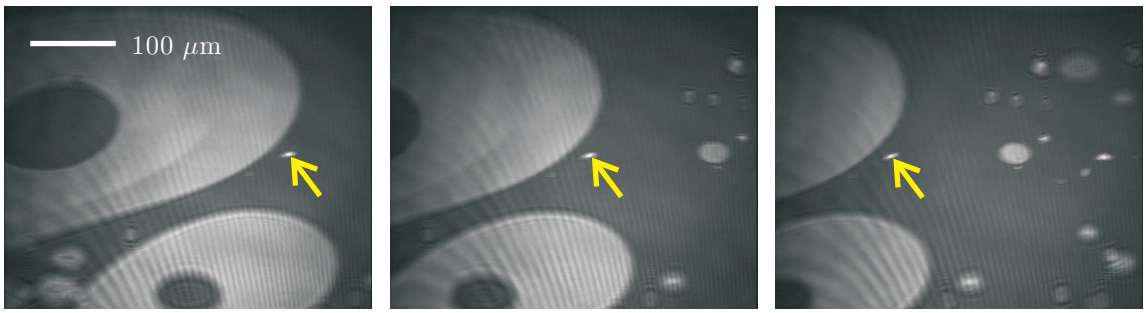

(a) (b) (c)

Figure 4.8. (a)–(c) Typical sequence of BAM images during the flow of the PDA monolayer from right to left. The boundary (see arrow) of a LC domain (bright) is followed frame-by-frame in order to extract the azimuthal velocity profile along the radius direction of the channel (PDA molecular area: $A = 21$ Å^2·molecule^{-1} at 23 ± 1 °C, subphase depth: $h = 4$ mm).

The radial profile of the azimuthal velocity along the interface, $v_{\theta,s}$, is therefore measured with the following experimental parameters:

- ◇ depth of subphase: $h = 10$, 7, and 4 mm,
- ◇ molecular areas: $A = 31$ to 15 Å^2·molecule^{-1}, large enough to get a dispersed LM whilst small enough to get stratifying stretched domains of condensed phase,
- ◇ and a series of five angular velocities ranging from $\Omega = 0.138$ rpm to $\Omega = 0.247$ rpm.

Area fraction measurement

The LE–LC co-existing phases of the PDA monolayer can be characterized by the area fraction of the LC phase (condensed fraction),

$$\alpha^{AF} = \frac{A_{LC}}{A_{LC} + A_{LE}} = \frac{A_{LC}}{A_{image}}, \tag{4.1}$$

with A_{image} the area of the BAM image, A_{LC} and A_{LE}, the areas of the condensed and expanded phases, respectively.

Note that the free surface is investigated from a laser beam at the Brewster angle $\theta_B = 53°$ (air-water interface) so that the BAM image appears shortened along the vertical direction, and a circular object seems apparently elliptical. As already mentioned in the previous chapter, BAM images are presented with unavoidable artifacts such like inhomogeneous illumination across the image; due to the Gaussian beam profile of the incident laser, and interference fringes due to the optical components. A typical full BAM image for PDA monolayer is shown in Fig. 4.9 (a). By rotating the quarter wave plate and the analyzer of the BAM, the polarization of the incident beam is set in such a way that the LE and LC phases appear black and bright, respectively. A smaller horizontal window is cut within the original BAM image (480×80 pixels) in order to perform image processing as shown in Fig. 4.9 (b). Afterwards, gray-scaled digital images of the LE–LC co-existing phases are processed by keeping always the same threshold in order to produce binary images and to compute the area fraction, α^{AF}, from the fraction of white pixels (Fig. 4.9 (c)). To avoid overlapping, BAM images are selected from the video sequence at a small enough frequency (1.25 frames·s^{-1}). The averaged value of α^{AF}, denoted $\overline{\alpha^{AF}}$, is computed at any location along the radial direction of the annular channel. All the digital images are processed with Matlab® software to determine the image size, to threshold the digital image, to remove the background noise and finally, to calculate the mean area fraction of the LC phase.

4.4.2 Other sources of experimental errors

Depth of the subphase h

The surface velocity $v_{\theta,s}$ is very sensitive to the depth of subphase. As an example, according to the modeling analysis by Drazek *et al.* [38], for a $h = 5$ mm, with inner radius, $r_i = 40$ mm, and with outer radius, $r_o = 70$ mm, it can be demonstrated that a

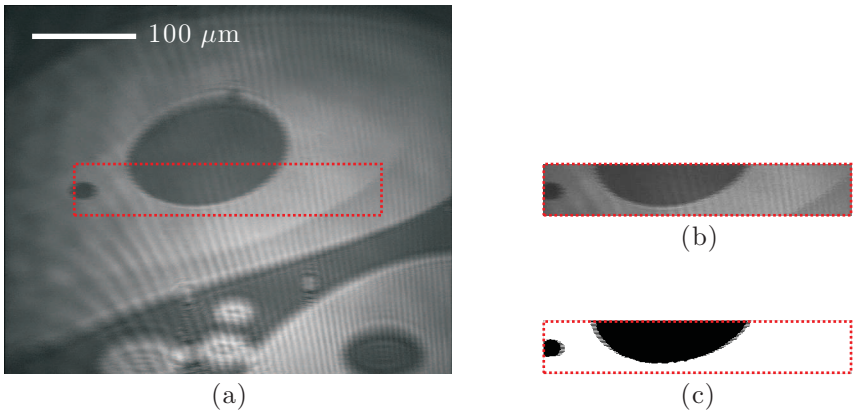

Figure 4.9. (a)–(c) Typical processing of original BAM image before computing α^{AF}.

reduction of 100 μm on the depth of a pure water subphase involves an increase of 3% on the maximum of surface velocity. In fact, a non negligible experimental error can be attributed to the measurement of the subphase depth h essentially for two reasons:

1. Although all mechanical components are manufactured with a high degree of accuracy, it is nevertheless difficult to reach a very small level of roughness and a constant value of h. For instance, to adjust the subphase depths to $h = 4$ and $h = 7$ mm, additional Delrin™ rings are inserted into the annular channel. Therefore, the ring thickness stands also as a possible source of experimental error. Consequently, several measurements of the subphase depth were performed at different radial locations, especially at the vicinity of the side walls. With a standard deviation as small as 0.049 mm, as measured, all the depths are found slightly overvalued with an error of 4.75 %.

2. Despite the large radial extent of the channel gap and the care paid to adjusting the flatness of the liquid interface, any slight meniscus can also affect the input value of h. Therefore, we fixed the vertical position of the BAM and the annular channel and then adjusted the depth of the subphase until we could get a clear image from the BAM all along the liquid surface. By this method, we can make sure that the position of the water surface is the same for all experiments.

Angular velocity Ω

In order to control the angular velocity, Ω, during the experiments, a Hall-effect sensor (Sick 7900264) is externally placed at the outer side wall and connected to an electronic counter (Kübler Codix, Germany). To estimate the experimental error, a scope (Tektronix TDS 1002) is also connected to the Hall sensor, separately. The control parameter Ω measured in these two ways is characterised by a relative error smaller than 8.24 % all over the relevant range, between 0.138 rpm and 8.767 rpm.

4.5 Experimental characterization of the two-phase Langmuir monolayer flow

The shear applied to the LM is expected to destabilize the thermodynamic equilibrium by enhancing deformation and further the break-up of the LC domains. If the competition between shearing and line tension has received much attention, especially as far as transient flows are concerned [110, 67, 72], it is clearly not true for a permanent flow because of the delay in obtaining it (about 15 h). In fact, as demonstrated in the following, this time delay remains unchanged if one compares between the situation for which the LM is at rest and the situation for which it is subjected to the annular shear flow.

4.5.1 Area fraction convergence

A specific effort was devoted to achieving a steady flow-induced organization of the PDA emulsion. According to Eq. (4.1), the LC-LE co-existing phases can be characterized by the area fraction of LC phase. To ensure convergence of the area fraction, time-dependent measurements are carried out at the radial locations, $r = 4$, 5, and 6 cm, for a subphase depth, $h = 10$ mm, and for a large molecular area, $A = 31$ Å^2·molecule^{-1}. For each radial locations, the channel floor is put in rotation after the

spreading of the PDA solution is completed (typical time delay of $\cong$ 30 min at most). At first, the monolayer on quiescent water consists of a dispersed phase characterized by circular condensed domains surrounded by a continuous LE phase with a lower molecular packing density (Figs. 4.6 (a) to (f)). Then, BAM image sequences are recorded just after starting the ring rotation. The resulting video is stored for about 14 minutes at frame frequency, 1.25 frames·s^{-1}. In this way, at least 1000 values of the area fraction can be computed at each radial position. It is thus possible to calculate a mean value of the area fraction from a given number of BAM images as shown in Fig. 4.10. The mean area fraction $\overline{\alpha_i^{AF}}$ is defined as:

$$\overline{\alpha_i^{AF}} = \frac{1}{N_i} \sum_{i=1}^{N_i} \alpha_i^{AF}, \tag{4.2}$$

where α_i^{AF} denotes the i^{th} area fraction calculated from the N_i^{th} BAM image. In this way, it is possible to test the convergence of the area fraction whether by increasing N_i or by storing video sequences after time delays of 2 h, 5 h, and 15 h (existence of a statistically invariant value of $\overline{\alpha_i^{AF}}$).

Competition between several timescales

As made evident from Fig. 4.10, the mean area fraction $\overline{\alpha_i^{AF}}$ is not capable of converging unless the number of averaged images is taken larger than $Ni \approx 200$. Even beyond $Ni \approx 200$, the Fig. 4.10 exhibits a slightly slope, that is found to be positive for a small radius ($r = 4$ cm) and negative for a large radius ($r = 6$ cm). At midhalf of the channel ($r = 5$ cm), no significant slope is observed and $\overline{\alpha_i^{AF}}$ is no longer affected during the timescale under consideration. This phenomenon is observed after the floor was set in motion for 2 or 5 h, but not after a delay as long as 15 h.

◇ Convective transport along the liquid surface

Considering that the timescale associated to the recirculating flow within the channel cross-section is of the order of several minutes (a timescale consistent with N_i ranging from 100 to 500 and a video frequency at 1.25 frames·s^{-1}),

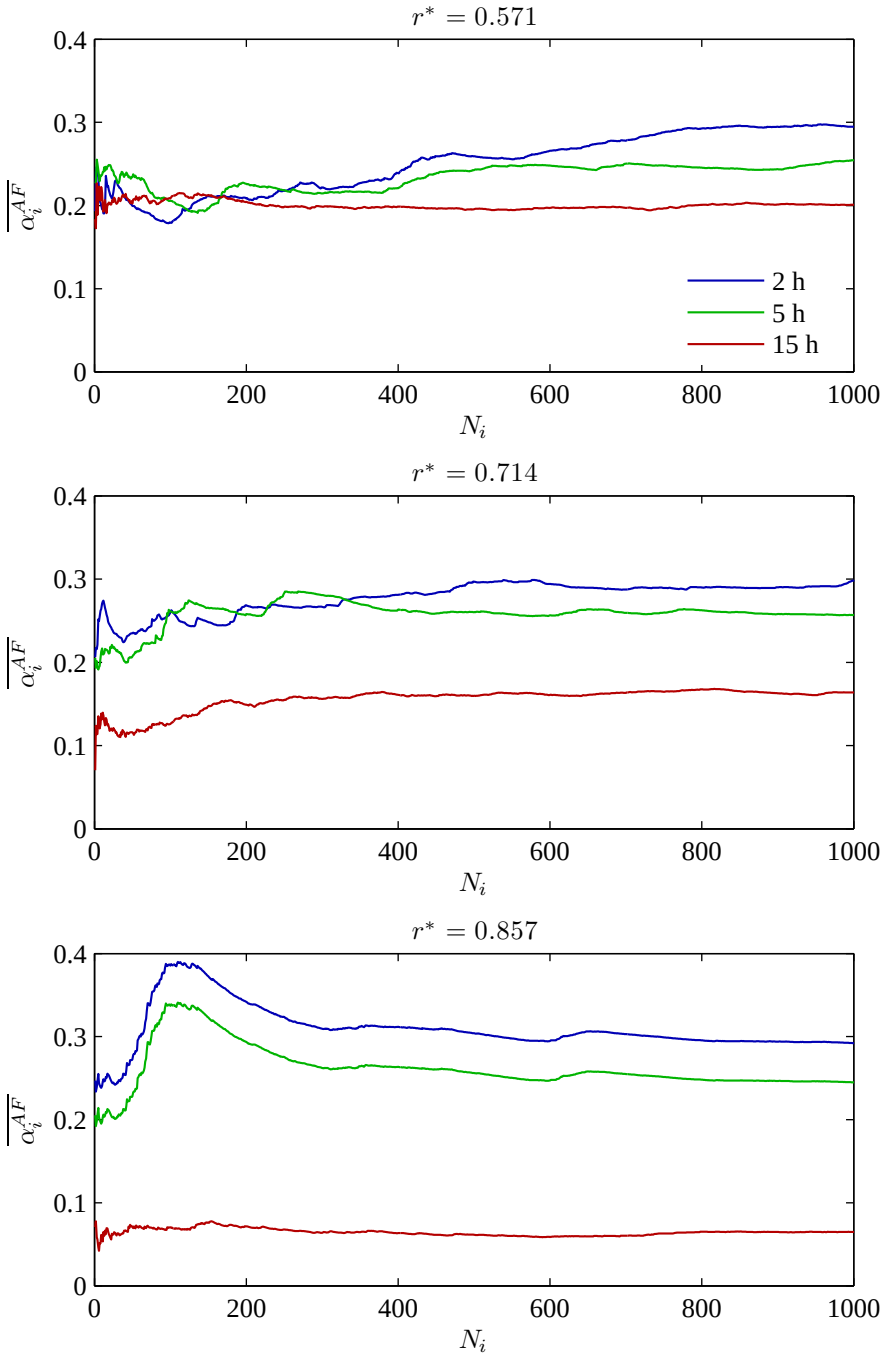

Figure 4.10. Area fraction convergence tests while the channel floor is rotating for 2, 5, and 15 h. The experiment is carried out at three different radii along the liquid surface with a monolayer of PDA (23 ± 1 °C, $h = 10$ mm, $A = 31$ Å^2·molecule^{-1}, and $\Omega = 0.138$ rpm).

an experimental scale for the radial component of the velocity along the liquid surface can be estimated:

$$v_{r,s} \sim \frac{r_o - r_i}{t} \approx 10^{-4}\ (\mathrm{m \cdot s^{-1}}).$$

It can be checked that this velocity scale is also fairly consistent with the one predicted from Eq. (C.6). According to the surface transport equation,

$$\frac{\partial \Gamma}{\partial t} \sim \nabla_s \cdot [v_\perp \Gamma],$$

the radially inwards flow along the surface is expected to transport and pack PDA molecules towards smaller and smaller radii. Hence, from the scaling analysis developed in Appendix C, and more particularly from Eq. (C.6) and the previous surface transport equation, the timescale for the flow-induced molecular packing can be estimated as,

$$T_{flow} \sim \frac{r_o}{v_{r,s}} = \frac{4\nu_b}{[\Omega h]^2} \approx 200\ \mathrm{s},$$

which remains nevertheless much smaller than the timescale observed in our experiments (about 15 h). We can conclude that even if the radially inwards flow along the liquid surface contributes to transient convergence of the area fraction at short times, as demonstrated by the positive and negative slopes near the inner and outer side walls (Fig. 4.10), this is definitely not the limited kinetics.

◇ Surface diffusion-limited kinetics

Taking into account the Π–A isotherm, one can expect that, due to the centrifugal flow-induced molecular packing, the size and the number of condensed domains will grow progressively from large to small radii (Appendix C). As confirmed later on, this is supported by the steady radial distribution of the averaged LC fraction (see Fig.4.11). Nevertheless, the time scale associated either to the growth or the coalescence of LC domains could be therefore the prior one observed in our experiments (more than 5 h). If now we consider that the growth process of the LC domains is limited by surface diffusion[4] (cf. Section 4.3.2), it

[4]In a frame attached to the shear flow along the liquid surface (no slip velocity).

can be worthwhile to write the surface transport equation as follows:

$$\frac{\partial \Gamma}{\partial t} \sim D_s \frac{1}{r} \frac{d}{dr} \left[r \frac{d\Gamma}{dr} \right],$$

a second timescale can be estimated,

$$T_{diff} \sim \frac{[r_o - r_i]^2}{D_s} \approx 40 \text{ h},$$

with a surface diffusion coefficient of PDA molecules,

$$D_s \approx 10^{-8} \, \text{m}^2 \cdot \text{s}^{-1},$$

typical of organic surfactants in LM [175]. Since T_{diff} is much closer to the experimental time delay observed to get a steady distribution of the LC domains (15 h), surface diffusion can be again considered as the limited kinetics in our experiments despite the flow imposed.

◇ On the impact of PDA solubility

Whatever the radial location considered, the asymptotic value of the averaged LC fraction $\overline{\alpha_i^{AF}}$ always exhibits a systematic and significant reduction after the floor is set in motion, even for a time delay far larger than 15 h. Even at mid-half of the channel, the asymptotic value of $\overline{\alpha_i^{AF}}$, defined as the value of $\overline{\alpha_i^{AF}}$ when $N_i = 1000$, exhibits a non negligible drift towards lower and lower values (see limit values of $\overline{\alpha_i^{AF}}$ after 2 h, 5 h, and 15 h).

We think that the very large timescale associated to a slow lowering of $\overline{\alpha_i^{AF}}$ originates from the solubility kinetics of PDA in the underlying acidified subphase. As a matter of fact, the solubility of a fatty acid in water decreases as the length of the alkyl chain grows [51]. To obtain an insoluble monolayer of a nonionized fatty acid (i.e., our situation with a low pH value), a fatty acid must contain at least 12 carbon atoms [133]. For instance, if a monolayer made from myristic acid ($C_{13}H_{26}O_2$) is held at a surface pressure of 10 mM·m^{-1} and a temperature of 20 °C, then the loss in monolayer area due to solubility in the water subphase is 0.1 %·min^{-1} [163]. This contrasts with a long-chain fatty acid such like stearic

acid ($C_{18}H_{36}O_2$) which demonstrates a decrease in its molecular area of less than 0.001 %·min^{-1} under similar conditions [51]. These figures simply reflect the different solubilities of two long-chain compounds in water subphase at 20 °C: 0.02 g·l^{-1} and 0.003 g·l^{-1} for myristic acid and stearic acid, respectively. In our case, the monolayer is made from PDA ($C_{15}H_{30}O_2$), a fatty acid whose chain length is placed between myristic and stearic acids.

To conclude, even with a low-Reynolds number flow, one needs a long time to get a steady pattern of the LE–LC co-existing phases and therefore to get a local convergence of $\overline{\alpha_i^{AF}}$. During all this time, the total amount of PDA over the liquid surface slowly decreases due to a slight solubility in the underlying subphase.

Steady distribution of the LC domains

In light of the aforementioned timescales, all the experimental results which follow are only concerned with the steady regime strictly obtained after a delay as long as 15 h. As shown in Fig. 4.10, and despite the aforementioned solubility of PDA, one considers that a sufficient level of convergence is achieved to investigate the flow-induced meso-patterning of the steady dispersed LM. At each radial location, BAM images are recorded at a capture frequency 1.25 frames·s^{-1} during a delay of about 7 min, which means that up to 500 values of the area fraction can be computed and averaged for each radial position. The mean area fraction,

$$\overline{\alpha^{AF}} = \frac{1}{500}\sum_{i=1}^{500}\alpha_i^{AF}, \tag{4.3}$$

is found to converge accordingly with our selection criterion since a same level of convergence is achieved whatever the radial location is (see Fig. 4.11).

The experimental error for the steady distribution of the mean area fraction is estimated from the standard deviation of $\overline{\alpha_i^{AF}}$ by removing systematically the first 150 values of the instantaneous area fraction α_i^{AF} while retaining the last 350 values.

As explained by the insert in Fig. 4.11, error bars represent the standard deviation calculated at each radial locations from the last 350 values of α_i^{AF}.

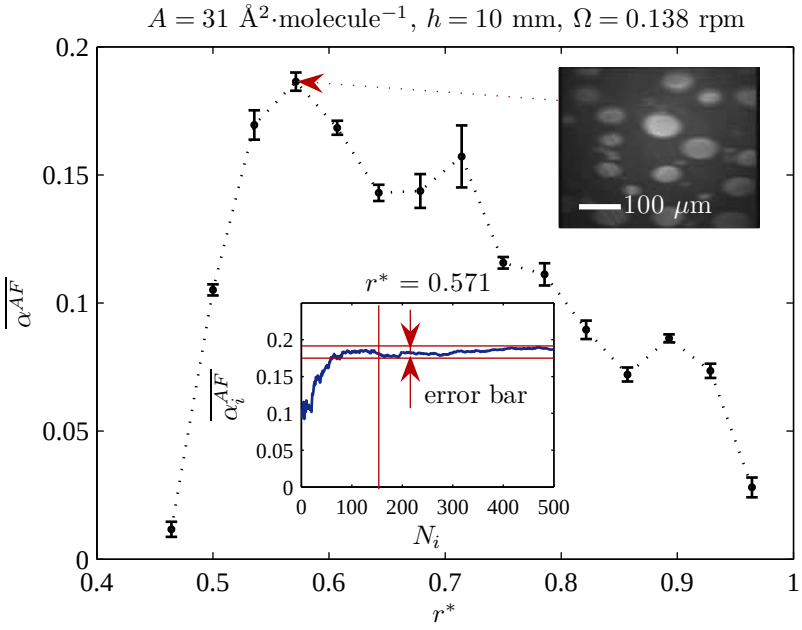

Figure 4.11. Steady distribution of the mean area fraction, $\overline{\alpha^{AF}} = \frac{1}{500}\sum_{i=1}^{500}\alpha_i^{AF}$ as measured after a time delay of 15 h. The protocol to estimate the experimental errors is illustrated by the insert at the radial location $r^* = 0.571$ ($r = 4$ cm) where a BAM image of the condensed domains (elliptical bright spots) under flow is also displayed ($A = 31$ Å^2·molecule^{-1}, $h = 10$ mm and $\Omega = 0.138$ rpm).

4.5.2 The case of a highly densified LM

We also investigated the convergence of the mean area fraction for a highly densified LM ($A = 15$ Å^2·molecule^{-1}, $h = 4$ mm, $\Omega = 0.206$ rpm). After the PDA monolayer is in thermodynamic equilibrium (after $\cong$ 30 min), BAM images shows that all the monolayer is LC phase. Then we start to rotate the channel floor and video sequences are recorded for different time delays. Fig. 4.12 shows that $\overline{\alpha_i^{AF}}$ is quickly convergent, being nearly constant as soon as $N_i \approx 250$ or more. Before convergence - and whatever the radial location is - all the values of $\overline{\alpha_i^{AF}}$ uniformly decrease.

This last experimental observation contrasts strongly with the previous experiment performed for a low densified LM with $A = 31$ Å^2·molecule^{-1}, a depth $h = 10$

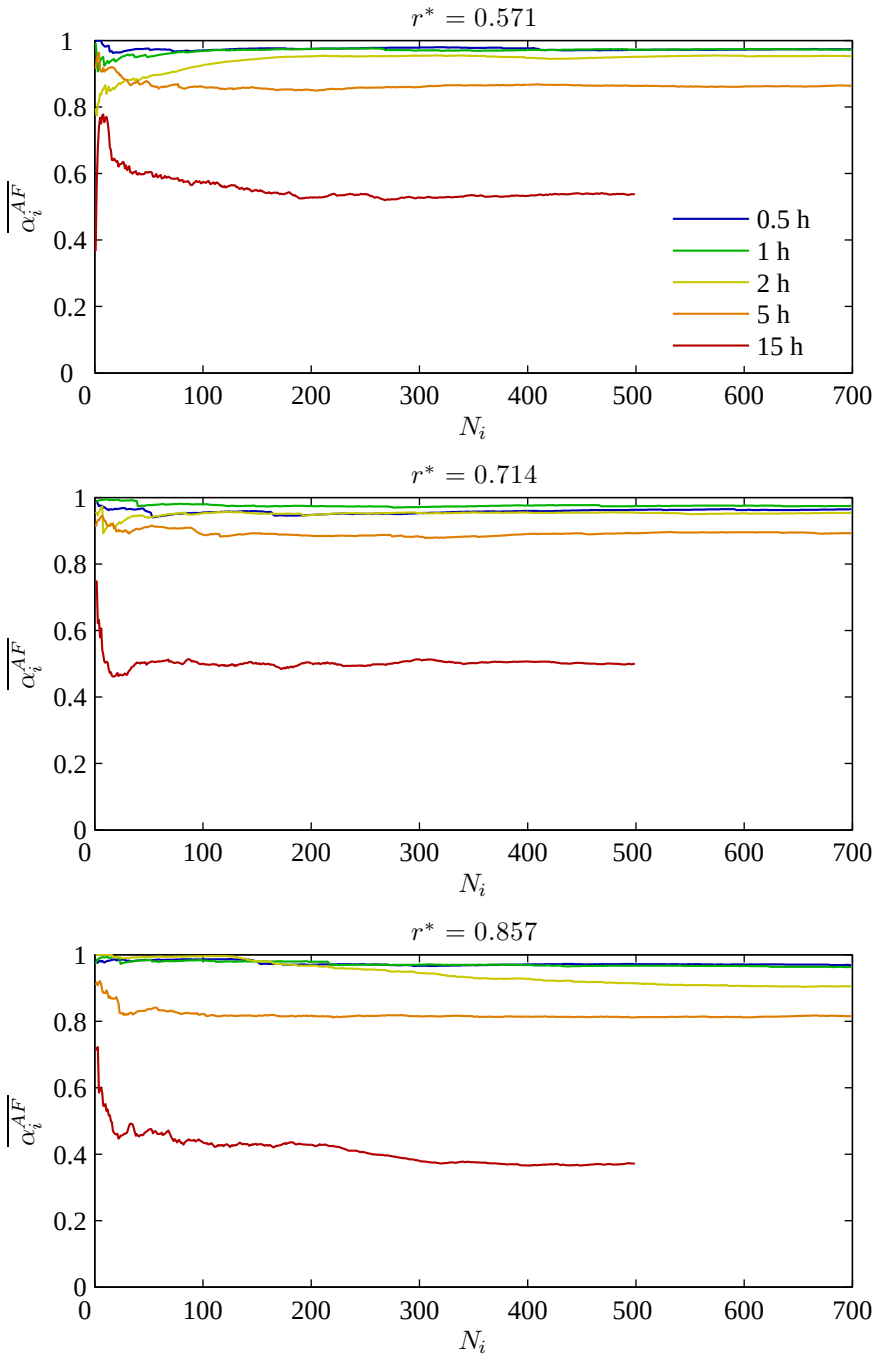

Figure 4.12. Convergence test for the mean area fraction after the channel floor was set in rotation for 0.5, 1, 2, 5, and 15 h. The experiments are carried out at three radial locations (23 ± 1 °C, $h = 4$ mm, $A = 15$ Å^2·molecule^{-1}, and $\Omega = 0.206$ rpm).

mm, and a low rotation speed $\Omega = 0.138$ rpm. For a highly densified LM ($A = 15$ Å^2·molecule^{-1}), the ability of the radial velocity along the monolayer to support molecular packing is no longer significant. Here, and as confirmed later, the shear is suspected to drive to an efficient fragmentation and subsequently, to the fast and steady organization of the LM.

In Fig. 4.12 whatever the radial location considered, the averaged LC fraction $\overline{\alpha_i^{AF}}$ again exhibits a significant reduction after the floor is set in motion for a time delay as large as 15 h. Even at mid-half of the channel, the asymptotic value of $\overline{\alpha_i^{AF}}$ exhibits a non negligible drift towards lower values (see limit values of $\overline{\alpha_i^{AF}}$ after 2, 5 and even 15 h). Here again, PDA solubility in the water subphase is suspected to play a key-role, as mentioned above. To consolidate this interpretation, it is worthy to estimate PDA solubility from our data. In Fig. 4.12, one gets $\overline{\alpha_i^{AF}} \approx 0.5$ after the floor was set in motion for 15 h. From Figs. 4.5 and 4.6, we can estimate that $A \approx 23$ Å^2·molecule^{-1} for $\overline{\alpha_i^{AF}} = 0.5$. Assuming that the long time decrease of $\overline{\alpha_i^{AF}}$ is due to solubility of PDA in the water subphase, the rate of PDA lost is found closed to 0.0386 %·min^{-1}: a value which is fairly consistent with the previous data on myristic and stearic acids.

4.5.3 Identification of the surface viscosity

One famous technique devoted to the measurement of the surface shear viscosity, μ_s, is the deep-channel (or canal) viscometer [27, 112, 180, 135, 105]. As already mentioned, the experimental set-up presented in our experiment can play the same role as the deep-channel viscometer since our annular geometry is very close especially when the subphase depth is the largest: $h = 10$ mm (Fig. 4.1). Nevertheless, compared to the classical deep-channel geometry, and as described later on, our experimental device distinguishes itself by a decisive technical improvement which allows user to handle soluble surfactants (small fatty acid chain length, detergents, functionalized bio-molecules...): no chemical leakage at the bottom of the side walls is made possible (for sake of comparison, see for instance [112, 72]).

Even if our prior aim is not to perform viscosity measurements, it is important (as seen in the following) to assess a possible change in surface shear viscosity during LE–LC phase transition. As a consequence, the surface flow can be advantageously modeled and compared to experimental measurements [112]. The modeling of a canal viscometer proposed by Mannheimer & Schechter is described in Appendix B.

The dimensionless velocity along the surface,

$$v^*_{\theta,s} = \frac{v_{\theta,s}}{r_o \Omega},$$

as measured for the angular velocity $\Omega = 0.138$ rpm and predicted in Appendix B from Eq. (B.12), is plotted in Fig. 4.13 for pure water with a surface viscosity considered as negligibly small ($\mu_s = 0$ sP). The agreement between measurements and calculated values for a pure interface is rather good if we consider that the average deviation between the measurements and predictions all along the liquid surface, $\frac{|v^*_{\theta,s,measured} - v^*_{\theta,s,prediction}|}{v^*_{\theta,s,measured}}$, are found to be 9.0 %, 5.2 %, and 6.0 % for the depths $h = 10$, 7, and 4 mm, respectively. These discrepancies may be due to the experimental errors already mentioned about h and Ω.

To obtain the estimation of μ_s, a least squares method is used to fit the experimental profile of dimensionless surface velocity, $v^*_{\theta,s}$, with the control parameters, $h = 7$ mm and $\Omega = 0.138$ rpm. This curve fitting involves Eq. (B.12) as the analytical model which relates the dimensionless radius r^* to $v^*_{\theta,s}$; μ_s stands as the parameter to adjust and therefore to identify. The best fits for μ_s for different molecular areas A are delivered in Table 4.3 with attached root mean square errors (RMSE).

Previous study performed on stearic acid showed that $\mu_s = 0.56$ msP, 0.94 msP, and 0.94 msP (1 sP = 10^{-3} kg·s^{-1}) for $A = 59$ Å^2·molecule^{-1}, 39.3 Å^2·molecule^{-1}, and 29.5 Å^2·molecule^{-1} respectively [71]. Note that the value of μ_s as measured here for PDA monolayers is in reasonable agreement with the values measured or referenced by Earnshaw & Winch [45].

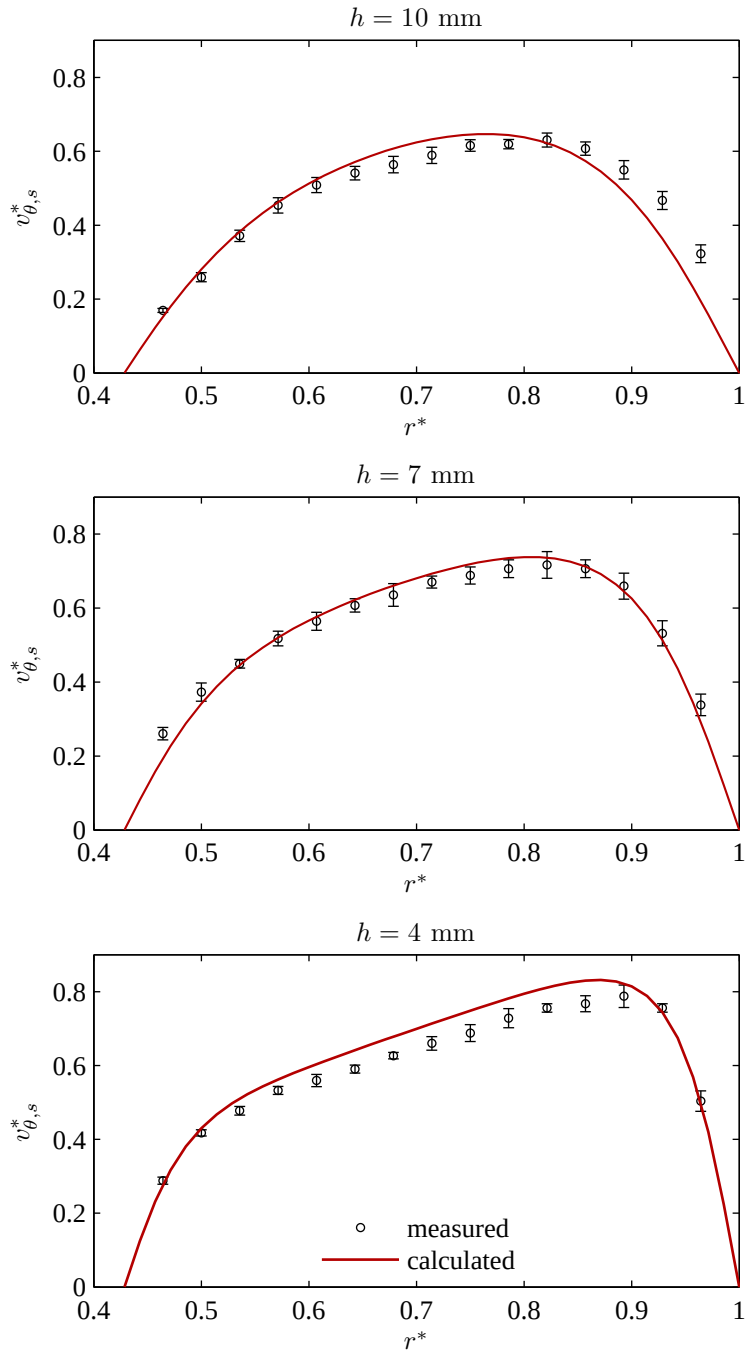

Figure 4.13. Non-dimensional surface velocity profile for $\Omega = 0.138$ rpm (pure water). The solid line is a curve fit of the measured data (○), as obtained from Eq. (B.12) with a negligibly small surface viscosity ($\mu_s = 0.00001$ sP).

Table 4.3. Dependence of the surface shear viscosity μ_s on the molecular area A for a PDA monolayer with the corresponding root mean square errors (RMSE) as calculated after curve fitting.

A (Å^2·molecule^{-1})	μ_s (msP)	RMSE
40	0.109	0.030
31	0.128	0.027
26	0.144	0.032
21	0.203	0.029
15	0.243	0.038
13	0.193[1]	0.046

[1]questionable since the state of the LM is perhaps no longer concerned with the co-existing LE–LC phases only: possible arising of a solid phase.

4.5.4 The azimuthal velocity profile along the interface $v_{\theta,s}$

The azimuthal velocity profile along the interface $v_{\theta,s}$ is measured as shown in Fig. 4.14 with the following experimental parameters:

- ◇ three depths of pure water subphase of $h = 10$, 7, and 4 mm,
- ◇ two angular velocities of $\Omega = 0.138$ rpm and $\Omega = 0.206$ rpm,
- ◇ different surface concentrations of the PDA monolayer A from 31 Å^2·molecule^{-1} to 13 Å^2·molecule^{-1}.

In addition, $v_{\theta,s}$-profile for pure water at different h and Ω is also shown in Fig. 4.14 (a).

In our experiment, the Reynolds number is defined as:

$$Re \equiv \frac{r_o \Omega e_{gap}}{\nu_b}, \tag{4.4}$$

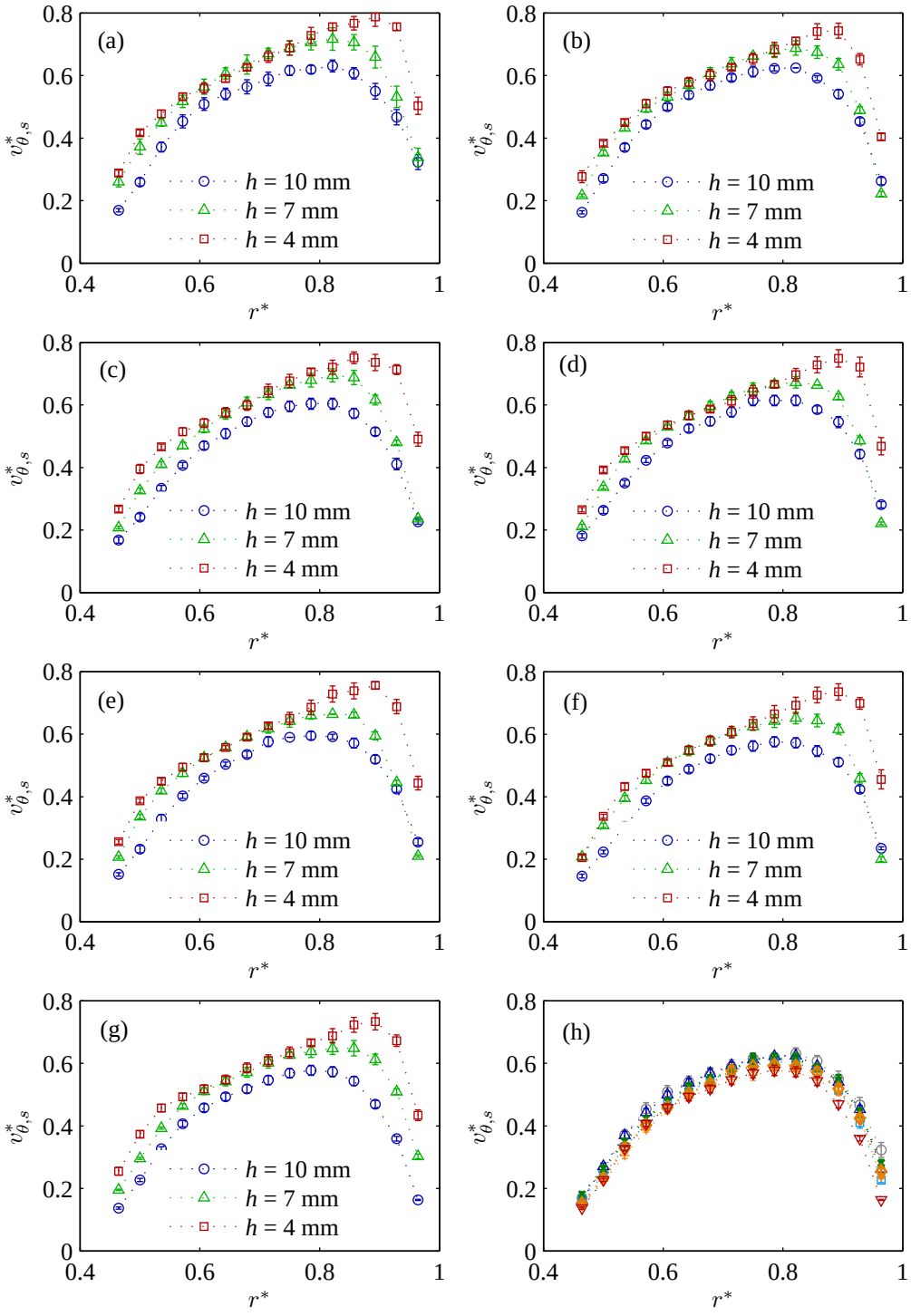

Figure 4.14. Dimensionless azimuthal velocity along the liquid surface $v^*_{\theta,s}$ with $\Omega = 0.138$ rpm and for (a) pure water, (b) $A = 40$ Å^2·molecule^{-1}, (c) $A = 31$ Å^2·molecule^{-1}, (d) $A = 26$ Å^2·molecule^{-1}, (e) $A = 21$ Å^2·molecule^{-1}, (f) $A = 15$ Å^2·molecule^{-1}, (g) $A = 13$ Å^2·molecule^{-1}. The last figure (h) displays $v^*_{\theta,s}$-profiles with $\Omega = 0.138$ rpm and $h = 10$ mm when LM molecular density increases (A: ○, pure water; △ 40; □, 31; ×, 26; ◇, 21; + 15; ▽, 13 Å^2·molecule^{-1}.)

where $e_{gap} = r_o - r_i$ and ν_b denote the channel gap and the molecular viscosity of the subphase, respectively. Its value remains moderate even with the maximum value taken by the angular velocity during our experiments, $\Omega = 0.247$ rpm ($Re \approx 70$).

Here, the angular velocity Ω is either 0.138 rpm or 0.206 rpm respectively. According to the definition of Eq. (4.4), because Re remains small enough, the flow in the annular channel is consistently found laminar. As made evident in Fig. 4.14 (a) to (g), changing the depth h drives to a stronger impact on the shape of the velocity profile than any change in the molecular area A (see Fig. 4.14 (h) for instance). The maximum value of $v_{\theta,s}$ observed on the velocity profile is seen to increase as h decreases while the velocity profile approaches the linear Couette profile imposed by the near rotating floor.

To take into account the coupling between the in-plane shear along the liquid surface and the shear in the underlying subphase, it is useful to introduce the (macroscopic) Boussinesq number:

$$\widetilde{Bo} \equiv \frac{\mu_s h}{\mu_b {e_{gap}}^2}, \tag{4.5}$$

where μ_s is the surface shear viscosity and μ_b is shear viscosity of the subphase. According to the identified value of μ_s in our experiment, the (macroscopic) Boussinesq number is of the order of, $\widetilde{Bo} \approx 0.4 \times 10^{-3}$, with $\mu_s \approx 0.2$ msP (1 sP $= 10^{-3}$ kg·s^{-1}), $\mu_b = 10^{-3}$ Pa·s and $h = 10$ mm. In our experiments, the surface shear viscosity is therefore not expected to impact the bulk flow near the interface ($\widetilde{Bo} \ll 1$). And apparently, the surface velocity $v_{\theta,s}$ is not clearly found sensitive to the molecular area A (Fig. 4.14).

4.5.5 Mean area fraction along the interface $\overline{\alpha^{AF}}$

The mean area fraction of LC phase along the interface, $\overline{\alpha^{AF}}$, is shown in Fig. 4.15. Major trends are worthy of note:

◇ For a weakly densified monolayer, and subsequently for a larger molecular area

(A = 31, 26, and 21 Å^2·molecule^{-1}), the value of $\overline{\alpha^{AF}}$ for h = 4 and 7 mm is lower than the one for h = 10 mm (see Figs. 4.15 (a), (b), and (c)).

- ◇ For a highly densified monolayer, as illustrated in Fig. 4.15 (d), if the molecular area A goes down to 15 Å^2·molecule^{-1}, the value of $\overline{\alpha^{AF}}$ for h = 4 mm is found larger than the one for the two larger depths h.

- ◇ In Fig. 4.15 (f), for the same molecular area A = 15 Å^2·molecule^{-1}, the rotation speed of the channel floor is increased and the initial trends observed at a large surface molecular area when h = 10 and 4 mm are recovered. In Figs. 4.15 (a), (b), (c), and (f), a slope on the area fraction can be distinguished. This is related to a radial segregation with the largest value of $\overline{\alpha^{AF}}$ located near the inner side wall when the subphase depth is h = 10 mm.

- ◇ Finally, for smaller molecular areas A (A = 15 and 13 Å^2·molecule^{-1}), the $\overline{\alpha^{AF}}$ profiles are uniform whatever the depth of the subphase is.

To elucidate these experimental findings, one has to take into account the interplay of:

1. the radially inwards flow along the surface,
2. the subphase and surface contributions to the shear-induced deformation experienced by the LC domains,
3. and evidently, the line tension.

The following chapter focuses on the respective abilities of these physical mechanisms.

4.6 Concluding remarks

The influence of a laminar annular flow, at a moderate Reynolds number ($Re \approx 10$ to 100), on the steady morphology of a LM made with co-existing LE–LC phases of

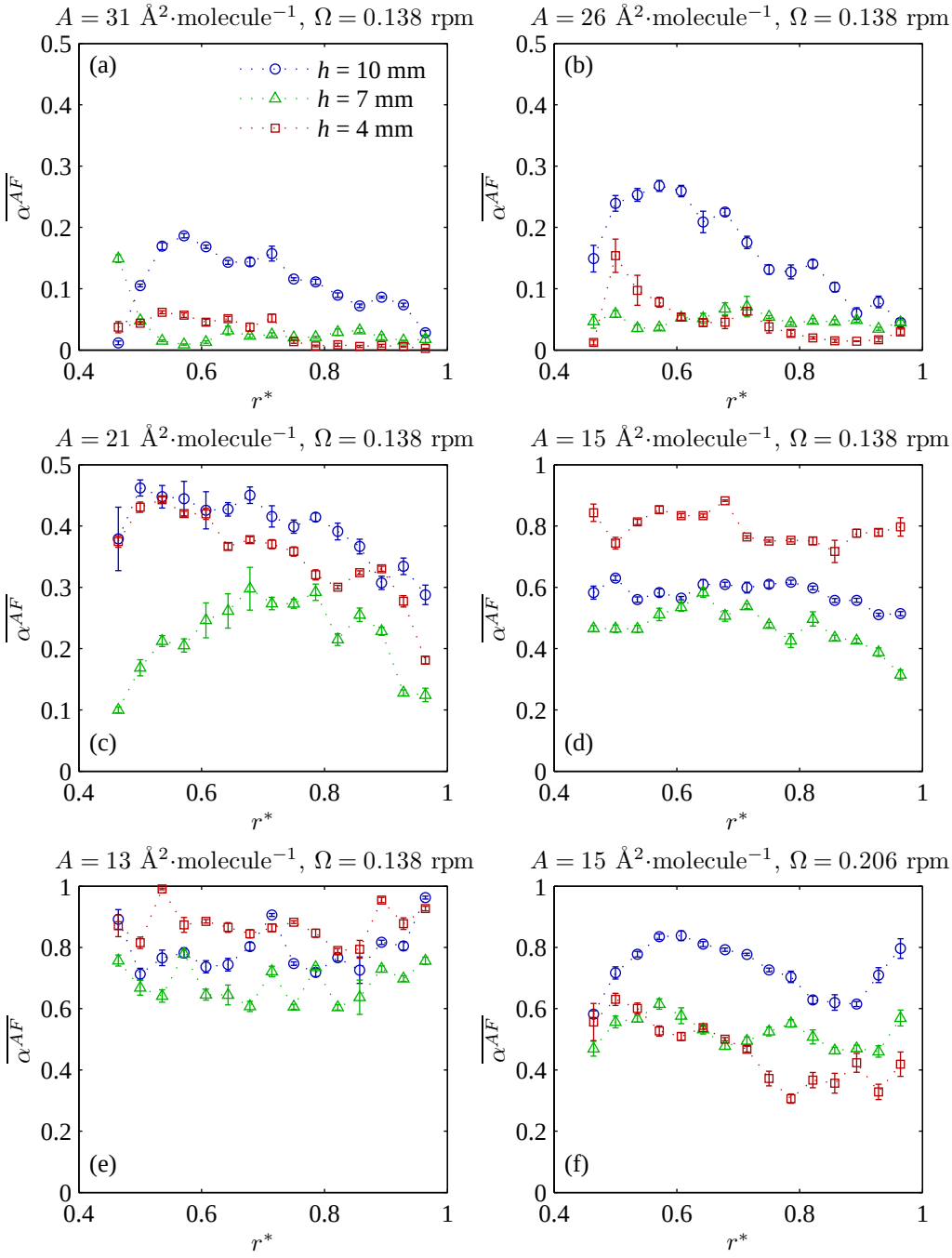

Figure 4.15. Mean area fraction of LC phase, $\overline{\alpha^{AF}}$, along the surface for different values of A, h, and Ω.

pentadecanoic acid (PDA) is investigated. Not surprisingly, due to a small macroscopic Boussinesq number, the surface velocity is found to be weakly modified by successive addings of PDA amounts during LE–LC transition. Nevertheless, an averaged surface shear viscosity of the PDA monolayer is estimated from our apparatus by considering it behaves also as a channel viscometer.

According to our Π–A isotherm, measured from the technique of successive addings, Marangoni effect is expected to reduce drastically during LE–LC phase transition provided that the laminar flow is considered as a perturbation of the thermodynamic equilibrium.

During the transition, and because of the flow, the monolayer shifts from a dispersed to a stratified regime. Due to the rotation of the channel floor, a weak centrifugal flow, responsible for a radial transport of the surfactants along the surface and balanced by Marangoni effect, is found to play a significant role only when the monolayer is dispersed. Above a given level of surface concentration, the monolayer is no longer dispersed and becomes stratified. The corresponding flattening of the Π–A isotherm suggests that Marangoni effect becomes vanishingly small. Accordingly, the area fraction distribution is found uniform. The condensed domains behave as stripes elongated along the shear flow.

It has to be mentioned that despite its very slow kinetics, due to the long time scale of our experiments, PDA solubility in the water subphase can become significant.

Chapter 5

Flow-induced patterning of a condensed phase within a Langmuir monolayer

5.1 Theoretical considerations

5.1.1 Thermodynamical equilibrium: the balance between dipolar electrostatic forces and line (excess) tension

The LM along the surface is conveniently modeled as a sheet of molecular dipoles with dipolar electrostatic moment mainly oriented perpendicular to the surface. As a consequence of Gauss' law, written as a jump at the liquid surface, the difference in surface dipole densities, which arises here, from the difference in molecular densification between inner and outer parts of a condensed domain, supports long-range dipole-dipole repulsive interactions. As described by [116], when the thermodynamic equilibrium is well-established, the shape of a condensed domain can be considered as governed by a balance between a line (excess) tension, λ_o, also referred to as bare

line tension[1], the short-range dipole electrostatic interactions inside a condensed domain and the aforementioned long-range dipole-dipole repulsive interactions. As a consequence, line excess tension enhances circular shape of the LC domains whereas the dipole-dipole electrostatic repulsive interactions support instability of the circular shape with transition from circular to elongated shapes such as n-fold symmetry shapes (see e.g. 2-fold symmetry associated to "dog-bone" domains [98]) or thin stripes [117]). Due to their negative contribution to an effective line tension, the long-range dipole–dipole interactions result in a process which promotes line edge density.

Since pioneering modeling proposed by McConnell and his collaborators [116], there is full agreement in the literature to write the total energy of a condensed domain as the sum of a bulk electrostatic energy, a line tension energy and electrostatic energy due to long-range interaction

$$F_s = A_{LC}\,\varepsilon + \lambda P - \frac{1}{2}{\mu_{LC/LE}}^2 \oiint_{\partial A_{LC}} \frac{ds\,ds'}{\sqrt{[r-r']^2 + {\Delta_t}^2}}, \tag{5.1}$$

where the shape of the condensed domain is described from the local variable $r(s)$, and ds and ds' are defined as line elements attached to its outer boundary (see [185] for instance). The symbols ∂A_{LC}, P and $\mu_{LC/LE}$ denote, respectively, the dividing edge around the LC domain, its length and the difference in dipole densities between the dipolar PDA molecules within the LC domain and those diluted in the surrounding LE continuous phase. The modified variables introduced in Eq. (5.1) are defined as follows:

$$\lambda = \lambda_o - {\mu_{LC/LE}}^2,$$

and

$$\varepsilon = \varepsilon_o + \frac{{\mu_{LC/LE}}^2}{\Delta_t},$$

where ε_o is the electrostatic energy per unit area within the LC domain and λ_o is the line (excess) tension. The symbol $\mu_{LC/LE}$ denotes the difference in dipole densities

[1] As an excess variable, analogous to the surface tension in 3-D, the bare line tension stands as a fictive mechanical variable due to the surface pressure difference between inside and outside of the closed line which delimitates one LC domain (Gibb's approach). The bare line tension integrates short-range forces (such like Van der Waals dispersive forces or steric repulsion) over a distance from the delimiting line significantly larger than several molecular scales [146].

between the dipolar PDA molecules within the LC domain and those diluted in the outer (continuous) LE phase. Finally, Δ_t can be understood as a cutoff thickness below which the dipole-dipole repulsive forces are more and more negligible and increasingly replaced by short-range forces.

Equation (5.1) of the energy F_s can be written down explicitly for a circular condensed spot of radius R (consider for instance updated modelling by Deutch & Low [36]):

$$F_s = 2\pi R \left[\lambda_o - {\mu_{LC/LE}}^2 \ln \left(\frac{8R}{e^2 \Delta_t} \right) \right], \tag{5.2}$$

where $e \equiv \exp(1)$ and, according to the literature, the modified line tension λ_o ranges between 1 and 10 pN.

The typical number of PDA molecules, N, packed inside one circular LC domain can be estimated from the approximation,

$$aN = A_{LC} = \pi R^2,$$

where a can be defined as the mean molecular area occupied by one PDA molecule. Keeping the condensed area A_{LC} constant, the energy per molecule, F_s is classically minimized with respect to the radius R of a LC domain so that the equilibrium radius [116] writes as:

$$R_{eq} = \frac{e^3 \Delta_t}{8} \exp \left(\frac{\lambda}{{\mu_{LC/LE}}^2} \right). \tag{5.3}$$

As already noticed, only a slow time-dependence allows for the PDA co-existing phases to attain thermodynamic equilibrium, which is highlighted in Fig. 4.7. This growth kinetics is related to the instantaneous radius which increases up to the equilibrium radius R_{eq} predicted from Eq. (5.3). It seems consistent to associate this kinetics with the very long time scale made evident during the time-dependent experiments which commented in Section 4.5.1 (see Fig. 4.10).

Beyond the static equilibrium regime defined by Eq. (5.3)

The instability of one isolated condensed domain has been the subject of many studies, especially when its shape allows the energy F_s to be written down explicitly [116]. All the literature is based on a linear stability approach and the involvement of harmonic modes for describing shape distortion: see for instance [98, 34, 167] for circular or nearly-circular islands of condensed matter, and more recently, de Koker *et al.* [33] and Alexander *et al.* [4] for a stripe and a tether, respectively.

Typically, a circular domain with a radius larger than the equilibrium one defined by Eq. (5.3) is linearly unstable with respect to a harmonic distortion of its initial shape. As found by [86], if the radius of a LC domain exceeds the following critical size,

$$R_{eq} = \frac{\Delta_t}{8} \exp\left(\frac{\lambda}{{\mu_{LC/LE}}^2} + Z_n\right), \tag{5.4}$$

a transition to a shape with a n-fold symmetry can be observed. Note that in the paper by Lee & McConnell (1993) (see Figs. 8 to 11 in [98]), shape transitions are successfully observed using either the initial domain size or the surface pressure as control parameters.

5.1.2 Non-equilibrium: relevance of the effective line tension

Here, our aim is to deal with a situation out of equilibrium i.e., with a flow externally imposed. The effective line tension, λ_{eff}, is introduced in order to take into account the balance between cohesive energy due to line (excess) tension and noncohesive energy due to dipolar electrostatic repulsions. Defining the quantity λ_{eff},

$$\lambda_{eff} = \left.\frac{\partial F_s}{\partial P}\right|_{A_{LC}},$$

from the partial derivative of the total energy of a condensed domain, F_s, with respect to its perimeter, P, de Koker & McConnell [34] demonstrated that the long-range

dipolar forces contribute in renormalizing line tension in such a way that

$$\lambda_{eff} = \lambda - {\mu_{LC/LE}}^2 \left[\ln \left(\frac{\sqrt{A_{LC}/\Pi}}{\Delta_t} \right) + \mathcal{I}_s \right],$$

provided that the cut-off length Δ_t (≈ 1 nm) remains much smaller than the typical size of the condensed domain $\sqrt{A_{LC}/\Pi}$ (a requirement which is commonly fulfilled). The variable Δ_t is nothing but a cut-off thickness below which the dipole–dipole repulsive forces are more and more negligible and increasingly replaced by short-range forces. Except if λ_{eff} becomes very small, the contribution $\mathcal{I}_s$ can be considered as negligibly small. Consequently, it can be demonstrated that shape transitions are mainly monitored by the control parameter,

$$\lambda_{eff} \simeq \lambda - {\mu_{LC/LE}}^2 \ln \left(\frac{\sqrt{A_{LC}/\Pi}}{\Delta_t} \right). \tag{5.5}$$

5.1.3 Shape change of a LC domain under shearing: the classical macroscopic approach

For the shape of a condensed domain to be modified by a steady shear, one has to take into account the balance between the effective line tension, λ_{eff}, and the shear stress whatever its origin is: from the surface, with the contribution of the in-plane shear stress τ_s, or from the underlying subphase, with the contribution of the shear stress valued at the surface: $\tau_b|_s$ (see Fig. 5.1).

Keeping in mind the approach of J. W. Gibbs based on a zero-mass dividing surface, the LM is considered as nothing but a 2-D continuum embedded within 3-D space (intrinsic point of view). Accordingly, we consider that the shear stress from the bulk, $\tau_b|_s$, behaves as a (surface) body force, in the same way that buoyancy in 3-D two-phase flows.

It follows that a surface Bond number can be classically defined at the macroscopic scale,

$$Bo_s \equiv \frac{\mu_b {r_o}^3 \Omega / h}{\lambda_{eff}}, \tag{5.6}$$

where r_o, h, and Ω denote the outer radius of the channel, the subphase depth, and the angular velocity, respectively.

Equivalently, the surface shear can be also taken into account by introducing either a surface capillary number at macroscopic scale,

$$Ca_s \equiv \frac{\mu_s r_o \Omega}{\lambda_{eff}}, \tag{5.7}$$

5.1.4 Shape change of a LC domain under shearing: the mesoscopic scale

To our knowledge, the literature mainly focuses on the transient relaxation of a condensed domain in a two-phase LM. For instance, it is established that when submitted to a transient shear rate imposed from the subphase, $\overset{o}{\gamma}$, a condensed domain is able to deform from a circular- to a bola-shaped domain. If $\overset{o}{\gamma}$ increases more, condensed domains break up. The resisting effect of the line tension is classically estimated from a viscous relaxation process originating from the subphase [72, 110] (small macroscopic Boussinesq number).

In our experiments, the macroscopic Boussinesq number is also much smaller than unity ($Bo \overset{\Delta}{=} \frac{Ca_s}{Bo_s} \approx 10^{-4}$) so that surface shearing can not be suspected to modify the end-driven flow within the subphase (one-way coupling). To confirm this statement, it has been checked that even if the molecular area is reduced down to $A = 15$ Å^2·molecule^{-1}, the profile of the surface velocity $v_{\theta,s}$ is not significantly changed.

However, here the flow under consideration is specific in the sense that it is permanent. The LC domains behave as 2-D liquid drops

$$\frac{\mu_{s,LC}}{\mu_{s,LE}} \sim \frac{\mu_s \left(A = 40 \text{ Å}^2 \cdot \text{molecule}^{-1}\right)}{\mu_s \left(A = 15 \text{ Å}^2 \cdot \text{molecule}^{-1}\right)} \approx 2;$$

this property fully opens the possibility of deformability under the impact of viscous shear. It follows that a surface Bond number can be defined at the mesoscopic scale,

that is to say, at the scale of an individual LC domain,

$$Bo_{LC,s} \equiv \frac{\tau_b|_s \, S_{LC}}{\lambda_{eff}}, \tag{5.8}$$

with the typical area of one condensed domain defined as

$$S_{LC} = R\delta\theta\delta R.$$

The variables $R\delta\theta$ and δR denote the typical length of a condensed domain along the direction of shearing (azimuthal cross section) and the typical width of a condensed domain (radial cross section), respectively (see Fig. 5.1). Surface shear stress, τ_s, is also taken into account by introducing the mesoscopic surface capillary number at the scale of one LC domain,

$$Ca_{LC,s} \equiv \frac{\tau_s R\delta\theta}{\lambda_{eff}}. \tag{5.9}$$

A mesoscopic Boussinesq number is therefore defined at the scale of one LC domain by writing the following ratio:

$$\widetilde{Bo_{LC}} \equiv \frac{Ca_{LC,s}}{Bo_{LC,s}} = \frac{\tau_s}{\tau_b|_s \, \delta R} \approx 1 \text{ to } 10, \tag{5.10}$$

with the values of the shear stresses estimated from Fig. 5.6, as follows:

$$\tau_s = \mu_s \Omega \left[\frac{dv^*_{\theta,s}}{dr^*} - \frac{v^*_{\theta,s}}{r^*} \right], \tag{5.11}$$

$$\tau_b|_s = \mu_b \frac{r_o \Omega}{h} \left. \frac{\partial v^*_\theta}{\partial z^*} \right|_s \sim \mu_b \frac{r_o \Omega}{h} \left[v^*_{\theta,s} - r^* \right], \tag{5.12}$$

with $\mu_s = 0.127 \times 10^{-6}$ kg·s^{-1} (estimated from the technique of the canal viscometer) and where μ_b, r_o, h, and Ω denote the Newtonian viscosity of the subphase, the outer radius of the channel, the subphase depth, and the angular velocity, respectively. Interestingly, the scale of $\widetilde{Bo_{LC}}$, which is found of order unity and even more[2], is affected by the stretching rate of the LC domains *via* its dependence on δR (≈ 10 to 100 μm).

[2]The Couette profile supposed to hold when writing Eq. (5.12) suggests that $\widetilde{Bo_{LC}}$ is clearly undervalued.

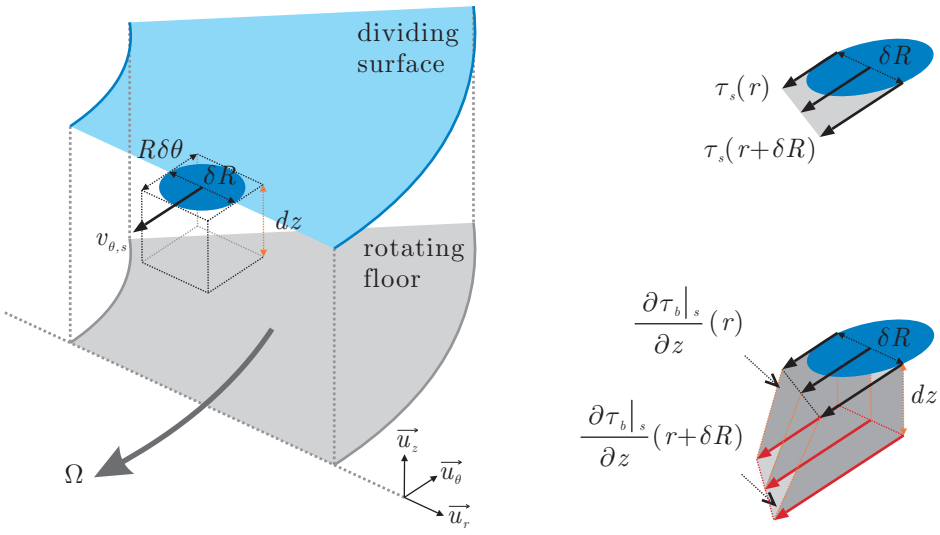

Figure 5.1. LC domain under stress-induced stretching, as sketched.

5.1.5 Brief comments on the potential impact of an externally-imposed flow

The equilibrium size of a LC domain in our PDA LM ranges from 100 μm down to 10 μm (see Fig. 4.6), the smallest size which remains nevertheless much larger than the cut-off distance. Therefore, the square of the factor $\mu_{LC/LE}$, involved in the expression of the effective line tension (5.5), is expected to contribute importantly to the steady radius.

If the Reynolds number is large enough ($Re \approx 100$), we expect that the LM, especially the LC domains, be packed under the radially inwards flow-induced pressure along the liquid surface. By modifying the value of $\mu_{LC/LE}$, the effective line tension and subsequent cohesion of the LC domains could be strongly impacted (see Eq. (5.5)). Considering the theoretical and experimental findings of Lee & McConnell [98], we expect that the recirculating flow enhances shape transitions and subsequent elongated shapes of the LC domains, promoting thus a larger value of the lineic edge density.

The shear flow along the channel could modify strongly the cohesion of a LC domain because of a competition between effective line tension and the viscous drag

force from the bulk [16] or the (in-plane) viscous drag force from the surface whether the Boussinesq number turns out large enough [185].

To anticipate the detailed interplay of all these physical mechanisms reveals to remain a difficult task at first. The experiments which follow are supposed to help in doing relevant selection among them.

5.2 Growing impact of the flow upon mesoscopic morphology

In order to investigate the flow-induced reorganization of the PDA monolayer, a collection of characteristic BAM images have been selected for different molecular areas, namely $A = 31$ and 26 $\text{Å}^2 \cdot \text{molecule}^{-1}$, as displayed in Figs. 5.2 - 5.3.

5.2.1 Low molecular packing and dispersed flow

At a low surface concentration ($A = 31$ $\text{Å}^2 \cdot \text{molecule}^{-1}$) and a low enough Reynolds number ($Re \simeq 40$), line (excess) tension remains large enough to prevent LC domains from in-plane fragmentation due to either the dipole-dipole repulsion, the in-plane shear stress along the liquid surface, or the shear stress from the subphase. As a consequence, the LC domains conserve a cohesive-circular or elliptic shape.

Molecular packing due to radial flow

As clearly demonstrated in Figs. 5.2 - 5.3, the radial distribution of $\overline{\alpha^{AF}}(r^*)$ exhibits a negative slope which delivers a first evidence of a radially inwards flow-induced segregation of the LC domains. The low molecular packing density of the LM confers to it a fluidity large enough to permit a radial flow along the surface. Taking into account the scaling analysis developed in the Appendix C, which relies on the hypothesis that the adsorption isotherm (Fig. 4.5) remains relevant, a decrease in the molecular area

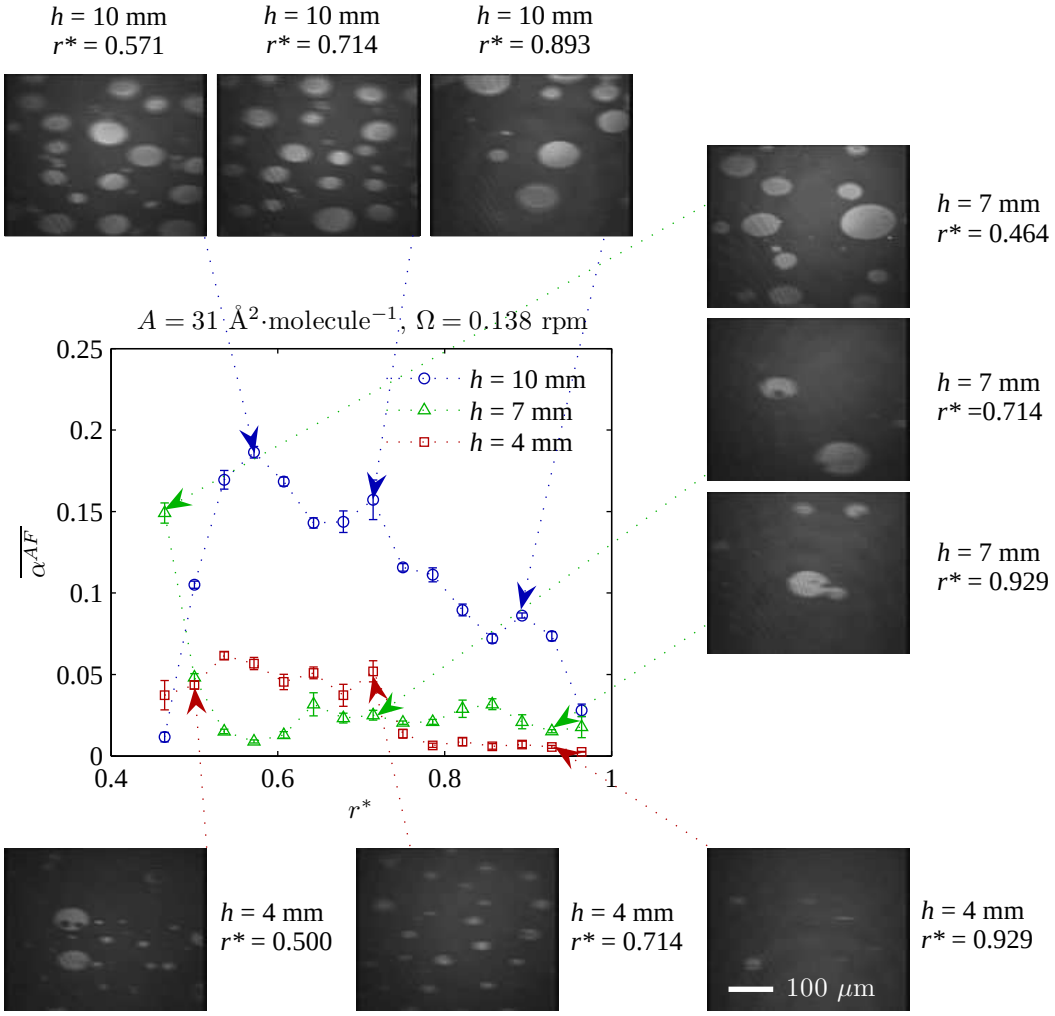

Figure 5.2. Radial distribution of $\overline{\alpha^{AF}}$ for $A = 31$ Å^2·molecule^{-1} and $\Omega = 0.138$ rpm with typical BAM snapshots. The flow direction is from right- to left-hand sides of each snapshot.

as small as 0.1 Å^2·molecule^{-1} (Eq. (C.7)) should be theoretically associated with the radial segregation of the area fraction along the liquid surface. This prediction is contradicted by the dependence of the mean area fraction on the molecular area as displayed in Fig. 4.5 during thermodynamic equilibrium: only a change in molecular area as large as 1 to 10 Å^2·molecule^{-1} could explain the slope observed on the $\overline{\alpha^{AF}}(r^*)$-profile (Fig. 4.11). We believe that the strong disagreement between our experimental observations and prediction in Eq. (C.7) demonstrates that the adsorption isotherm and the near-equilibrium approximation (Eq. (C.2)) are no longer valid when a shear flow is imposed however small its Reynolds number may be.

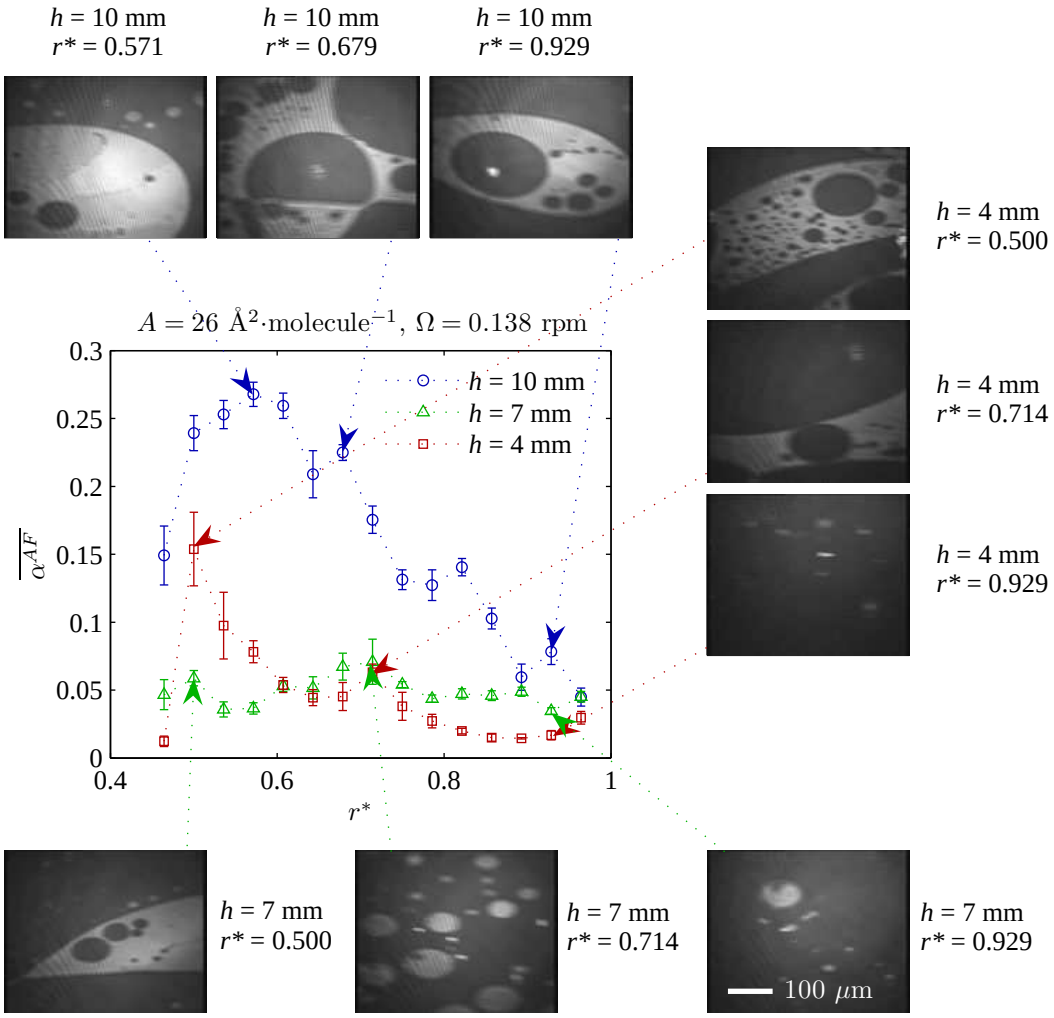

Figure 5.3. Radial distribution of $\overline{\alpha^{AF}}$ for $A = 26$ Å^2·molecule^{-1} and $\Omega = 0.138$ rpm with typical BAM snapshots. The flow direction is from right- to left-hand sides of each snapshot.

Arising of a barrier (Reynolds ridge) along the annular liquid surface

To support definitely the previous physical interpretation, a series of $\overline{\alpha^{AF}}$-profiles is measured for the low molecular density, $A = 31$ Å^2·molecule^{-1}, while the rotation speed is progressively increased (Fig. 5.4). A clear evidence is given of a flow-induced segregation on the molecular packing density: when the rotation speed is large enough ($\Omega = 0.206$ rpm), all the LC domains are removed from the right hand side (RHS) to the left hand side (LHS) of the liquid surface (see BAM images recorded at $r^* \simeq 0.86$). Proportionally, a peak is made evident on the $\overline{\alpha^{AF}}$-profile located on the LHS of the liquid surface at the radial location $r^* \simeq 0.57$. When radial convection intensifies, the

magnitude of the $\overline{\alpha^{AF}}$-peak becomes consistently larger and larger while it expands radially on the LHS of a (circular) Reynolds ridge. All along the liquid surface, rather than noting a significant increase in the total area of LC phase,

$$A_{LC,t} = \int_{r^*=\frac{r_i}{r_o}}^{r^*=1} A_{LC} dr^*,$$

to the detriment of the total area of LE phase, $A_{LE,t}$, the quantity $A_{LC,t}$ remains roughly unchanged.

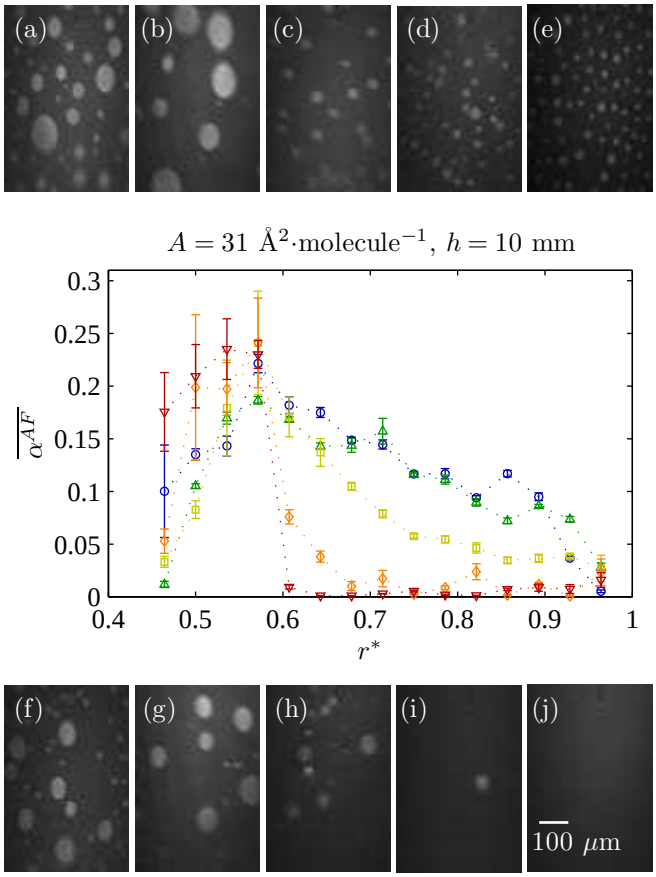

Figure 5.4. Mean area fraction along the interface $\overline{\alpha^{AF}}$ for a dispersed monolayer and the following values of the floor rotation speed: ○: $\Omega = 0.076$ rpm, ((a) and (f)); △: $\Omega = 0.138$ rpm, ((b) and (g)); □: $\Omega = 0.160$ rpm, ((c) and (h)); ◇: $\Omega = 0.206$ rpm, ((d) and (i)); ▽: $\Omega = 0.247$ rpm, ((e) and (j)). Significant BAM snapshots are displayed on both sides of the Reynolds ridge at two radial locations: (Figs. (a) to (e), top line) $r^* \simeq 0.57$ and (Figs. (f) to (j), bottom line) $r^* \simeq 0.86$.

To complete these observations, the typical diameter of the LC domains, d, is measured from BAM images recorded on both sides of the cumulating location $r^* \simeq$

0.57. Interestingly, Fig. 5.5 demonstrates that the $\overline{\alpha^{AF}}$-peak is not explained by the growing size of the LC domains. In contrast to this, the typical size of LC domain suddenly decreases by a factor of about 2 when the rotation speed of the annular floor grows up to the onset $\Omega = 0.160$ rpm. Correlatively, a sudden jump in the number of LC domains, n_{LC}, is observed at the same rotation speed, which allows us to understand why $A_{LC,t}$ is not significantly changed.

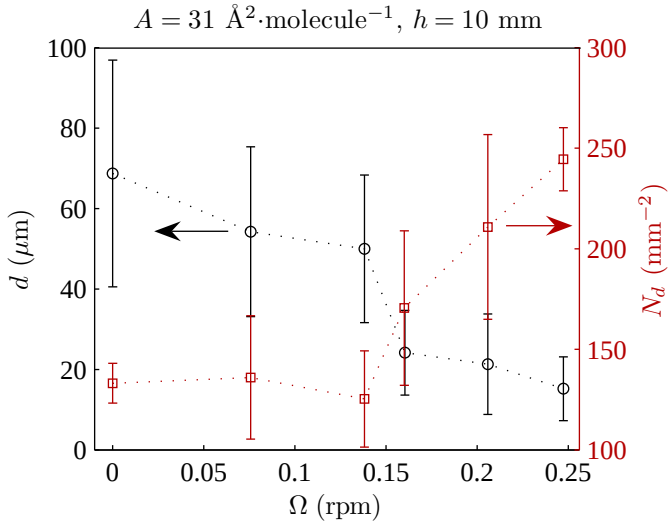

Figure 5.5. (○) Mean diameter (left axis) and (□) number density N_d (right axis) of the LC domains as measured at the radius, $r^* \simeq 0.57$, where the $\overline{\alpha^{AF}}$-peak is made evident.

Physical interpretation of the morphological transition

The LM experiences a strong morphological transition from a rough poly-dispersed two-phase monolayer (Figs. 5.4 (a) and 5.4 (b), $\Omega = 0.076$ rpm to 0.138 rpm) to a mono-dispersed matrix of tiny condensed drops (see Figs. 5.4 (c) and 5.4 (d), $\Omega = 0.160$ rpm to 0.206 rpm). If the radially inwards flow-induced pressure increases more (Ω as large as 0.247 rpm), the 2-D distribution of condensed drops becomes increasingly regular and exhibits a well-defined spatial frequency (see Fig. 5.4 (e), see also reducing in error bars for the typical diameter d in Fig. 5.5). Among consequences, there is a

strong increase of the number density (Fig. 5.5) defined as,

$$N_d = \frac{n_{LC}}{A_{image}},$$

where $A_{image} = A_{LC} + A_{LE}$ is the total area of the BAM image, already involved in Eq. (4.1) and where n_{LC} is also defined as the number of nucleation sites of the LC phase.

At the same time, the surface pressure in the LE phase, Π_{LE}, likely increases in order to satisfy mass conservation of PDA along the liquid surface. If one considers thermodynamic equilibrium, one can write a two-dimensional Laplace's law as [146],

$$\Pi_{LC} - \Pi_{LE} = \frac{\lambda}{d_{eq}/2},$$

with d_{eq}, the equilibrium diameter of one condensed drop. Now if one considers that line tension is not significantly reduced, whilst the difference in surface pressure reduces, the equilibrium radius should increase. Here, our experimental results fully contradict this expectation since the diameter of the condensed drops is reduced under the impact of flow-induced compression.

As a consequence, hydrodynamical ingredients must be introduced. Now, if one considers the velocity along the surface (Fig. 5.6), one can see the following:

- ◇ despite the growing impact of the radial segregation when the rotation speed increases, the dimensionless profile of the θ-component of the velocity along the surface, $v_{\theta,s}$, is virtually unchanged (Fig. 5.6) as well as the dimensionless profiles of the in-plane shear stress and the subphase stress at the surface;

- ◇ whatever the value of the rotating speed, the (macroscopic) Boussinesq number remains very small ($\widetilde{Bo} \approx 10^{-4}$) so that it cannot be retained as relevant to investigate the morphological transition observed;

- ◇ the (mesoscopic) Boussinesq number, $\widetilde{Bo_{LC}}$, defined from Eq. (5.10), is found to be of order unity and even more near the side walls (Fig. 5.7), which suggests that the shear along the surface is responsible for breakup of the LC domains and subsequent reduction in mean diameter (Fig. 5.5).

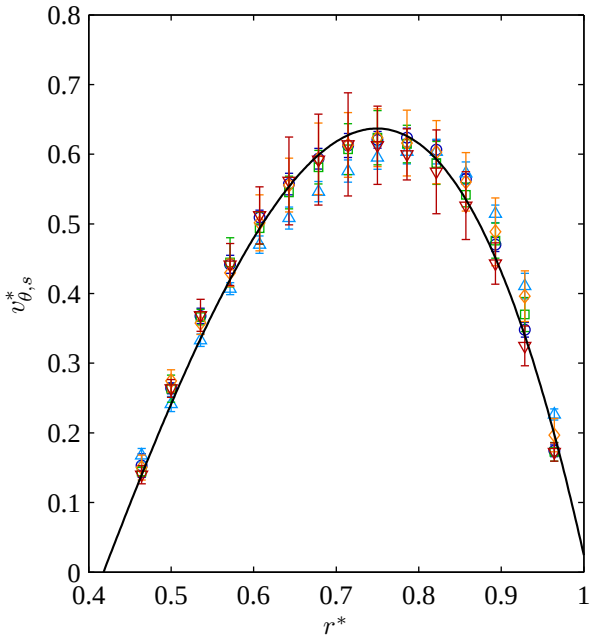

Figure 5.6. (—) Curve fitting of the dimensionless velocity along the surface, $v^*_{\theta,s}$ (r^*), for $A = 31$ Å^2·molecule^{-1} and the angular velocities: ($\circ$) $\Omega = 0.076$ rpm; ($\triangle$) $\Omega = 0.138$ rpm; ($\square$) $\Omega = 0.160$ rpm; ($\diamond$) $\Omega = 0.206$ rpm; ($\bigtriangledown$) $\Omega = 0.247$ rpm.

To explain the morphological transition experienced by the coexisting phases during flow-induced compression, it is worthwhile to come back to previous considerations about the effective line tension λ_{eff}. Due to molecular-packing-induced decrease in λ_{eff} and, simultaneously, the increase in shearing due to the growth of the rotating velocity, the surface capillary number at mesoscale, $Ca_{LC,s}$, can become large enough to trigger the morphological transition. This is especially true at the vicinity of the left side wall, $r^* \approx 0.4$ to 0.6 (see Fig. 5.7), where LC domains are packed by the radially inwards flow along the surface. Hence, a scale for the effective line tension can be put forward as follows:

$$\lambda_{eff} \sim R\delta\theta\ \tau_s \approx 2.5 \times 10^{-13}\ \text{N}, \tag{5.13}$$

with the triggering angular speed, $\Omega = 0.160$ rpm, the characteristic size, $R\delta\theta \approx 60$ μm (Fig. 5.5), and the shear stress along the surface, $\tau_s \approx 4 \times 10^{-9}$ N·m^{-1}, estimated at $r^* \approx 0.5$ from Fig. (5.6) and Eq. (5.11) where $\mu_s = 0.127 \times 10^{-6}$ kg·s^{-1}. The scaling

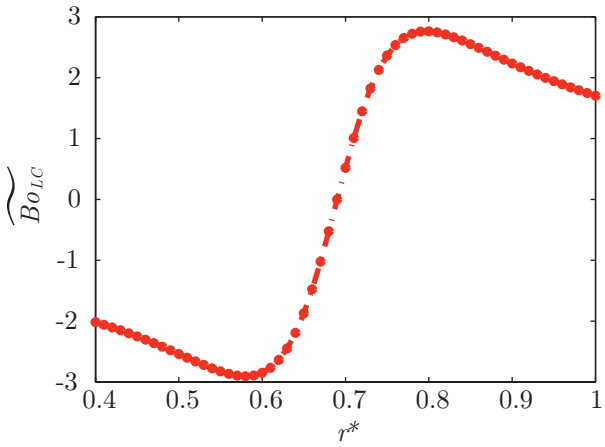

Figure 5.7. Mesoscopic Boussinesq number $\widetilde{Bo_{LC}}$ as calculated from Eq. (5.10) and curve fitting of $v^*_{\theta,s}(r^*)$-profile ($R\delta\theta = \delta R \approx 60$ μm). The value of $\widetilde{Bo_{LC}}$ is clearly underestimated since a (linear) Couette v^*_θ-profile is assumed all along the vertical direction.

law (5.13) delivers an order of magnitude ($\lambda_{eff} \approx 10^{-13}$ N) in fair agreement with existing literature, [16, 186].

Paying close attention to Fig. 5.5, the mean diameter and, correlatively, the number density are found to exhibit a jump around the critical angular velocity $\Omega = 0.15$ rpm. As an attempt to interpret this phenomenon, it can be interesting to mention the possible instability of a condensed domain. From the motion of a Langmuir barrier, Lee & McConnell [98] demonstrated how an increase in surface pressure, even small, can be capable of altering the value of $\dfrac{\lambda}{{\mu_{LC/LE}}^2}$, bringing about n-fold harmonic shape disturbances beyond the equilibrium radius. In our experiments, the moving Langmuir barrier of Lee & McConnell can be seen as virtually replaced by radially inwards surface flow which allows us to monitor accurately dynamical surface pressure, Π_d. From the scaling law (C.6) established for the radial velocity along the liquid surface, it is easy to show how Π_d is monitored by the angular velocity of the rotating floor Ω,

$$\Pi_d \sim \rho_s v_r^2 \sim \rho_s \left\{ \frac{r_o \left[\Omega \, h/2\right]^2}{\nu_b} \right\}^2 , \tag{5.14}$$

where the surface mass density writes

$$\rho_s = \frac{M_{PDA}}{A \, \mathcal{N}_\mathcal{A}}.$$

When increasing Π_d, it is also possible to scan sequentially the n-fold harmonic modes found by Lee & McConnell [98]. In our case, shearing as being superimposed to surface pressure plays a key role in the sense that it could break up the ligaments caused by the linear instability of the LC domains.

At the time being, we have no doubt about the importance of balance between a significant mesoscopic surface shear and a reduced effective line tension. The remaining question is to decide if the last scenario based on shape instabilities would apply as well, a point which warrants further investigation.

The experiments demonstrate clearly how the joint use of a shear flow and a centripetal surface flow yields atomization of the LC domains and subsequent reorganization of the LM at mesoscale. The subsequent patterning reveals to be original and increasingly structured with a regular matrix of mono-dispersed LC domains whose typical size becomes smaller and smaller as long as the flow-induced surface compression grows up.

5.2.2 High molecular packing and stratified flow

When the PDA monolayer is subjected to a significant shear flow, the original thermodynamical equilibrium is definitely broken. Under the effect of the flow, the LE to LC transition expands down to lower molecular areas after the monolayer has reached a new steady regime (time delay as long as 15 h). A close inspection to Figs. 4.5, 4.6 and 4.15, shows that the imposition of a flow makes the LE–LC transition to end below $A = 13$ Å^2·molecule^{-1}. The small but non negligible solubility of PDA in the underlying subphase during the time necessary to achieve steady regime is a natural explanation of the LE–LC transition enlargement.

The fact that the condensed phase self-assemblies as stratifying monolayers, is interestingly correlated to a large enough level of densification (Fig. 5.8 for $h = 4$ mm and for $r^* \cong 0.714$, $h = 7$ mm, see also Fig. 5.9). As clearly observed on the BAM images, the LC domains behave as ligaments which, under shear, are stretching along

the azimuthal direction with a larger and larger surface concentration ($\Gamma \equiv \frac{1}{A}$), or equivalently, a smaller and smaller molecular area A ($A < 26$ Å^2·molecule^{-1}). This time, with a high packing density and the subsequent growing destabilizing influence of the long range dipolar forces, the LC domains leave their circular (cohesive) shape and elongate themselves provided the shear stress is large enough. This reorganization of the Langmuir foam can therefore be attributed to a larger value of $Ca_{LC,s}$ and $Bo_{LC,s}$ defined by (5.9) and (5.8).

For $h = 4$ mm in Fig. 5.8, the value of $\overline{\alpha^{AF}}$ is relatively high. Once Ω increases, the condensed phase break up effectively and this is illustrated by a significant decrease of the $\overline{\alpha^{AF}}$ level and the arising of a radial slope on the $\overline{\alpha^{AF}}$ profile (see Fig. 5.9 for $h = 4$ mm). Figures. 5.8 and 5.9 also exhibit a stratified surface flow where the LE phase is organizing according to channels managed between LC ligaments aligned with the main flow direction. The formation of these channels drive to minimize the shear-induced deformation of the LC domains since, in this way, their typical cross-line effectively submitted to a differential shear is drastically reduced.

It is also interesting to point out the presence of an intermediate regime for which the differential shear, whatever its origin, is large enough to stretch the LC domains, against the resistive effect of the effective line tension, while it is not large enough to break them definitely (atomization process).

For a highly densified LM ($A = 15$ Å^2·molecule^{-1}), Fig. 5.4 clearly demonstrates the need to couple both the effect of a small subphase depth ($h = 4$ mm) and the condition of a large rotation speed ($\Omega = 0.206$ rpm) in order to recover a radial slope on the $\overline{\alpha^{AF}}$ profile. The ability of the subsequent shear in breaking up the LC domains is more and more pronounced moving from left to right along the liquid surface.

Of great interest here is the unexpected trend of $\overline{\alpha^{AF}}$ at $h = 4$ mm when Ω is increased (compare Figs. 5.8 and 5.9). When the depth h decreases, the value of $v_{\theta,s}$ increases, approaching the linear velocity profile along the rotating floor. Down to $A = 15$ Å^2·molecule^{-1}, the shear from the bulk is not sufficient to break up large LC

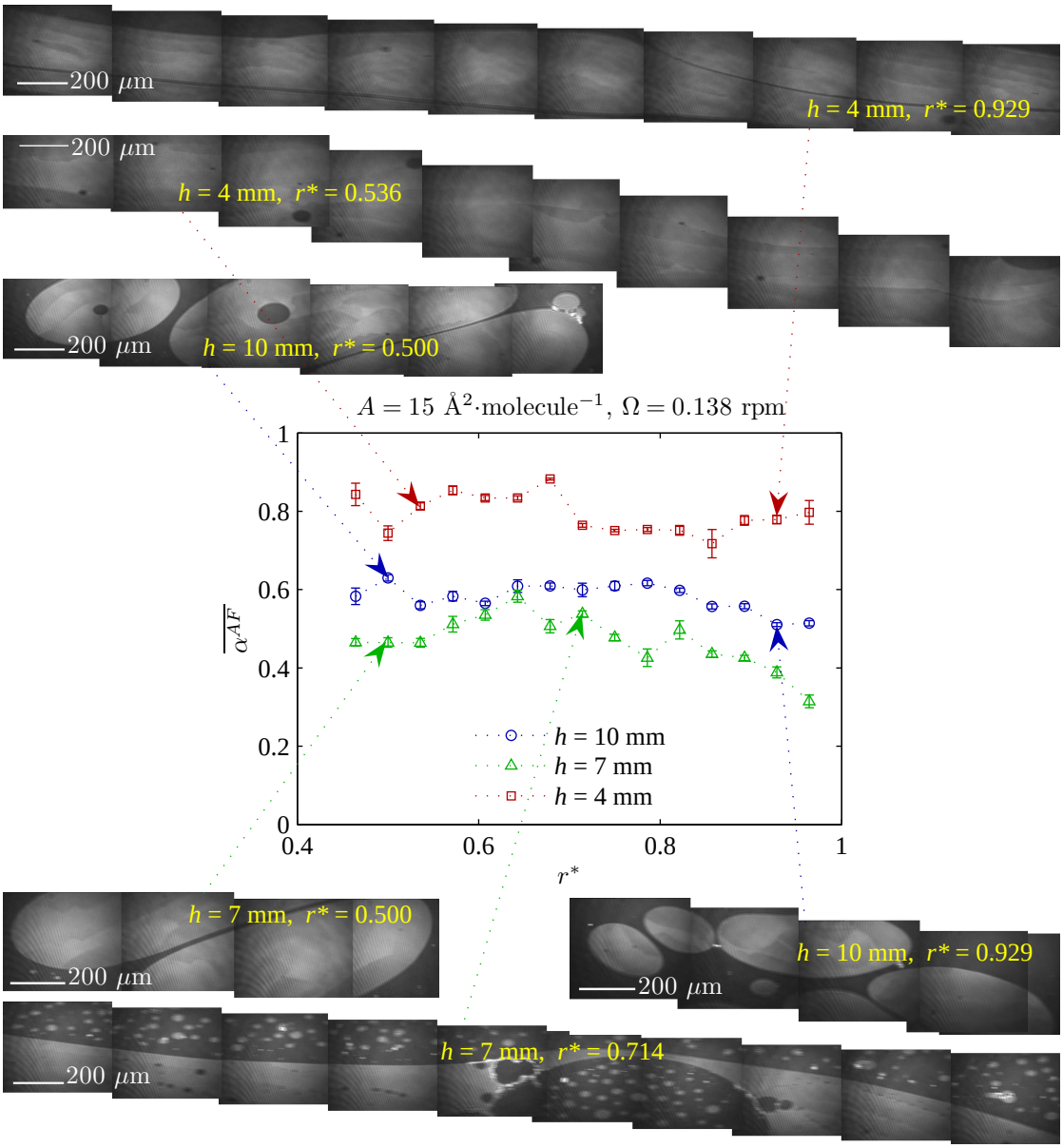

Figure 5.8. Radial distribution of $\overline{\alpha^{AF}}$ for $A = 15$ Å^2·molecule^{-1} and $\Omega = 0.138$ rpm with typical BAM snapshots. Inner and outer side walls are located at the top and bottom of all snapshots and the flow direction is from right- to left-hand sides.

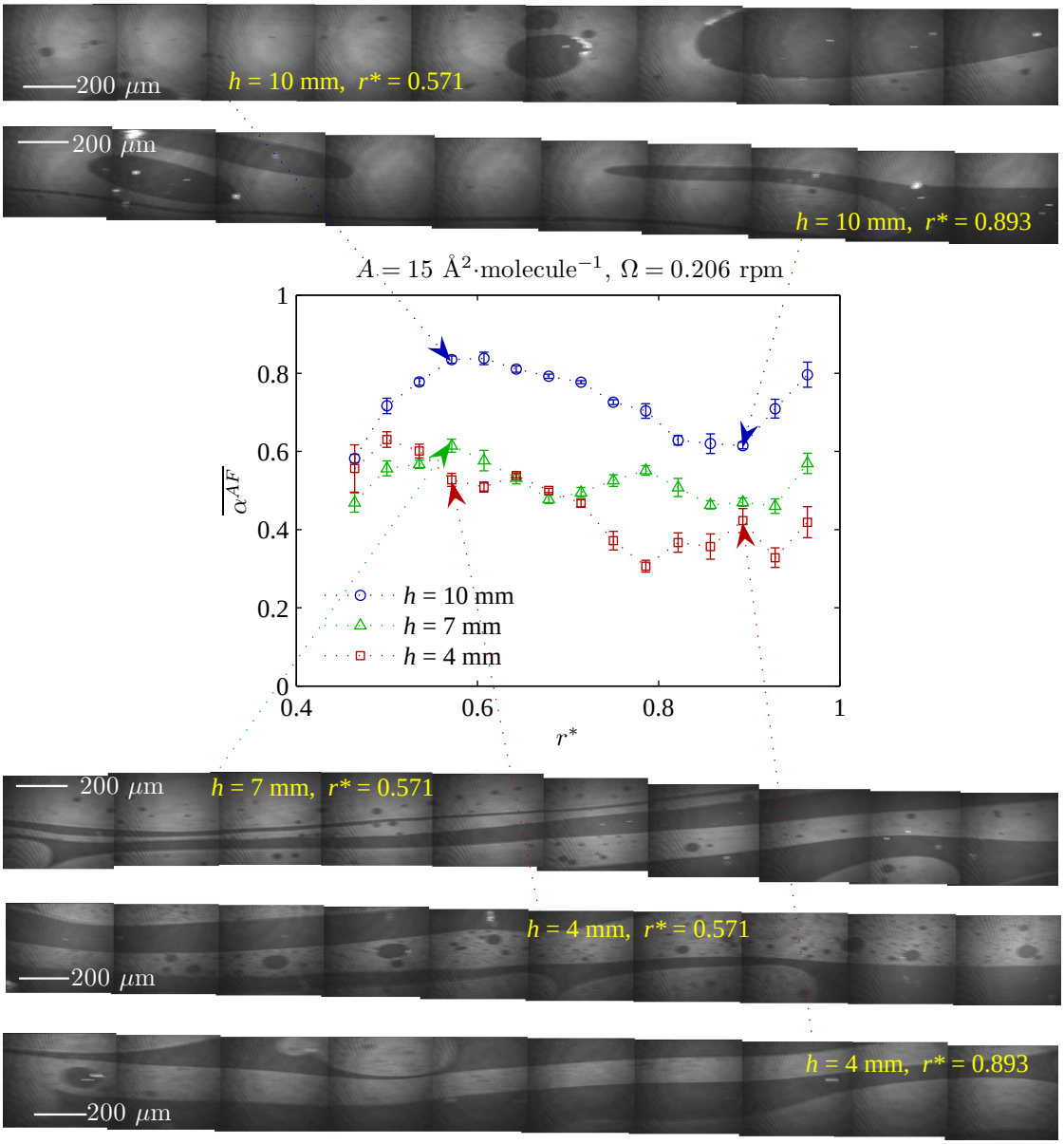

Figure 5.9. Radial distribution of $\overline{\alpha^{AF}}$ for $A = 15$ Å^2·molecule^{-1} and $\Omega = 0.206$ rpm with typical BAM snapshots. Inner and outer side walls are located at the top and bottom of all snapshots and the flow direction is from right- to left-hand sides.

domains unless one increases Ω to provide again a larger shear. As shown in Fig. 5.9, for $h = 4$ mm, the shear stress imposed by the subphase at the surface, $\tau_b|_s$, is large enough so that LC domains are stretched and gives rise to stripe-shaped LC domains. Therefore, the value of $\overline{\alpha^{AF}}$ at $h = 4$ exhibits a level lower than the one for the two larger depths and recovers in this way the classical trend already observed with a low enough surface concentration (dispersed regimes).

5.2.3 LC domains fragmentation at a larger *Re* number

Recently, Hirsa *et al.* [72] investigated the effect of a very inertial shear flow on the mesoscale structure of a LM made from vitamin K1. They considered a very inertial rotating flow ($Re = 1000$) just below the level from which it becomes unstable. Despite the absence of an inner wall in their experimental geometry, one expects that in our experiments, PDA LM reorganization induced by a highly inertial rotating flow is expected to share similar properties as regards its final mesoscale structure. Therefore, we also set $Re = 1000$ with a depth $h = 4$ mm and a molecular area $A = 15$ Å^2·molecule^{-1}. Figure 5.10 displays BAM snapshots obtained by scanning the microscope radially outwards along the channel gap.

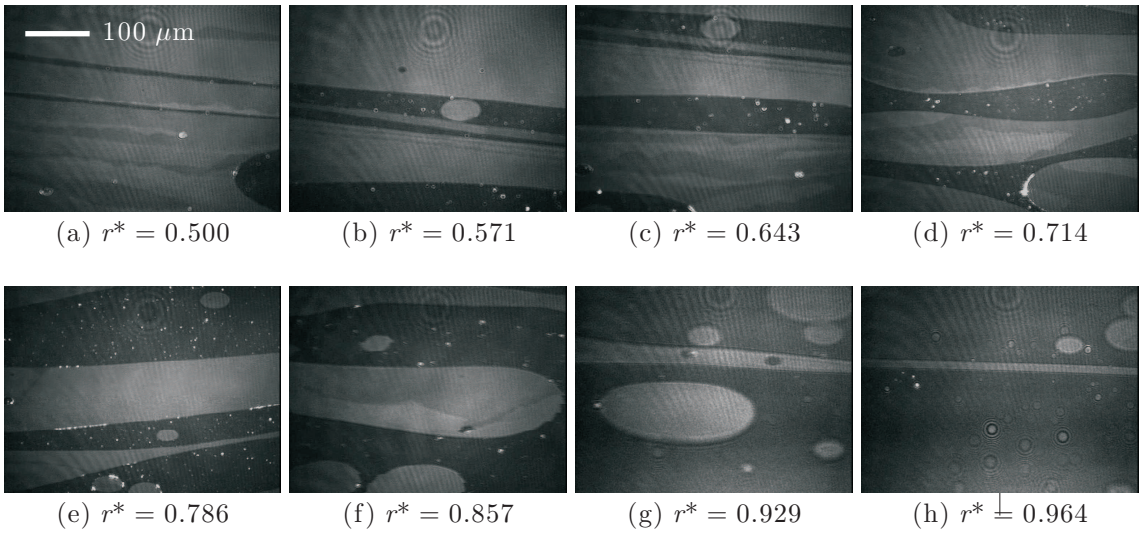

(a) $r^* = 0.500$ (b) $r^* = 0.571$ (c) $r^* = 0.643$ (d) $r^* = 0.714$

(e) $r^* = 0.786$ (f) $r^* = 0.857$ (g) $r^* = 0.929$ (h) $r^* = 0.964$

Figure 5.10. A collection of BAM snapshots along the channel gap and structure of the LC domains for a large Reynolds number ($Re = 1000$), a small depth ($h = 4$ mm) and a highly densified foam ($A = 15$ Å^2·molecule^{-1}).

Due to technical limitations[3], the BAM snapshots are triggered after the permanent flow of the PDA film was stopped (about 15 h after the start of the flow). Much attention was paid to check that the radial organization of the PDA film did not change significantly when the flow was temporarily stopped.

As the surface is scanned, stretching of the domains associated with wall regions of the interface with larger shear can be made evident as shown in Figs. 5.10 (b), (c), (d), and (e). Figure 5.10 also shows a reduction in the average coverage of the LC phase domains at larger radii. These phenomena were also demonstrated by Hirsa *et al.* [72]. This can be seen also from the radial gradient of area fraction of LC phase.

The physical mechanisms responsible for the arising of a radial gradient of $\overline{\alpha^{AF}}$ must be distinguished according to whether the molecular packing is high (small molecular area: $A \approx 10$ to 20 Å^2·molecule^{-1}) or low (large molecular area: $A \approx 20$ to 30 Å^2·molecule^{-1}).

For a large A (Fig. 5.2), LC phase domains are dispersed and free to migrate away from the wall. In complement, molecular packing due to radial convective flow along the surface is the prior mechanism which contributes to maintain a significant radial gradient of $\overline{\alpha^{AF}}$ over the channel gap but outside of the wall bounded shear regions.

Here, these mechanisms no longer hold as the PDA foam is highly densified with a molecular area as small as $A = 15$ Å^2·molecule^{-1}. The rotation speed of the channel floor is set to $\Omega = 3.4$ rpm so as to get $Re = 1000$. The smallest depth $h = 4$ mm is chosen in order to achieve the maximum shear from the bulk. As shown in Fig. 5.10, the shear-induced stretching of the LC domains is more and more pronounced while moving towards larger and larger radii. The application of a sufficiently large shear rate drives to highly elongated slender LC domains with rounded ends: a typical shape distortion often referred to as bolas-shaped condensed domains [16]. By attaining a thread-like shape in their mid-part, the LC domains eventually break up into much

[3]To avoid blurring, imaging of inertial flows usually requires a small time aperture of the camera sensor. In our experiments, the low level of sensitivity of the BAM camera and the limited power of the laser source (no more than 50 mW) prevent us to image the LM at very high Re flows.

smaller domains which recover their circular shape under the effect of the excess line tension (see e.g. Figs. 5.10 (f) to (h)). As mentioned by [72], this shear-induced fragmentation justifies the area reduction of the LC domains along the transverse direction made evident in our experiment from the radial gradient of the area fraction $\overline{\alpha^{AF}}$.

5.3 Concluding remarks

The impact of a laminar annular flow at a moderate Reynolds number ($Re \approx 10$ to 100) upon the steady structure of a dispersed LM made with coexisting LE–LC phases of PDA is investigated in this chapter. The shear stress from the subphase can be estimated by assuming a Couette profile and the surface shear stress can be calculated from the experimental profile of the velocity along the surface. Both of them are compared to a typical value of the effective line tension between coexisting phases.

Due to the rotation of the channel floor, a weak centrifugal flow, responsible for a centripetal transport of the surfactants along the surface, is found to play a significant role when the PDA monolayer is dispersed. Above a given level of centrifugation, for a low enough molecular density ($A \approx 30$ Å^2·molecule^{-1}), a new morphological transition is found during which the two-phase monolayer shifts to a finely divided mesoscopic morphology of LC domains. The combined impact of surface shearing and reducing in the effective line tension is proposed as being responsible for such a transition. Under the effect of the centrifugal flow, the dynamic surface pressure rises up to a level high enough to reduce significantly the effective line tension. Consequently, the condensed domains can be considered as literally shear-induced melted above a critical Reynolds number, $Re \approx 50$. One of the main experimental result of this chapter is that, unlike existing literature devoted to inertial regime ($Re \approx 100$ to 1000, [72]), when the Reynolds number remains moderate ($Re \approx 10$ to 100), the balance between the effective line tension and the surface shear (not the subphase shear) is found to control

the size of the condensed domains. An original[4] consequence is that the mesoscopic Boussinesq number, $\widetilde{Bo_{LC}}$, is found to be at least of order unity, which means that from the uniformly dispersed regime to the morphological transition included, the distribution of surface shear must be taken into account when interpreting the size reduction of the condensed domains.

Above a given level of surface concentration, the monolayer is no longer dispersed and becomes stratified. The corresponding flattening of the Π–A isotherm suggests that Marangoni effect become vanishingly small. Accordingly, the area fraction distribution is found uniform. The condensed domains behave as stripes elongated along the shear flow. These condensed stripes break up if the shear stress from the bulk is large enough (small depth of the channel, larger Reynolds numbers). It is only in this situation that some of typical results of the literature are recovered with, for instance, bola-shaped condensed domains and a non uniform radial distribution of the area fraction induced by the radial distribution of the shear stress.

[4]Unlike existing literature [72, 110], here, at mesoscale, the shear along the surface contributes more than the shear from the subphase in regard to the capability to distort the inclusions (see $\widetilde{Bo_{LC}}$-profile in Fig. 5.7). This is especially true at the vicinity of the side walls (Fig. 5.7). This is also right all along the liquid surface since the magnitude of $\tau_b|_s$ is clearly overvalued from Eq. (5.12) based on Couette assumption (a point which can be checked in the following chapter).

Chapter 6

Analytical modeling of a floor-driven shallow flow

6.1 Introduction: the state of the art

This chapter focuses on the long term application of this dissertation: the recognition of the primary structure of a protein from the growth of a 2-D crystal of this protein at a chemically functionalised Langmuir monolayer (LM). As a matter of fact, the annular shear flow can reveal itself to be relevant to the growth of a two-dimensional (2-D) crystal of protein along an air-water interface covered by a monolayer of lipids [30]. The protein of interest, introduced within aqueous buffer, is free to move under molecular diffusion up to the lipids staying over the liquid surface. Due to relevant chemical affinity, a binding between protein and lipids allows the protein to be trapped at the liquid surface and to move along it in a 2-D way. Under quiescent condition, 2-D molecular diffusion along the liquid surface is responsible for the growth of a 2-D self-assembly of proteins whose structure resembles to a crystalline powder. This 2-D crystalline powder does not really lend itself to the accurate determination of the protein structure from X-ray diffraction [99]. Consequently, it is necessary to improve the spatial periodicity of the 2-D self-assembly. As an attempt to find a solution, the use

of a surface flow to assist the growth of a protein self-assembly along a lipidic monolayer was originally proposed by Drazek *et al.* [39]. These authors proposed to use an annular trough in which a shear flow is generated by the rotation of a ring along its floor. Quite recently, Hirsa and co-workers [10] seem to be successful in implementing this idea with the characterization of a model protein (streptavidin).

The flow conditions (centrifugal flow and annular shear flow) are sought to promote the directed growth of a 2-D crystal of protein at a lipidic monolayer spread over a water bath. Here again, the boundary condition at the interface is mixed: the left side of the liquid surface is expected to be rigid where the 2-D crystal is staying while remaining fluid elsewhere (gaseous, expanded or condensed phases). The application briefly described above involves a one-dimensional stratification of surface contamination that can be also investigated under Brewster angle microscope (BAM).

Under the impact of surface flow focusing, proteins can be expected to condense towards smallest radii (radially-inwards molecular packing) in a way similar to the LC domains in the previous chapter. It should be therefore possible to promote the arising of a one-dimensional crystalline front [39, 10]. At the same time, a radial stratification of surface viscosity must be taken into account in order to explain the experimental distribution of the velocity along the surface.

This chapter addresses the crystal growth process proposed in [39], also considered recently in [10]. The analytical formulation developed in this chapter is expected to fit efficiently the annular velocity profile modified by a non-uniform distribution of surface viscosity. As such, it is expected to facilitate the macroscopic characterizations of a condensed patch of biomolecules trapped at a chemically-functionalized liquid surface.

6.2 Outlines of this chapter

The geometry of the annular channel complies with some biochemical and microfluidics requirements. Nowadays, any end-user of a surface viscometer has to cope

with small amounts of biomolecules (lipids, deoxyribonucleic acid (DNA) strands, antigenes, antibodies, proteins, etc.) because either the purchase price of biomolecules is expensive or, their extraction from rough biological samples is time-consuming. The geometry of our system (Fig. 6.1) permits to handle small amounts because the channel flow is annular and shallow. In other words, the aspect ratio, $\delta = \frac{h}{r_o}$, must be considered as small as possible (depth of the channel, h, much smaller than its outer radius, r_o).

All along this chapter (except in Appendix D), the liquid subphase is therefore confined within an annular channel whose two side walls (inner radius: r_i, outer radius: r_o) are maintained stationary (see Fig. 6.1). Note that in Appendix D, one can find the derivation of the surface flow for a full cylinder ($r_i \to 0$) since this geometry is also widespread in biochemical applications. The annular floor of the channel is put in slow rotation in such a way that an annular (azimuthal) shear flow is supplied at a small Reynolds number, defined as Eq. (4.4).

From our modeling of the annular floor-driven flow, the first objective of this chapter is to put forward a closed-form analytical expression of the shear stress at (and along) a contaminated surface and therefore to deliver a fairly good estimation of the Boussinesq number as compared to its definition in the literature which is basically founded on elementary scaling analysis (see Eq. (6.8)). This prior objective is typically relevant to the understanding of line tension and phases organization during flow-induced reorganization of Langmuir monolayers [110, 32]. Our second objective is a measurement one; this is to get at one disposal a simple analytical model devoted to quantify a biochemical contamination which departs from uniform conditions with, for instance, the arising of stratifying phases (see e.g. Fig. 4.5 in Chapter 4); each of them being characterized by a different level of molecular packing and therefore by different surface shear viscosities.

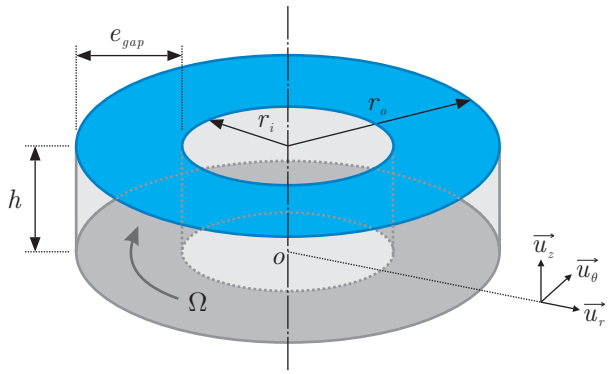

Figure 6.1. Geometry under consideration.

6.2.1 On one particular source of viscous stratification

As already demonstrated in the previous chapter, the rotation of the annular floor is also responsible for a radially outwards (centrifugal) force which gives rise to an additional meridian recirculating flow within the cross-section of the annular channel. The magnitude of it depends on control parameters such as the depth of the channel, the curvature of the channel and also on the Reynolds number. This meridian recirculating flow, as a perturbation of the main annular flow, gives rise to a swirling flow. As demonstrated by Lopez and co-workers from direct numerical simulation (DNS) [71], a Reynolds number as large as $Re \approx 1000$ is necessary to modify significantly the basic shear flow calculated from Stokes approximation.

Previous experiments, carried out at a moderate Re ($Re < 100$), have confirmed this statement: the recirculating flow gives rise to a radially inwards packing of amphiphilic molecules along the liquid surface while it does not modify the azimuthal component of the velocity along the surface [32]). This flow-induced packing of surfactants generates first, a stratified surface viscosity; and second, a surface tension gradient (Marangoni effect) which is mostly balanced by a viscous stress at the liquid surface (consider the radial component of the jump momentum balance at the interface [156]).

This chapter focuses on the modeling of the shear velocity along the liquid surface

in presence of a stratified surface viscosity. To do this, the mathematical model we solved is the azimuthal component of the jump momentum balance at the interface strongly coupled to the annular shear flow of the underlying subphase.

6.2.2 Assumptions and aims

The Reynolds number is considered small or at least moderate ($Re < 100$) so that use is made of the Stokes approximation when calculating the azimuthal velocity along the surface.

The first part of this chapter focuses on the situation of a uniform surface contamination. A matched asymptotic method is developed and a Green function is analytically calculated to find the azimuthal component of surface velocity at leading order. The results are compared with the available literature to validate the calculation of the Green function and to estimate the accuracy level of the leading order.

In the second part of this chapter, as an example relevant to our applications, the situation of a stratified surface contamination is investigated. A nonlinear function is proposed as a constitutive law for the stratified surface viscosity $\mu_s(r)$. On both sides, far from the segregation front, the viscosity is supposed to reach a constant level: a very large shear viscosity on the side of the interface where the more condensed phase is staying (near the small radii) and a small value of surface shear viscosity on the opposite side. By the way, surface velocity profile sensitive to a stratified surface contamination is made evident and hoped to serve as a tool to detect the radial extent of a condensed phase like a 2-D single crystal of protein.

6.3 Mathematical model

The annular shear flow is assumed to be creeping and the azimuthal component of the Stokes' equation is written in a dimensionless way as,

$$\delta^2 \frac{\partial}{\partial r^*}\left[\frac{1}{r^*}\frac{\partial\left[r^* v_\theta^*\right]}{\partial r^*}\right] + \frac{\partial^2 v_\theta^*}{\partial z^{*2}} = 0. \tag{6.1}$$

Here are considered the scales r_o, h and $(r_o\Omega)$ to non-dimensionalize the radial coordinate r, the vertical coordinate z and the azimuthal velocity v_θ, namely:

$$r^* = \frac{r}{r_o},$$
$$z^* = \frac{z}{h},$$
$$v_\theta^* = \frac{v_\theta}{r_o\Omega},$$

with Ω referring to as the angular velocity of the annular rotating floor.

The no-slip boundary conditions (BCs) for the azimuthal velocity must be written along the stationary sidewalls and the rotating floor:

$$v_\theta^*\left(r^* = \frac{r_i}{r_o}, z^*\right) = 0, \tag{6.2}$$

$$v_\theta^*\left(r^* = 1, z^*\right) = 0, \tag{6.3}$$

$$v_\theta^*\left(r^*, z^* = 0\right) = r^*. \tag{6.4}$$

As the last boundary condition (BC), a jump momentum balance at the 2-D interface can be derived from a momentum balance written upon an elementary heterogeneous volume straddling the liquid surface of zero-thickness (Gibbs approach). To model the dependence of surface stress to surface strain, use is made of the Boussinesq-Scriven constitutive law. As a consequence, the (azimuthal) θ-component of the jump momentum balance writes as [156]:

$$\underbrace{\mu_s\left[\frac{d^2 v_{\theta,s}}{dr^2} + \frac{1}{r}\frac{dv_{\theta,s}}{dr} - \frac{v_{\theta,s}}{r^2}\right]}_{\text{2-D viscous shear}} + \underbrace{\frac{d\mu_s}{dr}\left[\frac{dv_{\theta,s}}{dr} - \frac{v_{\theta,s}}{r}\right]}_{\substack{\text{2-D non-uniformity} \\ \text{in shear viscosity}}} = \underbrace{\mu_b \left.\frac{\partial v_\theta\left(r,z\right)}{\partial z}\right|_{z=h}}_{\substack{\text{liquid shear from} \\ \text{underlying subphase}}}. \tag{6.5}$$

The symbols $v_{\theta,s}$, $\mu_s(r)$ and μ_b denote, respectively, the θ component of surface velocity, the distribution of the (excess) shear viscosity of the liquid surface, and the Newtonian (shear) viscosity of the underlying subphase. Here, gaseous shearing above the interface is considered negligible as compared to the liquid shearing. To model the radially inwards accumulation of surfactants and subsequently the r-dependence of surface viscosity, a regular non-uniformity function $g(r^*)$ is introduced which yields an additional contribution to the uniform term of surface viscosity $\overline{\mu_s}$. If this last quantity is chosen to be the scale for the surface viscosity, then a constitutive law for the dimensionless surface viscosity can be written as:

$$\mu_s^*(r^*) = \frac{\mu_s(r)}{\overline{\mu_s}} = 1 + g(r^*). \tag{6.6}$$

Hence, if $g(r^*)$ vanishes, the situation of a uniform surface viscosity is recovered with $\mu_s(r) = \overline{\mu_s}$ or $\mu_s^*(r^*) = 1$, equivalently. Considering Eq. (6.6), BC (6.5) is now written in a non-dimensional way according to the following non-homogeneous linear ordinary differential equation (ODE):

$$[1+g(r^*)]\left[\frac{d^2v_{\theta,s}^*}{dr^*2}+\frac{1}{r^*}\frac{dv_{\theta,s}^*}{dr^*}-\frac{v_{\theta,s}^*}{r^{*2}}\right]+\frac{dg\,(r^*)}{dr^*}\left[\frac{dv_{\theta,s}^*}{dr^*}-\frac{v_{\theta,s}^*}{r^*}\right]=\frac{1}{Bo}\left.\frac{\partial v_\theta^*\,(r^*,z^*)}{\partial z^*}\right|_{z^*=1}. \tag{6.7}$$

The symbol Bo represents the Boussinesq number which compares the surface shear to the subphase shear at the vicinity of the interface (Fig. 6.2):

$$Bo \equiv \frac{\overline{\mu_s}\dfrac{v_{\theta,s}}{r_o^2}}{\mu_b\dfrac{v_{\theta,s}}{h}}. \tag{6.8}$$

A very small value of the Boussinesq number Bo indicates that the surface shear does not contribute significantly to subphase hydrodynamics (classical free surface BC recovered). If the Bo number becomes significant - which means here, $Bo \approx 0.001$ or more - a two-way coupling between the surface and subphase flows has to be taken into account.

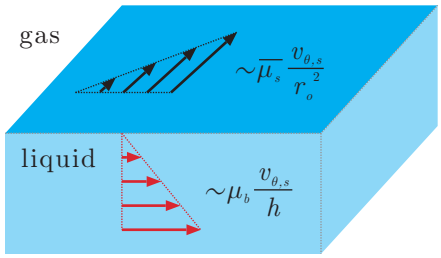

Figure 6.2. The Boussinesq number *Bo* as a ratio of shears.

6.4 Two-way coupling between surface and subphase flows

In the case of a uniform contamination, Mannheimer & Schechter [112] solved the flow in the deep channel viscometer and found the azimuthal velocity as a double series. Due to singularities at the left and right corners of the channel floor (see *e.g.* BCs (6.2) to (6.4)) an abnormal number of eigenvalues (larger than 100) is required to reach a right level of accuracy on the velocity along the liquid surface.

Moreover, for the problem of interest here, the Stokes Eq. (6.1) and its four BCs (6.2), (6.4), (6.3), (6.7) constitute a boundary value problem rather difficult to solve because of the non-linear nature of ODE (6.7) due to surface stratification.

If this problem is tackled as a mixed boundary value problem (only relevant to the particular situation of a singular front induced by surface stratification), one must give up definitely the idea to find a simple solution because dual integral equations are automatically involved (see *e.g.* [58]).

To model the impact of a regular viscous stratification, the working idea developed along this chapter consists of splitting the flow system into two components: a surface flow and a 3-D subphase flow while considering surface velocity $v_{\theta,s}(r)$ as a coupling variable. Accordingly, two coupled mathematical models must be written down for each of them.

6.4.1 Subphase flow

In the liquid subphase, the mathematical model for the azimuthal velocity, $v_\theta^*(r^*, z^*)$, is the Stokes Eq. (6.1) with the Dirichlet BCs (6.2), (6.3), (6.4) completed by the following Dirichlet BC at the upper boundary ($z^* = 1$):

$$v_\theta^*(r^*, z^* = 1) \;=\; v_{\theta,s}^*(r^*)\,. \tag{6.9}$$

As a consequence, the main unknown of interest in this chapter, the surface velocity $v_{\theta,s}^*(r^*)$, stands as a parameter in the expression of the subphase velocity; a point which demonstrates a first (one-way) coupling between first and second sub-systems.

6.4.2 Surface flow

Along the liquid surface, the surface velocity $v_{\theta,s}^*(r^*)$ is the solution of the Boussinesq-Scriven Eq. (6.7) completed by two Dirichlet end-points BCs:

$$v_{\theta,s}^*\left(r^* = \frac{r_i}{r_o}\right) = 0, \tag{6.10}$$

$$v_{\theta,s}^*(r^* = 1) = 0. \tag{6.11}$$

The subphase shear valued at the interface, $\frac{1}{Bo}\left.\frac{\partial v_\theta^*(r^*, z^*)}{\partial z^*}\right|_{z^*=1}$, on the r.h.s. of (6.7), can be interpreted as a forcing term which involves the unknown $v_{\theta,s}^*(r^*)$ *via* the general analytical expression to be found for the subphase velocity $v_\theta^*(r^*, z^*)$. The two-way coupling is therefore illustrated by this forcing term which originates from the contribution of the underlying subphase shear.

Figure (6.3) is illustrated this two-way coupling between surface flow and subphase flow.

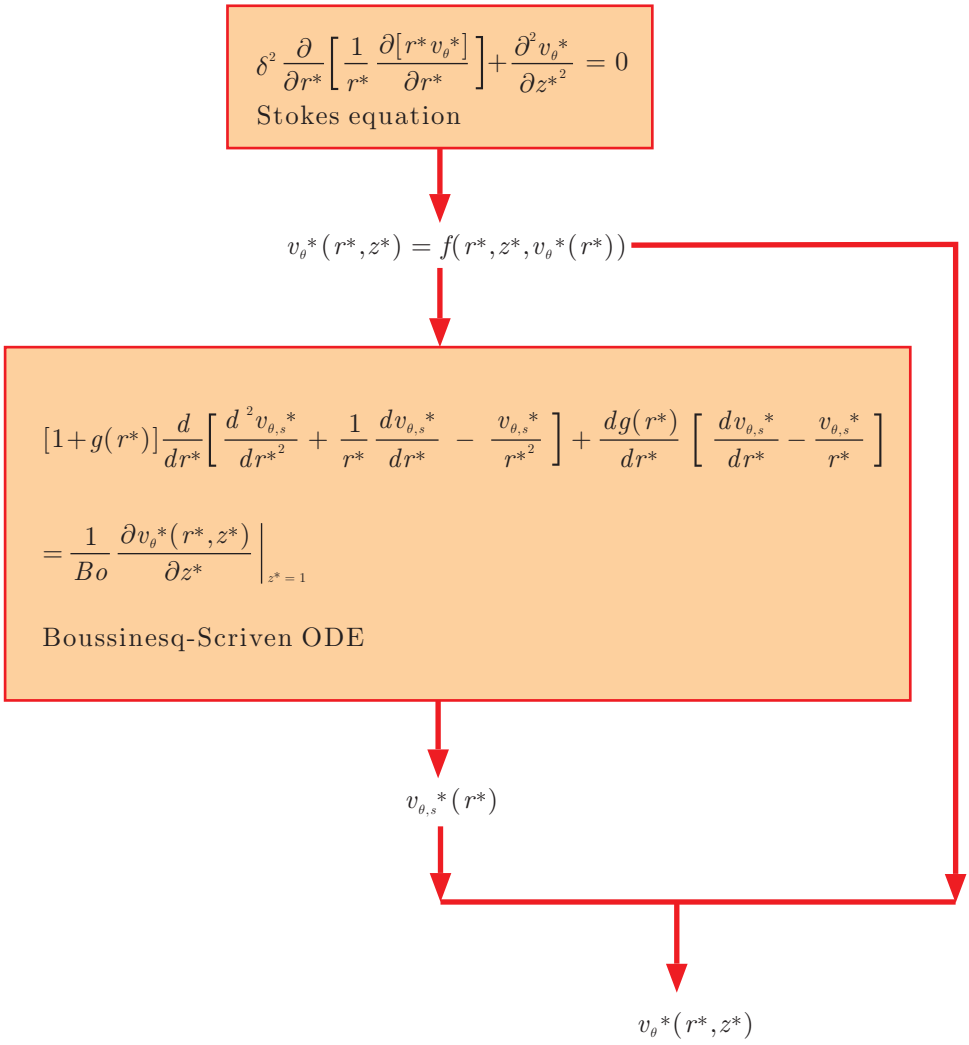

Figure 6.3. Two-way coupling between subphase flow $v_\theta^*(r^*,z^*)$ and surface flow $v_{\theta,s}^*(r^*)$.

6.5 Lubrication approximation

The shallow subphase flow is characterized by a small value of the aspect ratio δ. It is therefore possible to introduce a matched asymptotic technique by distinguishing a core flow, far from the two stationary side walls, from the flow in the boundary layers which develop along both stationary side walls. This asymptotic approach allows us to calculate a core solution without taking into account the no-slip BCs (6.3) and (6.4). In return, the flow of the boundary layers along the side walls must match the core solution far from the side walls while respecting the no-slip BCs (6.3) and (6.4). Finally, the subphase velocity is written as a composite solution derived from the core solution and the two inner solutions calculated within the boundary layers.

Before writing the model for the flow in the boundary layers, the following transformations are introduced [126]:

$$x_i = \frac{r^* - {}^{r_i}\!/_{r_o}}{\delta^\gamma}, \tag{6.12}$$

$$x_o = \frac{1 - r^*}{\delta^\gamma}, \tag{6.13}$$

as usual when making use of lubrication approximation ($\delta \ll 1$). When writing these last expression, use is made of two new length scales physically more significant. Here, the stretching parameter γ is found equal to unity.

The solutions for the azimuthal velocity in the core and the boundary layers along the left and right side walls will be referred to as, respectively, v_θ^{*c} (for the core solution) and $v_\theta^{*i}, v_\theta^{*o}$ (for the inner solutions). These solutions are then expanded as a regular perturbation series in powers of the small aspect ratio δ:

$$v_\theta^{*c} = v_\theta^{*c,0} + \mathcal{O}(\delta), \tag{6.14}$$

$$v_\theta^{*i} = v_\theta^{*i,0} + \mathcal{O}(\delta), \tag{6.15}$$

$$v_\theta^{*o} = v_\theta^{*o,0} + \mathcal{O}(\delta). \tag{6.16}$$

It is important to notice that the Boussinesq-Scriven ODE (6.7) is also linear and coupled to the former perturbation series by way of its forcing term. It is therefore also consistent to introduce the same perturbation series for surface velocity:

$$v^*_{\theta,s} = v^{*0}_{\theta,s}\left(r^*\right) + \mathcal{O}(\delta).$$

6.6 Subphase flow at leading order

6.6.1 Core flow

At leading order, taking into account the perturbation series (6.14), the Stokes' equation (6.1) simplifies to

$$\frac{\partial^2 v^{*c,0}_\theta\left(r^*, z^*\right)}{\partial {z^*}^2} = 0.$$

In the same way, the Dirichlet BCs (6.2) and (6.9) write as:

$$\begin{aligned} v^{*c,0}_\theta\left(r^*, z^* = 0\right) &= r^*, \\ v^{*c,0}_\theta\left(r^*, z^* = 1\right) &= v^{*0}_{\theta,s}\left(r^*\right), \end{aligned} \tag{6.17}$$

and consequently, the core velocity is easily derived as a radially dependent Couette profile:

$$v^{*c,0}_\theta\left(r^*, z^*\right) = \left[v^{*0}_{\theta,s}\left(r^*\right) - r^*\right] z^* + r^*. \tag{6.18}$$

6.6.2 Boundary layer flow

For sake of succinctness, only the calculation for the flow in the boundary layer along the left side wall ($r^* = \frac{r_i}{r_o}$) is given here: a similar calculation can be performed to get in the same way the azimuthal velocity in the boundary layer along the opposite side wall ($r^* = 1$). Taking account of (6.5) and (6.15), the mathematical model (6.1) at leading order writes as:

$$\frac{\partial^2 v^{*i,0}_\theta\left(x_i, z^*\right)}{\partial {x_i}^2} + \frac{\partial^2 v^{*i,0}_\theta\left(x_i, z^*\right)}{\partial {z^*}^2} = 0. \tag{6.19}$$

It has to be completed by the Dirichlet BCs (6.2), (6.3) and (6.9) which write at leading order:

$$v_\theta^{*i,0}\left(x_i = 0, z^*\right) = 0, \tag{6.20}$$

$$v_\theta^{*i,0}\left(x_i, z^* = 0\right) = \frac{r_i}{r_o}, \tag{6.21}$$

$$v_\theta^{*i,0}\left(x_i, z^* = 1\right) = v_{\theta,s}^*\left(\frac{r_i}{r_o} + \delta x_i\right) = v_{\theta,s}^*\left(\frac{r_i}{r_o}\right) = 0. \tag{6.22}$$

To match inner and core solutions, respectively $v_\theta^{*i,0}$ and (6.18), a simple Prandtl matching condition can be invoked [126] since only the leading order is under consideration:

$$\lim_{x_i \to +\infty} v_\theta^{*i,0}\left(x_i, z^*\right) = \lim_{r^* \to \frac{r_i}{r_o}} v_\theta^{*c,0}\left(r^*, z^*\right) = v_\theta^{*i/c,0}, \tag{6.23}$$

with

$$v_\theta^{*i/c,0} = \frac{r_i}{r_o}[1 - z^*],$$

and where use is made of (6.10).

To find the azimuthal velocity $v_\theta^{*i,0}$, it is worth introducing the separated modes s_i and t_i:

$$v_\theta^{*i,0}\left(x_i, z^*\right) = \sum_{n \in \mathbb{N}^*} s_n\left(x_i\right)\, t_n\left(z^*\right) + a\, x_i + b\, z^* + c, \tag{6.24}$$

with the following eigenvalues problem:

$$\forall n \in \mathbb{N}^*,\, \exists\, \omega_n \in \mathbb{R}^+ \text{ such as } \begin{cases} s_n''\left(x_i\right) - \omega_n^2\, s_n\left(x_i\right) = 0, \\ \\ t_n''\left(z^*\right) + \omega_n^2\, t_n\left(z^*\right) = 0. \end{cases}$$

Both the matching condition (6.23) and the Dirichlet BC (6.21) permit to simplify efficiently the general expression (6.24) while the Dirichlet BC (6.22) allows for finding the eigenvalue ω_n. Finally, the last Dirichlet BC (6.20) is taken into account during the vertical integration of the velocity performed to invoke the orthogonality of mode $t_n(z^*)$. By making use of (6.5), it can be demonstrated that the series for the azimuthal

velocity,

$$v_\theta^{*i,0}\left(r^*,z^*\right) = -2\,\frac{r_i}{r_o}\sum_{n\in\mathbb{N}^*}\frac{\sin\left(n\,\pi\,z^*\right)}{n\,\pi}\,\exp\left(-n\,\pi\,\frac{r^*-{}^{r_i}\!/_{r_o}}{\delta}\right)+\frac{r_i}{r_o}\left[1-z^*\right]. \tag{6.25}$$

satisfies the transport Eq. (6.19).

Same ideas strictly apply when calculating the leading order of the inner solution for the boundary layer flow along the right side wall:

$$v_\theta^{*o,0}\left(r^*,z^*\right) = -2\sum_{n\in\mathbb{N}^*}\frac{\sin\left(n\,\pi\,z^*\right)}{n\,\pi}\exp\left(-n\,\pi\,\frac{1-r^*}{\delta}\right)+\left[1-z^*\right]. \tag{6.26}$$

A first composite solution, supposed to hold for both a half part of the core and the left boundary layer ($r^* < \dfrac{r_i+r_o}{2r_o}$), is built according to matched asymptotic analysis [126]:

$$v_\theta^{*i,0}+v_\theta^{*c,0}-v_\theta^{*i/c,0}.$$

A second composite solution, supposed to hold for both the second half part of the core and the right boundary layer ($r^* > \dfrac{r_i+r_o}{2r_o}$), is found to be:

$$v_\theta^{*o,0}+v_\theta^{*c,0}-v_\theta^{*o/c,0},$$

with

$$v_\theta^{*o/c,0} = 1-z^*.$$

An overall composite solution for the azimuthal velocity is built as the sum of the left and right composite solutions to which is subtracted the core solution $v_\theta^{*c,0}$:

$$v_\theta^{*i,0}-v_\theta^{*i/c,0}+v_\theta^{*o,0}-v_\theta^{*o/c,0}+v_\theta^{*c,0}.$$

Finally, the leading order approximation for the azimuthal velocity in the liquid subphase writes explicitly as:

$$\begin{aligned} v_\theta^{*0}\left(r^*,z^*\right) = &\left[v_{\theta,s}^*\left(r^*\right)-r^*\right]z^*+r^* \\ &-2\sum_{n=1}^{\infty}\frac{\sin\left(n\,\pi\,z^*\right)}{n\,\pi}\left[\exp\left(-n\,\pi\,\frac{1-r^*}{\delta}\right)+\frac{r_i}{r_o}\,\exp\left(-n\,\pi\,\frac{r^*-{}^{r_i}\!/_{r_o}}{\delta}\right)\right]. \end{aligned} \tag{6.27}$$

6.7 Surface flow at leading order

As already mentioned, the ODE (6.7) for the surface motion is coupled to the underlying subphase flow by means of the forcing term:

$$\frac{1}{Bo}\left.\frac{\partial v_\theta^{*0}\left(r^*,z^*\right)}{\partial z^*}\right|_{z^*=1}.$$

Considering the solution (6.27) for the subphase velocity at leading order and given a radial location, it is evident that without the correction due to the shear boundary layers along the stationary side walls, the surface should be sollicitated by a shear typical of a Couette subphase flow.

Since Eq. (6.7) is linear, it is consistent to seek the associated leading order approximation for the surface azimuthal velocity $v_{\theta,s}^{*0}\left(r^*,z^*\right)$; the forcing term $\left.\frac{1}{Bo}\frac{\partial v_\theta^{*0}\left(r^*,z^*\right)}{\partial z^*}\right|_{z^*=1}$ being under consideration. The series $\sum_{n=1}^{\infty} u_n\left(z^*\right)$, with

$$u_n=\sum_{n=1}^{\infty}\frac{\sin\left(n\,\pi\,z^*\right)}{n\,\pi}\left[\exp\left(-n\,\pi\,\frac{1-r^*}{\delta}\right),\ \exp\left(-n\,\pi\,\frac{r^*-r_i/r_o}{\delta}\right)\right],$$

is found to be currently involved in the expression (6.27) for $v_\theta^{*0}\left(r^*,z^*\right)$. This series fills all the derivability conditions whatever the value of the radial coordinate. The forcing term $\left.\frac{1}{Bo}\frac{\partial v_\theta^{*0}\left(r^*,z^*\right)}{\partial z^*}\right|_{z^*=1}$ can thus be valued at the vicinity of the interface and doing that, it is easy to check that when $n\to\infty$, the dimensionless shear stress at the liquid surface tends uniformly to the closed-form analytical expression:

$$\begin{aligned}\tau_{b,comp}^*&=\left.\frac{\partial v_\theta^{*0}\left(r^*,z^*\right)}{\partial z^*}\right|_{z^*=1}\\&=v_s^*(r^*)-r^*+2\,\frac{\exp\left(-\pi\,\dfrac{1-r^*}{\delta}\right)}{1+\exp\left(-\pi\,\dfrac{1-r^*}{\delta}\right)}+2\,\frac{r_i}{r_o}\,\frac{\exp\left(-\pi\,\dfrac{r^*-r_i/r_o}{\delta}\right)}{1+\exp\left(-\pi\,\dfrac{r^*-r_i/r_o}{\delta}\right)}.\end{aligned}\tag{6.28}$$

6.8 The case of a uniform surface viscosity

Because this chapter focuses on the leading order, there is no longer any reason to distinguish the notations $v_{\theta,s}^*\left(r^*\right)$ and $v_{\theta,s}^{*0}\left(r^*\right)$. If the surface viscosity is considered as

uniform, the mathematical model for the surface flow simplifies according to:

$$Bo\left[\frac{d^2v^*_{\theta,s}}{dr^{*2}}+\frac{1}{r^*}\frac{dv^*_{\theta,s}}{dr^*}-\frac{v^*_{\theta,s}}{r^{*2}}\right]=\left.\frac{\partial v^{*0}_{\theta}\left(r^*,z^*\right)}{\partial z^*}\right|_{z^*=1}, \tag{6.29}$$

with two Dirichlet end-points BCs:

$$v^*_{\theta,s}\left(r^*=\frac{r_i}{r_o}\right)=0, \tag{6.30}$$

$$v^*_{\theta,s}\left(r^*=1\right)=0. \tag{6.31}$$

Introducing the forcing function f,

$$f(r^*)\;=\;-r^*+2\,\frac{\exp\left(-\pi\dfrac{1-r^*}{\delta}\right)}{1+\exp\left(-\pi\dfrac{1-r^*}{\delta}\right)}+2\,\frac{r_i}{r_o}\,\frac{\exp\left(-\pi\dfrac{r^*-{r_i}/{r_o}}{\delta}\right)}{1+\exp\left(-\pi\dfrac{r^*-{r_i}/{r_o}}{\delta}\right)}, \tag{6.32}$$

Equation (6.29) becomes:

$$Bo\left[\frac{d^2v^*_{\theta,s}}{dr^{*2}}+\frac{1}{r^*}\frac{dv^*_{\theta,s}}{dr^*}-\frac{v^*_{\theta,s}}{r^{*2}}\right]-v^*_{\theta,s}=f\left(r^*\right), \tag{6.33}$$

To solve the two end-points boundary value problem (6.31)-(6.30)-(6.33), it is worthwhile to introduce the Green function $G(r^*|\xi)$ (ξ denotes the influence variable) associated to the differential operator $\Im$:

$$\Im\equiv Bo\left[\frac{d^2}{d\xi^2}+\frac{1}{\xi}\frac{d}{d\xi}-\frac{1}{\xi^2}\right]-1.$$

6.8.1 Calculation of the Green function for the operator $\Im$

Making use of mathematical arguments (see *e.g.* [159]), and after simple but tedious calculations, the Green function $G(r^*|\xi)$ is found to be the following piecewise function:

$$G(r^*|\xi)\;=\;\begin{cases} A(r^*)\,\xi\,I_1\left(\dfrac{\xi}{\sqrt{Bo}}\right)+B(r^*)\,\xi\,K_1\left(\dfrac{\xi}{\sqrt{Bo}}\right) & \text{if } \xi\in\left[\frac{r_i}{r_o},r^*\right], \\ C(r^*)\,\xi\,I_1\left(\dfrac{\xi}{\sqrt{Bo}}\right)+D(r^*)\,\xi\,K_1\left(\dfrac{\xi}{\sqrt{Bo}}\right) & \text{if } \xi\in[r^*,1], \end{cases} \tag{6.34}$$

where the coefficients $A(r^*)$, $B(r^*)$, $C(r^*)$ and $D(r^*)$ write as:

$$A(r^*) = \frac{1}{Bo} K_1\left(\frac{1}{\sqrt{Bo}}\frac{r_i}{r_o}\right) \frac{I_1\left(\frac{r^*}{\sqrt{Bo}}\right) K_1\left(\frac{1}{\sqrt{Bo}}\right) - I_1\left(\frac{1}{\sqrt{Bo}}\right) K_1\left(\frac{r^*}{\sqrt{Bo}}\right)}{I_1\left(\frac{1}{\sqrt{Bo}}\right) K_1\left(\frac{1}{\sqrt{Bo}}\frac{r_i}{r_o}\right) - I_1\left(\frac{1}{\sqrt{Bo}}\frac{r_i}{r_o}\right) K_1\left(\frac{1}{\sqrt{Bo}}\right)}, \tag{6.35}$$

$$B(r^*) = -\frac{1}{Bo} I_1\left(\frac{1}{\sqrt{Bo}}\frac{r_i}{r_o}\right) \frac{I_1\left(\frac{r^*}{\sqrt{Bo}}\right) K_1\left(\frac{1}{\sqrt{Bo}}\right) - I_1\left(\frac{1}{\sqrt{Bo}}\right) K_1\left(\frac{r^*}{\sqrt{Bo}}\right)}{I_1\left(\frac{1}{\sqrt{Bo}}\right) K_1\left(\frac{1}{\sqrt{Bo}}\frac{r_i}{r_o}\right) - I_1\left(\frac{1}{\sqrt{Bo}}\frac{r_i}{r_o}\right) K_1\left(\frac{1}{\sqrt{Bo}}\right)}, \tag{6.36}$$

$$C(r^*) = \frac{1}{Bo} K_1\left(\frac{1}{\sqrt{Bo}}\right) \frac{I_1\left(\frac{r^*}{\sqrt{Bo}}\right) K_1\left(\frac{1}{\sqrt{Bo}}\frac{r_i}{r_o}\right) - I_1\left(\frac{1}{\sqrt{Bo}}\frac{r_i}{r_o}\right) K_1\left(\frac{r^*}{\sqrt{Bo}}\right)}{I_1\left(\frac{1}{\sqrt{Bo}}\right) K_1\left(\frac{1}{\sqrt{Bo}}\frac{r_i}{r_o}\right) - I_1\left(\frac{1}{\sqrt{Bo}}\frac{r_i}{r_o}\right) K_1\left(\frac{1}{\sqrt{Bo}}\right)}, \tag{6.37}$$

$$D(r^*) = -\frac{1}{Bo} I_1\left(\frac{1}{\sqrt{Bo}}\right) \frac{I_1\left(\frac{r^*}{\sqrt{Bo}}\right) K_1\left(\frac{1}{\sqrt{Bo}}\frac{r_i}{r_o}\right) - I_1\left(\frac{1}{\sqrt{Bo}}\frac{r_i}{r_o}\right) K_1\left(\frac{r^*}{\sqrt{Bo}}\right)}{I_1\left(\frac{1}{\sqrt{Bo}}\right) K_1\left(\frac{1}{\sqrt{Bo}}\frac{r_i}{r_o}\right) - I_1\left(\frac{1}{\sqrt{Bo}}\frac{r_i}{r_o}\right) K_1\left(\frac{1}{\sqrt{Bo}}\right)}. \tag{6.38}$$

Taking into account the definition of a Green function, the analytical expression for the leading order azimuthal surface velocity along the segment $\left[\frac{r_i}{r_o}, 1\right]$ writes as:

$$v^*_{\theta,s} = \int_{\frac{r_i}{r_o}}^{r^*} f(\xi)\, G(r^*|\xi)\, d\xi + \int_{r^*}^{1} f(\xi)\, G(r^*|\xi)\, d\xi. \tag{6.39}$$

Note the particular situation of a zero vertical aspect ratio ($\delta = 0$) for which the influence of the side boundary layers vanishes. Then, only the core flow at leading order is taken into account and the forcing term (6.32) simplifies drastically: $f(r^*) = -r^*$. Consequently, for this particular case, a closed-form analytical expression of $v^*_{\theta,s}$ can be derived since the integrals involved in Eq. (6.39) can be analytically calculated.

6.8.2 Surface velocity at leading order

For a non vanishing aspect ratio δ, the integrals involved in Eq. (6.39) must be numerically evaluated at each radial location r^*. The surface velocity profile is thus obtained from a curve fitting based on a set of discrete values obtained from Gauss integrations performed with Maple® (release 9.0). We investigate the sensitivity of $v^*_{\theta,s}(r^*)$ to the following non-dimensional numbers:

- ◇ the vertical aspect ratio $\delta = \frac{h}{r_o}$,
- ◇ and the Boussinesq number, Bo.

Contribution of the boundary layers

If boundary layers along the side walls are not taken into account when writing the subphase velocity (see *e.g.* Eq. (6.18)), it is not possible to take into account the impact of the vertical aspect ratio δ on the dimensionless surface velocity (see Fig. 6.4). Surface velocity is plotted for two cases:

- ◇ whether only the core flow is selected when writing the forcing term (see Eq. (6.18)),
- ◇ or the no-slip BC is also taken into account from matching between core flow and boundary layers (see Eq. (6.27)).

In Fig. 6.4, the additional viscous dissipation inside the boundary layers along the side walls is clearly responsible for a lowering of the overall surface velocity magnitude. Consequently, if boundary layers are taken into account, surface velocity profiles tend to flatten near the side walls; this is especially true for a large enough aspect ratio δ. A significant magnitude of the surface velocity is found when the subphase depth is small enough and therefore when the linear velocity profile imposed by the rotating floor is able to impact upon the liquid surface *via* viscosity-driven diffusion of mo-

mentum within the subphase (see *e.g.* Fig. 6.4 with $Bo = 10^{-4}$ to 10^{-3}, $\delta = \frac{4}{70}$ to $\frac{10}{70}$).

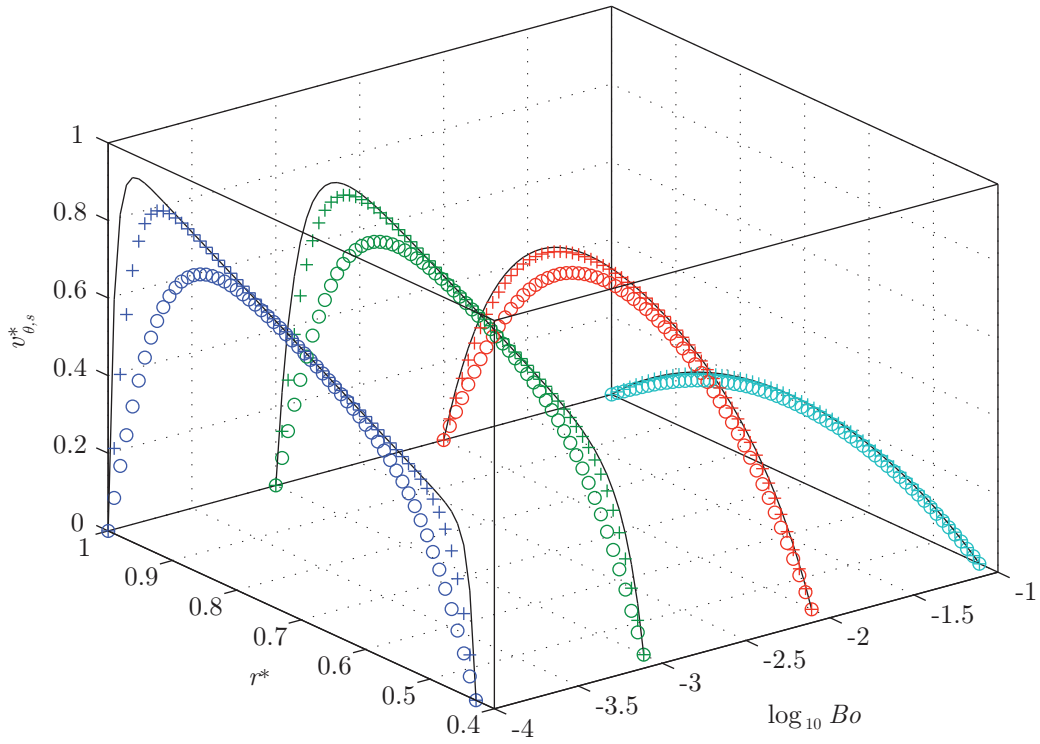

Figure 6.4. Shear velocity along the liquid surface as predicted from Couette approximation (continuous line, —) and from composite solution with $\delta = \frac{10}{70}$ (∘) and $\delta = \frac{4}{70}$ (+). Dependence on the Boussinesq number Bo.

Influence of the contamination

In Fig. 6.4, the dependence of surface velocity $v^*_{\theta,s}(r^*)$ on the Bo number is also illustrated with the aspect ratios of our experimental set-up: $\delta = \frac{4}{70}$, $\frac{10}{70}$ and $\frac{r_i}{r_o} = \frac{30}{70}$. Note that when surface viscosity decreases significantly (small Bo number), the mobility of the contaminated liquid surface increases accordingly. This is to correlate with the growing impact of subphase shearing at the liquid surface where τ_b behaves as a driving body stress for surface hydrodynamics. A point which is also confirmed for the smallest value of the vertical aspect ratio ($\delta = \frac{4}{70}$). For such a shallow flow,

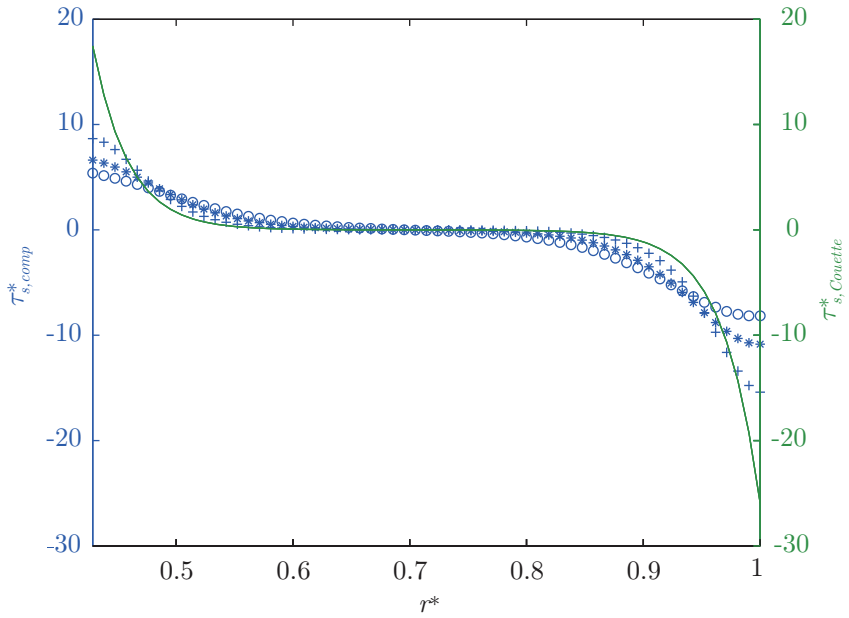

Figure 6.5. Surface stress along the liquid surface ($Bo = 0.001$) as calculated from Couette approximation (–, right y-axis) and from composite solutions (left y-axis) with $\delta = \frac{10}{70}$ (○), $\delta = \frac{7}{70}$ (*) and $\delta = \frac{4}{70}$ (+).

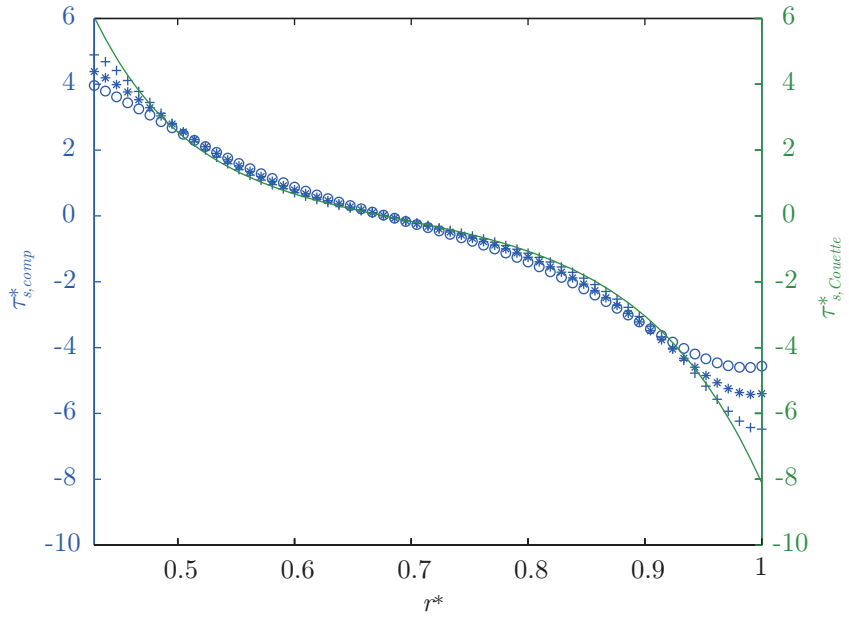

Figure 6.6. Surface stress along the liquid surface ($Bo = 0.01$) as calculated from Couette approximation (–, right y-axis) and from composite solutions (left y-axis) with $\delta = \frac{10}{70}$ (○), $\delta = \frac{7}{70}$ (*) and $\delta = \frac{4}{70}$ (+).

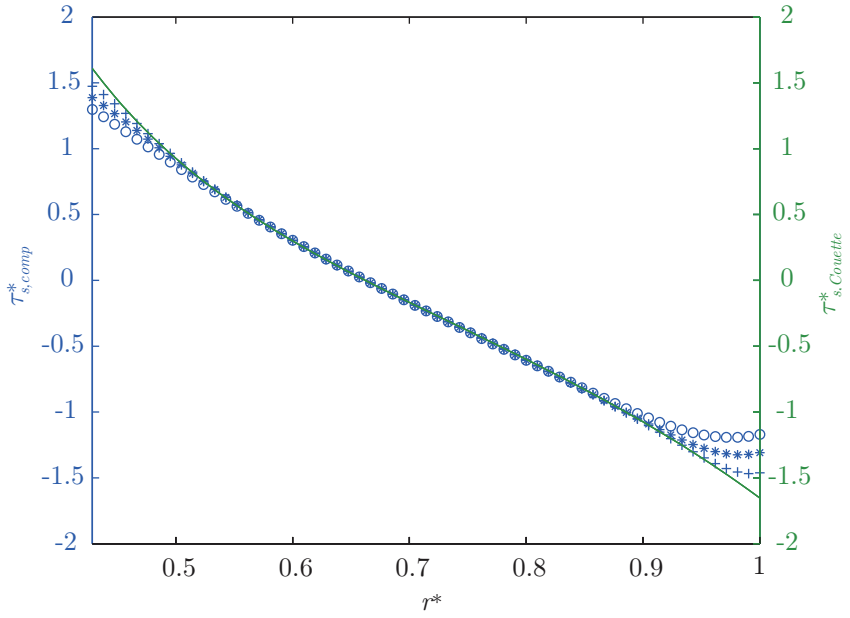

Figure 6.7. Surface stress along the liquid surface ($Bo = 0.1$) as calculated from Couette approximation (–, right y-axis) and from composite solutions (left y-axis) with $\delta = \frac{10}{70}$ (○), $\delta = \frac{7}{70}$ (*) and $\delta = \frac{4}{70}$ (+).

the magnitude of surface velocity grows and correlatively its profile becomes more and more linear as imposed by the rotating floor.

Finally, when the aspect ratio is small and when the Bo number is large enough ($Bo = 10^{-1}$, see Fig. 6.4), it is worthy to note that composite and Couette solutions merge into one single velocity profile. For this particular case, the core approximation is sufficient to describe surface flow whatever the value of δ is.

6.8.3 Subphase velocity at leading order

As illustrated in Fig. 6.3, surface velocity, when known, can be implemented into the expression of the azimuthal velocity in the subphase. From Eqs. (6.39) and (6.27), the velocity $v^*_\theta(r^*, z^*)$ is plot as a 3-D sheet (see Fig. 6.11). As expected, the profile of subphase velocity $v^*_\theta(r^*, z^*)$ tends to be linear at the vicinity of the rotating floor and merges into the surface velocity $v^*_{\theta,s}$ whose parabolic shape is apparently close to a 2-D Poiseuille flow. The two singularities on the Dirichlet BCs located at the left

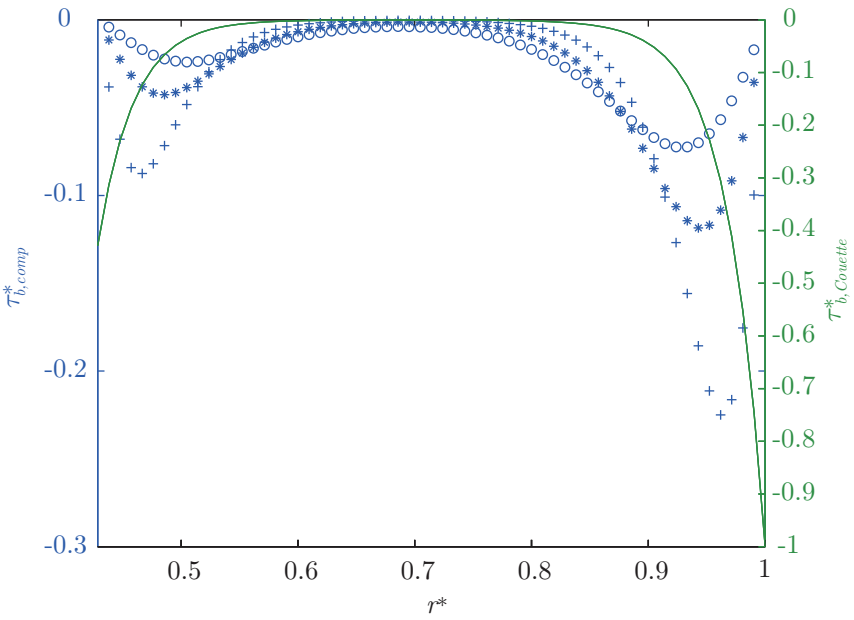

Figure 6.8. Subphase stress at the liquid surface ($Bo = 0.001$) as calculated from Couette approximation (–, right y-axis) and from composite solutions (left y-axis) with $\delta = \frac{10}{70}$ (∘), $\delta = \frac{7}{70}$ (*) and $\delta = \frac{4}{70}$ (+).

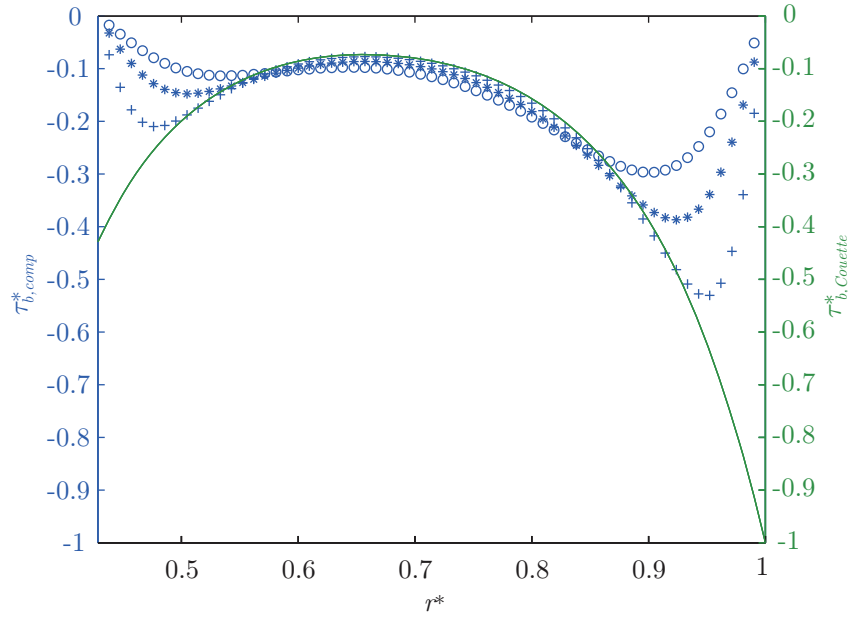

Figure 6.9. Subphase stress at the liquid surface ($Bo = 0.01$) as calculated from Couette approximation (–, right y-axis) and from composite solutions (left y-axis) with $\delta = \frac{10}{70}$ (∘), $\delta = \frac{7}{70}$ (*) and $\delta = \frac{4}{70}$ (+).

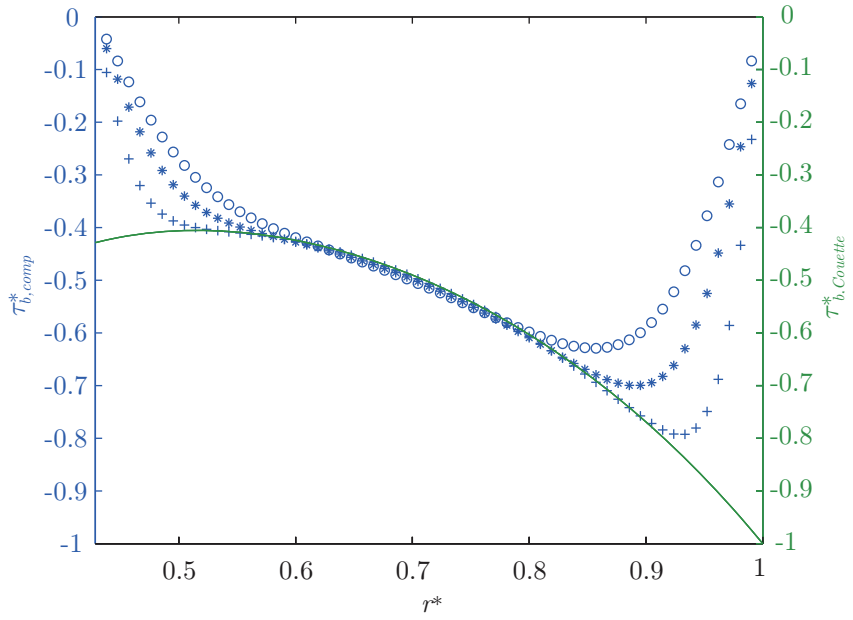

Figure 6.10. Subphase stress at the liquid surface ($Bo = 0.1$) as calculated from Couette approximation (–, right y-axis) and from composite solutions (left y-axis) with $\delta = \frac{10}{70}$ ($\circ$), $\delta = \frac{7}{70}$ (*) and $\delta = \frac{4}{70}$ (+).

and right corners of the channel floor yield small oscillations visible along the edges of the channel ($r^* = \frac{r_i}{r_o}$ and $r^* = 1$). These oscillations are due to the truncation ($n = 1 \ldots 50$) of the infinite series in the Eq. (6.27) leading to this plot.

6.8.4 On the need to get an accurate estimation of the Boussinesq number

The Boussinesq number, Bo, classically defined by Eq. (6.8) in the literature, is easily written from scaling arguments. With the impact of the side walls upon the flow system, it can be worthwhile here to calculate a local Boussinesq number. We introduce two definitions of the local Boussinesq number. A first one is based on the assumption of a Couette flow along the vertical direction within the subphase,

$$Bo_{Couette} \equiv \frac{\tau^*_{s,Couette}}{\tau^*_{b,Couette}} Bo,$$

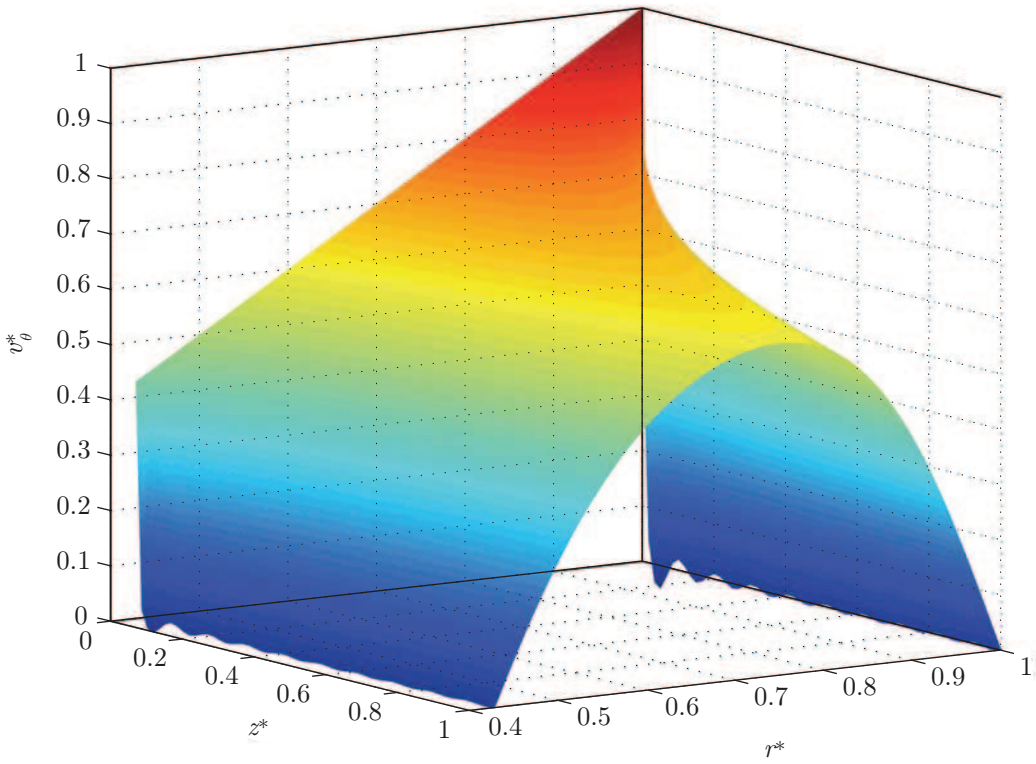

Figure 6.11. Subphase flow at leading order, $v_\theta^*(r^*, z^*)$ (with $Bo = 0.01$, $\delta = \frac{1}{7}$ and $\frac{r_i}{r_0} = \frac{3}{7}$).

while the second one is based on the composite solution for the flow of the subphase:

$$Bo_{comp} \equiv \frac{\tau^*_{s,comp}}{\tau^*_{b,comp}} Bo.$$

The dimensionless shear stress along the liquid surface writes as:

$$\tau_s^* = \frac{dv^*_{\theta,s}}{dr^*} - \frac{v^*_{\theta,s}}{r^*},$$

with $\tau^*_{s,Couette} = \tau_s^*$ if the surface velocity $v^*_{\theta,s}(r^*)$ is calculated from Eq. (6.18) or $\tau^*_{s,comp} = \tau_s^*$ if $v^*_{\theta,s}(r^*)$ is calculated from Eq. (6.27). The dimensionless shear stress at the liquid surface writes as:

$$\tau^*_{b,comp} = \tau^*_{b,Couette} + 2\,\frac{\exp\left(-\pi\,\dfrac{1-r^*}{\delta}\right)}{1+\exp\left(-\pi\,\dfrac{1-r^*}{\delta}\right)} + 2\,\frac{r_i}{r_o}\,\frac{\exp\left(-\pi\,\dfrac{r^*-r_i/r_o}{\delta}\right)}{1+\exp\left(-\pi\,\dfrac{r^*-r_i/r_o}{\delta}\right)},$$

with

$$\tau^*_{b,Couette} = v^*_{\theta,s}(r^*) - r^*.$$

As illustrated in Figs. 6.5 to 6.7 and Figs. 6.8 to 6.10, the shear stress along the liquid surface is significantly changed when switching from the Couette solution for the subphase flow to the composite solution. A point which is especially true near the side walls.

The composite solution delivers as well a far better estimation of the shear stress at the liquid surface. Typically, a zero value is consistently recovered at the side walls. It is interesting to notice that even at a large Bo number and a vertical aspect ratio as small as $\delta = \frac{4}{70}$, Couette approximation fails to deliver consistent values of the shear stress at the liquid surface, except at the middle of the channel. Such a result clearly demonstrates that Couette approximation must be disregarded in the second part of this chapter devoted to the situation of a viscous stratification especially when it is distributed all along the liquid surface.

In Fig. 6.11, it is clear that the dependence of the velocity $v^*_\theta(r^*, z^*)$ along z-axis is strongly damped far away from the rotating floor, especially at the liquid surface ($z^* \approx 1$). Consequently, it is consistent to notice that the shear stress at the liquid surface is over-estimated when predicted from Couette approximation. In fact, the local Boussinesq number, Bo_{comp}, estimated from the composite solution, exhibits corrected values of the Boussinesq number up to several orders of magnitude larger than those commonly accepted in the literature, especially near the side walls in the boundary layers (see Fig. 6.12).

A better estimation of the local Boussinesq number helps to understand why surface shearing cannot be systematically considered as negligible in surface hydrodynamics [32].

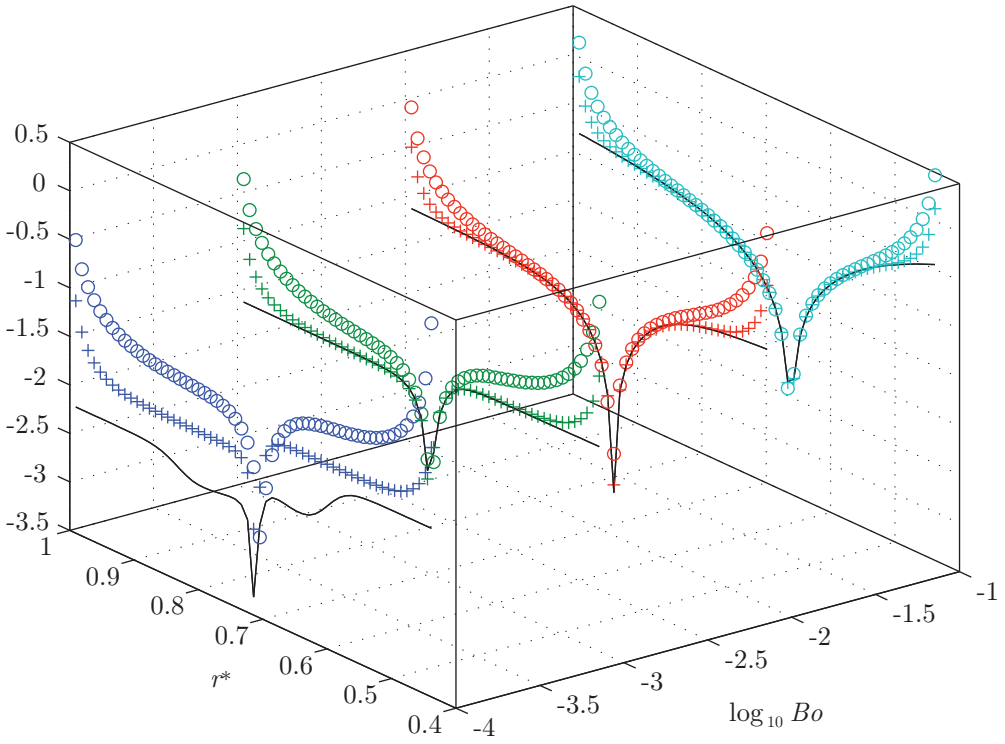

Figure 6.12. Local Boussinesq number, $Log_{10}(|Bo_{Couette}|)$, as calculated from Couette approximation (–) and local Boussinesq number, $Log_{10}(|Bo_{comp}|)$, as calculated from composite solutions with $\delta = \frac{10}{70}$ (∘) and $\delta = \frac{4}{70}$ (+).

6.9 Stratified surface viscosity

6.9.1 On the relevance of an integral formulation

To go beyond the situation of a uniform contamination [112], our purpose here is to address analytically the viscous stratification induced by the molecular packing of hydrophobic biomolecules. Modeling a viscous stratification, especially a regular one, is a little bit difficult since it is not necessarily described by co-existing slip/no-slip (mixed) BCs along the liquid surface. Typically a technique based on the use of dual integral equations (see *e.g.* [58]) is not relevant to a regular viscous stratification.

In the following, special attention will be given to the writing of the constitutive law (6.6) with the purpose of monitoring:

- ◇ the radial extent of a jump in surface viscosity, from the asymptotic case of a regular viscous stratification to the opposite asymptotic case of a localized segregation front,

- ◇ the magnitude of the jump in surface viscosity, ranging from zero, in order to recover uniform conditions of contamination, to several orders of magnitude, in order to take into account a radially inwards segregation spanning from a weakly viscous (almost gaseous) state to a very viscous (almost rigid) state, for instance.

Surface flow has to be calculated by not considering the linear non-homogeneous ODE (6.29) with a radius dependent coefficient ($g(r^*) \neq 0$). To gain benefit as much as possible from the calculations already performed to solve the previous ODE (6.29) in the case of a uniform surface viscosity, the same Green function $G(r^*|\xi)$, defined by Eq. (6.34), is again invoked. The ODE (6.7) is therefore written according to:

$$Bo\left[\frac{d^2v^*_{\theta,s}}{dr^{*2}} + \frac{1}{r^*}\frac{dv^*_{\theta,s}}{dr^*} - \frac{v^*_{\theta,s}}{r^{*2}}\right] - v^*_{\theta,s} = f(r^*) - Bo\,\frac{dg}{dr^*}\left[\frac{dv^*_{\theta,s}}{dr^*} - \frac{v^*_{\theta,s}}{r^*}\right] - Bo\,g(r^*)\left[\frac{d^2v^*_{\theta,s}}{dr^{*2}} + \frac{1}{r^*}\frac{dv^*_{\theta,s}}{dr^*} - \frac{v^*_{\theta,s}}{r^{*2}}\right], \tag{6.40}$$

while the Green function $G(r^*|\xi)$ enables us to write:

$$\int_{\frac{r_i}{r_o}}^{1}\left\{Bo\left[\frac{d^2v^*_{\theta,s}}{d\xi^2} + \frac{1}{\xi}\frac{dv^*_{\theta,s}}{d\xi} - \frac{v^*_{\theta,s}}{\xi^2}\right] - v^*_{\theta,s}(\xi)\right\}G(r^*|\xi)\,d\xi = v^*_{\theta,s}(r^*).$$

As a consequence, defining the forcing term $\phi(\xi)$ from the perturbation $\kappa(\xi)$ as,

$$\phi(\xi) = f(\xi) + \kappa(\xi), \tag{6.41}$$

with

$$\kappa(\xi) = -Bo\,\frac{dg}{d\xi}\left[\frac{dv^*_{\theta,s}}{d\xi} - \frac{v^*_{\theta,s}}{\xi}\right] - Bo\,g(\xi)\left[\frac{d^2v^*_{\theta,s}}{d\xi^2} + \frac{1}{\xi}\frac{dv^*_{\theta,s}}{d\xi} - \frac{v^*_{\theta,s}}{\xi^2}\right], \tag{6.42}$$

the surface velocity is equivalently expressed as:

$$v^*_{\theta,s}(r^*) = \int_{\frac{r_i}{r_o}}^{1}\phi(\xi)\,G(r^*|\xi)\,d\xi.$$

The differential Eqs. (6.40) and (6.33) differ only by their respective source term with the addition in Eq. (6.40) of the disturbance $\kappa(r^*)$ which reflects the discrepancy caused by the non-uniformity of viscosity. This principle of superposition follows from the specific writing of the constitutive law for the surface viscosity. It permits the iterative calculation of the surface velocity especially when the viscous stratification is particularly marked.

It is also worthy to note that even if the Green function $G(r^*|\xi)$ is not symmetric ($G(r^*|\xi) \neq G(\xi|r^*)$), it can nevertheless be written as the sum of two separable (degenerate) kernels:

$$G\left(r^*|\xi\right) = G_1\left(r^*|\xi\right)\ \mathcal{H}(r^* - \xi) + G_2\left(r^*|\xi\right)\ \mathcal{H}(\xi - r^*),$$

where $\mathcal{H}$ denotes Heaviside step function, and where

$$G_i(r^*|\xi)\ =\ \sum_{j=1,2} a_{ij}(r^*)\, b_j(\xi)\,, \quad i = 1, 2,$$

with:

$$\begin{cases} a_{11}\ =\ A(r^*)\,, & a_{21}\ =\ C(r^*), \\ a_{12}\ =\ B(r^*)\,, & a_{22}\ =\ D(r^*), \\ b_1\ =\ \xi\, I_1\left(\dfrac{\xi}{\sqrt{Bo}}\right)\,, & b_2\ =\ \xi\, K_1\left(\dfrac{\xi}{\sqrt{Bo}}\right). \end{cases}$$

Finally, the surface velocity can be equivalently written as:

$$v_{\theta,s}(r^*)\ =\ \int_{\frac{r_i}{r_o}}^{r^*} \phi(\xi)\, G_1(r^*|\xi)\, d\xi\ +\ \int_{r^*}^{1} \phi(\xi)\, G_2(r^*|\xi)\, d\xi. \tag{6.43}$$

The fact that the surface viscosity is not uniform confers to the non-homogenous (forcing) term $\phi(\xi)$ (defined by Eq. (6.41)) a dependence on $v^*_{\theta,s}$ and its derivatives. The way to solve this problem is same as the previous one before, at least as regards the homogeneous term of Eq. (6.40), but this time an additional integral term gives rise to an implicit formulation for $v^*_{\theta,s}$.

6.9.2 A Fredholm integral equation for $v^*_{\theta,s}$

This section shows how to expand (6.43) in order to get a Fredholm integral formulation which typically writes as:

$$\mu(r^*)\, v^*_{\theta,s}(r^*) \,+\, h(r^*) \,=\, \int_a^b v^*_{\theta,s}(\xi)\, k(r^*|\xi)\, d\xi.$$

Integrations by parts are systematically performed to remove first and second derivatives of $v^*_{\theta,s}(\xi)$. The first integral term in Eq. (6.43) is explicitly written according to:

$$\int_{\frac{r_i}{r_o}}^{r^*} \phi(\xi)\, G_1(r^*|\xi)\, d\xi \,=\, \int_{\frac{r_i}{r_o}}^{r^*} \phi(\xi)\, \left[a_{11}(r^*)\, b_1(\xi) \,+\, a_{12}(r^*)\, b_2(\xi)\right]\, d\xi.$$

In the same way, one finds for the second integral involved in Eq. (6.43):

$$\int_{r^*}^{1} \phi(\xi)\, G_2(r^*|\xi)\, d\xi \,=\, \int_{r^*}^{1} \phi(\xi)\, \left[a_{21}(r^*)\, b_1(\xi) \,+\, a_{22}(r^*)\, b_2(\xi)\right] d\xi.$$

The generic integral term, $\int_{\ominus}^{\oplus} a_{ij}(r^*) b_j(\xi)\phi(\xi) d\xi$, which can be identified from the two former expressions if the endpoints ($\ominus$, $\oplus$) take either the values ($\frac{r_i}{r_o}$, r^*) or the values (r^*, 1), is worth being developed and simplified. After simple calculations, the following integral equation can be made evident:

$$\mu^*_s(r^*) \,*\, v^*_{\theta,s}(r^*) \,+\, h(r^*) \,=\, Bo \sum_{i,j} \int_{\ominus}^{\oplus} k_{ij}(r^*|\xi)\, v^*_{\theta,s}(\xi)\, d\xi, \tag{6.44}$$

with,

$$h(r^*) = -\sum_{i,j} \int_{\ominus}^{\oplus} a_{ij}(r^*)\, b_j(\xi)\, f(\xi)\, \xi\, d\xi,$$

$$\mu^*_s\,(r^*) = 1 + g\,(r^*)\,,$$

and,

$$k_{ij}\,(r^*|\xi) = a_{ij}\;(r^*) \left\{ b_j\,(\xi)\;\left[\frac{1}{\xi}\frac{dg}{d\xi} + \frac{1}{\xi^2}\, g\,(\xi)\right] + \frac{d}{d\xi}\left[b_j\,(\xi)\left[\frac{dg}{d\xi} + \frac{1}{\xi}\, g\,(\xi)\right]\right]\right\}$$
$$- a_{ij}\,(r^*)\;\frac{d^2}{d\xi^2}\left[b_j\,(\xi)\;g\,(\xi)\right].$$

Assuming that the non-uniformity function is regular in such a way that $g \in \mathcal{C}^1$, the kernel $k_{ij}(r^*|\xi)$ can be simplified as:

$$k_{ij}(r^*|\xi) \,=\, a_{ij}(r^*) \left\{ g(\xi) \left[\frac{b'_j}{\xi} - b''_j\right] \,+\, g'(\xi) \left[\frac{2b_j}{\xi} - b'_j\right]\right\}. \tag{6.45}$$

Taking account of (6.6), the integral Eq. (6.44) can be written down in a more explicit way:

$$\mu_s^*(r^*) * v_{\theta,s}^*(r^*) = -h(r^*) + Bo \int_{\frac{r_i}{r_o}}^{r^*} k_1(r^*|\xi) v_{\theta,s}^*(\xi) d\xi + Bo \int_{r^*}^{1} k_2(r^*|\xi) v_{\theta,s}^*(\xi) d\xi, \quad (6.46)$$

with the kernels $k_1(r^*|\xi)$, $k_2(r^*|\xi)$, and the non-homogeneous term of the integral formulation, $h(r^*)$, writing as,

$$\begin{aligned} k_1(r^*|\xi) = A(r^*) \Bigg\{ & -\frac{\xi}{Bo} I_1\left(\frac{\xi}{\sqrt{Bo}}\right) g(\xi) \\ & + g'(\xi) \left[2 I_1\left(\frac{\xi}{\sqrt{Bo}}\right) - \frac{\xi}{\sqrt{Bo}} I_0\left(\frac{\xi}{\sqrt{Bo}}\right) \right] \Bigg\} \\ + B(r^*) \Bigg\{ & -\frac{\xi}{Bo} K_1\left(\frac{\xi}{\sqrt{Bo}}\right) g(\xi) \\ & + g'(\xi) \left[2 K_1\left(\frac{\xi}{\sqrt{Bo}}\right) + \frac{\xi}{\sqrt{Bo}} K_0\left(\frac{\xi}{\sqrt{Bo}}\right) \right] \Bigg\}, \end{aligned} \quad (6.47)$$

$$\begin{aligned} k_2(r^*|\xi) = C(r^*) \Bigg\{ & -\frac{\xi}{Bo} I_1\left(\frac{\xi}{\sqrt{Bo}}\right) g(\xi) \\ & + g'(\xi) \left[2 I_1\left(\frac{\xi}{\sqrt{Bo}}\right) - \frac{\xi}{\sqrt{Bo}} I_0\left(\frac{\xi}{\sqrt{Bo}}\right) \right] \Bigg\} \\ + D(r^*) \Bigg\{ & -\frac{\xi}{Bo} K_1\left(\frac{\xi}{\sqrt{Bo}}\right) g(\xi) \\ & + g'(\xi) \left[2 K_1\left(\frac{\xi}{\sqrt{Bo}}\right) + \frac{\xi}{\sqrt{Bo}} K_0\left(\frac{\xi}{\sqrt{Bo}}\right) \right] \Bigg\}, \end{aligned} \quad (6.48)$$

and,

$$\begin{aligned} h(r^*) = & - A(r^*) \int_{\frac{r_i}{r_o}}^{r^*} f(\xi) \xi I_1\left(\frac{\xi}{\sqrt{Bo}}\right) d\xi - B(r^*) \int_{\frac{r_i}{r_o}}^{r^*} f(\xi) \xi K_1\left(\frac{\xi}{\sqrt{Bo}}\right) d\xi \\ & - C(r^*) \int_{r^*}^{1} f(\xi) \xi I_1\left(\frac{\xi}{\sqrt{Bo}}\right) d\xi - D(r^*) \int_{r^*}^{1} f(\xi) \xi K_1\left(\frac{\xi}{\sqrt{Bo}}\right) d\xi. \end{aligned} \quad (6.49)$$

Then, the integral Eq. (6.46), which remains to solve in order to get the surface velocity $v_{\theta,s}^*$, can thus be considered as a Fredholm integral equation with, nevertheless, the continuous piecewise kernel $k(r^*|\xi)$ defined as :

$$k(r^*|\xi) = k_1(r^*|\xi) \mathcal{H}(\xi - r^*) + k_2(r^*|\xi) \mathcal{H}(r^* - \xi). \quad (6.50)$$

Two points are worthy of note:

◇ If the non-uniformity function vanishes ($g \equiv 0$), the expression (6.46) not only stands as a Fredholm integral equation of second kind ($\mu_s^*(r^*) \equiv 1$) but since $k_1 \equiv 0$ and $k_2 \equiv 0$, merges into the expression (6.39): surface velocity attached to the situation of a uniform viscosity is finally recovered.

◇ One easily checks that if $g \equiv 1$, then surface velocity calculated from Eq. (6.46) - at a given value of the Bo number - is consistently equal to the surface velocity calculated from Eq. (6.39) at twice the value of Bo.

6.9.3 Solution of the Fredholm integral equation

To solve Eq. (6.46), several difficulties are worth being mentioned first.

◇ Despite the fact that the kernels k_1 and k_2 write as a sum of degenerate kernels ($k_{ij}(r^*,\xi) = a_{ij}(r^*)b_j(\xi)$), the generic term, $\int_{\ominus}^{\oplus} a_{ij}(r^*)b_j(\xi)\phi(\xi)d\xi$ cannot be handled as a convolution. Consequently, any attempt to find an analytical expression of $v_{\theta,s}^*(r^*)$ by means of Fourier or Laplace transforms of Eq. (6.46) can be expected unsuccessful.

◇ Usually, a Fredholm integral equations with a degenerate kernel classically reduce to solving a system of linear equations [82]. Here, the last but not least hindrance is the split nature of the kernel $k(r^*|\xi)$ (see (6.50)) which prevents us to apply such a technique.

◇ It could be interesting to investigate what kind of conditions upon the function g could lead to a symmetric Hilbert-Schmidt kernel $k_{ij}(r^*|\xi)$ [159]. In such a case, one could seek an approximation for $v_{\theta,s}^*(r^*)$ written as a series based on a complete set of orthogonal functions ($v_{\theta,s}^*(r^*) = \sum_n a_n y_n(r^*)$). In our case, whatever the conditions one could apply to g, the kernel $k_{ij}(r^*,\xi)$ cannot be symmetric. Note that an alternative technique based on iterated kernels $k_L(r^*,\xi)$ and $k_R(r^*,\xi)$ could stem as a possible way to solve Eq. (6.46). Our choice in this chapter is to develop a very simple numerical method to solve Eq. (6.46): our

objective is to assess the ability of the matched asymptotic technique to take account of a stratification in surface viscosity; further mathematical developments based on Hilbert-Schmidt or Riemann techniques are going far beyond the scope of this chapter.

6.9.4 Discretization of the integral equation

The Fredholm integral Eq. (6.46) is finally calculated from the trapezoid rule, essentially due to its simplicity. Here again, both elaborate discretization techniques such as least square methods, Galerkin or Rayleigh-Ritz methods [159] or other quadrature integration techniques (see *e.g.* [7]) could be preferred. But this is not the background purpose of this chapter. The interval $\left[\frac{r_i}{r_o}, 1\right]$ is simply split into N intervals of constant width, Δr, and the series $(r_k)_{0<k<N}$ ($r_k = \frac{r_i}{r_o} + k\Delta r$) and $(v_{s,k})_{0<k<N}$ ($v_{s,k} = v_{\theta,s}(r_k)$) are defined. The subsequent linear system to solve writes as:

$$\forall k \in [1, N-1],$$

$$\begin{aligned}[1 + g(r_k)]\, v_{s,k} + h(r_k) = \frac{Bo}{2} \sum_{j=1}^{k-1} \left[k_1(r_k, r_{j+1}) v_{s,j+1} + k_1(r_k, r_j) v_{s,j}\right] \Delta r \\ + \frac{Bo}{2} \sum_{j=k}^{N-1} \left[k_1(r_k, r_{j+1}) v_{s,j+1} + k_1(r_k, r_j) v_{s,j}\right] \Delta r,\end{aligned}$$

with the two end-points Dirichlet BCs: $v_{s,0} = 0$ and $v_{s,N} = 0$.

6.9.5 Shear viscosity across a diffuse front

To illustrate the ability of our asymptotic approach to deal with the situation of a non-uniform surface viscosity, a model system well-known in 2-D bio-crystallization is retained: a lipidic monolayer is spread over an air-water interface. A soluble protein, which owns a chemical affinity for the lipidic monolayer (streptavidin for instance), is injected within the underlying water subphase. Molecular diffusion in the subphase drives the proteins up to the liquid surface where they bind to the lipidic matrix. 2-D

molecular diffusion allows the molecular complexes [protein–lipid] to self-assembly in such a way that, as a result, a crystalline powder is obtained (see *e.g.* [30, 25, 179]). This process therefore drives to a diffusion-limited poly-crystalline growth since it is realized in static conditions.

As briefly mentioned in the introduction of this chapter, the basic idea is to consider non-equilibrium conditions and typically, to gain benefit from the recirculating flow which originates from centrifugation along the rotating floor in the annular channel. At the time being, we know from the literature [10] that this recirculating flow is responsible for a radially inwards surface pressure which enhances the growth of a 2-D crystal of protein from the smallest to the largest radii of the annular channel.

To mimic the impact of the flow-induced protein packing upon surface shear viscosity μ_s, we consider the following variation law (inspired from Yih [188]):

$$g(r^*) = \frac{1 - \dfrac{\mu_{s,crystal}}{\mu_{s,monolayer}}}{1 + \dfrac{\mu_{s,crystal}}{\mu_{s,monolayer}}} \tanh\left(\frac{r^* - r_F}{\zeta}\right), \tag{6.51}$$

where $\mu_{s,monolayer}$, $\mu_{s,crystal}$, r_F and ζ denote, respectively, the viscosity of the water surface topped with the lipidic matrix, the viscosity of the flow-induced molecular packing made from the complexes $\{protein - lipid\}$, the location of a segregation front and finally, a stiffness parameter which can be seen as the typical thickness of a diffusive segregation front.

Typically, a radial distribution of the dimensionless surface viscosity $\mu_s^*(r^*)$ (see also Eq. 6.6) is represented in Fig. 6.13 (a) for the working conditions:

- ◇ the segregation front is located at the middle of the interface ($r_F = \dfrac{r_i + r_o}{2r_o}$),
- ◇ the lipidic monolayer is staying on the right hand side of the functionalized air-water interface with surface viscosity: $\dfrac{\mu_{s,monolayer}}{\overline{\mu_s}}$,
- ◇ the densified proteins adsorbed to the lipidic monolayer are staying on the left hand side with surface viscosity: $\dfrac{\mu_{s,crystal}}{\overline{\mu_s}}$,
- ◇ the jump in surface viscosity is: $\dfrac{\mu_{s,crystal}}{\mu_{s,monolayer}} = 50$, as one can expect from the

viscous behaviour of a proteomic self-assembly compared to the one of a lipidic matrix [176, 99]

- ◇ the typical thickness of the diffusive segregation front is: $\zeta = \frac{1 - {}^{r_i}/_{r_o}}{10}$ with $\frac{r_i}{r_o} = \frac{30}{70}$.
- ◇ the typical scale for the surface viscosity is :$\overline{\mu_s} = \frac{\mu_{s,crystal} + \mu_{s,monolayer}}{2}$.

The impact of viscous stratification upon surface flow is investigated for five different levels of surface contamination. The velocity profiles along the liquid surface (continuous line), as numerically calculated from Eq. (6.46), are displayed for five values of the Boussinesq number (defined form $\overline{\mu_s}$, see Eq. 6.8: $Bo = 0.001$, 0.01, 0.1, 1, and 10, see Fig. 6.13 (b) to Fig. 6.13 (f)). For sake of comparison, the jump in surface viscosity is kept constant for all the velocity profiles ($\frac{\mu_{s,crystal}}{\mu_{s,monolayer}} = 50$). The two other curves plotted on Figs. 6.13 (b) to 6.13 (f) represent surface velocity profile calculated for a low level and a high level of uniform surface contamination, namely with surface viscosity $\frac{\mu_{s,monolayer}}{\overline{\mu_s}}$ (○) and $\frac{\mu_{s,crystal}}{\overline{\mu_s}}$ (□). It is not possible to get a local value of the surface viscosity for a non-uniform distribution using a uniform approximation, as proven by the big difference between the red and blue curves and the full solution ($-\ominus-$) even close to the inner wall. A maximum of the azimuthal velocity is also made evident on the full solution: it consistently arises in the region where surface viscosity is the smallest. A remarkable point to notice is that the more rigid the interface (large viscosity $\mu_{s,crystal}$), the more sensitive surface velocity is to the jump in surface viscosity. Consequently, surface velocity field can be expected to behave as a sensitive and convenient tool to follow the flow-driven growth of a 2-D self-assembly of protein along a functionalised liquid surface.

6.10 Final comments

In this chapter, Stokes and lubrication approximations are considered. This allows us to address in a very simple way for the asymptotic modeling of an floor-driven

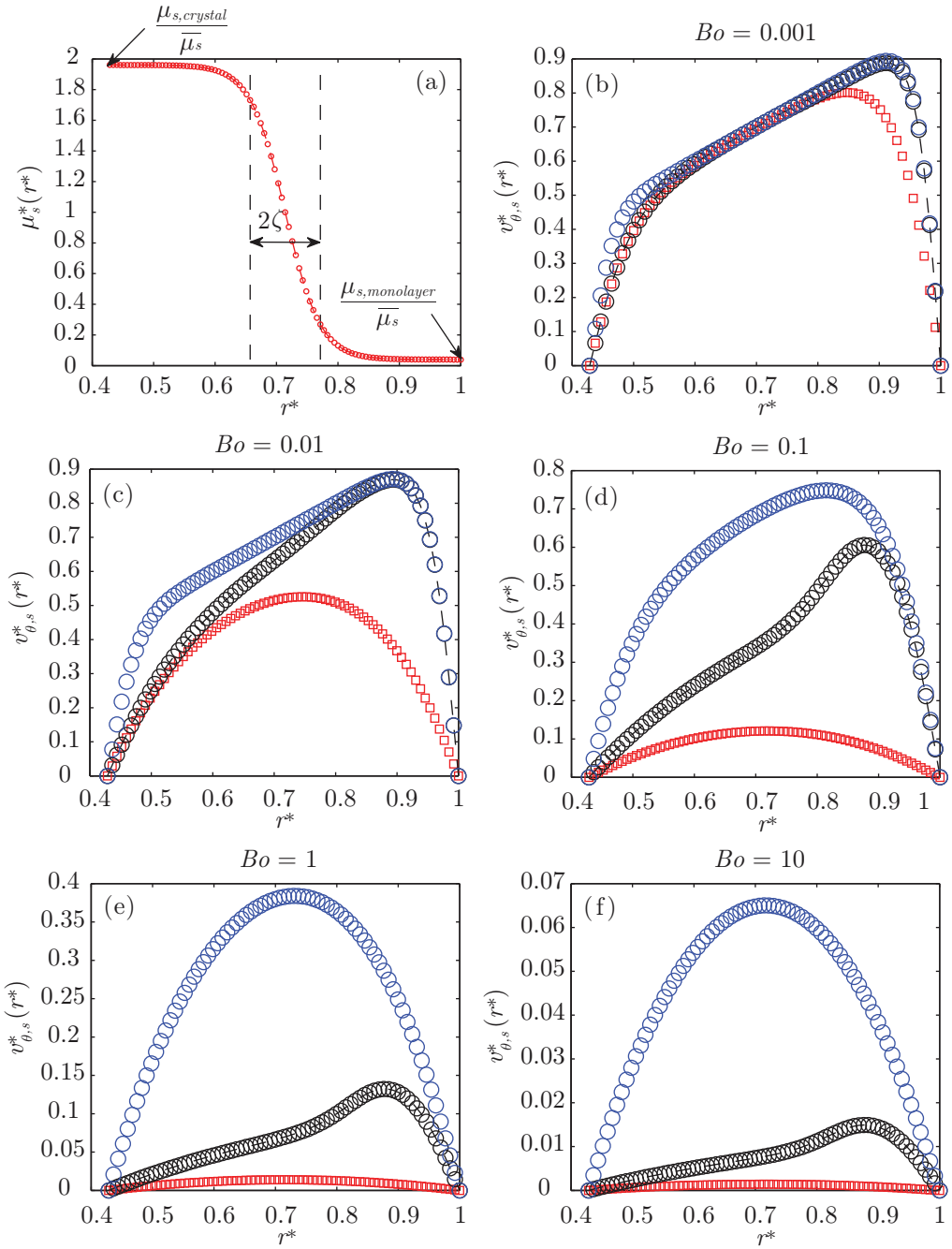

Figure 6.13. (a) Dimensionless surface viscosity, $\mu_s^*(r^*)$, as plotted according to (6.6) and (6.51). The symbol ζ is a typical thickness of viscous stratification. (b) to (f) Surface velocity profiles ($-\ominus-$) for five levels of surface contamination ($Bo = 0.001$ to 10), a constant jump in surface viscosity: $\frac{\mu_{s,crystal}}{\mu_{s,monolayer}} = 50$, a segregation front located at $r^* = r_F = \frac{r_i+r_o}{2r_o}$ with typical thickness $\zeta = \frac{1-r_i/r_o}{10}$ and finally, the aspect ratios: $\delta = \frac{4}{70}$ and $\frac{r_i}{r_o} = \frac{30}{70}$. For comparison, two surface velocity profiles are displayed for a uniform surface contamination with surface viscosities: $\frac{\mu_{s,crystal}}{\overline{\mu_s}}$ ($\square$) and $\frac{\mu_{s,monolayer}}{\overline{\mu_s}}$ ($\circ$).

annular flow ($Re < 100$) covered by a layer of amphiphilic molecules. A closed-form analytical formulation of the shear stresses, both at the liquid surface and along it, is put forward for the first time, which insures accurate estimation of the Boussinesq number.

In uniform conditions of surface contamination and for a small vertical aspect ratio δ, a fair agreement is consistently found between leading order solution and existing analytical models [39, 112].

Due to the flow-induced radially inwards packing of amphiphilic molecules along the liquid surface, a radial stratification of the surface shear viscosity is taken into account in this chapter from a modeling based on the azimuthal component of jump momentum balance at the liquid surface. In a given sense, this modeling is an extended version of the analytical model by Mannheimer & Schechter [112] based on a uniform contamination.

To incorporate the situation of a radial segregation between two stratifying phases covering the surface of a liquid bath, the constitutive law for surface viscosity is chosen to depend on the radial coordinate especially across a diffusive front which separates both phases. Far from the diffusive front, at the vicinity of the inner side wall, the condensed phase is characterized by a large value of surface viscosity. The bump of the velocity profile along the liquid surface is consistently found to move radially outwards where surface viscosity is imposed small. The value and the radial location of this velocity bump are related to both the jump in surface viscosity and the radial extent of the more condensed phase (a crystal of protein typically). When surface viscosity becomes large enough, surface hydrodynamics is seen to be sensitive enough and it can be expected as a convenient tool to characterize a stratified layer of biomolecules.

Chapter 7

Conclusions and outlook

Conclusions

A new experimental device is presented in this dissertation whose objective is to demonstrate the ability of an annular shear flow in reorganising the self-assembly of biomolecules within a Langmuir monolayer (LM). The device is nothing but a trough based on an annular channel at the bottom of which is placed a ring (inner radius: 30 mm, outer radius: 70 mm). The channel is filled with an acidified bath of ultra pure water (pH = 2) whose free surface is topped with an LM made from pentadecanoic acid (PDA). A main annular shear flow is driven by the rotation of the ring along the channel floor. The ring rotation and subsequently the magnitude of the shear flow, is remote-controlled by way of an external coupling with a rotating magnet. A small flow component originating from centrifugation along the rotating ring is also made evident which is responsible for a centripetal transport of the surfactants along the liquid surface. If the LM is diluted with a large enough molecular area - or equivalently, a small enough surface concentration of PDA, the centripetal transport along the surface is the source of a radially-inwards molecular packing. Because the LM also experiences phases transition from the liquid-expanded (LE) to the liquid-condensed (LC) state, this dissertation is also the opportunity to study the flow of a

perfectly two-dimensional two-phase Langmuir film at a small to moderate Reynolds number ($Re \approx 10$ to 100). The morphology of the two-phase LM is investigated at meso scale (10 μm to 1 mm) from the area fraction distribution of the LC phase when permanent regime has been established (10 h at least).

As demonstrated all along Chapters 4 to 5, four physical mechanisms contribute possibly to LM hydrodynamics:

- ◇ the (driving) shear stress from the rotating subphase, $\tau_b|_s$, which behaves as an (external) body force[1],
- ◇ the in-plane shear stress along the liquid surface, τ_s,
- ◇ the radially-inwards surface pressure along the liquid surface, Π,
- ◇ and finally, the effective line tension between condensed and expanded co-existing phases, λ_{eff}.

To deal with the respective competitions (or balances) between these mechanisms, relevant dimensionless numbers have been introduced in the dissertation, namely: the Reynolds number, Re (≈ 10 to 100), the classical (macroscopic) Boussinesq number, Bo ($\approx 10^{-4}$), and an original number referred to as a surface Bond number and defined from Eq. (5.6) in Chapter 5). Depending on their respective values, two main regimes can be distinguished: a dispersed regime and a stratified one.

As far as the dispersed regime is concerned, the radial distribution of the area fraction demonstrates a radially-inwards packing of the circular condensed domains along the liquid surface induced by the significant centripetal transport originating from centrifugation of the subphase. Above a given level of centrifugation, for a molecular area as large as $A \approx 30$ Å^2·molecule^{-1}, a new morphological transition is found during which the two-phase monolayer shifts to a finely divided mesoscopic morphology of the LC domains. The combined impact of surface shearing and reducing in the

[1]The subphase shear stress, $\tau_b|_s$, can be considered as playing a role equivalent to the one of the gravity force, ρ.g, in one vertical two-phase flow.

effective line tension is proposed as being responsible for such a transition. In fact, under the effect of centrifugation, the radially-inwards flow-induced pressure rises up to a level high enough, 0.18 mN·m^{-2} for $\Omega = 0.15$ rpm, to reduce significantly the effective line tension. Consequently, the condensed domains can be considered as literally shear-induced melted above a critical Reynolds number, $Re \approx 50$. The new patterning thus generated resembles to a perfectly monodispersed matrix of tiny condensed droplets, rather well-distributed according to one particular spatial frequency. Here, it is worthy to note that, unlike existing literature devoted to inertial regimes ($Re \approx 100$ to 1000), when the Reynolds number is small enough ($Re \approx 10$ to 100) and when the depth of the subphase is high enough, the subphase shear stress at the liquid surface is no longer significant. Consequently, competition between effective line tension, $\lambda_{eff} \approx 2.5 \times 10^{-13}$ N, and surface shear stress, $\tau_s \approx 4 \times 10^{-9}$ N·m^{-1}, is found to control the size of the condensed domains. An original consequence is that a Boussinesq number, $\widetilde{Bo_{LC}}$, defined at meso scale, is found to be at least of order unity ($\widetilde{Bo_{LC}} \approx 1$ to 10), which means that from the uniformly dispersed regime to the morphological transition included, the distribution of surface shear must be taken into account when interpreting size reduction subsequent to the melting of the condensed domains.

As far as the stratified regime is concerned now, which means a significant level of surface concentration ($A \approx 15$ Å^2·molecule^{-1}), the LM becomes stratified and the effective line tension decreases significantly. Note also that the corresponding flattening of the Π–A isotherm suggests that Marangoni effect become vanishingly small in this particular regime. Accordingly, the area fraction distribution is found uniform while the condensed domains behave as stripes elongated by the shear stress from the subphase, $\tau_b|_s$, for $\Omega = 0.206$ rpm and $h = 4$ mm. Due to the small level of line tension ($\lambda \approx 10^{-13}$ N), if the Re number is as large as 1000, these condensed stripes finally break up since $\tau_b|_s$ becomes large enough for $\Omega = 3.4$ rpm and $h = 4$ mm. It is only in this regime (shear-induced fragmentation) that typical results of the literature can be recovered with, for instance, the formation of bola-shaped condensed domains and a

non uniform radial distribution of the area fraction induced by the radial distribution of the shear stress $\tau_b|_s$ ([72]).

As a last step of this dissertation (Chapter 6), an analytical modelling has been developed in order to investigate the impact upon surface flow of a stratified surface viscosity whatever its source can be (a shear-induced fragmentation of condensed domains, a radially-inwards packing due to underlying centrifugation or even the radial growth of a crystal of protein...etc.). Stokes and lubrication approximations are considered which allows us to develop a simple matched asymptotic method for the prediction of the azimuthal surface velocity. A closed-form analytical formulation of the shear stresses, both at the liquid surface and along it, is put forward for the first time, which insures accurate estimation of the Boussinesq number ($10^{-1} \leq Bo \leq 10^{-4}$ is investigated). Despite its simplicity, the asymptotic model is also proved to take fair account of a stratified surface viscosity. As an example, a radial segregation between two stratifying phases covering the surface of a liquid bath is taken into account by way of a surface viscosity which is chosen to depend on the radial direction. Special attention is paid to describe the particular situation of a diffusive front which separates both phases with a more condensed phase located along the liquid surface in the inner part of the channel gap. Not surprisingly, the maximum of the surface velocity moves radially outwards where the surface viscosity is the smallest. The shape of the velocity profile along the liquid surface as well as the value and the radial location of the maximum of surface velocity are completely different from any prediction which could be made from the approximation of a uniform surface viscosity. Therefore, a simple measurement of the surface velocity, from particle tracking velocimetry for instance, is expected to deliver a fair estimation of the radial extent of a growing condensed phase (a 2-D crystal of protein, typically).

Outlook

This dissertation has demonstrated the validity of a new hydrodynamical process to control and monitor the flow-induced reorganization of a Langmuir film of biological molecules spread over a liquid surface. At short term, our results should help to investigate the flow-assisted two-dimensional growth of a crystal protein at a air-water interface functionalized by a monolayer of lipids. In order to mimic the hydrodynamic behavior of a air-water interface covered by a film of lipids, we chose to work prior with a well-known fatty acid as a model system, referred to as pentadecanoic acid (PDA) in the dedicated literature. The non-equilibrium behavior of a Langmuir monolayer of PDA subjected to a centripetal flow has revealed to be in itself a complex matter: as shown in Chapter 5 of this dissertation, the LM reorganisation can be understood from the interplay between three hydrodynamical mechanisms (3-D shearing, 2-D shearing, surface pressure dynamics) and one physico-chemical mechanism (line tension). This is only now that the conditions are gathered to consider the investigation of the flow-assisted self-assembly of a monolayer of lipids. Then, as a further step, it should be possible to include the phenomenon of protein adsorption to these lipids provided their hydrophilic termination is suitably functionalised. In that case, it could be necessary to introduce three additional chemical mechanisms: 3-D diffusion of proteins in the subphase up to (or from) the liquid surface, adsorption (desorption) of the proteins to (from) the lipids, 2-D diffusion of the molecular complexes [lipids+proteins] along the liquid surface. Here again, analytics developed in Chapter 6 should be extended in order to take into account the coupling with previous chemical kinetics and to be relevant to the analysis of crystal growth experiments in 2-D. Here again, the delicate balance between a monitored centripetal compression along the liquid surface (in favor with a crystal growth), and the destabilizing shearing (in favor with crystal melting), could be analyzed and controlled by following the main lines of the strategy put in place during this dissertation.

References

[1] N. K. Adam. The properties and molecular structure of thin films. Part II.—Condensed films. *Proc. R. Soc. London, Ser. A*, 101(712):452–472, 1922.

[2] A. W. Adamson and A. P. Gast. *Physical chemistry of surfaces*. John Wiley & Sons, Inc., New York, sixth edition, 1997.

[3] S. Akamatsu and F. Rondelez. Fluorescence microscopy evidence for two different LE-LC phase transitions in Langmuir monolayers of fatty acids. *J. Phys. II France*, 1(10):1309–1324, 1991.

[4] J.C. Alexander, A. Bernoff, E. Mann, J. Adin Mann Jr., J.R. Wintersmith, and L. Zou. Domain relaxation in langmuir films. *J. Fluid Mech.*, 571:191–219, 2007.

[5] J. M. Andreas, E. A. Hauser, and W. B. Tucker. Boundary tension by pendant drops. *J. Phys. Chem.*, 42(8):1001, 1938.

[6] R. Aris. *Vectors, Tensors, and Basic Equations of Fluid Mechanics*. Dover books on engineering. Dover Publications, New York, 1990.

[7] Kendall E. Atkinson and Lawrence F. Shampine. Algorithm 876: Solving fredholm integral equations of the second kind in matlab. *ACM Trans. Math. Softw.*, 34(4):1–20, 2008.

[8] R. Aveyard, B. P. Binks, N. Carr, and A. W. Cross. Stability of insoluble monolayers and ionization of langmuir-blodgett multilayers of octadecanoic acid. *Thin Solid Films*, 188(2):361–373, 1990.

[9] A. N. Azadani, J. M. Lopez, and A. H. Hirsa. Protein crystallization at the air/water interface induced by shearing bulk flow. *Langmuir*, 23(10):5227–5230, 2007.

[10] A. N. Azadani, J. M. Lopez, and A. H. Hirsa. Coupling between protein-laden films and a shearing bulk flow. *J. Colloid Interface Sci.*, 322(1):79–86, 2008.

[11] R. M. A. Azzam and N. M. Bashara. *Ellipsometry and polarized light*. North Holland Physics, Amsterdam, first edition, 1977.

[12] C. Barentin, C. Ybert, J.-M. di Meglio, and J.-F. Joanny. Surface shear viscosity of gibbs and langmuir monolayers. *J. Fluid Mech.*, 397:331–349, 1999.

[13] G. Barnes and I. Gentle. *Interfacial Science an Introduction*. Oxford University Press, 2005.

[14] D. Beaglehole. Ellipsometric study of the surface of simple liquids. *Physica B*, 100:163–174, 1980.

[15] D. Beaglehole. Performance of a microscopic imaging ellipsometer. *Rev. Sci. Instrum.*, 59(12):2557–2559, 1988.

[16] D. J. Benvegnu and H. M. McConnell. Line tension between liquid domains in lipid monolayers. *J. Phys. Chem.*, 96(16):6820–6824, 1992.

[17] H. Bercegol, F. Gallet, D. Langevin, and J Meunier. Coexistence of an ordered anisotropic phase and a liquid expanded phase in an amphiphilic monolayer. *J. Phys. France*, 50(16):2277–2289, August 1989.

[18] A. M. Bibo, C. M. Knobler, and I. R. Peterson. A monolayer phase miscibility comparison of long-chain fatty acids and their ethyl esters. *J. Phys. Chem.*, 95(14):5591–5599, 1991.

[19] A.M. Bibo and I.R. Peterson. Phase diagrams of monolayers of the long chain fatty acids. *Adv. Mater.*, 2(6-7):309–311, 1990.

[20] B. P. Binks. Insoluble monolayers of weakly ionising low molar mass materials and their deposition to form langmuir-blodgett multilayers. *Adv. Colloid Interface Sci.*, 34:343–432, 1991.

[21] T. M. Bohanon, B. Lin, M. C. Shih, G. E. Ie, and P. Dutta. Determination of lattice structure and calculation of molecular tilt in lipid monolayers on water using x-ray diffraction. *Phys. Rev. B*, 41(9):4846–4849, 1990.

[22] A.G. Bois, M.G. Ivanova, and I.I. Panaiotov. Marangoni effect and relaxations of surface potential in pentadecanoic acid and octadecanol monolayers. *Langmuir*, 3:215–217, 1987.

[23] M. J. Boussinesq. The application of the formula for surface viscosity to the surface of a slowly falling droplet in the midst of a large unlimited amount of fluid which is at rest and possesses a smaller specific gravity. *Ann. Chim. Phys.*, 29:357, 1913.

[24] D. Brewster. On the laws which regulate the polarisation of light by reflexion from transparent bodies. *Philos. Trans. R. Soc. London*, 105:125–159, 1815.

[25] A. Brisson, W. Bergsma-Schutter, F. Oling, O. Lambert, and I. Reviakine. Two-dimensional crystallization of proteins on lipid monolayers at the air/water interface and transfer to an electron microscopy grid. *J. Cryst. Growth*, 196:456–470, 1999.

[26] J. H. Brooks and A. E. Alexander. Spreading and collapse phenomena in the fatty alcohol series. *J. Phys. Chem.*, 66(10):1851 – 1853, 1962.

[27] R. A. Burton and R. J. mannheimer. Ordered fluids and liquid crystals. *Adv. Chem. Ser.*, 63:315–328, 1967.

[28] C.W. Frank C.F. Brooks, G.C. Fuller and C. R. Robertson. An interfacial stress rheometer to study rheological transitions in monolayers at the air-water interface. *Langmuir*, 15:2450–2459, 1999.

[29] Y. Lane Chen, M. Sano, M. Kawaguchi, H. Yu, and G. Zografi. Static and dynamic properties of pentadecanoic acid monolayers at the air-water interface. *Langmuir*, 2(3):349–354, 1986.

[30] S. A. Darst, M. Ahlers, P. H. Meller, E. W. Kubalek, R. Blankenburg, H. O. Ribi, H. Ringsdorf, and R. D. Kornberg. Two-dimensional crystals of streptavidin on biotinylated lipid layers and their interactions with biotinylated macromolecules. *Biophys. J.*, 59(2):387–396, 1991.

[31] J. T. Davies. A quantitative kinetic theory of emulsion type, I. Physical chemistry of the emulsifying agent. *Proc. 2nd Int. Congr. Surface Activity*, 1:426–438, 1957.

[32] L. Davoust, Y.-L. Huang, and S.-H. Chang. Flow-induced melting of condensed domains within a dispersed langmuir film. *Phys. Fluids*, 20(8):082105–082105–8, 2008.

[33] R. de Koker, W. Jiang, and H.M. McConnell. Instabilities of the stripe phase in lipid monolayers. *J. Phys. Chem.*, 99:6251–6257, 1995.

[34] R. de Koker and H.M. McConnell. Circle to dogbone: shapes and shape transitions of lipid monolayer domains. *J. Phys. Chem.*, 97:13419–13424, 1993.

[35] D. G. Dervichian. Changes of phase and transformations of higher order in monolayers. *J. Chem. Phys.*, 7(10):931–948, 1939.

[36] J.M. Deutch and F.E. Low. Theory of shape transitions of two-dimensional domains. *J. Phys. Chem.*, 96:7097–7101, 1992.

[37] Junqi Ding, Heidi E. Warriner, Joseph A. Zasadzinski, and Daniel K. Schwartz. Magnetic needle viscometer for langmuir monolayers. *Langmuir*, 18(7):2800–2806, 2002.

[38] L. Drazek. *Contrôle par l'hydrodynamique de l'assemblage 2-D de protéines dans une interface eau-air. Modélisation, premières expériences.* PhD Thesis, Université Joseph Fourier - Grenoble I, Laboratoire des Ecoulements Géophysiques et Industriels de Grenoble, 2004.

[39] L. Drazek, J.-F. Legrand, and L. Davoust. A first attempt to enhance the 2-d single-crystal growth of a protein at an air/water interface from hydrodynamics. *J. Cryst. Growth*, 275(1-2):e1467–e1472, 2005.

[40] P. K. L. Drude. Über die reflexion und brechung ebener lichtweelen beim durchgang durch eine mit oberflächenschichten behaftete planparallel platte. *Ann. Phys.*, 43:126–157, 1891.

[41] P. Lecomte du Noüy. A new apparatus for measuring surface tension. *J. Gen. Physiol.*, 1:521–524, 1919.

[42] DuPont Company, U.S.A. *Du Pont Delrin acetal resin Design Guide—Module III.*

[43] M. K. Durbin, A. Malik, A. G. Richter, R. Ghaskadvi, T. Gog, and P. Dutta. Transitions to a new chiral phase in a langmuir monolayer. *J. Chem. Phys.*, 106(19):8216–8220, 1997.

[44] M.K. Durbin, A. Malik, R. Ghaskadvi, P. Zschack M.C. Shih, and P. Dutta. X-ray diffraction study of a recently identified phase transition in fatty acid Langmuir monolayers. *J. Phys. Chem.*, 98(7):1753–1755, 1994.

[45] J. C. Earnshaw and P. J. Winch. Viscoelasticity of monolayers of n-pentadecanoic acid: a light scattering study. *J. Phys.: Condens. Matter*, 2(42):8499–8516, 1990.

[46] D. A. Edwards, H. Brenner, and B. T. Wasan. *Interfacial transport processes and rheology.* Butterworth-Heinemann, Boston, first edition, 1991.

[47] V. B. Fainerman and D. Vollhardt. Surface pressure isotherm for the fluid state of langmuir monolayers. *J. Phys. Chem. B*, 110(21):10436–10440, 2006.

[48] V. B. Fainerman, D. Vollhardt, and V. Melzer. Equation of state for insoluble monolayers of aggregating amphiphilic molecules. *J. Phys. Chem.*, 100(38):15478–15482, 1996.

[49] B. Fischer, M.-W. Tsao, J. Ruiz-Garcia, T. M. Fischer, D. K. Schwartz, and C. M. Knobler. Observation of a change from splay to bend orientation at a phase transition in a langmuir monolayer. *J. Phys. Chem.*, 98(31):7430–7435, 1994.

[50] W. Frey, W. R. Schief Jr., D. W. Pack, C.-T. Chen, A. Chilkoti, P. Stayton, V. Vogel, and F. H. Arnold. Two-dimensional protein crystallization via metal-ion coordination by naturally occuring surface histidines. *Proc. Nat. Acad. Sci. U.S.A.*, 93:4937–4941, 1996.

[51] G. L. Gaines. *Insoluble Monolayers at Liquid-Gas Interfaces.* Interscience. Wiley, New York, 1966.

[52] A. P. Gast, C. R. Robertson, S.-W. Wang, and M. T. Yatcilla. Two-dimensional streptavidin crystals: macropatterns and micro-organization. *Biomol. Eng.*, 16:21–27, 1999.

[53] H. E. Gaub, V. T. Moy, and H. M. McConnell. Reversible formation of plastic two-dimensional lipid crystals. *J. Phys. Chem.*, 90(8):1721–1725, 1986.

[54] R. S. Ghaskadvi, Sharon Carr, and Michael Dennin. Effect of subphase ca^{++} ions on the viscoelastic properties of langmuir monolayers. *J. Chem. Phys.*, 111(8):3675–3678, 1999.

[55] R. S. Ghaskadvi and Michael Dennin. Alternate measurement of the viscosity peak in heneicosanoic acid monolayers. *Langmuir*, 16(26):10553–10555, 2000.

[56] R. S. Ghaskadvi, J. B. Ketterson, and P. Dutta. Nonlinear shear response and anomalous pressure dependence of viscosity in a langmuir monolayer. *Langmuir*, 13(19):5137–5140, 1999.

[57] J. W. Gibbs. On the equilibrium of heterogeneous substances. *Trans. Conn. Acad.*, 3:343–524, 1878.

[58] F. C. Goodrich. The theory of absolute shear viscosity. i. *Proc. R. Soc. London, Ser. A*, 310:359–372, 1969.

[59] G. W. Gray and J. W. Goodby. *Smectic Liquid Crystals: Textures and Structures*. World Science, Singapore, 1988.

[60] N. J. Hardy, T. H. Richardson, and F. Grunfeld. Minimising monolayer collapse on langmuir troughs. *Colloids Surf., A*, 284-285(15):202–206, 2006.

[61] W. D. Harkins. *The physical chemistry of surface films*. Reinhold New York, New York, 1952.

[62] W. D. Harkins and E. Boyd. The states of monolayers. *J. Phys. Chem.*, 45(1):20–43, 1941.

[63] W. D. Harkins and F. E. Brown. The determination of surface tension (free surface energy), and the weight of falling drops: the surface tension of water and benzene by the capillary height method. *J. Am. Chem. Soc*, 41(4):499–524, 1919.

[64] W. D. Harkins and L. E. Copeland. A superliquid in two dimensions and a first-order change in a condensed monolayer i. energy, compressibility, and order of phase transformations. *J. Chem. Phys.*, 10(5):272–286, 1942.

[65] W. D. Harkins and R. J. Meyers. Viscosity of monomolecular films. *Nature*, 140:465, 1937.

[66] W. D. Harkins, T. F. Young, and E. Boyd. The thermodynamics of films: Energy and entropy of extension and spreading of insoluble monolayers. *J. Chem. Phys.*, 8(12):954–965, 1940.

[67] P. Heinig and D. Langevin. Domain shape relaxation and local viscosity in stratifying foam films. *Eur. Phys. J. E.*, 18(12):483–488, 2005.

[68] S. A. Hemming, A. Bochkarev, S. A. Darst, R. D. Kornberg, P. A., D. S. C. Yang, and A. M. Edwards. The mechanism of protein crystal growth from lipid layers. *J. Mol. Biol.*, 246(2):308–316, 1995.

[69] S. Hénon. *Microscopie à l'angle de Brewster : transitions de phases et défauts d'orientation dans des films monomoléculairess*. PhD Thesis, Université Paris VI, 1993.

[70] S. Hénon and J. Meunier. Microscope at the Brewster angle: Direct observation of first-order phase transitions in monolayers. *Rev. Sci. Instrum.*, 62(4):936–939, 1991.

[71] A. H. Hirsa, J. M. Lopez, and R. Miraghaie. Determination of surface shear viscosity via deep-channel flow with inertia. *J. Fluid Mech.*, 470:135–149, 2002.

[72] A. H. Hirsa, J. M. Lopez, M. J. Vogel, and J. F. Leung. Effects of shearing flow with inertia on monolayer mesoscale structure. *Langmuir*, 22(23):9483 –9486, 2006.

[73] D. Hönig and D. Möbius. Direct visualization of monolayers at the air-water interface by brewster angle microscopy. *J. Phys. Chem.*, 95(12):4590–4592, 1991.

[74] D. Hönig, G. A. Overbeck, and D. Möbius. Morphology of pentadecanoic acid monolayers at the air/water interface studied by BAM . *Adv. Mater.*, 4(6):419–424, 1992.

[75] J. Ignés-Mullol and D. K. Schwartz. Alignment of hexatic Langmuir monolayers under shear. *Phys. Rev. Lett.*, 85(7):1476–1479, 2000.

[76] J. Ignés-Mullol and D. K. Schwartz. Molecular orientation in langmuir monolayers under shear. *Langmuir*, 17(10):3017–3029, 2001.

[77] J. Ignés-Mullol and D. K. Schwartz. Shear-induced molecular precession in a hexatic langmuir monolayer. *Nature*, 410(6826):348–351, 2001.

[78] J. Israelachvili. Self-assembly in two Dimensions: surface micelles and domain formation in monolayers. *Langmuir*, 10(10):3774–3781, 1994.

[79] A. Ivanova, M. Levent Kurnaz, and D. K. Schwartz. Temperature and flow rate dependence of the velocity profile during channel flow of a langmuir monolayer. *Langmuir*, 15(13):4622–4624, 1999.

[80] M. Iwahashi, N. Maehara, Y. Kaneko, T. Seimiya, S. R. Middleton, N. R. Pallas, and B. A. Pethica. Spreading pressures for fatty-acid crystals at the air/water interface. *J. Chem. Soc., Faraday Trans. 1*, 81(4):973–981, 1985.

[81] A. Jákli and A. Saupe. *One- and Two- Diemnsional Fluids, Properties of Smectic, Lamellar and Columnar Liquid Crystals*. Condensed Matter Physics. Taylor & Francis Group, 2006.

[82] A.J. Jerri. *Introduction to integral equations with applications*. John Wiley & Sons, second edition, 1999.

[83] R. Johann. *Thermodynamic, morphological and structural properties of dissociated fatty acid monolayers at the air-water interface*. PhD Thesis, Universität Potsdam, Mathematisch-Naturwissenschaftlichen Fakultät, Mar 2001.

[84] V. M. Kaganer and E. B. Loginov. Symmetry and phase transitions in langmuir monolayers: The landau theory. *Phys. Rev. E*, 51(3):2237–2249, Mar 1995.

[85] V. M. Kaganer, H. Möhwald, and P. Dutta. Structure and phase transitions in Langmuir monolayers. *Rev. Mod. Phys.*, 71(3):779–819, 1999.

[86] D. J. Keller, J. P. Korb, and H. M. McConnell. Theory of shape transitions in two-dimensional phospholipid domains. *J. Phys. Chem.*, 91(25):6417–6422, 1987.

[87] B. M. J. Kellner, F. Müller-Landau, and D. A. Cadenhead. The temperature-dependence characterization of insoluble films at the air-water interface. *J. Colloid Interface Sci.*, 66(3):597–601, 1978.

[88] R. M. Kenn, C. Bohm, A. M. Bibo, I. R. Peterson, and H. Möhwald. Mesophases and crystalline phases in fatty acid monolayers. *J. Phys. Chem.*, 95(5):2092–2097, 1991.

[89] A. Neil Kensington. *The physics and chemistry of surfaces*. Oxford University Press, London, third edition, 1941.

[90] M. Won Kim and D. S. Cannell. Experimental study of a two-dimensional gas-liquid phase transition. *Phys. Rev. A*, 13(1):411–416, 1976.

[91] M. Won Kim and D. S. Cannell. Surface potential of a two-dimensional film of pentadecanoic acid in the coexistence region. *Phys. Rev. A*, 14(3):1299–1300, 1976.

[92] K. Kjaer, J. Als-Nielsen, P. Tippmann-Krayer, and H. Möhwald. Synchrotron x-ray diffraction and reflection studies of arachidic acid monolayers at the air-water interface. *J. Phys. Chem.*, 93(8):3200–3206, 1989.

[93] J.F. Klingler and H.M. McConnell. Brownian motion and fluid mechanics of lipid monolayer domains. *J. Phys. Chem.*, 97:6096–6100, 1993.

[94] C. M. Knobler. Seeing phenomena in flatland: Studies of monolayers by fluorescence microscopy. *Science*, 249(4971):870–874, 1990.

[95] C.M. Knobler and Rashmi C. Desai. Phase transitions in monolayers. *Annu. Rev. Phys. Chem.*, 43(1):207–236, 1992.

[96] I. Langmuir. The constitution and fundamental properties of solids and liquids. *J. Am. Chem. Soc.*, 39(9):1848–1906, 1917.

[97] I. Langmuir. Oil lenses on water and the nature of monomolecular expanded films. *J. Chem. Phys.*, 1(11):756–776, 1933.

[98] K.Y.C. Lee and H. M. McConnell. Quantized symmetry of liquid monolayer domains. *J. Phys. Chem.*, 97:9532–9539, 1993.

[99] P-F. Lenne, B. Berge, A. Renault, C. Zakri, C. Venien-Bryan, S. Courty, F. Balavoine, W. Bergsma-Schutter, A. Brisson, G. Grübel, N. Boudet, O. Konovalov, and J.-F. Legrand. Synchrotron radiation diffraction from two-dimensional protein crystals at the air/water interface. *Biophys. J.*, 79(1):496–500, 2000.

[100] C. Lheveder, S. Hénon, R. Mercier, G. Tissot, P. Fournet, and J. Meunier. A new Brewster angle microscope. *Rev. Sci. Instrum.*, 69(3):1446–1450, 1998.

[101] J. Li, R. Miller, W. Wüstneck, H. Möhwald, and A. W. Neumann. Use of pendent drop technique as a film balance at liquid/liquid interfaces. *Colloids Surf., A*, 96:295–299, 1995.

[102] D. R. Lide, editor. *Handbook of Chemistry and Physics*. CRC Press, 87th edition, 2006-2007.

[103] B. Lin, M. C. Shih, TM Bohanon, G. E. Ice, and P. Dutta. Phase diagram of a lipid monolayer on the surface of water. *Phys. Rev. Lett.*, 65(2):191–194, 1990.

[104] S. Y. Lin, K. McKeigue, and C. Maldarelli. Diffusion-limited interpretation of the induction period in the relaxation in surface tension due to the adsorption of straight chain, small polar group surfactants: theory and experiment. *Langmuir*, 7(6):1055 – 1066, 1991.

[105] J. M. Lopez and A. Hirsa. Direct determination of the dependence of the surface shear and dilatational viscosities on the thermodynamic state of the interface: Theoretical foundations. *J. Colloid Interface Sci.*, 206(1):231–239, 1998.

[106] M. Lösche, H. P. Duwe, and H. Möhwald. Quantitative analysis of surface textures in phospholipid monolayer phase transitions. *J. Colloid Interface Sci.*, 126(2):432–444, 1988.

[107] M. Lundquist. Relation between polymorphism in "two-dimensional" monomolecular films on water to polymorphism in the three-dimensional state, and the formation of multimolecular films on water. I. n-Alkyl acetates. *Chem. Scr.*, 1(1):5–20, 1971.

[108] M. Lundquist. Relation between polymorphism in two-dimensional monomolecular films on water to polymorphism in the three-dimensional state, and the formation of multimolecular films on water. ii. ethyl esters of n-aliphatic acids. *Chem. Scr.*, 1(5):197–209, 1971.

[109] E. K. Mann, S. Heéron, D. Langevin, and J. Meunier. Molecular layers of a polymer at the free water surface: microscopy at the Brewster angle. *J. Phys. II France*, 2:1683–1704, 1992.

[110] E. K. Mann, S. Hénon, D. Langevin, J. Meunier, and L. Léger. Hydrodynamics of domain relaxation in a polymer monolayer. *Phys. Rev. E*, 51(6):5708–5720, Jun 1995.

[111] R. J. Mannheimer and R. S. Schechter. A comparison of linear and annular canal viscometers for surface rheological measurements. *J. Colloid Interface Sci.*, 27(2):324–327, 1968.

[112] R. J. Mannheimer and R. S. Schechter. An improved apparatus for surface rheological measurement. *J. Colloid Interface Sci.*, 32(2):195, 1970.

[113] C. G. M. Marangoni. Uber die ausbreitung der tropfen einer flussigkeit auf der oberfluche einer anderen. *Ann. Phys.*, 3:337–354, 1871.

[114] T. Maruyama, G. Fuller, C. Frank, and C. Robertson. Flow-induced molecular orientation of a langmuir film. *Science*, 274(5285):233–235, 1996.

[115] T. Maruyama, J. Lauger, G. G. Fuller, C. W. Frank, and C. R. Robertson. Orientation in a fatty acid monolayer: Effect of flow type. *Langmuir*, 14(7):1836–1845, 1998.

[116] H.M. McConnell. Structures and transitions in lipid monolayers at the air-water interface. *Annu. Rev. Phys. Chem*, 42:171–195, 1991.

[117] H.M. McConnell and V. Moy. Shapes of finite two-dimensional lipid domains. *J. Phys. Chem.*, 92:4520–4525, 1988.

[118] S. R. Middleton, M. Iwahashi, N. R. Pallas, and B. A. Pethica. Absolute surface manometry: thermodynamic fixed points for air-water monolayers of pentadecanoic acid at 25°c. *Proc. R. Soc. London, Ser. A*, 396(1810):143–154, 1984.

[119] R. Miller, P. Joos, and V. B. Fainerman. *Prog. Colloid Polym. Sci.*, 97:188, 1994.

[120] L. Ter Minassian-Saraga. Recent work on spread monolayers, adsorption and desorption. *J. Colloid Sci.*, 11(4-5):398–418, 1956.

[121] R. Miraghaie, J.M. Lopez, and A.H. Hirsa. Flow induced patterning at the air-water interface. *Phys. Fluids*, 15(6):597–604, 2003.

[122] B. G. Moore, C.M. Knobler, S. Akamatsu, and F. Rondelez. Phase diagram of Langmuir monolayers of pentadecanoic acid: quantitative comparison of surface pressure and fluorescence microscopy results. *J. Phys. Chem.*, 94(11):4588–4595, 1990.

[123] P. Muller and F. Gallet. First measurement of the liquid-solid line energy in a Langmuir monolayer. *Phys. Rev. Lett.*, 67(9):1106–1109, 1991.

[124] C. A. Murray. *Experimental studies of melting and hexatic order in two-dimensional colloidal suspensions,in Bond-orientational order in condensed matter systems*. Springer-Verlag, New York, 1992.

[125] Nanofilm surface analysis, Anna-Vandenhoeck-Ring 5 D-37081 Göttingen Germany. *I-Elli2000 imaging ellipsometer hypertext user manual*, 4 edition, 2004.

[126] A. H. Nayfeh. *Perturbation Methods*. Wiley-Interscience, New-York, 1973.

[127] S.-G. Oh and J. C. Slattery. Disk and biconical interfacial viscometers. *J. Colloid Interface Sci.*, 67(3):516–525, 1978.

[128] G. A. Overbeck, D. Hönig, and D. Möbius. Visualization of first- and second-order phase transitions in eicosanol monolayers using Brewster angle microscopy. *Langmuir*, 9(2):555–560, 1993.

[129] G. A. Overbeck and D. Moebius. A new phase in the generalized phase diagram of monolayer films of long-chain fatty acids. *J. Phys. Chem.*, 97(30):7999–8004, 1993.

[130] N. R. Pallas and B. A. Pethica. Liquid-expanded to liquid-condensed transition in lipid monolayers at the air/water interface. *Langmuir*, 1(4):509–513, 1985.

[131] N. R. Pallas and B. A. Pethica. The liquid–vapour transition in monolayers of n-pentadecanoic acid at the air/water interface. *J. Chem. Soc., Faraday Trans. 1*, 83(3):585–590, 1987.

[132] I. R. Peterson, V. Brzezinski, R. M. Kenn, and R. Steitz. Equivalent states of amphiphilic lamellae. *Langmuir*, 8(12):2995–3002, 1992.

[133] M. C. Petty. *Langmuir-Blodgett Films an Introduction*. Cambridge University Press, 1996.

[134] A. J. Pintar. *The measurement of surface viscosity*. PhD thesis, Illinois Institute of Technology, 1968.

[135] A. J. Pintar, A. B. Israel, and D. T. Wasan. Interfacial shear viscosity phenomena in solutions of macromolecules. *J. Colloid Interface Sci.*, 37(1):52–67, 1971.

[136] J. Plateau. Experimental and theoretical researches into the figures of equilibrium of a liquid mass without weight VIII. Researches into the causes upon which the easy developemnt and the presistence of liquid films depend. — On the superficial tension of liquids. — On a new principle relating to the surfaces of liquid. *Phil. Mag.*, 38(4):445–455, 1869.

[137] A. Pockels. Letter to the editor. *Nature*, 43:437–439, 1891.

[138] A. Poskanzer and F. C. Goodrich. A new surface viscometer of high sensitivity: Ii. experiments with stearic acid monolayers. *J. Colloid Interface Sci.*, 52(2):213–221, 1975.

[139] X. Qiu, J. Ruiz-Garcia, and C.M. Knobler. Domain structures and phase transitions in Langmuir monolayers . *Mater. Res. Soc. Symp. Proc.*, 237:263–270, 1992.

[140] X. Qiu, J. Ruiz-Garcia, K. J. Stine, C.M. Knobler, and J. V. Selinger. Direct observation of domain structure in condensed monolayer phases. *Phys. Rev. Lett.*, 67(6):703–706, 1991.

[141] Lord Rayleigh. Investigations in capillarity. *Phil. Mag.*, 48:321–330, 1899.

[142] W. Rettig and F. Kuschel. Spreading and compression of n-hexadecyl acrylate at liquid-air interface. *Colloid Polym. Sci.*, 267(2):151–158, 1989.

[143] I. Reviakine and A. Brisson. Streptavidin 2D crystals on supported phospholipid bilayers: Toward constructing anchored phospholipid bilayers. *Langmuir*, 17:8293–8299, 2001.

[144] P. A. Rice and H. M. McConnell. Critical shape transitions of monolayer lipid domains. *Proc. Nat. Acad. Sci. U.S.A.*, 86(17):6445–6448, 1989.

[145] T. W. Richards and E. K. Caver. A critical study of the capillary rise method of determining surface tension, with data for water, benzene, toluene, chloroform, carbon tetrachloride, ether and dimethyl aniline. *J. Am. Chem. Soc.*, 43(4):827–847, 1921.

[146] S. Rivière, S. Hénon, J. Meunier, G. Albrecht, M. M. Boissonnade, and A. Baszkin. Electrostatic pressure and line tension in a Langmuir monolayer. *Phys. Rev. Lett.*, 75(13):2506–2509, 1995.

[147] S. Rivière, S. Hénon, J. Meunier, D. K. Schwartz, M.-W. Tsao, and C. M. Knobler. Textures and phase transitions in langmuir monolayers of fatty acids. a comparative brewster angle microscope and polarized fluorescence microscope study. *J. Chem. Phys.*, 101(11):10045–10051, dec 1994.

[148] E. Ruckenstein and B. Li. Surface equation of state for insoluble surfactant monolayers at the air/water interface. *J. Phys. Chem. B*, 102(6):981 –989, 1998.

[149] A.I. Rusanov. Classification of line tension. *Colloids Surf., A*, 156:315–322, 1999.

[150] D. K. Schwartz. Mechanisms and kinetics of self-assembled monolayer formation. *Annu. Rev. Phys. Chem.*, 52(1):107–137, 2001.

[151] D. K. Schwartz, C. M. Knobler, and R. Bruinsma. Direct observation of Langmuir monolayer flow through a channel. *Phys. Rev. Lett.*, 73(21):2841–2844, 1994.

[152] D. K. Schwartz, M. L. Schlossman, and P. S. Pershan. Re-entrant appearance of phases in a relaxed langmuir monolayer of tetracosanoic acid as determined by x-ray scattering. *J. Chem. Phys.*, 96(3):2356–2370, feb 1992.

[153] D.K. Schwartz and C.M. Knobler. Direct observations of transitions between condensed Langmuir monolayer phases by polarized fluorescence microscopy. *J. Phys. Chem.*, 97(35):8849–8851, 1993.

[154] L. E. Scriven. Dynamics of a fluid interface-equation of motion for newtonian surface fluids. *Chem. Eng. Sci.*, 12(2):98–108, 1960.

[155] M. C. Shih, T. M. Bohanon, J. M. Mikrut, P. Zschack, and P. Dutta. X-ray-diffraction study of the superliquid region of the phase diagram of a Langmuir monolayer. *Phys. Rev. A*, 45(8):5734–5737, apr 1992.

[156] J. C. Slattery. *Interfacial transport phenomena*. Springer-Verlag, New York, 1990.

[157] R. D. Smith and J. C. Berg. The collapse of surfactant monolayers at the air-water interface. *J. Colloid Interface Sci.*, 74(1):273–286, 1980.

[158] T. Smith. Monolayers on water iii. kinetics and mechanism of the reaction of erucic acid with copper ions. *J. Colloid Interface Sci.*, 25(4):443–461, 1967.

[159] I. Stackgold. *Boundary value problems of mathematical physics*, volume 1 of *Classics in Applied Mathematics*. SIAM, 2000.

[160] S. Ställberg-Stenhagen and E. Stenhagen. Phase transitions in condensed monolayers of normal chain carboxylic acids. *Nature*, 156:239, 1945.

[161] H. E. Stanley. *Introduction to Phase Transitions and Critical Phenomena*. Oxford University Press, 1971.

[162] P. Steffen, P. Heinig, S. Wurlitzer, Z. Khattari, and T.M. Fisher. The translational and rotational drag on langmuir monolayer domains. *J. Chem. Phys.*, 115(2):994–997, 2001.

[163] E. Stenhagen. *Determination of Organic Structures by Physical Methods*. Acadimic Press, New York, 1955.

[164] C. V. Sternling and L. E. Scriven. Interfacial turbulence: hydrodynamic instability and the Marangoni effect. *AIChE J.*, 5:514–523, 1959.

[165] K. J. Stine, C. M. Knobler, and R. C. Desai. Buckling instability in monolayer network structures. *Phys. Rev. Lett.*, 65(8):1004–1007, 1990.

[166] K. J. Stine, S. A. Rauseo, B. G. Moore, J. A. Wise, and C. M. Knobler. Evolution of foam structures in Langmuir monolayers of pentadecanoic acid. *Phys. Rev. A*, 41(12):6884–6892, 1990.

[167] H. A. Stone and H. M. McConnell. Hydrodynamics of quantized shape transitions of lipid domains. *Proceedings of the Royal Society: Mathematical and Physical Sciences (1990-1995)*, 448(1932):97–111, 1995.

[168] K. A. Suresh, J. Nittmann, and F. Rondelez. Pattern formation during phase transition in Langmuir monolayers near critical temperature. *Europhys. Lett.*, 6(5):437–443, 1988.

[169] K. L. Sutherland. The oscillating jet method for the measurement of surface tension. *Aust. J. Chem.*, 7(7):319–328, 1954.

[170] T. Tate. On the magnitude of a drop of liquid formed under different circumstances. *Phil. Mag.*, 27:176–180, 1864.

[171] P. Tippmann-Krayer and H. Möhwald. Precise determination of tilt angles by x-ray diffraction and reflection with arachidic acid monolayers. *Langmuir*, 7(10):2303–2306, 1991.

[172] H. G. Tompkins. *A user's guide to elipsometry*. Harcourt Brace Jovanovich, San Diego, 1993.

[173] Harland G. Tompkins and William A. McGahan. *Spectroscopic ellipsometry and reflectometry: A user's guide*. John Wiley & Sons, Inc., New York, 1999.

[174] M.-W. Tsao. *Studies on molecular orientation of Langmuir monolayers*. PhD thesis, University of California, Los Angeles, 1994.

[175] D. S. Valkovska and K. D. Danov. Determination of bulk and surface diffusion coefficients from experimental data for thin liquid film drainage. *J. Colloid Interface Sci.*, 223:314–316, 2000.

[176] C. Vénien-Bryan, P.-F. Lenne, C. Zakri, A. Renault, A. Brisson, J.-F. Legrand, and B. Berge. Characterization of the growth of 2D protein crystals on a lipid monolayer by ellipsometry and rigidity measurements coupled to electron microscopy. *Biophys. J.*, 74(5):2649–2657, 1998.

[177] M. J. Vogel. *Measurements of monolayer hydrodynamics at air/water interface.* PhD thesis, Rensselaer Polytechnic Institute, New York, July 2002.

[178] M.J. Vogel, R. Miraghaie, J.M. Lopez, and A.H. Hirsa. Flow-induced patterning of langmuir monolayers. *Langmuir*, 20(14):5651 – 5654, 2004.

[179] S.-W. Wang, C. Robertson, and A. Gast. Role of N-and C-terminal amino acids in two-dimensional streptavidin crystal formation. *Langmuir*, 16(11):5199–5204, 2000.

[180] D. T. Wasan, L. Gupta, and M. K. Vora. Interfacial shear viscosity at fluid-fluid interfaces. *AIChE J.*, 17(6):1287–1295, 1971.

[181] R.M. Weis and H. M. McConnell. Two-dimensional chiral crystals of phospholipid. *Nature*, 310(8):47–49, 1984.

[182] F. M. White. *Viscous fluid flow.* McGraw-Hill, second edition, 1991.

[183] L. Wilhelmy. Ueber die abhangigkeit der. capillaritats-constanten des alkohols von substanz und. gestalt des benetzten festen korpers. *Ann. Phys.*, 119:177–217, 1863.

[184] P. J. Winch and J. C. Earnshaw. A light scattering study of phase transitions in monolayers of n-pentadecanoic acid. *J. Phys.: Condens. Matter*, 1:7187–7250, 1989.

[185] S. Wurlitzer, P. Steffen, and Th. M. Fischer. Line tension of langmuir monolayer phase boundaries determined with optical tweezers. *J. Chem. Phys.*, 112(12):5915–5918, 2000.

[186] S. Wurlitzer, P. Steffen, M. Wurlitzer, Z. Khattari, and Th. M. Fischer. Line tension in langmuir monolayer probed by point forces. *J. Chem. Phys.*, 113(9):3822–3828, 2000.

[187] C. Ybert, W. Lu, G. Moller, and C.M. Knobler. Collapse of a monolayer by three mechanisms. *J. Phys. Chem. B*, 106(8):2004–2008, 2002.

[188] C.-S. Yih. Instability due to viscosity stratification. *J. Fluid Mech.*, 27(2):337–352, 1967.

[189] B. J. A. Zielinska, D. Bedeaux, and J. Vlieger. Electric and magnetic susceptibilities for a fluid-fluid interface; the ellipsometric coefficient. *Physica A*, 107(1):91–108, 1981.

[190] H. Zocher and F. Stiebel. Dark-field microscopy of thin films on liquid surfaces. *Z. Phys. Chem.*, 147:401–435, 1930.

Appendix A

On molecular orientations in Langmuir monolayers

In principle, there are four order parameters considered to describe the structures of different liquid crystal phases [59]:

1. Positional order:

   One can think of positional order (or in-plane positional order) as the degree of translational symmetry shown by the position of a group of molecules. Quantitatively, positional order is described by means of a density or position correlation function $G^{PO}(\overrightarrow{r})$ [161]:

   $$G^{PO}\left(\overrightarrow{r}-\overrightarrow{r}'\right)=\left\langle n\left(\overrightarrow{r}\right)n\left(\overrightarrow{r}'\right)\right\rangle-n^{2}, \tag{A.1}$$

   where $n(\overrightarrow{r})$ and $n(\overrightarrow{r}')$ are molecular densities at positions $\overrightarrow{r}$ and $\overrightarrow{r}'$, respectively, and n is the mean density of the sample. The brackets $\langle\rangle$ denote the statistical average. The product $n(\overrightarrow{r})n(\overrightarrow{r}')$ corresponds to the probability of meeting a certain density $n(\overrightarrow{r})$ at $\overrightarrow{r}$ and simultaneously a certain density $n(\overrightarrow{r}')$ at $\overrightarrow{r}'$.

2. Bond[1] orientational order:

   Bond orientational order (or lattice orientational order) concerns the relative geometrical arrangement of adjacent molecules. The degree of order is described by a bond orientational correlation function $G_n^{BO}(r)$ [124]:

   $$G^{BO}\left(\overrightarrow{r}-\overrightarrow{r}'\right)=\left\langle\Psi_n\left(\overrightarrow{r}\right)\Psi_n\left(\overrightarrow{r}'\right)\right\rangle, \tag{A.2}$$

   where

   $$\Psi_n\left(\overrightarrow{r}\right)=\frac{1}{N}\sum_{i=1}^{N}\exp\left[j\theta_i\left(\overrightarrow{r}\right)\right]$$

   is the bond orientational order parameter for n-fold symmetry [124]. $\theta_i(\overrightarrow{r})$ is the angle between a near neighbor bond at position $\overrightarrow{r}$ and external reference line. N is the number of direction neighbors.

[1] "Bond" refers to the geometrical line between nearest neighbors.

3. Tilt orientational order:

   The phenomenon that neighboring rod-like molecules (such as a long-chain amphiphile) adopt the same tilt angle and align parallel to each other is denoted as tilt orientational order (or molecular tilt azimuth order). This order can exist only when the molecules are tilted from the normal of the packing plane of the systems. Optical techniques, such as BAM and polarized FM, reveal that in condensed monolayer phases the molecules can be ordered by tilt over hundreds of μm [73, 174].

4. Herringbone order:

   If rod-like molecules hindered rotate, the molecules densely pack in the herringbone staking in the plane of the layers with herringbone order (or broken axial symmetry).

Each of these different kinds of orders can be described by its correlation function. The length scales on which the order is preserved will dominate the behavior of these correlation functions. One can distinguish *short range*, *quasi long range* and *long range*, which describe the level of the order parameters, from these correlation functions.

The classification of various smectic phases in Fig. A.1 is based on the above order parameters and the behavior of their correlation functions [174]. All phases in the right column of Fig. A.1 have long range tilt orientational order with some difference in the directions in which the molecular axis points. Only the crystalline phases (smectic BC, E, J, G, K and H) in Fig. A.1 have long rang positional order. Phases with short range positional order and long or quasi-long range 6-fold bond orientational order are term hexatic phases (*e.g.* smectic BH, I, L and F phases shown in Fig. A.1). When tilt occurs in the hexatic phase (smectic I, L and F phases), the tilt azimuth is not arbitrary but related to azimuth of the hexatic. Two symmetry-related tilt directions are along hexatic bonds (to the nearest neighbor, NN, such as smectic I and L phases) or between them (to the next-nearest neighbor, NNN, such as smectic F phases). In the smectic E, K, H and N phases, the rotation of molecules is partially hindered and the molecules exhibit herringbone stacking in the plane of the layers.

Figure A.1 illustrates the structures of various smectic liquid crystal phases [59, 18, 174]. From published X-ray diffraction data and existing isotherm information, it is possible to demonstrate a correspondence between the known monolayer phases and existing smectic categories. From the side view as shown in Fig. A.1, the distinction between the categories in the second and the third rows is meaningless for a monolayer system since these differ only in the correlations between different molecular layers. It is found that there is a strong resemblance between the structural features of single layers of smectic mesophases[2] and those of monolayers of long chain amphiphiles on water, such as the same types of molecular order, the variety of smectic phases based on. Therefore, the smectic liquid crystal phases can be applied to description of the different phases of Langmuir monolayers [18].

The phases in Fig. 2.4 have been characterized according to liquid crystalline smectic phases. The smectic categories have been taken from Ref. [18] (see Fig. A.1). We will describe these phases briefly [2]:

[2]synonym of liquid crystal phases

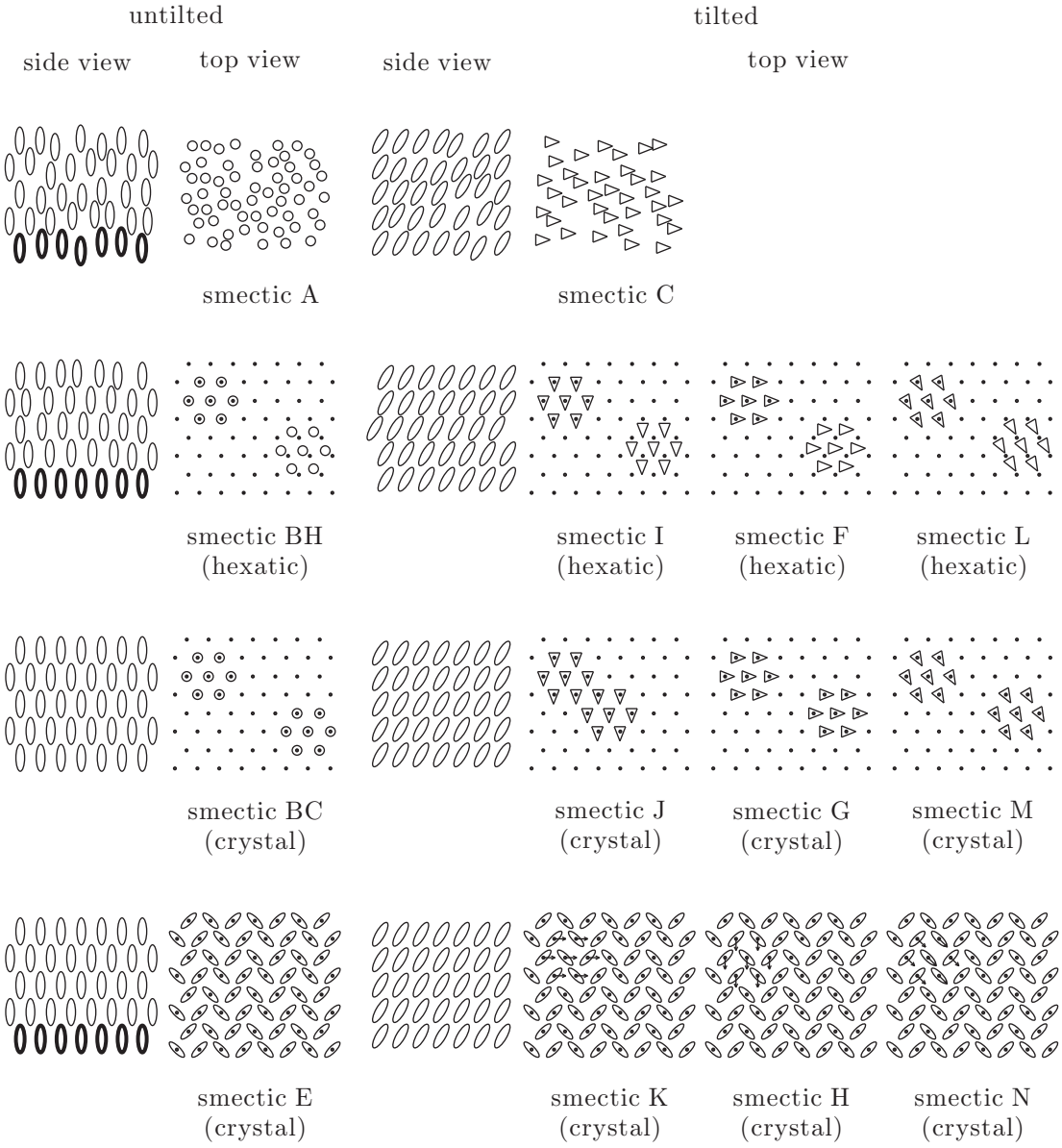

Figure A.1. Pictorial representations of the molecular statistics in the well-established smectic categories (adopted from Ref. [59]). The side view illustrates the layer stacking of molecules. Only the first row (thick line) is meaningful for Langmuir monolayers. The top view shows the in-plane ordering of molecules. In the top view, the dots are a triangular reference net. The open circles indicate the location of molecules and the molecules are freely and independently rotate about their long axes; the open triangles indicate the location and tilt direction of the molecules; and the open ellipses indicate location and hindered rotation of the molecules with respect to a triangular reference net (dots). The arrows indicate the tilt direction of the molecules.

◇ L_2

This is the primary liquid-condensed (LC) phase first considered by Adam [89] and Langmuir [97] as a semisolid film having hydrated polar heads. Now it is identified as a smectic I, or rotator phase, having short-range-positional order yet enough cross-sectional area to allow free rotation. The molecules are tilted relative to the normal, and the tilt angle varies with surface pressure. As the monolayer is compressed, the tilt angle diminishes in magnitude, and across the transition the tilt direction switches toward the next nearest neighbor. Ov denotes the phase discovered by Overbeck & Möbius [128]. It has only been detected by optical measurements and X-ray diffraction, but not by the isotherm measurements [128]. For symmetry reasons, the separation of the L_2 phase into herringbone ordered L_{2h} and disordered L_{2d} was proposed by Kaganer *et al.* [85]. Two tilted hexatic phase L_{2d} and Ov differ in their tilt azimuth (NN and NNN, respectively) [85].

◇ $L_2^{'}$

This region has been divided into two phases, L_2^* and $S^{'}$. The L_2^* phase differs from the L_2 phase in the direction of tilt. Molecules tilt toward their nearest neighbors in L_2 and toward next nearest neighbors in L_2^* (a smectic F phase). The $S^{'}$ phase comprises the higher-Π and lower-T part of $L_2^{'}$. This phase is characterized by smectic H or a tilted herringbone structure and there are two molecules (of different orientation) in the unit cell. Another phase having a different tilt direction, $L_1^{'}$, can appear between the L_2 phase and $L_2^{'}$ phase. A new phase has been identified in the $L_2^{'}$ domain. It is probably a smectic L structure of different azimuthal tilt than $L_2^{'}$ [129].

◇ LS

In the LS phase the molecules are oriented normal to the surface in a hexagonal unit cell. It is identified with the hexatic smectic BH phase. Chains can rotate and have axial symmetry due to their lack of tilt. This phase is optically isotropic and possesses equal mean distances between all neighbor molecules [85].

◇ S

Experimentally, a S phase is a mesophase with finite correlation lengths of translational order [85]. Chains in S phase are oriented normal to the surface, yet the unit cell is rectangular possibly because of restricted rotation. This structure is characterized as the smectic E or herringbone phase.

◇ CS

The CS phase is true 2-D crystal with chains oriented vertically. It exists at low T and high Π in the phase diagram of Fig. 2.4. This phase characterized by resolution-limited peaks in the X-ray diffraction experiments [85]. The structure exhibits long-range translational order.

Phases transitions at the scale of molecular interactions

BAM and polarized FM observations of the transition between condensed phases can be grouped into three categories with different changes of optical anisotropy [147, 85]:

1. transitions between an isotropic and an anisotropic phase (L_2'–LS, L_2–LS, Ov–LS, S–LS) are visible due to the complete loss of contrast;

2. transitions between a highly anisotropic tilted phase and a weakly anisotropic untitled phase (L_2''–CS, L_2'–CS, L_2'–S) also appear as a complete loss of contrast in polarized fluorescence microscopy experiments, but with BAM they are identified by a substantial decrease in the level of contrast between domains;

3. transitions between two anisotropic phases with approximately the same degree of anisotropy (L_2–L_2'', L_2'–L_2'', L_2–L_2', L_2–Ov, S–CS) are visible because the domain structure undergoes a sudden and repeatable rearrangement.

The phase transitions of fatty acids monolayers depend on temperature and the hydrocarbon chain length of fatty acids. For example, Earnshaw & Winch [45] demonstrated that the LE–LC phase transition depends on temperature for pentadecanoic acid monolayer as shown in Fig. 2.5. Bibo & Peterson [19] matched the phase-transition lines of fatty acids monolayers on a generalized Π–T phase diagram by shifting systematically the temperature axis by 5 to 10 °C per additional methylene group. The phase diagrams for C_{20}, C_{22} and C_{24} fatty acids were matched unambiguously based on positions of the LS–L_2'–L_2 triple points, while matching of the shorter-chain phase diagrams remained somewhat ambiguous. Discovery of the LS–O_v–L_2 triple point [129] allows us to place these phase diagrams more precisely. In Fig. A.2, the phase diagrams are matched by bringing both triple points in coincidence [132, 129, 85]. Then, a fixed shift of the temperature axis by 5 °C per each methylene group is required for chain lengths from C_{16} to C_{22}. Thus, monolayers of fatty acids formed by molecules differing only in the length of the chain experience the same sequence of phase transitions, but at different temperatures. Figs. 2.5 and A.2 reveal that an increase in temperature has increased the surface pressure of the L_1–L_2 (LE–LC) phase transition. In addition, Fig. A.2 shows that a decrease in the hydrocarbon chain length produces a similar result. Both effects may be understood by considering the forces between the molecules in the floating monolayer. A decrease in the length of the chain leads to decreased van der Waals' force between the molecules, which results in reduced cohesion within the monolayer; in contrast, a decrease in temperature leads to less thermal motion, which tends to condense the monolayer [133]. Qualitatively, the constructed phase diagram (Fig. A.2) has a similar topology to that previously reported in the literatures [160, 19, 103, 88, 18, 129, 153]. The phase diagrams (Figs. 2.4 and A.2) are not final yet for Langmuir monolayers since there are various other indications for presence of phase transitions; however these are not sufficiently well established and sometimes contradict each other [85].

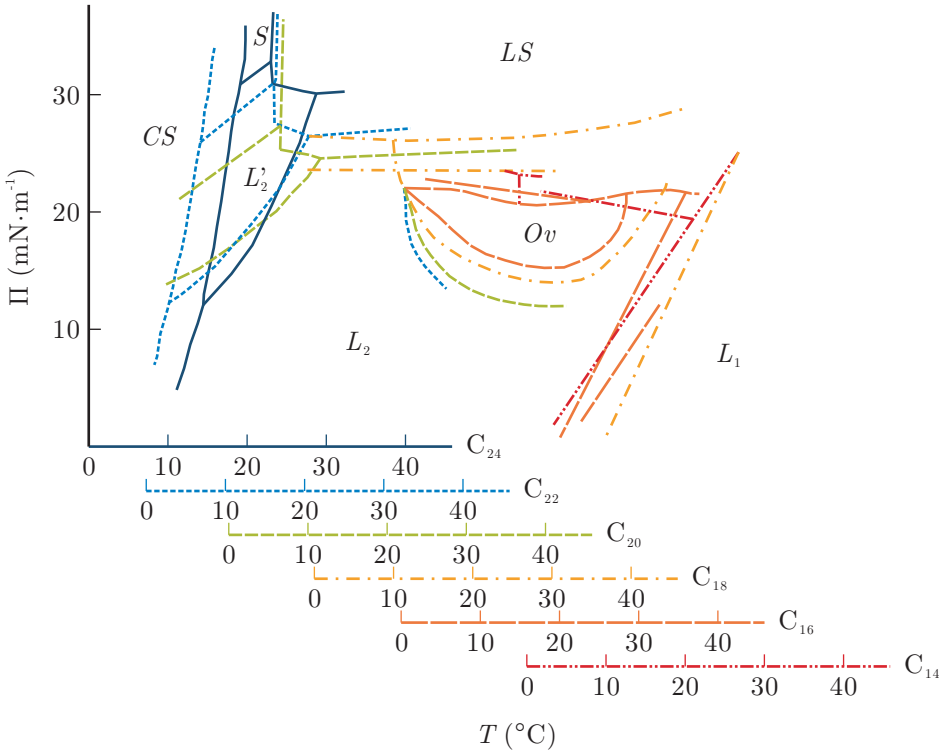

Figure A.2. Π–T phase diagrams of fatty acid monolayers (C_{14} to C_{24} acids). Adapted from Peterson *et al.* [132], with data by Overbeck & Möbius [129] added to locate the relative positions of the C_{16} to C_{20} phase diagrams more precisely (adopted from Ref. [85]).

Appendix B

Mannheimer & Schechter's modeling of the deep-channel surface viscometer

For a incompressible fluid, the governing equations are: the continuity equation

$$\operatorname{div} \overrightarrow{v} = 0 \,, \tag{B.1}$$

and the Navier-Stokes equation

$$\rho \left[\frac{\partial \overrightarrow{v}}{\partial t} + \overrightarrow{v} \cdot \nabla \overrightarrow{v} \right] = -\nabla P + \mu_b \nabla^2 \overrightarrow{v} + \rho \overrightarrow{g} \,. \tag{B.2}$$

A theoretical analysis of the annular channel of the viscometer was performed by Mannheimer & Schechter [112]. The governing equations are the axisymmetric Navier-Stokes equations, together with the continuity equation and appropriate boundary and initial conditions. A cylindrical polar coordinate system (r, θ, z) with associated sub-phase velocity $\overrightarrow{v} = (u_r, v_\theta, w_z)$ is used, and on the interface the surface velocity vector is $\overrightarrow{v_s} = (u_{r,s}, v_{\theta,s})$. Then, the governing equations will be written in cylindrical polar coordinates as:

$$\frac{1}{r}\frac{\partial r v_r}{\partial r} + \frac{\partial w_z}{\partial z} = 0, \tag{B.3}$$

$$\rho \frac{\partial u_r}{\partial t} = -\frac{\partial P}{\partial r} + \mu_b \left\{ \frac{1}{r}\frac{\partial}{\partial r}\left[r \frac{\partial u_r}{\partial r} \right] - \frac{u_r}{r^2} + \frac{\partial^2 u_r}{\partial z^2} \right\}, \tag{B.4}$$

and

$$\rho \frac{\partial w_z}{\partial t} = -\frac{\partial P}{\partial z} + \rho g + \mu_b \left\{ \frac{1}{r}\frac{\partial}{\partial r}\left[r \frac{\partial w_z}{\partial r} \right] + \frac{\partial^2 w_z}{\partial z^2} \right\}. \tag{B.5}$$

The hydrodynamical coupling between surface and sub-phase flow is taken into account through the the components of the jump of momentum balance (Eq. (3.12)) at the the liquid surface. As demonstrated by [156], the jump of momentum balance (JMB) can be projected tangentially along the air-water interface and doing that, is is possible to derive relevant boundary conditions for the sub-phase flow: the azimuthal

and radial tangential component of the JMB write:

$$\mu_b \frac{\partial v_\theta}{\partial z} = \mu_s \left[\frac{\partial^2 v_{\theta,s}}{\partial r^2} + \frac{1}{r}\frac{\partial v_{\theta,s}}{\partial r} - \frac{v_{\theta,s}}{r^2} \right] + \frac{\partial \mu_s}{\partial r} \left[\frac{\partial v_{\theta,s}}{\partial r} - \frac{v_{\theta,s}}{r} \right], \tag{B.6}$$

and

$$\begin{aligned} \mu_b \left.\frac{\partial u_r}{\partial z}\right|_s + \frac{\partial \Pi}{\partial r} = [\kappa_s + \mu_s] \left[\frac{1}{r}\left.\frac{\partial w_z}{\partial z}\right|_s + \frac{\partial^2 u_{r,s}}{\partial r^2} + \frac{2}{r}\frac{\partial u_{r,s}}{\partial r} \right] \\ - \frac{\partial [\kappa_s + \mu_s]}{\partial r} \left.\frac{\partial w_z}{\partial z}\right|_s + \frac{2u_{r,s}}{r}\frac{\partial \mu_s}{\partial r}, \end{aligned} \tag{B.7}$$

respectively. The boundary condition (B.7) exhibits the balance between the Marangoni term, $\frac{\partial \Pi}{\partial r}$, and the shear stress $\mu_b \left.\frac{\partial u_r}{\partial z}\right|_s$ due to the centrifugation-induced radial flow at the liquid surface.

The following assumptions are formulated to calculate the velocity profile along the channel:

1. Flat interface.
2. Viscous subphase in the channel.
3. Viscous interface.
4. Air above the monolayer considered as negligible in regard of the momentum transport.
5. Laminar flow with only one significant azimuthal velocity component (no secondary flow[1]).
6. The surface shear viscosity is therefore uniform ($\nabla_s \mu_s = 0$).
7. Permanent flow.
8. No surface aging.

With the above assumptions, it is consistent to disregard (B.5) and (B.7) and to solve the following set of coupled Stokes equations (B.4) - (B.6) in polar coordinates:

$$\frac{\partial^2 v_\theta}{\partial r^2} + \frac{1}{r}\frac{\partial v_\theta}{\partial r} - \frac{v_\theta}{r^2} + \frac{\partial^2 v_\theta}{\partial z^2} = 0, \tag{B.8}$$

with the following boundary conditions:

$$\begin{aligned} v_\theta(r_o, z) = 0, \\ v_\theta(r_i, z) = 0; \end{aligned} \tag{B.9}$$

$$v_\theta(r, 0) = r\Omega; \tag{B.10}$$

[1]This assumption remains consistent if the Reynolds number is small enough (Re << 100) or if the LM is saturated (vanishingly small Marangoni effect).

$$\mu_s \left[\frac{d^2 v_{\theta,s}}{dr^2} + \frac{1}{r}\frac{dv_{\theta,s}}{dr} - \frac{v_{\theta,s}}{r^2} \right] = \mu_b \frac{\partial v_\theta\,(r,z)}{\partial z}\bigg|_{z=h}. \tag{B.11}$$

Equation (B.9) states that the velocity is zero at both the inner wall (r_i) and the outside wall (r_o), Eq. (B.10) describes the Couette flow along the moving floor, and Eq. (B.11) is the reduced form of the boundary condition (B.6).

An analysis of this boundary value problem resulted in the following series solutions for the surface velocity [111]:

$$v^*_{\theta,s} = \frac{2}{\frac{r_o}{e}} \sum_{i=1}^{\infty} \left\{ \frac{\left[\left[\frac{r_o}{e}\right]^2 \psi_0\left(\frac{r_o}{e}\beta_i\right) - \left[\frac{r_i}{e}\right]^2 \psi_0\left(\frac{r_i}{e}\beta_i\right)\right]}{\beta_i \left[\left[\frac{r_i}{e}\right]^2 \psi_0^2\left(\frac{r_i}{e}\beta_i\right) - \left[\frac{r_o}{e}\right]^2 \psi_0^2\left(\frac{r_o}{e}\beta_i\right)\right]} \cdot \frac{\psi_1\left(\frac{r}{e}\beta_i\right)}{\left[\cosh\left(\beta_i\frac{h}{e}\right) + \beta_i\frac{\mu_s}{\mu_b e}\sinh\left(\beta_i\frac{h}{e}\right)\right]} \right\} \tag{B.12}$$

where

$$v^*_{\theta,s} = \frac{v_{\theta,s}}{r_o\Omega},$$

$$\psi_0\left(\frac{r}{e}\beta_i\right) = J_0\left(\frac{r}{e}\beta_i\right) Y_1\left(\frac{r_i}{e}\beta_i\right) - J_1\left(\frac{r_i}{e}\beta_i\right) Y_0\left(\frac{r}{e}\beta_i\right),$$

and

$$\psi_1\left(\frac{r}{e}\beta_i\right) = J_1\left(\frac{r}{e}\beta_i\right) Y_1\left(\frac{r_i}{e}\beta_i\right) - J_1\left(\frac{r_i}{e}\beta_i\right) Y_1\left(\frac{r}{e}\beta_i\right).$$

The quantities J and Y are Bessel functions of the first and second kind with subscripts to denote their orders. Here β_i is the $i$the root of the relation:

$$J_1\left(\frac{r_o}{e}\beta_i\right) Y_1\left(\frac{r_i}{e}\beta_i\right) - J_1\left(\frac{r_i}{e}\beta_i\right) Y_1\left(\frac{r_o}{e}\beta_i\right) = 0.$$

To obtain the estimation of μ_s, the least squares method which minimizes the summed square of residuals was used to fit the experimental surface velocity. The fitting process used Eq. (B.12) as a model that relates r to $v^*_{\theta,s}$ with adjusting μ_s.

Appendix C

Impact of the radial flow on the packing density: scaling analysis

As already mentioned in the theoretical part (Section 5.2), the molecular packing due to the radial flow along the surface is to be considered if the LM remains weakly densified. If the shear deformation induced by the leading azimuthal flow is small enough, the LC domains are close to condensed drops whose typical shape is circular as long as the effective line tension is large enough to balance inertial forces or shear stresses. In such conditions, it remains that the condensed drop diameter is possibly driven by the radial distribution of the molecular area along the dividing surface. If shear-induced deformation becomes significant, this typical diameter can be reduced under the effect of shear atomization but it remains nevertheless that the density number of condensed drops can significantly increase if molecular area is significantly small.

The radial flow along the surface, issued from the centrifugation of the underlying subphase, can generate a surface chemical gradient and consequently, a nonuniform distribution of the condensed drops. The radial component of the jump momentum balance along the liquid surface involves that the shear stress at the interface sustains a (compositional) Marangoni stress:

$$\mu_b \left.\frac{\partial v_r}{\partial z}\right|_s \sim \frac{\partial \Pi}{\partial r}, \tag{C.1}$$

as long as the energy dissipation due to surface viscosities is not significant, with

$$\frac{\partial \Pi}{\partial r} \cong \frac{\partial A}{\partial r}\left.\frac{d\Pi}{dA}\right|_{equilibrium}, \tag{C.2}$$

provided that the flow-induced reorganization does not question the experimental isotherm $\Pi = f(A)$, a condition which is supposed to hold only for a weak perturbation of the thermodynamic equilibrium. From Eq. (C.1), we can estimate

$$\frac{\partial \Pi}{\partial r} \sim \frac{\delta \Pi}{r_o} \sim \frac{\mu_b v_r}{h}.$$

Hence, from Eq. (C.2), the molecular segregation scales as:

$$\frac{\partial A}{\partial r} \sim \frac{\frac{\mu_b v_r}{h}}{\left.\frac{d\Pi}{dA}\right|_{equilibrium}}. \tag{C.3}$$

A typical scale for the radial flow, v_r, remains to be estimated. The radial pressure gradient within the subphase can be approximated from the centrifugal force,

$$\nabla_r P \sim \rho_b r_o \Omega^2, \tag{C.4}$$

where ρ_b denotes the density of the subphase. By considering that inertia is negligible compared to viscous friction, the balance between the viscous term and the pressure gradient writes

$$\nu_b \Delta v_r \sim \frac{1}{\rho_b} \nabla_r P. \tag{C.5}$$

From Eqs. (C.4) and (C.5), a scale for the recirculating flow writes

$$v_r \sim \frac{r_o \left[\Omega \, h/2\right]^2}{\nu_b}. \tag{C.6}$$

Finally, according to Eq. (C.3), the radially inwards flow-induced molecular packing along the channel gap scales as

$$\delta A \sim \frac{\rho_b {r_o}^2 h \Omega^2}{\left.\frac{d\Pi}{dA}\right|_{equilibrium}} \approx 0.1 \text{ Å}^2 \cdot \text{molecule}^{-1}, \tag{C.7}$$

with $h = 10$ mm, $\rho_b = 1000$ kg·m^{-3}, $r_o = 70$ mm, $\Omega \approx 0.1$ rpm and

$$\left.\frac{d\Pi}{dA}\right|_{equilibrium} \approx -0.1 \text{ (mN} \cdot \text{m}^{-1}) \cdot (\text{Å}^2 \cdot \text{molecule}^{-1})^{-1},$$

as made evident from adsorption isotherm (Fig. 4.5).

Appendix D

Modelling of surface flow: the asymptotic case of a full cylinder

This appendix, as a complement of section (6.8), addresses the modelling of surface flow when the trough becomes a full cylinder since it is also a geometry currently involved in the literature [9, 10]. From our point of view, this corresponds to a particular case of the present modelling: it is easily checked that the velocity along the liquid surface, $v^*_{\theta,s}$, tends toward a finite value for a vanishingly small aspect ratio:

$$\frac{r_i}{r_o} \to 0.$$

In the expressions of $v^*_{\theta,s}$, only the forcing term $f(r^*)$ and the coefficients $A(r^*)$, $B(r^*)$, $C(r^*)$, $D(r^*)$ depend on ${}^{r_i}/_{r_o}$. Hence, for a full cylinder, the expressions (6.32) and (6.35)-(6.38) must be updated as follows:

$$f(\xi) \underset{\frac{r_i}{r_o}\to 0}{\to} -\xi + 2\frac{\exp\left(-\pi\dfrac{1-\xi}{\delta}\right)}{1+\exp\left(-\pi\dfrac{1-\xi}{\delta}\right)}, \tag{D.1}$$

$$A(r^*) \underset{\frac{r_i}{r_o}\to 0}{\to} \frac{1}{Bo}\,\frac{I_1\left(\dfrac{r^*}{\sqrt{Bo}}\right)K_1\left(\dfrac{1}{\sqrt{Bo}}\right) - I_1\left(\dfrac{1}{\sqrt{Bo}}\right)K_1\left(\dfrac{r^*}{\sqrt{Bo}}\right)}{I_1\left(\dfrac{1}{\sqrt{Bo}}\right)}, \tag{D.2}$$

$$B(r^*) \underset{\frac{r_i}{r_o}\to 0}{\to} 0, \tag{D.3}$$

$$C(r^*) \underset{\frac{r_i}{r_o}\to 0}{\to} \frac{1}{Bo}\,K_1\left(\frac{1}{\sqrt{Bo}}\right)\frac{I_1\left(\dfrac{r^*}{\sqrt{Bo}}\right)}{I_1\left(\dfrac{1}{\sqrt{Bo}}\right)}, \tag{D.4}$$

$$D(r^*) \underset{\frac{r_i}{r_o}\to 0}{\to} -\frac{1}{Bo}\,I_1\left(\frac{r^*}{\sqrt{Bo}}\right). \tag{D.5}$$

A straightforward consequence is that the shear stress at the liquid surface simpli-

fies to:

$$\tau^*_{b,comp} = v_s(r^*) - r^* + 2\frac{\exp\left(-\pi\dfrac{1-r^*}{\delta}\right)}{1+\exp\left(-\pi\dfrac{1-r^*}{\delta}\right)}. \tag{D.6}$$

For a uniform contamination, it is worthy to calculate explicitly the velocity along the liquid. Doing this, it is necessary to verify that the integral

$$\int_{\frac{r_i}{r_0}}^{r^*} f(\xi)G(r^*|\xi)d\xi$$

is not singular when

$$\frac{r_i}{r_o} \to 0,$$

a requirement which is clearly fulfilled since

$$f(\xi)\xi\, I_1\left(\frac{\xi}{\sqrt{Bo}}\right) \underset{\xi\to 0}{\to} 0.$$

As a consequence, when

$$\frac{r_i}{r_o} \to 0,$$

the velocity $v_{\theta,s}$ writes explicitly:

$$\begin{aligned} v^*_{\theta,s}(r^*) = \frac{1}{Bo}\,&\frac{I_1\left(\dfrac{r^*}{\sqrt{Bo}}\right)K_1\left(\dfrac{1}{\sqrt{Bo}}\right) - I_1\left(\dfrac{1}{\sqrt{Bo}}\right)K_1\left(\dfrac{r^*}{\sqrt{Bo}}\right)}{I_1\left(\dfrac{1}{\sqrt{Bo}}\right)}\int_0^{r^*} f(\xi)\xi\, I_1\left(\frac{\xi}{\sqrt{Bo}}\right)d\xi \\ &+ \frac{1}{Bo}\,K_1\left(\frac{1}{\sqrt{Bo}}\right)\frac{I_1\left(\dfrac{r^*}{\sqrt{Bo}}\right)}{I_1\left(\dfrac{1}{\sqrt{Bo}}\right)}\int_r^1 f(\xi)\xi\, I_1\left(\frac{\xi}{\sqrt{Bo}}\right)d\xi \\ &- \frac{1}{Bo}\,I_1\left(\frac{r^*}{\sqrt{Bo}}\right)\int_r^1 f(\xi)\xi\, K_1\left(\frac{\xi}{\sqrt{Bo}}\right)d\xi. \end{aligned}$$

Interestingly, the impact of the outer boundary layer upon $v^*_{\theta,s}(r^*)$ is significantly reduced (if δ is small enough) as it can be demonstrated from the linearity of the velocity profile near the axis of revolution.

For the situation of a regular (smooth) viscous stratification, the integral formulation to solve is still defined from (6.46) but with Green kernels, $k_1(r^*|\xi)$ and $k_2(r^*|\xi)$, and the non-homogeneous term, $h(r^*)$ (see (6.47) to (6.49)), to be updated by taking into account the new coefficients (D.2) to (D.5).
Nevertheless, it is worthy to note that this modeling is limited to the situation of either a uniform contamination or a regular stratification at most. As a matter of fact, for a steep segregation front arising for instance from the radial growth of a 2-D crystal at the centre of the liquid surface, there is the possibility that the crystal could rotate under the effect of shearing [1].

[1] An alternative way to avoid crystal rotation could be to maintain it at rest by applying an external force at the centre (wire technique for instance).

D.1 Rsum

L'objectif de cette thse est de contrler un coulement recirculant dans une sous-phase permettant la densification en 2-D de biomolcules amphiphiles une surface liquide. Pour cela, une exprience base sur une cuve annulaire est dveloppe afin d'tudier le comportement d'une monocouche d'acide pentadecanoque (PDA) soumise simultanment des cisaillements volumique et surfacique. Ces deux cisaillements sont produits par la rotation d'une couronne annulaire aimante dispose au fond d'une cuve annulaire maintenue immobile. Une nouvelle organisation msoscopique dans le film de PDA, sous la forme de deux phases 2-D (liquide expanse et liquide condense), est mise en vidence et tudie en rgime permanent par microscopie Brewster. A partir de la distribution de fraction arolaire de la phase condense, on montre que l'coulement centrifuge le long du fond tournant engendre une compression radiale centripte le long de l'interface. Celle-ci privilgie la condensation de domaines condenss vers les rayons les plus petits. Pour un niveau suffisant de centrifugation, le film de Langmuir exprimente une transition morphologique pilote par l'quilibre entre cisaillement de surface et tension de ligne effective. En particulier, le cisaillement surfacique induit la fusion des domaines condenss et engendre une nouvelle organisation morphologique sous la forme d'une matrice monodisperse de gouttelettes 2-D condenses. Dans des conditions plus densifies, la phase condense s'organise sous la forme de films stratifis. Dans ce cas, si la vitesse de rotation augmente (nombre de Reynolds de l'ordre de 1000 ou plus), le niveau de cisaillement volumique devient suffisant pour engendrer la fragmentation radiale des films condenss, en bon accord avec la littrature. Une nouvelle formulation (analytique) intgrale de l'coulement annulaire cisaill est propose pour estimer le nombre de Boussinesq et la stratification de viscosit de surface.

D.2 Mots-clefs

Ecoulement, cisaillement, tensioactifs, monocouche de Langmuir, viscosit de surface, Stokes, lubrification

D.3 Abstract

This thesis is devoted to a flow process whose aim is to densify amphiphilic biomolecules along an air-water interface. Use is made of pentadecanoic acid (PDA) as a model system. The experiments are based on a shear flow provided in an annular channel whose floor is put in rotation while its two vertical cylindrical side walls

are maintained stationary. The flow is considered as permanent and axisymmetric with a low Reynolds number (Re¡100). The liquid surface at the top of the annular channel is covered by a Langmuir layer of PDA submitted to a bulk shear at the liquid surface as well as a surface 2-D shear along it. Flow-induced morphology of the PDA film at mesoscopic scale is made evident and investigated under a Brewster angle microscope (BAM). During phase transition from the liquid-expanded (LE) to the liquid-condensed (LC) state, a dispersed Langmuir film of PDA is investigated based on area fraction distribution of the LC phase after a permanent regime is established. The distribution demonstrates a radially inwards packing along the liquid surface induced by a centripetal flow originating from centrifugation of the subphase along the rotating floor. For a growing level of centrifugation, the Langmuir film experiences a strong morphological transition driven by a balance between surface shear and a reduced line tension. As a result, a shear-induced melting of the condensed domains generates a new patterning which can be described as a regular and monodispersed matrix of tiny condensed droplets. For a highly densified PDA film, LC domains are organised according to stratifying films. If sub-phase rotation is large enough, (Re as large as 1000), the bulk shear is responsible for the break-up of the streched LC domains in agreement with existing literature. A new analytical modelling is proposed to include the impact of a radial molecular packing on surface viscosity at a small Reynolds number. A new integral formulation is made evident which enables a fair estimation of the Boussinesq number as well as a measurement of a stratified surface viscosity.

D.4 Key-words

Annular flow, shear, surfactants, Langmuir monolayer, surface viscosity, Stokes, lubrication